

WISCONSIN HIGHWAY RESEARCH PROGRAM # 0092-07-05

**DEVELOPMENT OF TESTING METHODS TO DETERMINE INTERACTION
OF GEOGRID-REINFORCED GRANULAR MATERIAL FOR MECHANISTIC
PAVEMENT ANALYSIS**

A DRAFT REPORT

Principal Investigators: Tuncer B. Edil and Dante Fratta

Graduate Research Assistants: Craig C. Schuettpelz

Geo Engineering Program
Department of Civil and Environmental Engineering
University of Wisconsin-Madison

SUBMITTED TO THE WISCONSIN
DEPARTMENT OF TRANSPORTATION

March 1, 2009

ACKNOWLEDGEMENT

Financial support for this study was provided by the Wisconsin Department of Transportation (WisDOT) through the Wisconsin Highway Research Program (WHRP). Mr. Felipe F. Camargo provided resilient modulus test data. Mr. X. Wang provided technical support with the experiments.

DISCLAIMER

This research was funded through the Wisconsin Highway Research Program by the Wisconsin Department of Transportation and the Federal Highway Administration under Project # 0092-07-05. The contents of this report reflect the views of the authors who are responsible for the facts and accuracy of the data resented herein. The contents do no necessarily reflect the official views of the Wisconsin Department of Transportation or the Federal Highway Administration at the time of publication.

This document is disseminated under the sponsorship of the Department of Transportation in the interest of information exchange. The United State Government assumes no liability for its contents or use thereof. This report does not constitute a standard, specification or regulation.

The United States Government does not endorse products or manufacturers. Trade and manufacturers' names appear in this report only because they are considered essential to the object of the document.

Technical Report Documentation Page

1. Report No. WHRP XXXXX	2. Government Accession No	3. Recipient's Catalog No	
4. Title and Subtitle DEVELOPMENT OF TESTING METHODS TO DETERMINE INTERACTION OF GEOGRID-REINFORCED GRANULAR MATERIAL FOR MECHANISTIC PAVEMENT ANALYSIS		5. Report Date March 2009	6. Performing Organization Code University of Wisconsin-Madison
7. Authors Tuncer B. Edil, Dante Fratta, Craig C. Shuettpezl		8. Performing Organization Report No.	
9. Performing Organization Name and Address Geological Engineering Program, Department of Civil and Environmental Engineering University of Wisconsin-Madison 1415 Engineering Drive Madison, WI 53706		10. Work Unit No. (TRAIS)	11. Contract or Grant No. WisDOT SPR# 0092-07-05
12. Sponsoring Agency Name and Address Wisconsin Department of Transportation Division of Business services Research Coordination Section 4802 Sheboygan Avenue Room 104 Madison, WI 53707-7965		13. Type of Report and Period Covered Final report, 2004-2007	14. Sponsoring Agency Code
15. Supplementary Notes			
16. Abstract <p>A new method of examining soil stiffness based on the propagation of elastic waves is proposed and compared to traditional resilient modulus tests. A laboratory testing program is undertaken to study the effect of changing bulk stress, strain level, and void ratio on the velocity of elastic waves. Using a proposed formulation, low-strain ($\sim 10^{-6}$ mm/mm) moduli calculated with seismic methods are converted to higher strain ($\sim 3 \times 10^{-4}$ mm/mm) resilient moduli. Results of this study indicate that resilient moduli are approximately 29 % that of the seismic moduli based on stress and strain. A simplified seismic testing scheme that can be used on the soil surface was developed and provides an efficient method to compare seismic and resilient moduli. The new proposed methodology allows for the characterization of materials containing large grains (>25 mm) (e.g., breaker run, pit run sand and gravel) that cannot be easily tested with the current resilient modulus methodology.</p> <p>Soil modulus and particle rotation were monitored using micro-electronic-mechanical-systems to determine the aggregate-geogrid interaction in base course materials. Velocity results indicate that the geogrid stiffens soil near the geogrid by a minimum factor of 1.3 (geogrid placed at a depth of 75 mm from the surface) to a maximum of 2.6 (geogrid at 100 mm depth). Rotation tests show a "zone of influence" no more than 50 mm on both sides of the geogrid reinforcement; however, the "zone of influence" depends on the position of the geogrid, geogrid at 100 mm depth seems to be the most effective. Comparisons made with available field geogrid reinforcement cases support these findings.</p>			
17. Key Words Granular materials, materials with large particles, geogrid, modulus, resilient modulus test, large-scale model test, seismic test, micro-electronic-mechanical-systems		18. Distribution Statement No restriction. This document is available to the public through the National Technical Information Service 5285 Port Royal Road Springfield VA 22161	
19. Security Classification (of this report) Unclassified	19. Security Classification (of this page) Unclassified	20. No. of Pages	21. Price

EXECUTIVE SUMMARY

DEVELOPMENT OF TESTING METHODS TO DETERMINE INTERACTION OF GEOGRID-REINFORCED GRANULAR MATERIAL FOR MECHANISTIC PAVEMENT ANALYSIS

Deformation of the asphalt pavement system depends on the stiffness of subsurface materials. The use of geogrid reinforcement in base courses and subgrade materials is a method to improve the mechanical behavior of the pavement system for extended road life. Methods for quantitatively assessing the benefits of the geogrid have yet to be determined. This research uses local rotations and changes in elastic wave velocity to examine the change in stiffness and soil structure surrounding a geogrid reinforcing layer.

The stiffness of base course and subgrade soils is typically characterized with the resilient modulus test. A new method of examining soil stiffness based on the propagation of elastic waves is proposed and compared to traditional resilient modulus tests. A laboratory testing program is undertaken to study the effect of changing bulk stress, strain level, and void ratio on the velocity of elastic waves. Using a proposed formulation, low-strain ($\sim 10^{-6}$ mm/mm) moduli calculated from seismic wave velocity are converted to higher strain ($\sim 3 \times 10^{-4}$ mm/mm) resilient moduli. Results of this study indicate that resilient moduli are approximately 30 % that of the seismic moduli based on stress and strain levels. A simplified seismic testing scheme that can be used on the soil surface was developed and provides an efficient method to estimate resilient moduli from seismic wave velocity. The proposed methodology allows for the characterization of materials containing large grains (>25 mm) (e.g., breaker run, pit run sand and gravel) that cannot be easily tested with the current resilient modulus methodology.

The “zone of influence” of the geogrid layer on surrounding aggregate particles and the presumed increase in modulus of this zone are unknown. Soil modulus and particle rotation were monitored using micro-electronic-mechanical-systems (MEMS) accelerometers to determine the aggregate-geogrid interaction in base course materials. Both elastic wave velocity and the shear strain induced by a plate load are examined to assign a “zone of influence” of the geogrid layer on surrounding soil. Wave velocity results indicate that the geogrid stiffens soil near the geogrid by a factor of 1.4 to 2.6. Expected soil rotation with and without geogrid reinforcement was modeled with PLAXIS, a finite element code, and compared to laboratory tests. Rotation tests show a “zone of influence” no more than 50 mm on both sides of the geogrid reinforcement. A geogrid placed at 100 mm depth below a loading plate (150 mm in diameter) seems to be the most effective compared to placing at depths of 75 and 150 mm. Comparisons made with available field geogrid reinforcement tests support these findings.

Based on the research reported above, certain observations relevant to practical applications can be advanced.

1. Pit run gravel and breaker run have P-wave calculated resilient moduli of 280 MPa and 320 MPa, respectively, at specified field compaction

- densities. As a means of comparison, these moduli are 25 % and 34 % greater than the moduli of grade 2 gravel at field density conditions.
2. Mean grain size relative to geogrid aperture size is an important factor to generate geogrid interaction and should be carefully considered. Materials with too large or too small mean grain size may not effectively engage the geogrid depending on the aperture size.
 3. In-plane modulus, web and node strengths as well as aperture size of the geogrid should be specified for unbound material modulus improvement purposes taking into consideration of the grain size of the granular material.
 4. A conservative resilient modulus improvement of 1.5 can be used with a reinforced zone thickness of 50 mm on both sizes of the geogrid.
 5. There seems to be an optimum location for placing the geogrid (e.g., 100 mm below the loading plate); however, this conclusion can not be simply extrapolated to the field without further investigation. Practical considerations also determine the location of the geogrid.

Table of Contents

ACKNOWLEDGEMENT	ii
EXECUTIVE SUMMARY	v
Table of Contents	vii
LIST OF FIGURES	xi
LIST OF TABLES	xix
1 INTRODUCTION	1
2 BACKGROUND	6
2.1 GEOSYNTHETICS IN ROAD CONSTRUCTION	6
2.2 MECHANISM OF REINFORCEMENT BY GEOGRID-PARTICLE INTERACTION.....	8
2.3 STRESS DISTRIBUTION BELOW A CIRCULAR PLATE	12
2.4 SOIL STIFFNESS AND MODULUS	19
2.4.1 Modulus	19
2.4.2 Resilient Modulus	23
2.4.3 Strain Dependency of Modulus	28
2.4.4 Non-Strain Dependent Direct Resilient Modulus/Seismic Modulus Condition.....	36
2.4.5 Large-scale Cyclic Load Conditions.....	38
2.5 WAVE PROPAGATION AND THE RELATIONSHIP BETWEEN STRESS, MODULUS, AND VELOCITY	39
2.5.1 Hertz Contact Theory	39
2.5.2 Modes of Wave Propagation.....	43
2.6 MODULUS REINFORCEMENT FACTOR.....	47
2.7 ROTATION OR SHEARING OF SOIL	48
2.7.1 Modeling Rotation with PLAXIS	49
3 MEASUREMENT TECHNIQUES, MATERIALS, AND METHODS	51
3.1 MICRO-ELECTRO-MECHANICAL SYSTEMS (MEMS) ACCELEROMETERS	51
3.1.1 Description.....	51
3.1.2 Principles of Operation.....	53

3.2	MEASURING ELASTIC WAVE VELOCITY WITH MEMS ACCELEROMETERS	56
3.3	MONITORING ROTATION WITH MEMS ACCELEROMETERS	57
3.4	TEST MATERIALS	61
	Figure 3.6. Grain size distribution for materials tested in laboratory experiments....	64
3.5	TESTING CELLS.....	66
3.6	MODULUS COMPARISON TEST METHODS	69
3.6.1	Preliminary Tests	69
3.6.2	Seismic Modulus Tests	69
3.6.3	Large-scale Elastic Modulus Test Method	75
3.7	GEOGRID INTERACTION TEST METHODS	78
3.7.1	Seismic Tests	78
3.7.2	Rotation Tests.....	78
4	RESULTS AND ANALYSIS OF COMPARISON BETWEEN RESILIENT MODULUS AND MODULUS BASED ON SEISMIC MEASUREMENTS.....	81
4.1	EFFECTIVENESS OF MEMS ACCELEROMETERS TO DETERMINE THE CHANGE IN VELOCITY IN SAND	82
4.2	RESILIENT MODULUS TESTS.....	86
4.3	LARGE-SCALE CYCLIC LOAD MODULUS TESTS	91
	Figure 4.5. Large-scale cyclic load modulus (E_{LS}) as a function of bulk stress.	93
4.4	SEISMIC MODULUS TESTS	93
4.5	MECHANISTIC METHOD FOR DETERMINING THE RESILIENT MODULUS OF BASE COURSE BASED ON ELASTIC WAVE MEASUREMENTS.....	96
4.5.1	Stress Level Corrections.....	96
4.5.2	Void Ratio Corrections.....	98
4.5.3	Strain Level Corrections.....	99
	Figure 4.9. Final average backbone curve showing resilient modulus results.	102
4.5.4	Conversion of Constraint Modulus to Young's Modulus	103
	Figure 4.11. Determination of angle of repose (β).....	105
4.5.5	Evaluation of Corrected Seismic Modulus on Base Course Materials and Large-Grain Materials.....	107

4.5.6	Summary of Mechanistic Evaluation of Resilient Modulus Using P-wave Velocities	109
4.5.7	Large-Scale Cyclic Load Test Moduli	111
4.5.8	Additional Backbone Curve Results.....	112
4.6	SMALL SCALE SIMPLE SEISMIC TEST RESULTS.....	113
5	RESULTS AND ANALYSIS OF THE INFLUENCE OF GEOGRID ON ELASTIC WAVE PROPAGATION AND ROTATION	116
5.1	SURFACE DISPLACEMENTS	116
5.2	FINITE ELEMENT ANALYSIS OF GEOGRID-REINFORCED BASE COURSE MATERIAL IN LARGE LABORATORY TESTING CELL	119
5.2.1	Material Models and Properties	119
5.2.2	Model Setup.....	121
5.2.3	PLAXIS Model Results	123
5.2.4	Summary of PLAXIS Results	133
5.3	MEASURING GEOGRID INTERACTION WITH ELASTIC WAVE VELOCITY	134
5.3.1	Portage Sand Tests	134
5.3.2	Grade 2 Gravel Tests.....	139
5.4	MEASURING STIFF GEOGRID INTERACTION WITH ROTATION ANGLE OF GRADE 2 GRAVEL	142
5.4.1	Test Method One – Measuring a Two-Dimensional Array of Rotations.....	142
5.4.2	Test Method Two – Measuring a Dense Array of Rotation Angles Along the Plate Edge	153
5.4.3	Discussion of Possible Mechanisms of Geogrid Reinforcement	161
5.5	SUMMARY AND RECOMMENDATIONS OF GRADE 2 GRAVEL TESTS WITH STIFF GEOGRID	164
6	SUPPLEMENTAL ANALYSES the effect OF GEOGRID ON modulus and zone of influence.....	167
6.1	Summary of Tests Completed to Determine Interaction Between Geogrid and Aggregate Material.....	167
6.2	Field-Scale Comparison I (Kwon et al. 2008)	171
6.3	Field Scale Comparison II (Kim 2003)	176
6.4	Modified Grade 2 Gravel Test with lower-modulus Extruded Geogrid	176
6.5	Pit Run Sand and Gravel Geogrid Tests	178
6.6	Breaker Run Tests.....	181

6.7	Summary of Field and Laboratory Tests and Effect of Flexural Stiffness	184
7	CONCLUSIONS AND RECOMMENDATIONS	186
8	PRACTICAL IMPLICATIONS	189
8.1	Small Scale Seismic Test	191
8.2	Use of Proposed Simplified Methodology for Field Studies	193
	REFERENCES	195
	Analog Devices (2007). Analog Devices, Inc. Web Site. http://www.analog.com ..	195
	Minnesota Department of Transportation (Mn/DOT). Mn/ROAD Aggregate Profile.	199
	Moghaddas-Nejad F. and Small J. (2003). Resilient and Permanent Characteristics of Reinforced Granular Materials by Repeated Load Triaxial Tests. ASTM Geotechnical Testing Journal. Vol. 26, No. 2, pp. 152-166	199
	Appendix A. TYPES OF ELASTIC MODULUS	202
	Figure A.1. Methods of determining the elastic modulus of soil.	203
	Appendix B. SHEAR (S) WAVES.....	204
	Appendix C. WAVE ATTENUATION.....	205
	Appendix D. PICKING THE FIRST ARRIVAL	207
	<i>Akaike Information Criteria (AIC)</i>	207
	<i>Cross Correlation</i>	210
	<i>An Analysis of the AIC Picker and Cross Correlation</i>	213
	<i>Manual Picking</i>	214
	Appendix F. TAMPING COMPACTION EFFORT	220
	Appendix G. SOIL STIFFNESS GAUGE (SSG) DATA	221

LIST OF FIGURES

Figure 1.1. Typical flexible pavement system design over soft subgrade soil (modified from Yoder and Witczak 1975).	2
Figure 1.2. An example of surface rutting (National Road Maintenance Condition Survey 2007).	3
Figure 2.1. "Strike-through" and interlocking of granular particles and geogrid.	8
Figure 2.2. Pavement system reinforcement mechanisms: (a) lateral resistance, (b) increased bearing capacity, (c) increased stiffness caused by tensioned geosynthetic (Perkins and Ismeik 1997).	9
Figure 2.3. Theoretical deformation of soil-geosynthetic-aggregate system beneath a distributed load. Notice the tension forces developed in the geosynthetic (Bender and Barenberg 1978).	10
Figure 2.4. Strain amplitude and direction for (a) unreinforced and (b) reinforced base course material over soft subgrade (modified from Love et al. 1987).	13
Figure 2.5. Distribution of stress components laterally beneath a load plate: (a) the variation caused by the deviator stress, (b) the variation of shear stress, and (c) the variation of the principal stress difference (Ishihara 1996).	16
Figure 2.6. Distribution of the components of bulk stress directly beneath the center of a circular loading plate when an external load is applied to the surface.	17
Figure 2.7. General shear failure surface induced in subsurface soils (a) before failure and (b) after failure (Bender and Barenberg 1978).	18
Figure 2.8. Shear stress as a function of depth in the soil column at the edge of a 150 mm diameter loading plate.	19
Figure 2.9. Different modulus are triggered under different deformation fields (Lambe and Whitman 1969).	22
Figure 2.10. Typical response of resilient modulus of granular material to increasing bulk stress where the reference stress p_r is 1 kPa (after Hicks and Monismith 1971).	25
Figure 2.11. Variation of coefficient k_1 with water content on several granular materials (modified from Hicks and Monismith 1971).	27

Figure 2.12. Hysteresis behavior of soil showing original shear modulus (G_0), shear stress and failure (τ_f), and the definition of the reference strain (γ_r , modified from Ishihara 1996).....	30
Figure 2.13. Hyperbolic stress-strain relationship of soil. The reference strain is given as the maximum shear strain considering the maximum shear modulus (Hardin and Drnevich 1972).....	31
Figure 2.14. Shear modulus as a function of shear strain for clean, dry sand (after Hardin and Drnevich 1972).....	32
Figure 2.15. Shear modulus and damping ratio in the hyperbolic model as a function of shear strain. The graph shows the range of shear strain for the resilient modulus test and seismic test (modified from Ishihara 1996).	33
Figure 2.16. Shear modulus as a function of strain level for sand at several different confining pressures (Kokusho 1980).	34
Figure 2.17. Shear modulus as a function of shear strain for crushed rock and round gravel for confining pressures between 50 and 300 kPa (Kokusho 1980).	35
Figure 2.18. An example test setup for obtaining a modulus based on the propagation of an elastic wave. The dimensions of the sample are 150 mm in diameter and 300 mm in height (Nazarian et al. 2003).	37
Figure 2.19. Resilient modulus as a function of constraint modulus (D_{seismic} , based on elastic wave velocity analysis) for (a) over two dozen soils and for (b) a granular base course (Nazarian et al. 2003; Williams and Nazarian 2007).	38
Figure 2.20. Hertzian contact theory and Mindlin shear stress behavior along a grain contact between two spherical particles. The diagram shows the parabolic stress distribution along the grain boundary and the required shear stress to induce slippage (modified from Mindlin 1949).	41
Figure 2.21. The relationship between force and displacement between spherical grains as described by Hertzian contact theory.	42
Figure 2.22. Different modes of wave propagation include both compression (P) waves (a), and shear (S) waves (b). (Rendering by Damasceno 2007).	45
Figure 2.23. Relative displacement and rotation of particle in two dimensions with respect to x and y axes.....	50

Figure 3.1. Analog Devices ADXL 203CE accelerometer and corresponding printed circuit board (PCB, Sparkfun Electronics).	52
Figure 3.2. Smoothcast 327 coating applied to MEM accelerometer and PCB (ruler gradations are in cm).....	56
Figure 3.3. Coordinate axes and voltage outputs of ADXL 203 CE MEMS accelerometers on orthogonal axes with respect to gravitational acceleration.	59
Figure 3.4. Calculating the rotation of each accelerometer with respect to the horizontal.....	60
Figure 3.5. DC voltage output and resolution of MEMS accelerometer as the angle of orientation of the measuring axis to horizontal changes.....	61
Figure 3.6. Grain size distribution for materials tested in laboratory experiments....	64
Figure 3.7. Photographs of materials used in research project. Bold divisions on graph paper are 10 mm increments and fine lines are 5 mm increments: a. Portage sand, b. Grade 2 gravel, c. Class 5 gravel, d. RPM, e. Pit run sand and gravel, and f. Breaker run.	65
Figure 3.8. Preliminary test cell. The outside diameter of the PVC shell is 35.6 cm, while the inside diameter is 330 mm. The height of the cylindrical cell is 600 mm.	68
Figure 3.9. Wooden box test cell. The box is 0.91 m long, 0.61 m wide, and 0.61 m deep and is filled with Portage sand in this figure. The bellofram air cylinder is attached to a load frame.	68
Figure 3.10. Three-dimensional cut-away schematic of the large wood test cell and placement of MEMS accelerometers in both the vertical and horizontal directions.	70
Figure 3.11. Cross section through testing cell with soil and accelerometers in place. The accelerometers are suspended vertically with a string and electrical signals are transmitted via wires from each accelerometer to the side of the testing cell.	70
Figure 3.12. The 6 inch (150 mm) diameter load application plate.	72
Figure 3.13. Simplified test setup to determine low strain constraint modulus with applied stress near the surface.	73
Figure 3.14. The haversine function is used to simulate traffic loading. The period of the cycle is 0.1 seconds. The rest time between haversine functions is	

0.9 seconds. Since air was used as the hydraulic fluid in this study, the pulse was applied for 1 second and released for 9 seconds.	76
Figure 3.15. Schematic of test setup to measure in situ soil rotation with MEMS accelerometers.	79
Figure 3.16. Test schematic for rotation measurements of grade 2 gravel. MEMS accelerometers were spaced 20 mm apart (center to center) near the geogrid and 25 mm apart further from the geogrid.	80
Figure 4.1. Static load test with Portage sand in the cylindrical test cell. The graph shows the depth-velocity relationship and a schematic of the test setup is shown on the right where the plate has a 150 mm diameter and the test cell has a 330 mm diameter.	82
Figure 4.2. A static load test in the cylindrical test cell where velocity is plotted as a function of external applied load at several depths. Velocity increases nonlinearly with depth and applied load.	84
Figure 4.3. Static load test results from a test performed on Portage sand in the large wood test cell.	85
Figure 4.4. Resilient modulus of Portage sand, grade 2 gravel, class 5 gravel, and RPM as a function of bulk stress.	89
Figure 4.5. Large-scale cyclic load modulus (E_{LS}) as a function of bulk stress.	93
Figure 4.6. Constraint modulus based on P-wave velocities as a function of bulk stress in large wood box tests.	95
Figure 4.7. Direct comparison of resilient modulus (M_r) as a function of modulus based on P-wave velocities for grade 2 gravel, class 5 gravel, RPM, and Portage sand after correcting for stress.	97
Figure 4.8. Resilient modulus as a function of modulus based on P-wave velocities corrected for stress and void ratio using (a) the expression proposed by Hardin and Richart (1963) and (b) a normalized void ratio correction factor.	100
Figure 4.9. Final average backbone curve showing resilient modulus results.	102
Figure 4.10. Resilient modulus as a function of modulus based on P-wave velocities corrected for stress level, void ratio, and strain level.	103
Figure 4.11. Determination of angle of repose (β).	105

- Figure 4.12. Resilient modulus and Young's modulus comparison based on P-wave velocities and corrected for stress, void ratio, and strain level..... 106
- Figure 4.13. General comparison between resilient modulus and Young's modulus based on P-wave velocities and corrected for stress, void ratio, and strain level for all soils. 107
- Figure 4.14. Summary moduli (computed at bulk stress = 208 kPa) based on resilient modulus tests, Young's modulus based on velocity results, and KENLAYER (box) tests for Portage sand, grade 2 gravel, class 5 gravel, RPM, Pit run gravel, and Breaker run. 109
- Figure 4.15. Final average backbone curve showing resilient modulus results, large scale cyclic load tests, SSG results (grey diamond), and previous results from Kokusho (1980). The error bars for the SSG results show the range over which the SSG estimated modulus of the grade 2 gravel..... 112
- Figure 4.16. Comparison of corrected moduli based on large box test and simple test. Moduli compared at bulk stress of 208 kPa. 115
- Figure 5.1. Surface displacement at several static loads and geogrid positions in grade 2 gravel after the application of 400 cycles of loading. PLAXIS deformations at 165 kPa applied load are shown for comparison. ... 118
- Figure 5.2. Modulus of reaction as a function of geogrid position for cyclic loading conditions. 118
- Figure 5.3. Axis-symmetric FE model simulation using PLAXIS. The axis-symmetric method allows a symmetric slice to be removed from a three-dimensional space for analysis..... 124
- Figure 5.4. Final FE mesh used in PLAXIS analysis for the case with geogrid at 75 mm depth. 125
- Figure 5.5. Shear strain from PLAXIS analysis below a circularly loaded plate when (a) no geogrid is present, (b) geogrid is buried at 75 mm depth, (c) geogrid is buried at 100 mm depth, and (d) geogrid is buried at 150 mm depth. 128
- Figure 5.6. Difference in shear strain between reinforced and unreinforced sections for geogrid at 75, 100, and 150 mm depth..... 129
- Figure 5.7. Horizontal displacement from PLAXIS analysis below a circularly loaded plate when (a) no geogrid is present, (b) geogrid is buried at 75 mm depth, (c) geogrid is buried at 100 mm depth, and (d) geogrid is buried at 150 mm depth..... 132

- Figure 5.8. Depth vs. velocity profile at three external loads with (a) no geogrid layer (b) geogrid layer at 110 mm depth, and (c) geogrid layer at 220 mm depth. The shaded area shows the decrease in velocity beneath the geogrid, especially at high applied deviator stress. 138
- Figure 5.9. A velocity-depth comparison at the peak applied load of 70 kPa before and after tension was released in the geogrid. The arrows on the graph indicate the direction of velocity change adjacent to the geogrid..... 139
- Figure 5.10. Velocity as a function of depth for three tests performed on grade 2 gravel with stiff geogrid. The grey line represents the theoretical change in velocity with changing stress without geogrid. 142
- Figure 5.11. Measured rotation of soil at different stages of cyclic loading. Cyclic loading was applied for 200 cycles, removed, and applied for another 200 cycles. No geogrid was incorporated into the soil. δ is vertical deflection of the surface plate in mm. 145
- Figure 5.12. Measured rotation of soil at different stages of static loading. Static loading was applied after 400 cycles of cyclic loading. No geogrid was incorporated into the soil. δ is vertical deflection of the surface plate in mm. 146
- Figure 5.13. Measured rotation of soil at different stages of cyclic loading. Cyclic loading was applied for 200 cycles, removed, and applied for another 200 cycles. Tensioned geogrid was placed at 7.5 cm depth. δ is vertical deflection of the surface plate in mm..... 147
- Figure 5.14. Measured rotation of soil at different stages of static loading. Static loading was applied after 400 cycles of cyclic loading. Tensioned geogrid was placed at 7.5 cm depth. δ is vertical deflection of the surface plate in mm. 148
- Figure 5.15. Measured rotation of soil at different stages of cyclic loading. Cyclic loading was applied for 200 cycles, removed, and applied for another 200 cycles. Tensioned geogrid was placed at 10 cm depth. δ is vertical deflection of the surface plate in mm. 149
- Figure 5.16. Measured rotation of soil at different stages of static loading. Static loading was applied after 400 cycles of cyclic loading. Tensioned geogrid was placed at 10 cm depth. δ is vertical deflection of the surface plate in mm. 150
- Figure 5.17. Measured rotation of soil at different stages of cyclic loading. Cyclic loading was applied for 200 cycles, removed, and applied for another

- 200 cycles. Tensioned geogrid was placed at 15 cm depth. δ is vertical deflection of the surface plate in mm. 151
- Figure 5.18. Measured rotation of soil at different stages of static loading. Static loading was applied after 400 cycles of cyclic loading. Tensioned geogrid was placed at 15 cm depth. δ is vertical deflection of the surface plate in mm. 152
- Figure 5.19. Rotation angle at the plate edge as a function of depth and applied surface load without geogrid reinforcement. PLAXIS analyses are shown at two deformation levels for comparison. 156
- Figure 5.20. Rotation angle at the plate edge as a function of depth and applied surface load with geogrid reinforcement at 75 mm depth. PLAXIS analyses are shown at two deformation levels for comparison. 157
- Figure 5.21. Rotation angle at the plate edge as a function of depth and applied surface load with geogrid reinforcement at 100 mm depth. PLAXIS analyses are shown at two deformation levels for comparison. 158
- Figure 5.22. Rotation angle at the plate edge as a function of depth and applied surface load with geogrid reinforcement at 150 mm depth. PLAXIS analyses are shown at two deformation levels for comparison. 160
- Figure 5.23. Measured tilt angles in grade 2 gravel and at 550 kPa applied load and geogrid positions: (a) no geogrid, (b) non-tensioned geogrid at 75 mm depth, (c) tensioned geogrid at 75 mm depth. 162
- Figure 5.24. Rotation angles at the plate edge and for maximum surface displacement (6.3 - 7.3 mm) in Portage sand. 163
- Figure 5.25. "Zone of influence" from rotation angle test results: (a) non-tensioned geogrid at 75 mm depth, (b) geogrid at 75 mm depth, (c) geogrid at 100 mm depth, and (d) geogrid at 150 mm depth. The solid symbols represent the raw rotation angles for each reinforcement test and the open symbols represent the difference between the rotation angles with and without reinforcement. The shaded area is the "zone of influence" of each reinforcement case. 165
- Figure 6.1. Grain size distribution of aggregate used by Kwon et al. (2008) and the aggregate manufactured at the University of Wisconsin – Madison (modified from grade 2 gravel). 172
- Figure 6.2. Constraint modulus of seismic test on modified grade 2 gravel (based on grain size distribution from Kwon et al. 2008). 173

- Figure 6.3. “Zone of influence” (grey area) of lower-modulus geogrid at 100 mm depth and two plate loads on modified grade 2 gravel. PLAXIS results show the expected rotation at the larger load. Also shown is the velocity distribution for the corresponding rotation measurements... 177
- Figure 6.4. “Zone of influence” (grey area) of the higher-modulus geogrid at three depths and two surface displacements on pit run sand and gravel. PLAXIS results show the expected rotation at the larger surface displacement (~7 mm). Also shown is the velocity distribution for the corresponding rotation measurements. 181
- Figure 6.5. Rotation and P-wave velocity results from Breaker run tests. PLAXIS results show the expected rotation at the larger surface displacement (~7 mm). Also shown is the P-wave velocity distribution for the corresponding rotation measurements. 183
- Figure 6.6. Particle-accelerometer interaction in breaker run tests. The accelerometer may only contact a few particles, providing questionable results of rotation and P-wave velocity. 183
- Figure 8.1. Simplified test setup to evaluate elastic wave velocities under applied stress near the surface. 191

LIST OF TABLES

Table 2.1. Soil behavior and modeling techniques based on shear strain amplitude (Ishihara 1996).	29
Table 3.1. Specifications for Analog Devices ADXL 203CE accelerometer (Source: www.analog.com).	54
Table 3.2. Physical properties of materials tested in laboratory experiments.	64
Table 3.3. Physical properties of geogrids used in testing	66
Table 3.4. Test scheme followed for tests performed in the large, wood test cell. ...	77
Table 4.1. Proposed methods for the evaluation of resilient modulus using P-wave velocity information.	81
Table 4.2. Physical properties and results of resilient modulus tests on granular materials tested.	90
Table 4.3. Non-linear constant k_1 and recoverable deformation at the surface used for KENLAYER and MICHPAVE analyses.	92
Table 4.4. Physical properties and results of seismic modulus tests on granular materials tested in the large wood box.	96
Table 4.5. Ratio of resilient modulus to maximum modulus (based on seismic results) and shear strain induced by resilient modulus tests.	101
Table 4.6. Poisson's ratios based on velocity of elastic waves.	105
Table 4.7. An analysis of the mechanistic approach of converting a resilient modulus based on P-wave velocities to a traditional resilient modulus.	110
Table 5.1. Material properties of grade 2 gravel used in PLAXIS analyses.	121
Table 5.2. Virtual thicknesses or "zone of influence" based on laboratory tests with stiff geogrid and grade 2 gravel.	166
Table 6.1. Geogrid/aggregate interaction tests performed.	168
Table 6.2. Comparison between KENLAYER and field results from Kwon et al. (2008).	175
Table 8.1. Recommended Moduli for Select Working Platform Materials	190

1 INTRODUCTION

Approximately 26,000 km (10 %) of the nation's roads are undergoing construction improvement in any given year (Perkins et al. 2005a). The large amount of time and capital invested in road construction projects has led engineers to actively seek improved road construction techniques. In the past 20 years, many new road improvement techniques have revolved around the use of geosynthetics and an empirical-mechanistic approach toward analyzing the stress-strain relationship in the flexible pavement system (Figure 1.1). A traditional flexible pavement system consists of three or four key components including (from the surface): asphalt surface layers of the final road, base course, subbase, and subgrade. Geosynthetics are most commonly installed in the base course layer or at the base course/subgrade contact. The implementation of a geosynthetic layer in the pavement system provides many advantages over traditional road construction techniques.

Although the four components of a flexible pavement system specify a time-proven design method, the need for more durable roads is a desire of transportation agencies. The need for more durable roads comes with the increased amount of traffic stemming from population growth and construction of the Eisenhower Interstate System beginning in the late 1950's and early 1960's. Between 1970 and 2000, approximately 110 million vehicles have been added to the nation's roadways, doubling the amount of registered vehicles in the United States. In addition, about 60

% of these vehicles are considered heavy vehicles such as buses and trucks (Federal Highway Administration 2003).

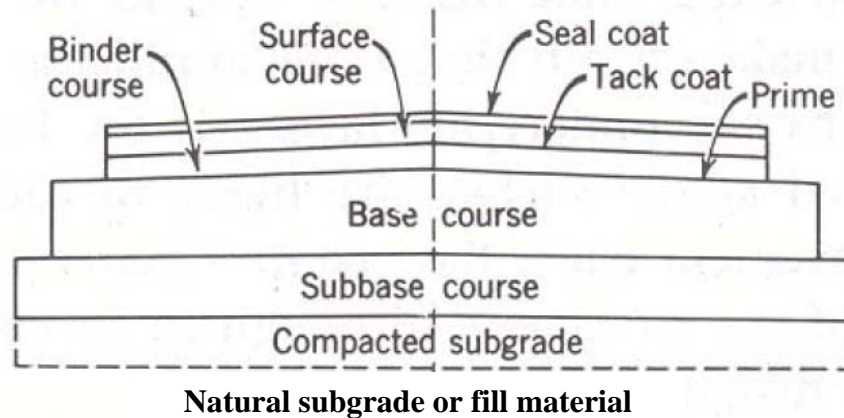


Figure 1.1. Typical flexible pavement system design over soft subgrade soil (modified from Yoder and Witczak 1975).

Besides the need to construct new roads, many roads constructed during the late 20th century need repairs and reconstruction. Aging roads, continually increasing traffic, and safety improvements require that roads be either redesigned or modified. New designs help take into account these modifications and improvements, providing an opportunity for expanded road life and decrease the need for replacement and adaptation in the future.

Cyclic loading of roadways caused by traffic and exacerbated by the climate and poor subgrade soils cause the physical deterioration of the asphalt surface of roads and the differential settlement and decline in quality of base course and subgrade soils. Approximately 60 % of subgrade soils in Wisconsin are silts and clays classified “poor” for road construction (Edil et al. 2002). Differential settlement

of road surfaces is commonly referred to as surface rutting (Figure 1.2). Surface rutting typically occurs where vehicle tires continually pass over the same areas of a flexible pavement, applying vertical loads to the pavement structure and causing non-recoverable (i.e., plastic) deformations to accumulate. Granular base course material is typically installed to decrease the amount of surface rutting, but in areas having poor subgrade soils, deterioration of the pavement system is unavoidable (Moghaddas-Nejad and Small 2003; Yoder and Witczak 1975; Giroud and Han 2004).



Figure 1.2. An example of surface rutting (National Road Maintenance Condition Survey 2007).

Surface rutting of roadways is only one of several problems associated with traffic loading and pavement performance degradation. Physical deterioration can be accelerated by tension and compression induced in concrete and asphalt at the surface by repetitive traffic loading if excessive recoverable (elastic) deformations occur. The road bed can crack and water may seep through cracks into subsurface materials. Ponding of water in ruts and freeze/thaw cycling in harsher environments also deteriorate roadways further.

The incorporation of a geogrid (a reinforcement geosynthetic) in the asphalt pavement system can have a significant impact on road construction and maintenance. Geogrid increases the service life of roads by reducing the amount of rutting and potential physical deterioration. Furthermore, the increased stiffness of the asphalt pavement system provided by the installation of a geogrid reduces cracking by laterally constraining subsurface soils. Evidence suggests that adding tensile strength to unbound materials in the asphalt pavement system that does not typically have resistance to tension significantly improves load distribution in the base course and subgrade materials (Bender and Barenberg 1978; Steward et al. 1977; Perkins et al. 2005b).

In addition to the strength and stiffening benefits, research has shown that geogrids can act as a replacement or supplement to base course material, thereby reducing the thickness of the base course (Bender and Barenberg 1978). Reducing required base course thicknesses in the asphalt pavement system is expected to reduce the cost of construction since less material will be required to be transported to the site and compacted (Geosynthetic Materials Association 1998; Edil et al.

2002; Giroud and Han 2004; Kim et al. 2005; Haas et al. 1989; Perkins and Ismeik 1997; Sprague and Cashatt 2005; Barksdale et al. 1989; Huntington and Ksaibati 2000; Hsieh and Mao 2005).

In spite of the benefits from the use of geogrids, the mechanical quantification of the aggregate-geogrid composite system is not yet fully understood. The motivation of this research project is to develop a testing scheme that can be used to monitor and evaluate changing physical properties of the pavement structure with depth, specifically in the vicinity of a geogrid layer. The most effective position of the geogrid and required thickness of base course material can be analyzed with knowledge of how stiffness changes with the presence of geogrid.

2 BACKGROUND

2.1 GEOSYNTHETICS IN ROAD CONSTRUCTION

Geosynthetics were originally used as layers of separation, filtration, drainage, and reinforcement between soils in a pavement system (Steward et al. 1977; Bender and Barenberg 1978). Separation refers to the ability of the geosynthetic to physically separate two materials such as the engineering-specified base course and the weak fine-grained subgrade (Perkins and Ismeik 1997). During road construction, contamination across layers is typically a result of equipment traveling back and forth across an unpaved and unreinforced section of roadway. Longer-term contamination across layers is also caused by movement of fines due to frost heave, not just construction equipment. The separation of aggregates from underlying subgrade materials in the pavement system is still an important function of the geosynthetic as the infiltration of fines into the coarse-grained base course may change the physical properties of the base and reduce load carrying capacity. Geotextiles are typically used as layers of separation because of their small openings and ability to transmit water.

The properties of filtration and drainage are closely related and refer to the ability of a geosynthetic to filter fine particles and act as a drainage layer that will allow water to easily escape subsurface soils. Geosynthetics with high permeabilities such as geotextiles and geonets allow the dissipation of pore water pressures, a driving factor in the strength of underlying sediments. The removal of water by placement of a geosynthetic drainage layer will greatly enhance the strength and life

of a road and surrounding embankments by reducing pore water pressure of subsurface materials. Geonets and geotextiles are effective layers for filtration, drainage, and separation, but do not directly provide strengthening to the pavement system (Christopher et al. 2000). Researchers soon realized the potential strength and durability benefits offered by incorporating geosynthetics in road design. In the 1980's, much time was devoted to determining which geosynthetic parameters had the greatest impact on road design. Barksdale (1989) listed several important variables to consider:

- Type and stiffness of the geosynthetic
- Vertical location of geosynthetic
- Surface pavement thickness
- Type and thickness of subgrade and base course material
- Potential slip between the subgrade, base course, and geosynthetic
- Geosynthetic pre-tension
- Pre-rutting of the geosynthetic
- Pre-stressing

Geogrids are specifically manufactured for reinforcement applications. Stiff geogrids are typically plastics molded with large openings to allow particles to “strike-through” the geogrid from one side to another (Figure 2.1). Sarsby (1985) found that the ratio of geogrid aperture to the mean particle size (D_{50}) should be approximately 3.5 or greater to most efficiently transfer shear stresses from the soil to the geogrid. In addition, the percentage of open area in the geogrid is usually 40 – 95 % to allow particles to interlock with the reinforcing layer (Koerner 1998).

The potential benefits of using geosynthetics in road construction are not only related to increased strength and stiffness. Short-term and long-term costs are the most substantial influences on engineering design of roads (Bender and Barenberg 1978). Economic improvements associated with geogrid reinforcement include the transport and compaction of less base course material. As a result, decreased time and capital can be invested in construction and long-term maintenance cost will decline.

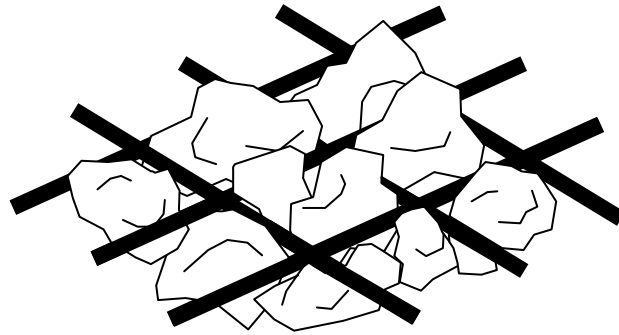


Figure 2.1. "Strike-through" and interlocking of granular particles and geogrid.

2.2 MECHANISM OF REINFORCEMENT BY GEOGRID-PARTICLE INTERACTION

The reinforcement of the pavement system has three major components including the enhancement of lateral resistance, increased bearing capacity, and increased stiffness (Figure 2.2). Several researchers have noted the increased lateral resistance from geogrid reinforcement (Haas et al. 1989; Huntington and Ksaibati 2000; Gnanendran and Selvadurai 2001; Giroud and Han 2004; Perkins

and Ismeik 1997; Tutumluer and Kwon 2006; Al-Qadi et al. 2007; Kwon et al. 2005). The increase in lateral resistance is caused by the interlocking of granular material in the base course with the geogrid (Figure 2.1 - Huntington and Ksaibati 2000; Haas et al. 1989). Interlocking provides tensile strength to granular materials that do not naturally have resistance to tensile forces.

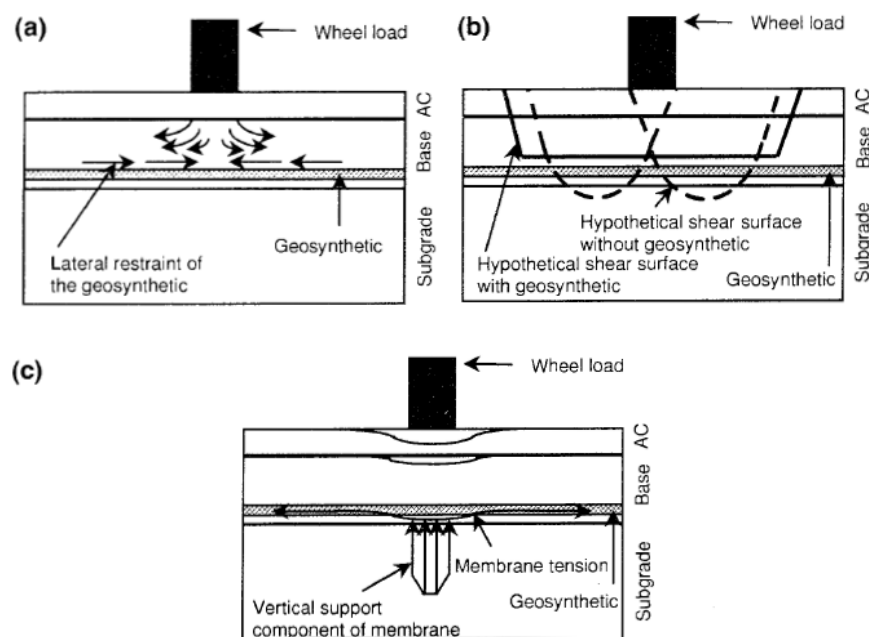


Figure 2.2. Pavement system reinforcement mechanisms: (a) lateral resistance, (b) increased bearing capacity, (c) increased stiffness caused by tensioned geosynthetic (Perkins and Ismeik 1997).

The inclusion of a geogrid also acts to increase the bearing capacity of subsurface aggregates by transferring part of the shear stresses induced in the subsurface to the geosynthetic, which is able to accept tensile forces and distribute them over a large area (Bender and Barenberg 1978; Perkins and Ismeik 1997; Giroud and Han 2004). Figure 2.3 shows how tensile stresses develop along the

geosynthetic due to a distributed load on the surface. Tensile stresses that develop at the interface between the geogrid and the surrounding material promote an increase in the frictional resistance and an overall increase in bearing capacity of the pavement system. The modification of the shear failure surface (Figure 2.2b) and an effective increase in the angle of friction caused by the interaction between the aggregate and the geogrid causes the bearing capacity of the entire pavement system to increase (Steward et al. 1977).

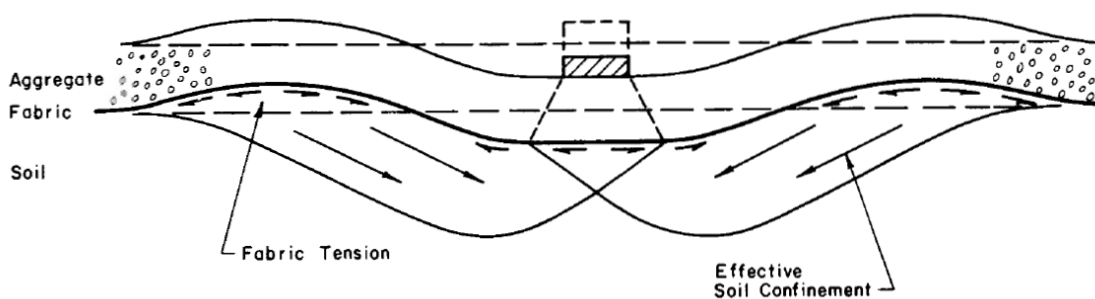


Figure 2.3. Theoretical deformation of soil-geosynthetic-aggregate system beneath a distributed load. Notice the tension forces developed in the geosynthetic (Bender and Barenberg 1978).

The stiffness of underlying materials can be defined as the applied stress divided by the corresponding settlement (DeMerchant et al. 2002). A geogrid can be used to increase stiffness of underlying soils by confining material above and below the geogrid with an inward compressive force (caused by the tensile force in the geogrid, illustrated in Figure 2.2c). The majority of model tests seem to require an applied vertical stress before noticeable confinement of materials near the geogrid. Research suggests a specified force or vertical displacement is required to initiate

stiffening of the pavement system as the applied force induces shear stresses downward to the geogrid layer and individual grains become interlocked with the geogrid (Perkins et al. 2005b, Kim et al. 2005). Visual experiments and finite element modeling results indicate that confinement is more immediate and the rate of stiffness increase is more rapid in materials reinforced with geogrid (Love et al. 1987). Once substantial shear stresses come into contact with the geogrid layer, tension develops in the geogrid and stiffening is noticed at the surface.

Horizontally positioned geogrid is expected to induce a state of confinement in aggregates, affecting the rotation and displacement of particles above and below the geogrid. Love et al. (1987) performed visual experiments to determine the strain of base course material over soft subgrades. The strain vectors plotted in Figure 2.4 show the results for unreinforced and reinforced conditions. In the unreinforced condition, shear strains are higher near the surface of the subgrade material and extend laterally at greater magnitudes near the surface. In the reinforced condition, the strains extend to a deeper zone, but quickly dissipate when reaching the reinforcement layer. Also, strains are laterally confined to a much smaller area when reinforcement is placed in the subsurface.

Including a geogrid in the subgrade or base course of a flexible pavement system can enhance the strength and stiffness of the road. Ultimately, road life will increase and more traffic can be accommodated on newly designed roads. The geogrid constrains subsurface materials, distributing cyclic loads caused by automotive traffic over a larger area and giving tensile strength to granular material.

The volume of material affected by the placement of a geogrid is an important design consideration.

The overall objective of the proposed research is to resolve remaining questions relating to the interaction of geogrids with granular materials, such as developing a new test method to quantify the interaction of base material with geogrid, and to determine the contribution of such a composite layer to pavement structure design. To obtain this objective, the project can be divided into three phases consisting of 1) a thorough review and analysis of the pertinent literature, 2) laboratory testing, analyses of the resultant data, and development of conclusions, and 3) assessment of full-scale field installations. Additional objectives include, establishment of equivalent breaker run and pit run thicknesses with and without geogrid, evaluation of differences in support/stiffness between stiff and flexible geogrids, and recommending MEPDG design input, and verifying the findings with full-size field tests.

2.3 STRESS DISTRIBUTION BELOW A CIRCULAR PLATE

The stiffness of granular materials is controlled by the state of effective stress. If a wheel load applied can be represented by a circular area, the stress changes can be estimated. The induced vertical stress under the center of a circularly loaded plate in an elastic medium can be calculated using Boussinesq's solution:

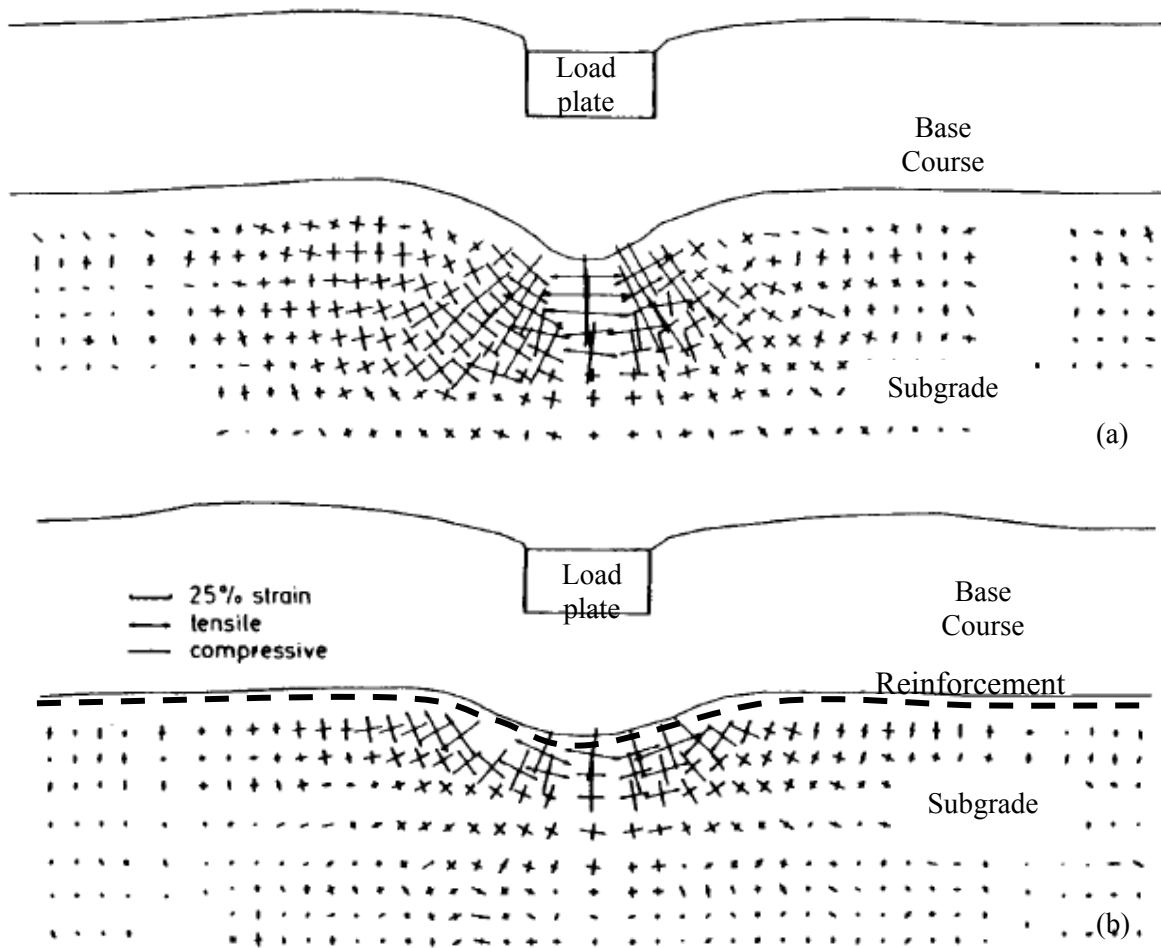


Figure 2.4. Strain amplitude and direction for (a) unreinforced and (b) reinforced base course material over soft subgrade (modified from Love et al. 1987).

$$\sigma_z = p \left[1 - \left\{ \frac{1}{1 + \left(\frac{a}{z} \right)^2} \right\}^{\frac{3}{2}} \right] \quad (2.1)$$

where σ_z is the induced vertical stress due to a load (p), z is depth, and a is the radius of the circular load application plate.

The change in tangential (σ_θ) and radial stresses (σ_r) due to the applied load also influences the state of stress in the soil column, especially at shallow depths. Vertically under the center of the loading plate, the tangential and radial stresses are equal to one another:

$$\sigma_r = \sigma_\theta = \frac{p}{2} \left[(1 + 2\nu) - \frac{2(1 + \nu)z}{(a^2 + z^2)^{1/2}} + \frac{z^3}{(a^2 + z^2)^{3/2}} \right] \quad (2.2)$$

where ν is Poisson's ratio. Directly beneath the center of a load plate, principal stress axes are oriented orthogonal to the vertical and horizontal directions and the shear stress on the xz plane is zero. Further from the center of the loading plate, shear stresses increase and particles tend to rotate. Shear stresses are maximized at the plate edge and dissipate with distance from the plate edge. A graphical representation of the distribution of vertical stresses, principal stresses, and shear stresses laterally beneath a loading plate is shown in Figure 2.5. Note that stresses calculated in equations (2.1) and (2.2) have ignored all contributions from the self-weight of the soil.

To explain the complete state of stress in the soil column, the vertical and horizontal stress contributions from the self-weight of the soil must also be taken into account. Although stress contributions caused by the self-weight of the soil in this research are typically much smaller than those caused by the deviator load, the self weight of the soil is important below depths of 250 mm for a 150 mm diameter load plate. Beyond 250 mm depth, the stress contribution due to self weight is higher than that of the deviator load. Vertical effective stress due to self-weight (σ_v') is:

$$\sigma'_v = (\gamma_{sat} - \gamma_w)z \quad (2.3)$$

where γ_{sat} is the saturated unit weight of the soil and γ_w is the unit weight of water. Unlike liquids where stresses are the same in all directions (hydrostatic pressure), the horizontal and vertical stresses are almost always not equal in soil (Holtz and Kovacs 1981). Horizontal stresses are calculated using the coefficient of lateral earth pressure at rest (K_0):

$$\sigma'_h = K_0 \sigma'_v \quad (2.4)$$

K_0 can be approximated by the empirical relationship proposed by Jaky (1948) for normal loading (i.e., first applied load neglecting the load history):

$$K_o = 1 - \sin \phi' \quad (2.5)$$

where ϕ' is the effective internal friction angle. Therefore, the bulk stress (the sum of the three principal stresses) caused by the self-weight of the soil can be written as:

$$\sigma_{sw} = \gamma z(1 + 2K) \quad (2.6)$$

The bulk stresses include the contributions from the self-weight of the soil and the applied load at the surface (θ):

$$\theta = \sigma_x + \sigma_y + \sigma_z + \gamma z(1 + 2K_o) \quad (2.7)$$

The relative contributions of each of these stress components directly beneath the center of a 150 mm diameter load plate are shown in Figure 2.6. External plate loads

dominate at shallow depth, but dissipate quickly allowing stresses caused by the unit weight of the soil to dominate at depths greater than approximately 250 mm.

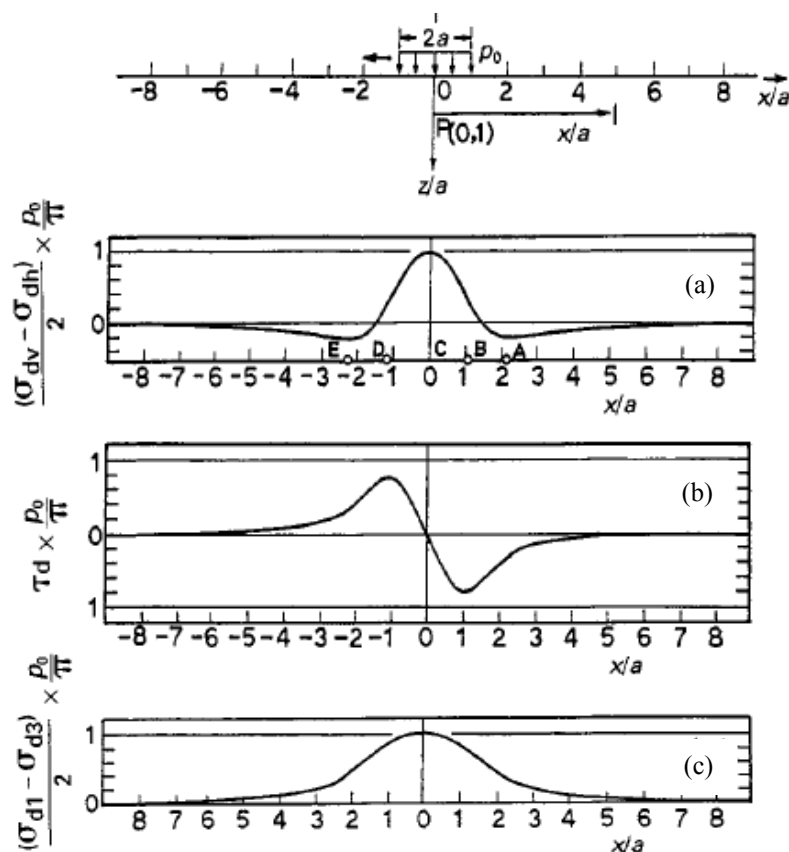


Figure 2.5. Distribution of stress components laterally beneath a load plate: (a) the variation caused by the deviator stress, (b) the variation of shear stress, and (c) the variation of the principal stress difference (Ishihara 1996).

A pavement systems program such as KENLAYER can be used to model the distribution of stress and strain in a layered subsurface for a large, field scale situation. KENLAYER calculates the distribution of stresses and strains in the subsurface based on the solution for a non-linear elastic, multi-layered system over a circularly loaded area (Huang 1993). MICHPAVE is also a nonlinear finite element program used to analyze the stress-strain relation in flexible pavement systems.

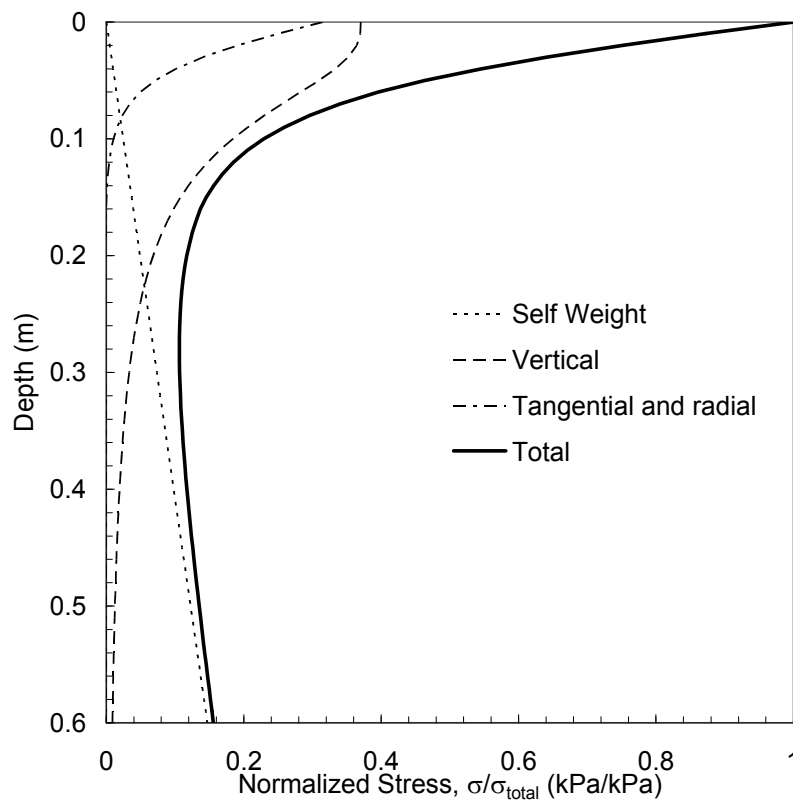


Figure 2.6. Distribution of the components of bulk stress directly beneath the center of a circular loading plate when an external load is applied to the surface.

Tangential and radial stresses due to plate loads are most prevalent in the near surface, close to the loading plate. The tangential and radial stresses in the near subsurface induce shear stresses and a shear failure plane develops around the loading plate that typically pushes soil away from the loading plate (Figure 2.7). With a large enough normal force at the surface, the soil can fail along these shear planes (Figure 2.7b - Terzaghi and Peck 1967).

Stress conditions at the edges of the load plate are different than those directly beneath the center of the plate. Instead of being influenced mostly by the

vertical component of applied stress, the horizontal (tangential and radial) components become much more influential and shear stresses increase. The stress conditions at the edge of a 150 mm diameter load plate are shown in Figure 2.8.

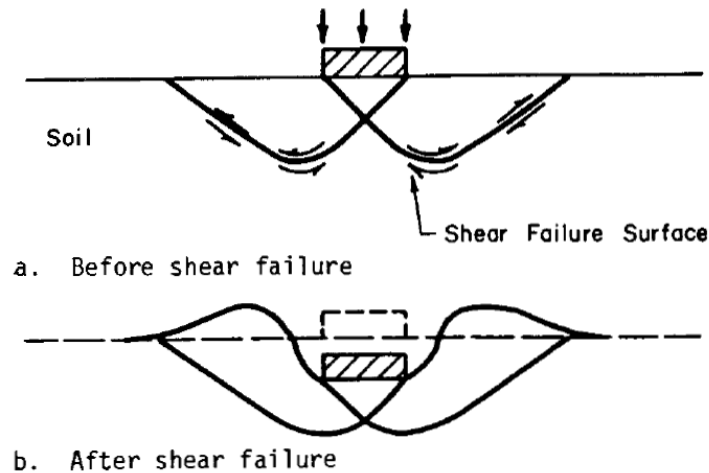


Figure 2.7. General shear failure surface induced in subsurface soils (a) before failure and (b) after failure (Bender and Barenberg 1978).

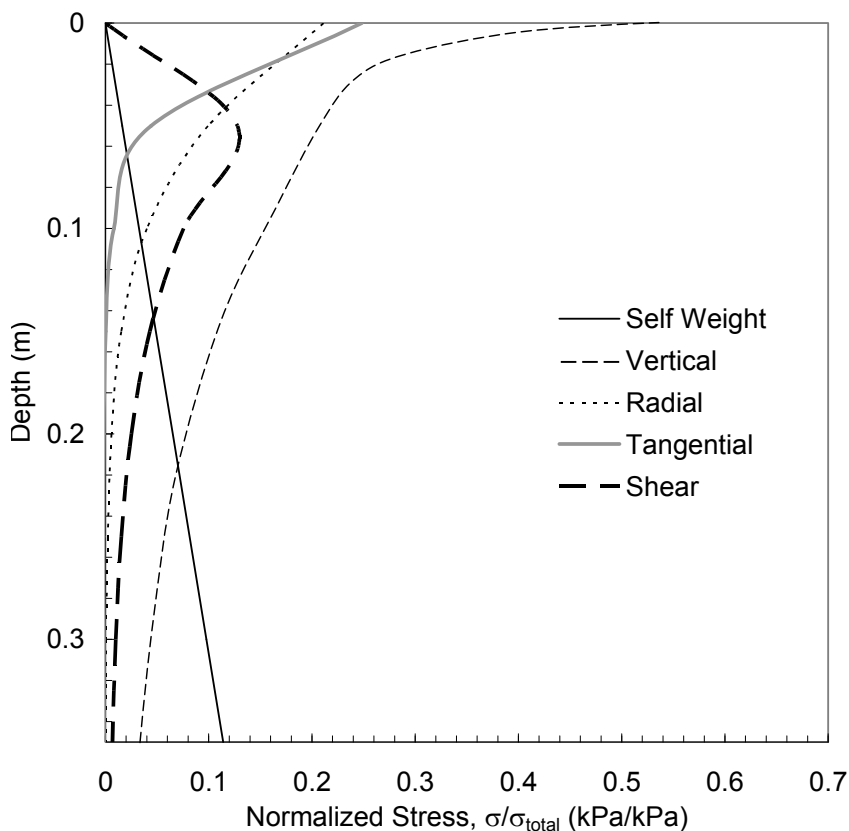


Figure 2.8. Shear stress as a function of depth in the soil column at the edge of a 150 mm diameter loading plate.

2.4 SOIL STIFFNESS AND MODULUS

2.4.1 Modulus

Stiffness is generally defined as an increment of stress ($\Delta\sigma_z$) divided by the resulting deformation (Δ). The stiffness of the soil system is similar to that of a spring with one caveat. Springs are considered to be a one-dimensional system whereas the soil mass is three-dimensional. As a result the “modulus of reaction” (k) of a spring is written in terms of a force per unit length as opposed to a force per unit area per unit length. k of a soil mass is defined with the following expression:

$$k = \frac{p}{\Delta} \quad (2.8)$$

where p is the reactive pressure and Δ is the deflection of the soil surface (Yoder and Witczak 1975). The modulus of reaction is an essential tool to analyze the elastic deformation of a soil mass given a specified load.

When a force is applied to a spring, the spring deforms an amount that depends on the length and stiffness of the spring coil. When more force is applied to the spring, the spring deflects proportionally an even greater amount and when force is released from the spring, the spring returns to the original length. However, if the spring is compressed beyond its yield strength, the spring will be unable to rebound back to the original height and instead remains shorter than the original height due to plastic yielding. The soil skeleton behaves in a similar manner to the spring in that there are two parts of deformation to consider under cyclic loading conditions: plastic (permanent) deformation and elastic (recoverable) deformation.

Figure 2.9 shows the different types of modulus and how each is defined on an elementary soil volume. The linear elastic variation between stress and strain can be characterized by two material properties: Young's modulus (E) and Poisson's ratio (ν). The elastic modulus of materials is defined as the ratio of the stress applied (σ_z) to the resulting axial strain (ϵ_z) and is important in analyzing the behavior of a material affected by cyclic loading conditions. The resilient modulus (M_r) is a special case of the elastic modulus where the deviator stress (σ_d) causes a change in recoverable axial strain (ϵ_r):

$$E = \frac{\sigma_z}{\varepsilon_z}$$

$$M_r = \frac{\sigma_d}{\varepsilon_r}$$
(2.9)

The shear modulus is defined similarly to the elastic modulus, but is defined as the shear stress (τ) divided by shear strain (γ).

$$G = \frac{\tau}{\gamma} = \frac{E}{2(1+\nu)} = D \frac{1-2\nu}{2(1-\nu)}$$
(2.10)

D is the constraint modulus and is similar to the elastic modulus with the restriction that the system does not deform perpendicular to the applied load. The propagation of P-waves through a large volume of material is controlled by the constraint modulus (as opposed to elastic modulus where lateral deformation is allowed in an unconstrained specimen) and is essential to mechanistically examine the relationship between moduli calculated based on the resilient modulus tests and moduli based on seismic tests (Richart et al. 1970; Santamarina et al. 2001). The constraint modulus from P-wave velocity results will be called the P-wave modulus (D_{seismic}) in this paper.

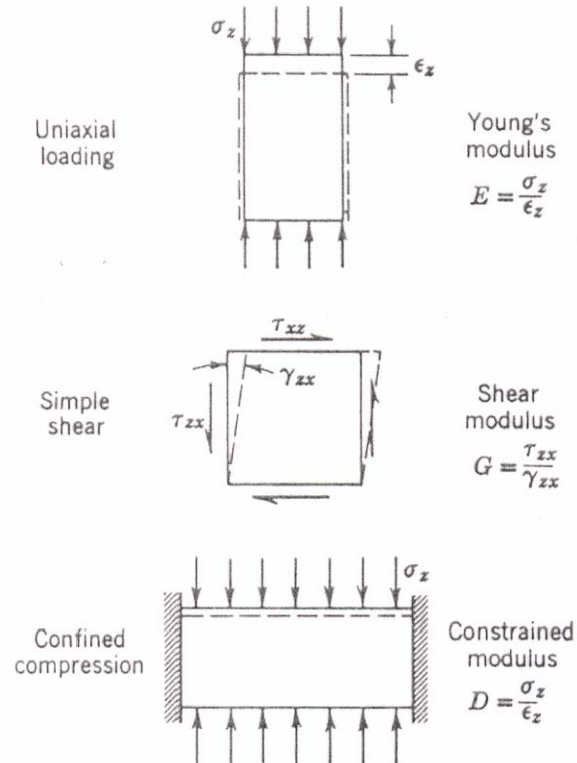


Figure 2.9. Different modulus are triggered under different deformation fields (Lambe and Whitman 1969).

Poisson's ratio is the second parameter needed to analyze the relationship between normal stress, shear stress, normal strain, and shear strain in a linear elastic material. Poisson's ratio is defined as:

$$\nu = -\frac{\epsilon_{\perp}}{\epsilon_{\parallel}} = \frac{0.5\left(\frac{V_p}{V_s}\right)^2 - 1}{\left(\frac{V_p}{V_s}\right)^2 - 1} \quad (2.11)$$

where ϵ_{\perp} is the strain perpendicular to the applied stress, ϵ_{\parallel} is the strain parallel to the applied stress, V_p is P-wave velocity and V_s is S-wave velocity. Poisson's ratio is assumed to be between 0.3 and 0.4 for granular materials undergoing large strains

or elastoplastic deformation (Bardet 1997). Poisson's ratio is a function of the strain level or modulus and therefore changes depending on the amount of strain induced during testing. In contrast to higher strain conditions, at low strain levels induced during elastic wave propagation, Poisson's ratio of granular materials typically drops to 0.15 to 0.25 (Yoder and Witczak 1975; Santamarina et al. 2001). When examining Equation (2.11), a higher Poisson's ratio would indicate a greater amount of deformation perpendicular to applied load with respect to deformation parallel to the applied load.

2.4.2 Resilient Modulus

A higher modulus of each layer in the pavement system indicates a lesser amount of deformation for the same applied stress and less potential for deterioration of a road due to cyclic loading. Resilient modulus was recognized as a more effective method to examine stiffness of subgrade materials after research indicated that road failures were not only related to permanent (plastic) deformation at the surface caused by densification. The repeated loading of the surface causes shear deformation of underlying materials without volume change and weakening of the pavement system (Yoder and Witczak 1975). Resilient modulus tests were developed to study the variation of stiffness of materials with applied load. Currently, resilient modulus tests are defined in accordance with the procedure established by the National Cooperative Highway Research Program (NCHRP 1-28 A). NCHRP 1-28 A specifies load increments and durations depending on the material being

considered (e.g., subgrade or base course) and also presents the detailed testing procedures designed to simulate cyclic traffic loading over flexible pavement systems. The response of the pavement system is analyzed based on the elastic rebound of the material due to the applied loading conditions.

A number of factors affect resilient modulus results and the ability of particulate media to elastically rebound to applied loads, including (Li and Selig 1994): loading conditions (e.g., magnitude, number of cycles, and lateral earth pressure), soil type (e.g., grain size, plasticity, soil structure), and physical properties of soil (water content, dry density, stress/strain relationship). Although Li and Selig (1994) specified several parameters controlling the resilient modulus, loading conditions are the most important parameters when calculating modulus. The constitutive relationship between resilient modulus and bulk stress (θ) for granular materials can be efficiently fitted with a power model (Moossazadeh and Witczak 1981):

$$M_r = k_1 \left(\frac{\theta}{p_r} \right)^{k_2} \quad (2.12)$$

where k_1 refers to the resilient modulus of the material at the reference stress p_r , and k_2 is typically 0.5 for granular, base course materials (Huang 1993). Figure 2.10 shows resilient modulus test data and fitted power relationships. Figure 2.10 was constructed from early resilient modulus tests on granular materials by Hicks and Monismith (1971) where experiments were performed in triaxial compression cells.

After approximately 50 – 100 cycles of loading, an effective resilient modulus can be computed. As the number of cycles increases beyond this point, the resilient

strain remains approximately constant and plastic deformation decreases substantially (Hicks and Monismith 1971).

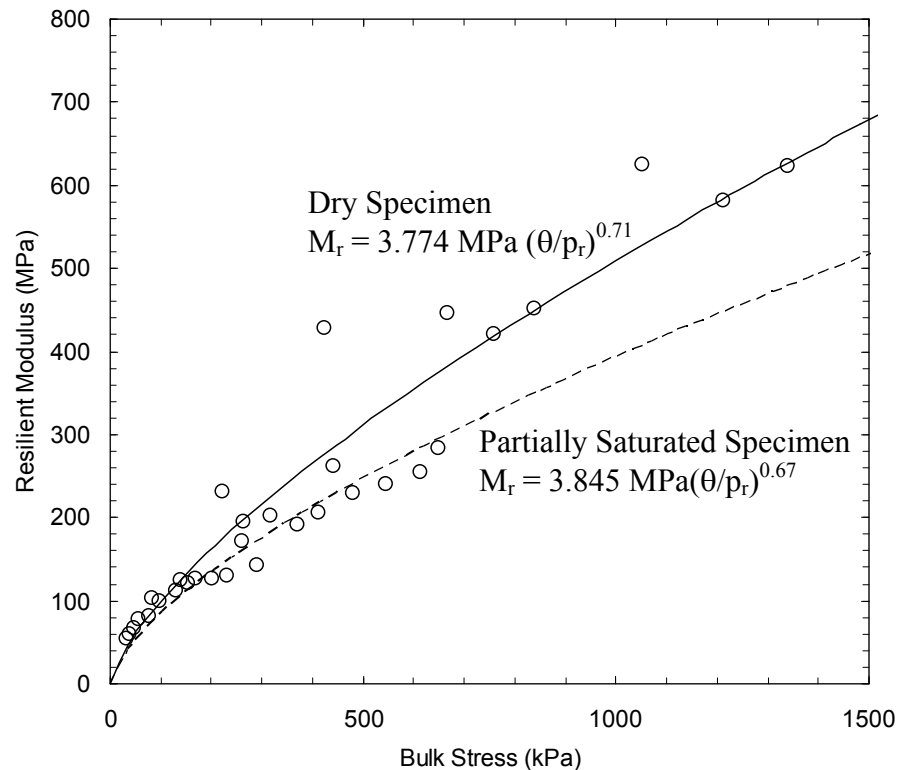


Figure 2.10. Typical response of resilient modulus of granular material to increasing bulk stress where the reference stress p_r is 1 kPa (after Hicks and Monismith 1971).

Granular materials also typically have a higher resilient modulus when dry of optimum rather than wet of optimum and early tests performed by Hicks and Monismith (1971) and others show a decreasing k_1 with increasing water content (Figure 2.11). The effect of water content on k_2 was less pronounced or not apparent.

The simple power model described above was used to fit resilient modulus data most extensively up until 2004 when the NCHRP suggested the use of a modified power model that involves both the deviator stress and octahedral shear stress (τ_{oct}). For simplicity and to compare results more easily to previous studies done on materials used in this research, the power model was used instead of the modified power model. The NCHRP modified power model is:

$$M = k_1 p_a \left(\frac{\theta - 3k_6}{p_a} \right)^{k_2} \left(\frac{\tau_{oct}}{p_a} + k_7 \right)^{k_3} \quad (2.13)$$

where k_3 , k_6 , and k_7 are additional fitting parameters. k_3 , and k_7 are dimensionless quantities, while k_6 has units of stress. Also, k_3 and k_6 are ≤ 0 while k_7 is ≥ 1 . τ_{oct} is defined as follows:

$$\tau_{oct} = \frac{1}{3} \sqrt{(\sigma_1 - \sigma_2)^2 + (\sigma_2 - \sigma_3)^2 + (\sigma_3 - \sigma_1)^2} \quad (2.14)$$

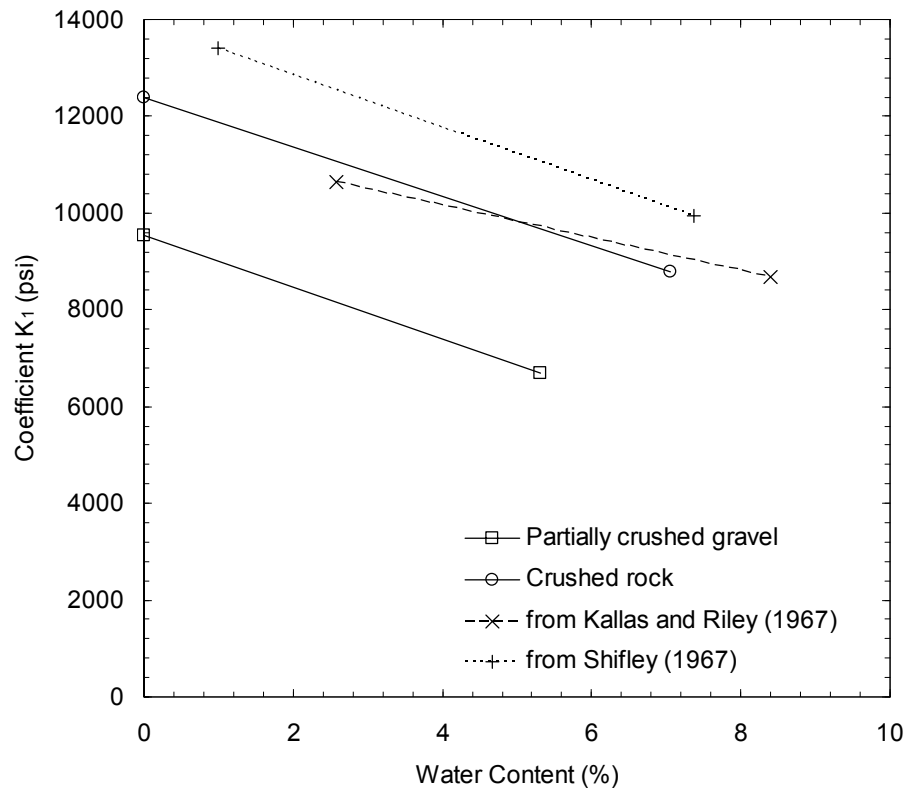


Figure 2.11. Variation of coefficient k_1 with water content on several granular materials (modified from Hicks and Monismith 1971).

The research presented herein proposes a mechanistic approach based on P-wave velocities toward estimating resilient modulus. Calculating resilient modulus based on seismic techniques provides a new method for estimating the resilient modulus of materials that may be able to be applied quickly and easily at field stress conditions. A method of estimating resilient modulus based on a large-scale cyclic load test modulus (E_{LS}) is also presented and offers a comparison to a similar cyclic load test, but on a larger scale.

2.4.3 Strain Dependency of Modulus

The first method involves acquiring a P-wave constraint modulus (D_{seismic}) from P-wave velocity results and correcting that modulus for stress level, void ratio, and strain level. The constraint modulus based on seismic tests has to be converted to a seismic elastic modulus (E_{seismic}) to be compared to resilient modulus since the propagation of P-waves through an infinite medium is assumed to represent a constraint condition. The constraint modulus can also be converted to a shear modulus (G) and the following discussion of the dependency of modulus on strain level will focus on the shear modulus to be consistent with past studies.

The non-linear modulus/strain relationship depends on the shear strain excited in the system. The resilient modulus test induces shear strains on the order of 10^{-4} mm/mm, large-scale cyclic load tests produce shear strains on the order of 10^{-3} mm/mm, and seismic efforts create a shear strain less than 10^{-6} mm/mm. Table 2.1 presented by Ishihara (1996) is useful for determining the expected shear strains when considering the degree of elasticity and the type and rate of loading.

At small shear strains such as those induced during seismic tests, elastic methods are acceptable and the soil recovers nearly all the displacement that occurs during excitation. However, at larger strains such as those induced by resilient modulus testing, elasto-plastic models are necessary to describe load-deformation behavior. The soil has both an elastic deformation and plastic deformation associated with the applied stress. The plastic deformations collapse void space and change the soil properties, changing modulus when different strains are induced.

Table 2.1. Soil behavior and modeling techniques based on shear strain amplitude (Ishihara 1996).

Shear strain	10^{-6}	10^{-5}	10^{-4}	10^{-3}	10^{-2}	10^{-1}
	Small strain	Medium strain		Large strain	Failure strain	
Elastic						
Elasto-plastic						
Failure						
Effect of load repetition						
Effect of loading rate						

The elasto-plastic behavior of soil describes both elastic and plastic deformation with an applied load. A typical hysteresis curve is shown in Figure 2.12. The low-strain shear modulus (G_0), shear stress at failure (τ_f), and reference strain (γ_r) are all shown. The reference strain is defined as the strain at the intersection of maximum shear stress and shear modulus (Hardin and Drnevich 1972):

$$\gamma_r = \frac{\tau_{\max}}{G_{\max}} \quad (2.15)$$

γ_r is small for granular materials, falling between 10^{-6} and 10^{-4} mm/mm for sands (Santamarina et al. 2001).

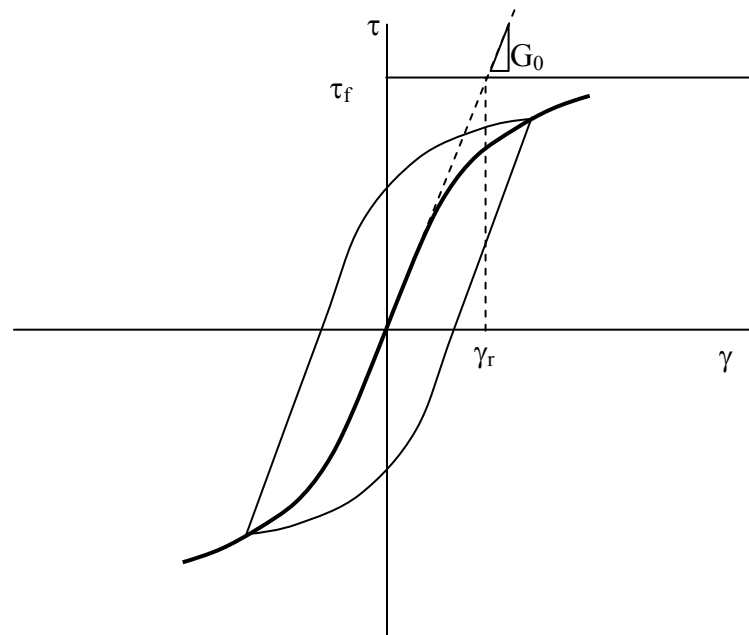


Figure 2.12. Hysteresis behavior of soil showing original shear modulus (G_0), shear stress and failure (τ_f), and the definition of the reference strain (γ_r , modified from Ishihara 1996).

Hardin and Drnevich (1972) proposed a method to analyze the relationship between shear modulus calculated at different levels of strain. The model follows a hyperbolic shear stress-shear strain relationship typical among soils (Figure 2.13).

1. The maximum shear can be approximated as:

$$\tau_{\max} = \sqrt{\left(\frac{1+K_o}{2}\sigma'_v \sin \phi' + c' \cos \phi'\right)^2 - \left(\frac{1+K_o}{2}\sigma'_v\right)^2} \quad (2.16)$$

where K_o is the coefficient of lateral earth pressure at rest, σ'_v is the vertical effective stress (equal to total stress in this testing since there is no pore water pressure), and ϕ' and c' are the effective shear strength parameters (Hardin and Drnevich 1972). The strains induced by a small (lightweight)

hammer on the surface cause negligible strains ($<10^{-6}$ mm/mm). Therefore, G_0 and G_{max} are equal and the maximum shear modulus can be estimated using the velocity of elastic waves.

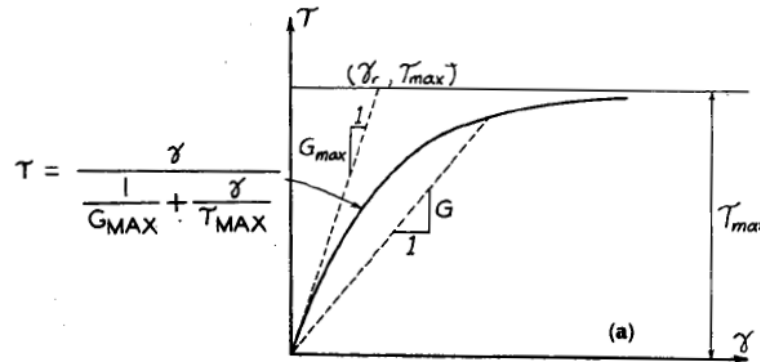


Figure 2.13. Hyperbolic stress-strain relationship of soil. The reference strain is given as the maximum shear strain considering the maximum shear modulus (Hardin and Drnevich 1972).

2. The relation between shear modulus and shear strain can be approximated with a hyperbolic function:

$$\frac{G}{G_{max}} = \frac{1}{1 + \gamma_h} \quad (2.17)$$

where Hardin and Drnevich refer to γ_h as the hyperbolic strain. The hyperbolic strain is the strain normalized with respect to the reference strain:

$$\gamma_h = \frac{\gamma}{\gamma_r} \left[1 + a e^{-b \left(\frac{\gamma}{\gamma_r} \right)} \right] \quad (2.18)$$

where a and b describe the shape of the backbone curve. A typical backbone curve comparing modulus as a function of shear strain is given in Figure 2.14.

Currently, the modulus used for road construction projects is based on the resilient modulus test, but a modulus calculated based on elastic wave velocity could be used if the relationship between modulus and strain can be found using the methodology above to convert the low strain modulus obtained with seismic tests to a high strain modulus comparable to the resilient modulus test (Figure 2.15). Although the relationship seems relatively simple, the problem is quite complex since modulus depends on several other parameters including water content, void ratio, stress history, grain shape, and soil structure (Hardin and Black 1968). However, the development of such relationship can provide great economic savings as the seismic technique could be easily implemented in the field improving material characterization and increasing the inspection density of compacted layers.

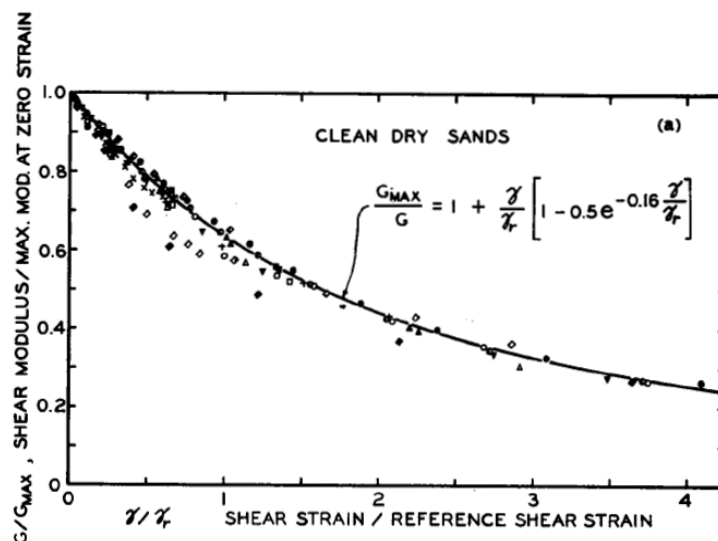


Figure 2.14. Shear modulus as a function of shear strain for clean, dry sand (after Hardin and Drnevich 1972).

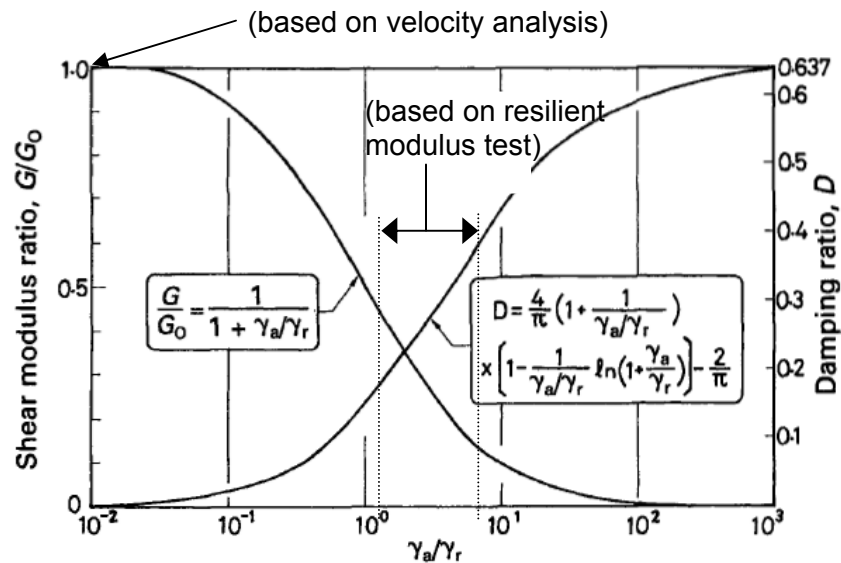


Figure 2.15. Shear modulus and damping ratio in the hyperbolic model as a function of shear strain. The graph shows the range of shear strain for the resilient modulus test and seismic test (modified from Ishihara 1996).

Figure 2.15 represents the most general relationship between modulus and strain amplitude. Kokusho (1980) examined some of the properties affecting modulus including confining stress and grain characteristics. Figure 2.16 shows the influence of confining pressure on the shear modulus-shear strain relationship. Modulus increases with confining pressure, as the soil is able to deform less with the increased confinement of particles. The backbone curve shifts to the right on a graph of shear modulus versus shear strain.

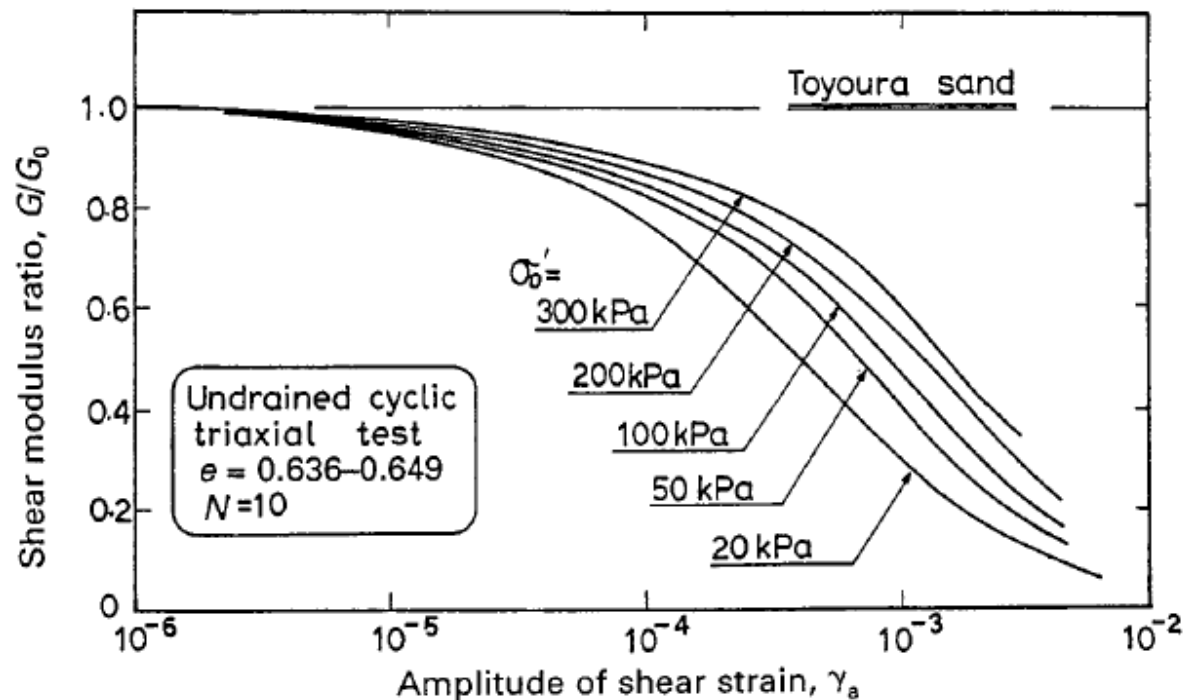


Figure 2.16. Shear modulus as a function of strain level for sand at several different confining pressures (Kokusho 1980).

Grain characteristics can also have an influence on the relationship between modulus and shear strain. Grain shape (i.e., roundness) has two effects. First, along with grain size distribution characteristics, it affects the packing characteristics i.e., the amount of void space. More well-rounded, well graded soils can typically pack to a denser state and a lower void ratio (Edil et al. 1975). Modulus has a strong dependency on void ratio (Hardin and Drnevich 1972; Edil and Luh 1978). Therefore, materials with more well-rounded gravel and sand particles such an alluvial deposit in a river in their natural state of void ratio could potentially have a higher normalized modulus at a given strain level than crushed rock with lower density. Figure 2.17 shows the approximate effect of particle roundness on shear

modulus. Second, particle shape (as well as grain size distribution) affects particle interaction through number of particle contacts and amount of interlocking. Both the low-strain modulus (Edil and Luh 1978) and high-strain behavior, i.e., friction angle (Bareither et al. 2008) are shown to decrease with increasing roundness at the same void ratio. It is observed that well-compacted crushed aggregate as used in highway construction typically has higher resilient modulus and friction angle than more-rounded sand and gravel. This is a result of the combined effects of grain characteristics as well as compaction.

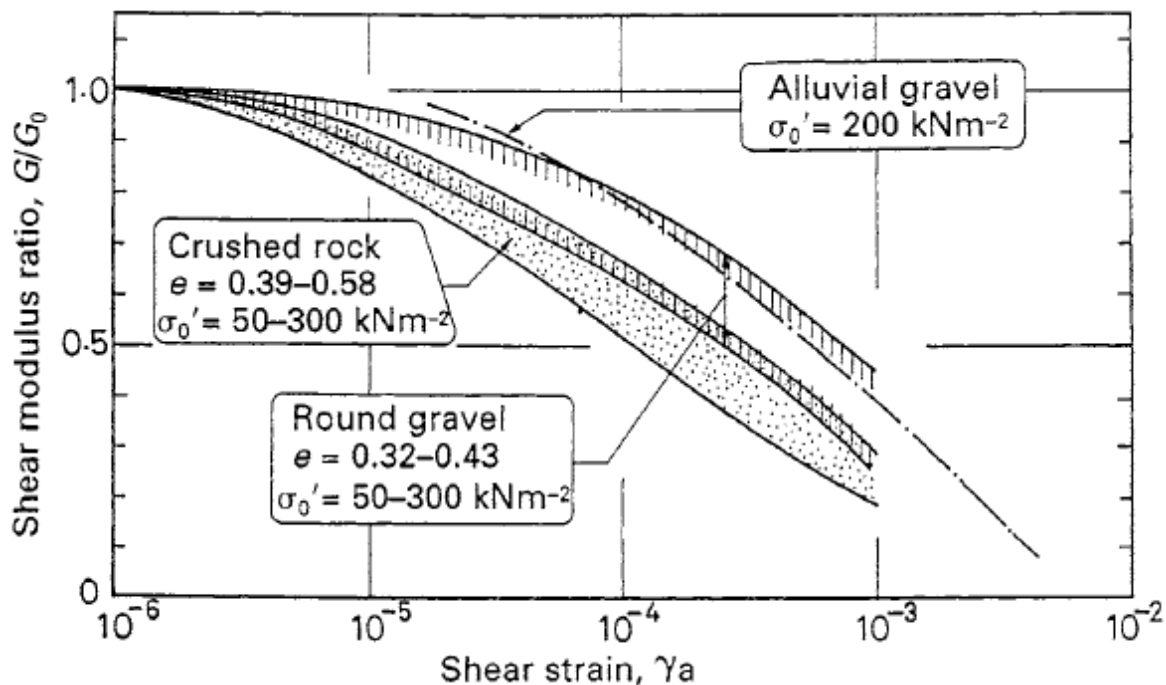


Figure 2.17. Shear modulus as a function of shear strain for crushed rock and round gravel for confining pressures between 50 and 300 kPa (Kokusho 1980).

2.4.4 Non-Strain Dependent Direct Resilient Modulus/Seismic Modulus Condition

Direct comparison studies ignore the strain dependency of modulus and attempt to directly relate the modulus from P-wave velocities to the resilient modulus at higher strain level. Such correlations essentially provide an empirical relationship.

Typical studies comparing moduli at different strain levels have focused on performing resilient modulus tests and seismic tests on unconfined specimens representing near-surface low confinement conditions (Nazarian et al. 2003; Williams and Nazarian 2007). In the majority of research studies, the specimens considered for seismic tests have the same dimensions as those of the resilient modulus tests in an attempt to keep testing conditions as consistent as possible. Also, researchers in past studies have focused on directly comparing the resilient modulus to a seismic constraint modulus without converting to an elastic modulus. However, the mechanistic approach requires converting seismic constraint modulus to seismic Young's modulus before comparing with resilient modulus. Figure 2.18 shows a typical seismic test setup employed by Nazarian et al. (2003) to measure the seismic modulus on a sample with the same dimensions as a typical resilient modulus test.

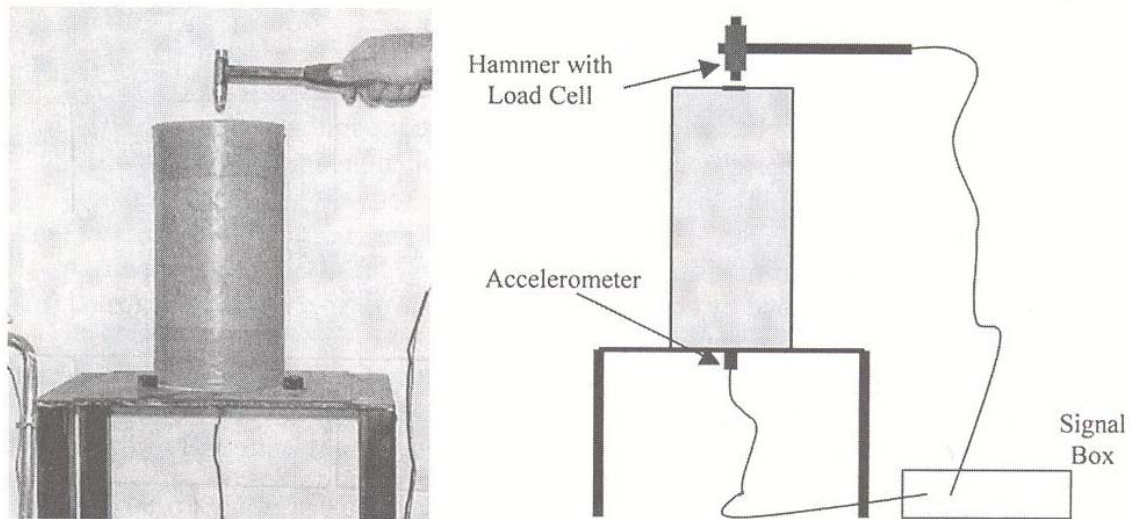


Figure 2.18. An example test setup for obtaining a modulus based on the propagation of an elastic wave. The dimensions of the sample are 150 mm in diameter and 300 mm in height (Nazarian et al. 2003).

Results of two studies comparing moduli obtained from the different testing schemes are presented by Nazarian et al. (2003) and Williams and Nazarian (2007) in Figure 2.19. Figure 2.19a is a generic figure based on tests on more than two dozen soils. The resilient modulus does not correlate well to lower moduli based on P-wave results, but the trend indicates resilient moduli are 47 % that of seismic moduli. Researchers also note that a better correlated solution can be found considering a single material. Williams and Nazarian (2007) tested a granular base course material and found that the resilient modulus is about 26.6 % that of the constraint seismic modulus Figure 2.19b.

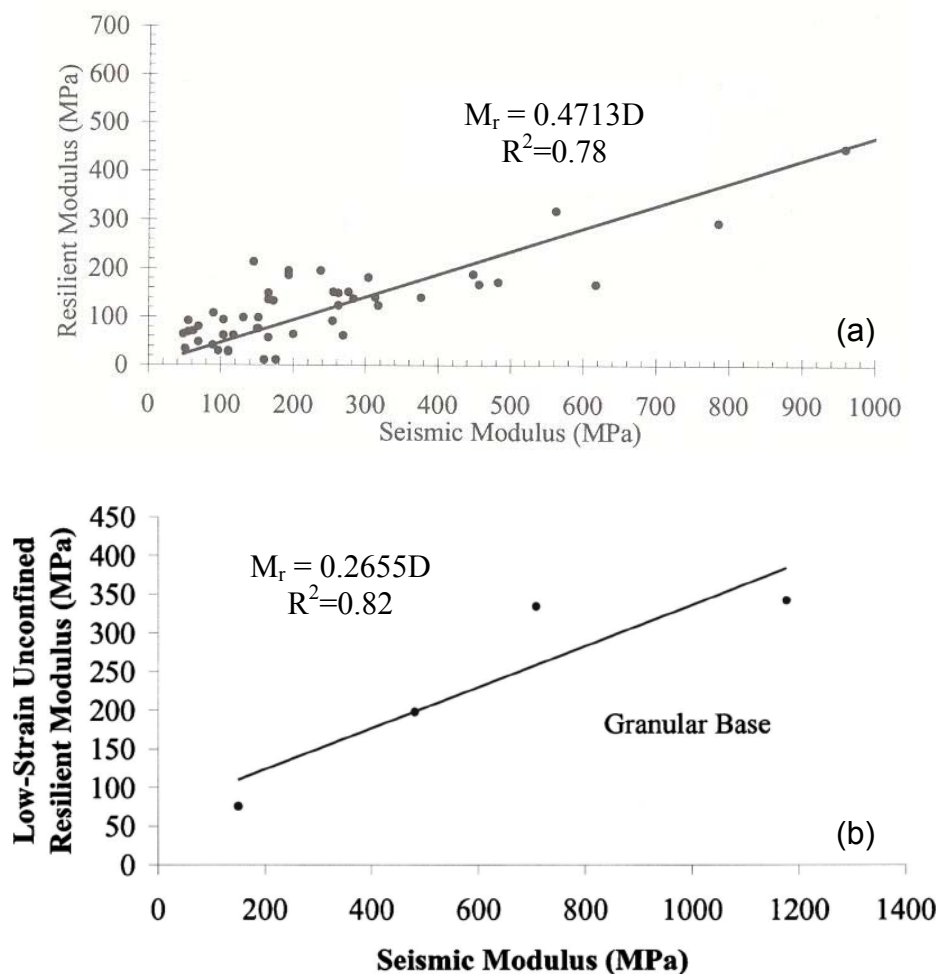


Figure 2.19. Resilient modulus as a function of constraint modulus (D_{seismic} , based on elastic wave velocity analysis) for (a) over two dozen soils and for (b) a granular base course (Nazarian et al. 2003; Williams and Nazarian 2007).

2.4.5 Large-scale Cyclic Load Conditions

Another method of assessing modulus is also presented. This method does not rely on seismic methods, but instead uses a large-scale cyclic load test and the recoverable deformation from that cyclic load to calculate an elastic modulus (E_{LS}). A pavement analysis software program, such as KENLAYER or MICHPAVE can be

used to back-calculate the modulus of the material based on plate loads and deformations of the soil surface in large-scale cyclic load test.

2.5 WAVE PROPAGATION AND THE RELATIONSHIP BETWEEN STRESS, MODULUS, AND VELOCITY

The following section continues with the description of the relationship between stress and modulus, but emphasizes how that relationship can be related to parameters (i.e., wave velocity) that can be measured in laboratory experiments. The velocity of elastic waves in particulate media depends on the stress-strain behavior of interacting particles.

2.5.1 Hertz Contact Theory

Equation (2.9) shows that less deformation at a given stress produces a higher modulus. Hertz contact theory can be used to describe the relation between stress, strain, and modulus among particles. More specifically, Hertz contact theory can be used to describe the increase in material stiffness when two elastic solids come into contact with one another. The normal force (F_N) acting on adjacent grains increases when an external stress (σ) is applied to a soil column as defined below:

$$\sigma = \frac{F_N}{A_c} \quad (2.19)$$

As a result, grains are pushed against each other and the interparticle contact area (A_c) between grains enlarges. Equation (2.19) demonstrates that when the area

increases, a larger force F_N is required to impart the same stress on the soil. The stress distribution at the contact between two grains is parabolic as shown in Figure 2.20 and with the following expression:

$$\sigma(r') = \frac{3F_N}{2\pi r^2} \sqrt{1 - \left(\frac{r'}{r}\right)^2} \quad (2.20)$$

where r' is the radial distance from the center of the contact area and r is the radius of the circular contact surface between adjacent grains (Hertz 1882; Johnson et al. 1971). Stiffness of the soil increases and bulk volume of the soil decreases as grain boundaries flatten under external loading. The elastic modulus is proportional to the stress between individual grains raised to the one-third power:

$$E_{\tan} = \frac{3}{2} \left[\frac{2G}{3(1-\nu)} \right]^{2/3} \sigma^{1/3} \quad (2.21)$$

where G and ν are the shear modulus and Poisson's ratio of the individual particles, respectively (Richart et al. 1970).

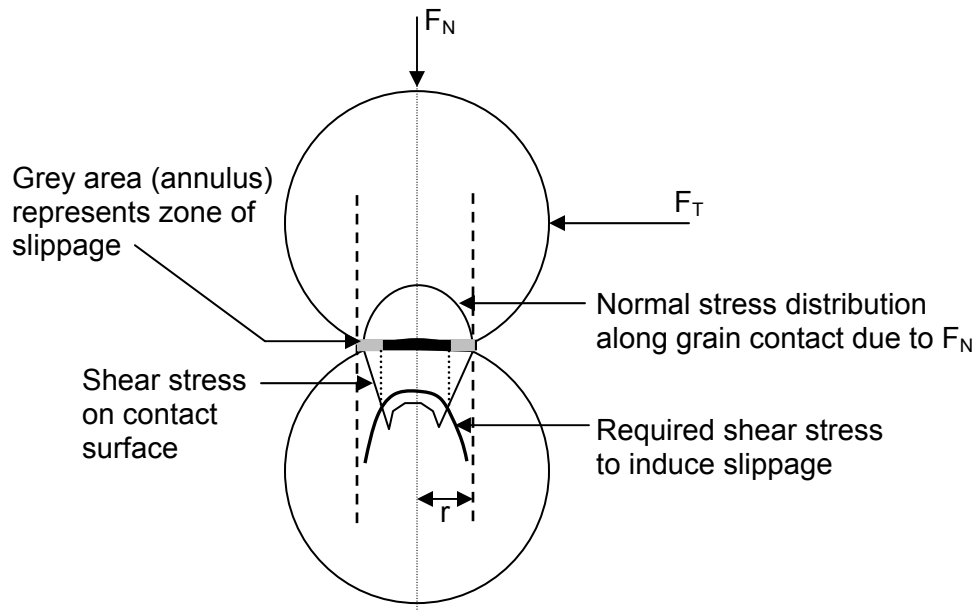


Figure 2.20. Hertzian contact theory and Mindlin shear stress behavior along a grain contact between two spherical particles. The diagram shows the parabolic stress distribution along the grain boundary and the required shear stress to induce slippage (modified from Mindlin 1949).

Hertz contact theory describes the important idea that the relationship between force and displacement in particulate media is non-linear. As grain boundary contact areas continue to flatten with more applied force, the amount of deformation in the form of displacement over the soil column decreases. A decrease in deformation as force increases results in an increased stiffness of soil. Force is proportional to the displacement between grains raised to the $3/2$ (Figure 2.21).

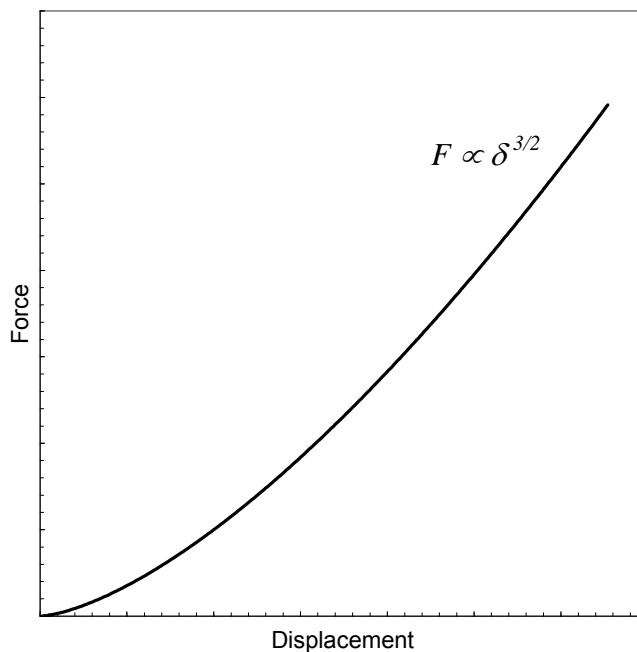


Figure 2.21. The relationship between force and displacement between spherical grains as described by Hertzian contact theory.

The lateral stiffness of the soil should also increase with increasing normal force as described by Mindlin contact theory. When a tangential force is applied to the two grains in contact, shear stresses develop along the grain contact resulting in an increase in shear stiffness and a corresponding increase in shear wave velocity. The normal stress is highest at the center of the contact area and lowest (zero) at the grain contact boundary (Equation (2.20)). The low normal forces acting along an annulus around the grain contact area cause shear stresses to exceed the required shear stresses for failure at grain contact edges and slippage occurs in the annulus shown in Figure 2.20 (Johnson et al. 1971).

2.5.2 Modes of Wave Propagation

Compression (P) waves and shear (S) waves are the two types of body waves that travel through the bulk soil mass (Figure 2.22). An important property of these small amplitude waves is that they are assumed to cause negligible permanent deformations. The speed with which these waves travel depends to a large degree on the contact area between the grains (described by Hertz and Mindlin's theories). The contact area between grains can be described using stress and strain characteristics of the material. Therefore, the velocity of elastic waves can be described in terms of the modulus (stress and strain) and material density.

The physical propagation of waves through space depends on the movement of individual particles as the energy from the wave is transferred along the particle-particle contacts. Since seismic wave propagation is an elastic phenomenon, forces and moments in an elementary volume are balanced. When equilibrium is satisfied, elastic waves do not cause permanent effects to the soil. The equilibrium equation in terms of normal and shear stresses for a P-wave traveling in the x-direction is:

$$\frac{\partial \sigma_x}{\partial x} + \frac{\partial \tau_{xz}}{\partial z} + \frac{\partial \tau_{yx}}{\partial y} + X = 0 \quad (2.22)$$

where χ is the body force in the x-direction. Equation (2.22) includes the normal stress on the particle (σ_x) and the shear stresses in the y (τ_{yx}) and z (τ_{zx}) directions.

Equilibrium equations describe elastic waves in terms of the state of stress applied to the representative volume of soil, but are not sufficient to describe the relation between stress and strain. Compatibility equations are used to express the strain (ϵ_x) in terms of a displacement vector (u_x):

$$\varepsilon_x = \frac{\partial u_x}{\partial x} \quad (2.23)$$

Shear strain (γ_{xy}) can be written in a similar manner to the axial strain:

$$\gamma_{xy} = \frac{\partial u_x}{\partial y} + \frac{\partial u_y}{\partial x} \quad (2.24)$$

Combining equilibrium (Equation (2.22)), constitutive (Equations (2.9) and (2.10)), and compatibility (Equation (2.23) and (2.24)) equations, the wave equation for compression waves can be written in terms of constraint modulus (in semi-infinite media), density, time, and position:

$$\frac{\partial^2 u_x}{\partial t^2} = \frac{D}{\rho} \frac{\partial^2 u_x}{\partial x^2} \quad (2.25)$$

The solution to Equation (2.25) is defined in terms of the amplitude (A), the angular frequency (ω), and the wave number (κ) and is written in terms of both time (t) and position (x). The wave number is $\kappa = \frac{2\pi}{\lambda}$ where λ is the wavelength.

$$u = Ae^{j(\omega t \pm \kappa x)} \quad (2.26)$$

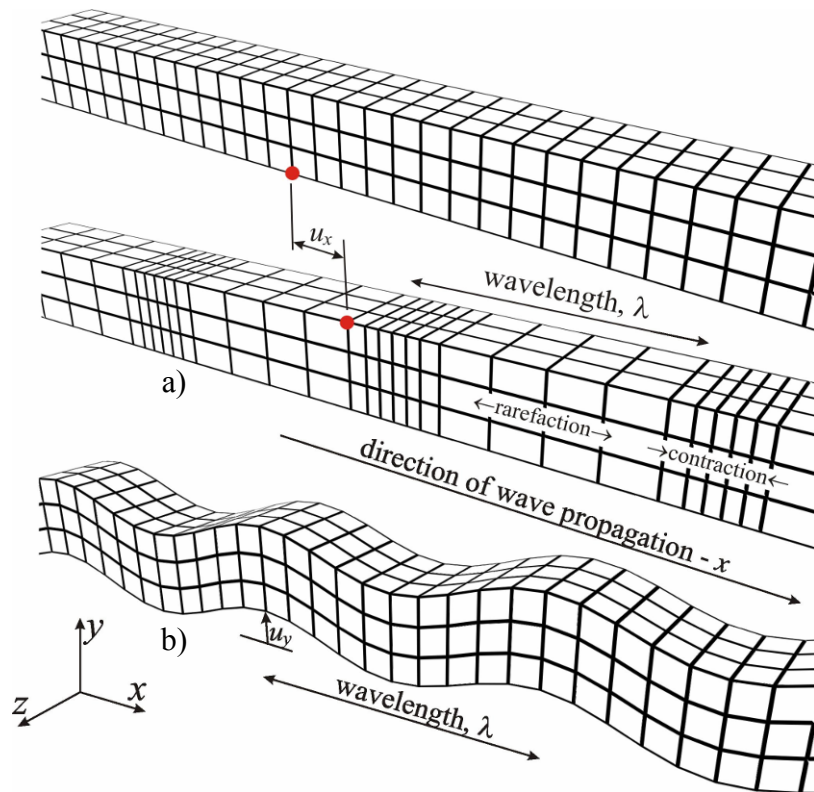


Figure 2.22. Different modes of wave propagation include both compression (P) waves (a), and shear (S) waves (b). (Rendering by Damasceno 2007).

The velocity of wave propagation can be found by solving the wave equation after inserting the expression for the displacement vector (Equation (2.26)) into the wave equation. The left side of equation (2.25) can be integrated in terms of x , while the right side can be integrated in terms of t . After integration, the wave equation appears as follows:

$$\rho(\pm A\kappa^2 e^{j(\omega t \pm \kappa x)}) = D(\pm A\omega^2 e^{j(\omega t \pm \kappa x)}) \quad (2.27)$$

Several terms on both sides of the wave equation cancel since the displacement vector appears on both sides of the wave equation:

$$\frac{\omega^2}{\kappa^2} = \frac{D}{\rho} \quad (2.28)$$

The wave equation shows that particle displacement is related to both the stiffness and density of a particulate medium. The velocity of wave propagation increases with applied load and an increase in soil stiffness. P-wave velocity in particulate media is dependent on the constraint modulus (D) and density and can also be defined in terms of angular frequency and wave number (Santamarina et al. 2001; Graff 1975; Richart et al. 1970):

$$V_p = \frac{\omega}{\kappa} = \sqrt{\frac{D}{\rho}} = \sqrt{\frac{E(1-\nu)}{\rho(1+\nu)(1-2\nu)}} \quad (2.29)$$

S-waves are described in more detail in Appendix B.

P-wave velocity is proportional to the square root of constraint modulus and is also proportional to the confining pressure raised to the 1/6 power for a simple cubic packing. If density is assumed a constant in laboratory tests and the volume of soil changes relatively little with respect to sample size, an estimation of velocity at applied stress can be made. A semi-empirical relationship between P-wave velocity (V_p) and effective stress parallel to the direction of particle motion (σ_{\parallel}) at a point in the soil specimen is shown in the following expression (Santamarina et al. 2001):

$$V_p = \alpha \left(\frac{\sigma'_{\parallel}}{p_r} \right)^{\beta} \quad (2.30)$$

where α and β are material-dependent constants and p_r is a reference stress (1 kPa). The coefficient α is the P-wave velocity of an elastic wave through material confined to an effective stress of 1 kPa. The exponent β indicates how sensitive the wave velocity is to effective stress changes (Santamarina et al. 2001; Fratta et al. 2004). Equation (2.30) shows that velocity does not change substantially at large applied pressures when the constant β is less than 1 (Fratta et al. 2005).

2.6 MODULUS REINFORCEMENT FACTOR

The ultimate goal of the velocity results is not only to obtain a comparable resilient modulus based on seismic tests, but also to use that modulus to compare the change in stiffness near the geogrid reinforcement. Large-scale tests performed with geogrid by Kim (2003) indicate that a modulus reinforcement factor can be applied to the reinforced base material that compares the ratio of reinforced and unreinforced resilient moduli:

$$\text{Reinforcement Factor} = \frac{M_{r-\text{reinforced}}}{M_{r-\text{unreinforced}}} \quad (2.31)$$

Kim (2003) found that the reinforcement factor for geogrid reinforced grade 2 gravel was approximately 2.0 when secured between a 300 mm thick base course material and soft subgrade material. The reinforcement factor is applied to the whole layer, but this research attempts to define a “zone of influence” over which to apply a factor in the base course material. The reinforcement factor may only apply to a

certain volume of base course, thus modifying the stress and strain distribution in subsurface soils.

2.7 ROTATION OR SHEARING OF SOIL

The above discussion focused on the use of seismic tests and a computation of modulus based on velocity to determine the properties of the soil and resulting change in modulus surrounding a geogrid reinforcement layer. The stiffness or rigidity of the bulk soil mass can also be analyzed by considering the amount of shear deformation induced in the soil by the propagation of shear stresses to and around the geogrid reinforcement. The rotation or shear of soil is expected to be relatively large beneath the edge of a loading plate and if rotations of materials can be monitored in the soil system, especially in close proximity to a geogrid, the influence zone of the geogrid may be visualized qualitatively. A “zone of influence” can then be assigned to the material surrounding the geogrid and a stiffer modulus may be applied to this small zone where particles are being confined developing a reinforcement factor similar to the reinforcement factor assigned by Kim (2003).

Figure 2.7 showed the expected zone of shearing as a circular plate is loaded. The shear stresses develop in near-surface soils and propagate further into the subsurface causing rotation of individual particles. The rotation of particles in the soil column can be calculated knowing the displacement of the particle with respect to neighboring particles in orthogonal directions. Although computationally intensive by hand, a computer program can be used to estimate the amount of deformation in

subsurface soils and to predict the amount of rotation expected beneath a load plate with and without geogrid reinforcement.

2.7.1 Modeling Rotation with PLAXIS

PLAXIS is a finite elements (FE) code used for stress/strain analysis of soil and rock. The program contains features that allow for the analysis of the geotechnical behavior of soil, rock, and other interfaces including geogrids. PLAXIS is a powerful modeling tool that allows for the approximate determination of stress and strain characteristics of underlying soil, physical properties that can be used to estimate the rotation of individual “soil elements.”

To estimate the amount of shear, relative displacements are measured with respect to the horizontal (x) and vertical (y) coordinates. The rotation tensor (ω_{xy}) can be expressed with the following relationship:

$$\omega_{xy} = \frac{1}{2} \left(\frac{\partial u_x}{\partial y} - \frac{\partial u_y}{\partial x} \right) \quad (2.32)$$

where $\delta u_x / \delta y$ is the partial derivative of the displacement in the x-direction with respect to y and $\delta u_y / \delta x$ is the partial derivative of the displacement in the y-direction with respect to x (Achenbach 1975). Figure 2.23 shows the parameters used for the computation of Equation (2.32). The PLAXIS-calculated rotations based on the displacement vectors can then be compared to the rotation angle of the soil

monitored in laboratory tests. Appendix E has a more detailed description of the calculation of the rotation tensor using PLAXIS.

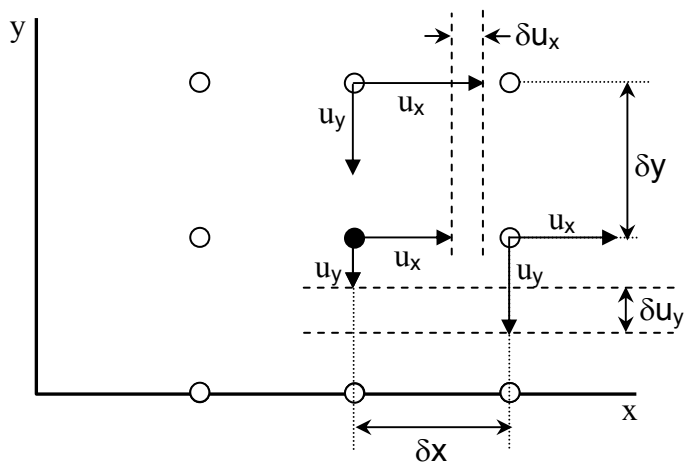


Figure 2.23. Relative displacement and rotation of particle in two dimensions with respect to x and y axes.

3 MEASUREMENT TECHNIQUES, MATERIALS, AND METHODS

Laboratory tests involved measuring the following four parameters:

- Load
- Displacement of the load plate
- Dynamic acceleration caused by propagation of elastic waves
- Soil rotation

Forces applied to the plate were measured with a load cell (3.3 mV/V at 2000 lbs) and the displacement of the plate was measured with an LVDT with a resolution of 0.01 mm. Both load cell and LVDT measurements were acquired and saved to a computer using LabVIEW. Subsurface measurements (dynamic and gravitational acceleration) were acquired using accelerometers buried in the soil column. The following section outlines the description and use of accelerometers.

3.1 MICRO-ELECTRO-MECHANICAL SYSTEMS (MEMS) ACCELEROMETERS

3.1.1 Description

Analog Devices first developed their micro-electro-mechanical systems (MEMS) accelerometers 15 years ago for use in automobiles as triggers for airbag systems (Analog Devices 2007). In general, MEMS can be mechanical components, sensors, actuators, and electronics that have dimensions on the order of millimeters (McDonald 1997). The MEMS accelerometers developed by Analog Devices are 4 mm x 4 mm x 1.5 mm in size and are sensitive to both static (e.g., gravity) and dynamic (e.g., vibration) accelerations. In addition to measuring the acceleration of a

propagating wave, accelerometers used in this study can be utilized to measure rotational deformation or shearing in materials by determining the vertical and horizontal contributions to gravity.

The laboratory research presented herein uses small MEMS accelerometers and corresponding printed circuit boards (PCB) 18 mm by 18 mm manufactured by Sparkfun Electronics (Figure 3.1). The accelerometers are able to measure particle accelerations caused by a propagating elastic wave as it travels vertically through a soil column and are also able to measure the horizontal and vertical components of the acceleration caused by the gravitational field. By measuring the components of gravity, the tilt angle of the accelerometer can be calculated after a load is applied at the surface. Each printed circuit board contains 0.1 μF filtering capacitors and a 1 M Ω resistor required for operation.



Figure 3.1. Analog Devices ADXL203CE accelerometer and corresponding printed circuit board (PCB, Sparkfun Electronics).

The accelerometers used for all tests in this research project are Analog Devices ADXL 203CE dual axis MEMS. The ADXL 203CE accelerometers have a sensitivity of 1000 mV/g up to 1.5 g. More detailed specifications of the ADXL 203CE accelerometers are given in Table 3.1.

3.1.2 Principles of Operation

In this research study, between 4 and 12 accelerometers were used to measure changing velocity and rotation in an experimental pavement model system. Each accelerometer requires the connection of four ports including: a power supply of between 3 and 6 V (i.e., 5 V in this project), a ground, and two analog outputs. The analog signal is monitored from X and Y ports, enabling for the collection of dynamic and gravitational acceleration in two normal directions.

The use of small MEMS accelerometers allows for the detection of small changes in velocity in the laboratory on the scale of centimeters in a similar way that geophones can detect these changes on the order of meters and kilometers in field scale seismic studies. Although MEMS accelerometers can be used on a scale of centimeters, great care must be taken to ensure precise measurement of the distance between accelerometers. A small change in separation distance between accelerometers can produce a large change in the calculated velocity and unreliable results.

Table 3.1. Specifications for Analog Devices ADXL 203CE accelerometer (Source: www.analog.com).

$T_A = -40^{\circ}\text{C}$ to $+125^{\circ}\text{C}$, $V_S = 5\text{ V}$, $C_X = C_Y = 0.1\ \mu\text{F}$, acceleration = 0 g, unless otherwise noted.

Table 1.

Parameter	Conditions	Min ¹	Typ	Max ¹	Unit
SENSOR INPUT					
Measurement Range ²	Each axis	± 1.7			g
Nonlinearity	% of full scale		± 0.2	± 1.25	%
Package Alignment Error			± 1		Degrees
Alignment Error (ADXL203)	X sensor to Y sensor		± 0.1		Degrees
Cross-Axis Sensitivity			± 1.5	± 3	%
SENSITIVITY (RATIOMETRIC)³					
Sensitivity at X_{out}, Y_{out}	Each axis $V_S = 5\text{ V}$	960	1000	1040	mV/g
Sensitivity Change Due to Temperature ⁴	$V_S = 5\text{ V}$		± 0.3		%
ZERO g BIAS LEVEL (RATIOMETRIC)					
0 g Voltage at X_{out}, Y_{out}	Each axis $V_S = 5\text{ V}$	2.4	2.5	2.6	V
Initial 0 g Output Deviation from Ideal	$V_S = 5\text{ V}, 25^{\circ}\text{C}$		± 25		mg
0 g Offset vs. Temperature			± 0.1	± 0.8	mg/ $^{\circ}\text{C}$
NOISE PERFORMANCE					
Output Noise	<4 kHz, $V_S = 5\text{ V}$		1	3	mV rms
Noise Density			110		$\mu\text{g}/\sqrt{\text{Hz}}$ rms
FREQUENCY RESPONSE⁵					
C_X, C_Y Range ⁶		0.002		10	μF
R_{FIL} Tolerance		24	32	40	k Ω
Sensor Resonant Frequency			5.5		kHz
SELF TEST⁷					
Logic Input Low				1	V
Logic Input High		4			V
ST Input Resistance to Ground		30	50		k Ω
Output Change at X_{out}, Y_{out}	Self Test 0 to Self Test 1	450	750	1100	mV
OUTPUT AMPLIFIER					
Output Swing Low	No load	0.05	0.2		V
Output Swing High	No load		4.5	4.8	V
POWER SUPPLY					
Operating Voltage Range		3		6	V
Quiescent Supply Current			0.7	1.1	mA
Turn-On Time ⁸			20		ms

¹ All minimum and maximum specifications are guaranteed. Typical specifications are not guaranteed.

² Guaranteed by measurement of initial offset and sensitivity.

³ Sensitivity is essentially ratiometric to V_S . For $V_S = 4.75\text{ V}$ to 5.25 V , sensitivity is 186 mV/W/g to 215 mV/W/g.

⁴ Defined as the output change from ambient-to-maximum temperature or ambient-to-minimum temperature.

⁵ Actual frequency response controlled by user-supplied external capacitor (C_X, C_Y).

⁶ Bandwidth = $1/(2 \times \pi \times 32\text{ k}\Omega \times C)$. For $C_X, C_Y = 0.002\ \mu\text{F}$, bandwidth = 2500 Hz. For $C_X, C_Y = 10\ \mu\text{F}$, bandwidth = 0.5 Hz. Minimum/maximum values are not tested.

⁷ Self-test response changes cubically with V_S .

⁸ Larger values of C_X, C_Y increase turn-on time. Turn-on time is approximately $160 \times C_X$ or $C_Y + 4\text{ ms}$, where C_X, C_Y are in μF .

Prior to placing each accelerometer into a specimen, the accelerometers were coated with a durable, water tight epoxy seal. The seal not only ensures that water or dust will not short out the electronic components of the system, but will also mechanically protect the fragile accelerometer, PCB, and wires connected to the accelerometer. Protection of the MEMS accelerometers was crucial, especially when

using aggregates with gravel-sized particles that are on the same scale of size as the accelerometers. Each accelerometer was coated with Smoothcast 327 liquid plastic. Smoothcast 327 comes as two liquid components and, when set, is similar in nature to an epoxy. The liquid components are combined and the resulting compound hardens over a period of several hours. After hardening, the plastic has a compressive strength of 31,400 kPa and a hardness of 72D on the Shore hardness scale (to put this in perspective, the hardness of a construction hardhat is approximately 75D). Excess plastic is trimmed from the accelerometers with either a saw or knife to minimize the size of each accelerometer to reduce the impact of the plastic coating on wave propagation. An attempt to constrain the size of the coated accelerometers was also made to prevent the accelerometers from influencing test material properties such as bearing capacity or strength, although little could be done to constrain the influence of the wires extending from each accelerometer. A sample of the coating applied to the accelerometers is shown in Figure 3.2.

Once the protective coating is applied to the accelerometer and PCB, the accelerometers are placed in the soil. When several accelerometers are situated a known distance apart, the velocity of a propagating elastic wave can be calculated and each accelerometer produces a voltage response. The change in voltage is a result of the change in separation between capacitor plates within MEMS (Acar and Shkel 2003). The capacitor plates in the MEMS accelerometers used in this study are separated by polysilicon springs and voltage is proportional to the acceleration caused by the propagation of the elastic wave.



Figure 3.2. Smoothcast 327 coating applied to MEM accelerometer and PCB (ruler gradations are in cm).

As opposed to the acceleration measured by the propagation of the elastic wave, gravitational acceleration is measured by monitoring the direct current (DC) output voltage of accelerometers. One component of the voltage can be measured from the x-axis and a second component of voltage can be measured from the y-axis. Although the accelerometer can measure two components of gravitational acceleration, only one component is necessary to compute the angle of rotation of the accelerometer if the two axes of the accelerometer remain in the vertical plane. A rotation of 90° of an accelerometer causes a change in voltage of ± 1 V in each axis depending on the original orientation of the accelerometer.

3.2 MEASURING ELASTIC WAVE VELOCITY WITH MEMS ACCELEROMETERS

MEMS accelerometers were used to measure the dynamic response of the accelerometer to the propagation of an elastic wave. As the elastic wave progresses

the acceleration changes and the arrival of the elastic wave can be captured with each accelerometer. The velocity of an elastic wave between accelerometers can be measured knowing the arrival time (indicated by the acceleration) of the wave at each accelerometer and the distance between accelerometers. The methods and importance of choosing the first arrival of elastic waves are discussed in Appendix D.

3.3 MONITORING ROTATION WITH MEMS ACCELEROMETERS

Subsurface soil rotation is monitored using the MEMS' DC output. The Analog Devices MEMS have a 2.5 V output at an acceleration of 0 g. The relative contributions to acceleration caused by gravity on each accelerometer axis indicate the degree of rotation of each accelerometer. Figure 3.3 shows an example MEMS accelerometer and the corresponding voltage outputs at 0° (parallel to the surface of the earth) and 90° (perpendicular to the surface of the earth) with respect to the positive x and y-axes.

The rotation of the accelerometer is based on the change in voltage output with respect to gravitational acceleration and is expressed with simple trigonometric expressions. The analysis and variables defined in the following discussion are shown in Figure 3.4.

The angle θ_1 is the original rotation of the accelerometer when placed in the soil. Accelerometers are not originally oriented orthogonal to earth's gravitational axis, but are reoriented and displaced with the addition of soil and due to the tamping compaction effort. Voltage output at an angle θ_1 can be expressed as:

$$V(\theta_1) = A - Sens \cdot g \cdot \sin(\theta_1) \quad (3.1)$$

where $A = 2.5 \text{ V}$, $Sens=1\text{V/g}$ is the accelerometer sensitivity when each axis originally receives 2.5 V , and g is the acceleration due to gravity (9.81 m/s^2). Equation (3.1)) can also be used to calculate the angle θ_2 , which is the angle from the horizontal axis to the new orientation after external loading.

The same steps above can be applied to obtain the angle of orientation from the vertical axis to the new orientation; however, the DC output resolution of the MEMS accelerometers depends on the orientation of the accelerometer with respect to the horizontal and the resolution of the voltmeter. The maximum resolution of the MEMS is 0.06° .

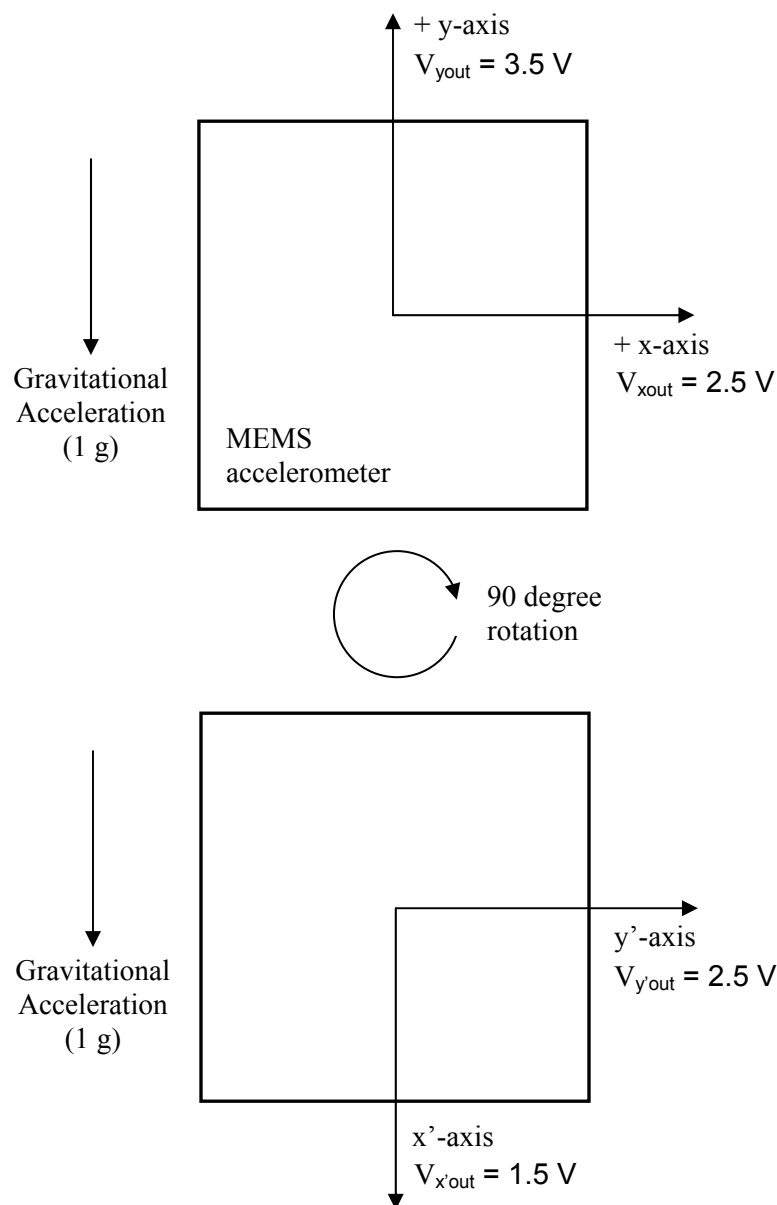


Figure 3.3. Coordinate axes and voltage outputs of ADXL 203 CE MEMS accelerometers on orthogonal axes with respect to gravitational acceleration.

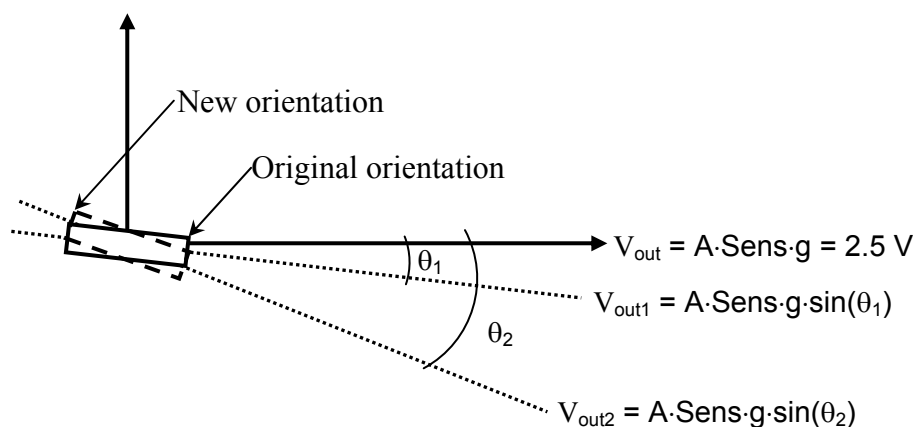


Figure 3.4. Calculating the rotation of each accelerometer with respect to the horizontal.

Each accelerometer axis is most sensitive when parallel to the earth's surface (perpendicular to gravitational acceleration) and least sensitive when perpendicular (parallel to earth's gravity). The sensitivity of the accelerometer most closely follows the slope of a sinusoidal function. When the accelerometer axis is oriented at 0° to the horizontal, the slope of the sine function is at a maximum as is resolution. When tilted to an angle of 90° , the slope of the sine function is zero and the resolution is decreased. A comparison of voltage output and resolution is shown in Figure 3.5. Resolution decreases between 0 and 45° from horizontal and more sharply beyond rotation angles of 45° to the horizontal, making measurements of DC voltage at high angles to the horizontal impractical. However, using dual axis MEMS accelerometers prevents the need to acquire DC output voltages from accelerometers at angles greater than 45° . Tilt angles considered in this research are generally less than 10° where resolution is degraded by less than about 2.5 %. In contrast, at an angle of 45° , the resolution is decreased by approximately 30 %.

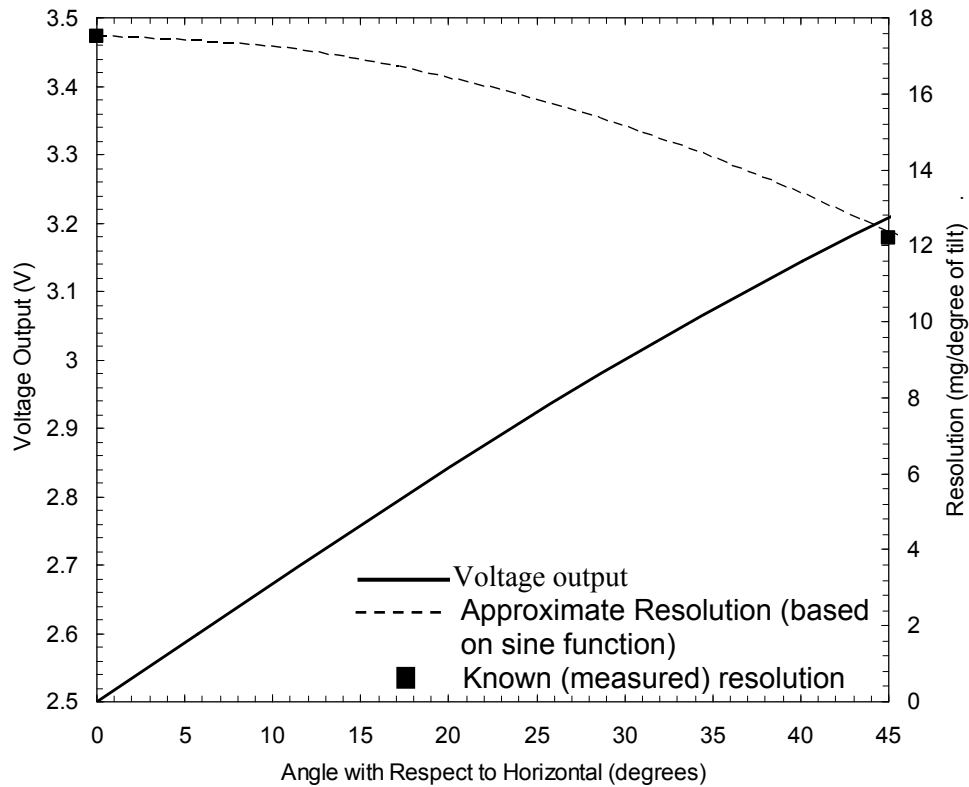


Figure 3.5. DC voltage output and resolution of MEMS accelerometer as the angle of orientation of the measuring axis to horizontal changes.

3.4 TEST MATERIALS

Laboratory tests to determine the relation between seismic modulus and resilient modulus were performed on the following materials: Portage sand (clean, poorly graded sand), Wisconsin grade 2 gravel (crushed limestone road base gravel), Minnesota class 5 gravel (road base sand and gravel – Mn/DOT 2008), recycled pavement material (RPM), and pit run sand and gravel (poorly graded sand and gravel with large particles), and breaker run (crushed rock with large particles).

Grain size distributions for Portage sand, grade 2 gravel, class 5 gravel, RPM, pit run gravel, and breaker run are shown in Figure 3.6. Additional physical properties of each material are noted in Table 3.2 and photographs are shown in Figure 3.7.

The materials were chosen based on the range of gradation and typical use of the materials in road design and construction. Portage sand is a poorly graded sand material that was used in preliminary tests and as a comparison to more coarsely graded materials. Poorly graded sand is not a good choice for a base course material, but was easy to work with and allowed for rapid testing of the effectiveness of MEMS accelerometers at detecting the change in velocity associated with applied stress. Furthermore, the dynamic properties of the sand are better-defined.

The procedures were developed with grade 2 gravel, a common aggregate used to construct base courses. Specifications for grade 2 gravel are given by the Wisconsin Department of Transportation (WisDOT) section 304 (Wisconsin Standard Specifications for Highway and Structure Construction 1996). The grade 2 gravel used in this study was retrieved from a quarry near Madison, Wisconsin and consisted of crushed limestone. Grade 2 gravel used in this study contains angular grains and approximately 18 % fines. The tests in grade 2 gravel provided the validation for the seismic methodology for the resilient modulus since we also have its resilient modulus from the standard specimen test. After this calibration, characterization of the resilient modulus of materials such as breaker run and pit run gravels could be made on the basis of the seismic method. These last two materials

cannot be tested in the common resilient modulus test cells because of the large-size particles they contain.

Class 5 gravel consists of rounded sand and gravel particles. This gravel was “manufactured” to conform to standard specifications proposed by the Minnesota Department of Transportation.

RPM is retrieved when the pavement and part of the underlying base course material are removed and crushed. Material larger than 1 inch was removed from the RPM so that seismic test results can be compared with resilient modulus tests. The RPM used in this study was obtained from a construction project south of Madison, Wisconsin.

Pit run gravel is poorly graded sand with rounded gravel particles (up to 50 mm in diameter) and less than 5 % fines. Breaker run (crushed rock) and Pit run gravel cannot be tested in traditional resilient modulus testing equipment because of the large-size particles (>25 mm) they contain and were chosen to determine whether seismic methods are a valid method to determine an equivalent resilient modulus.

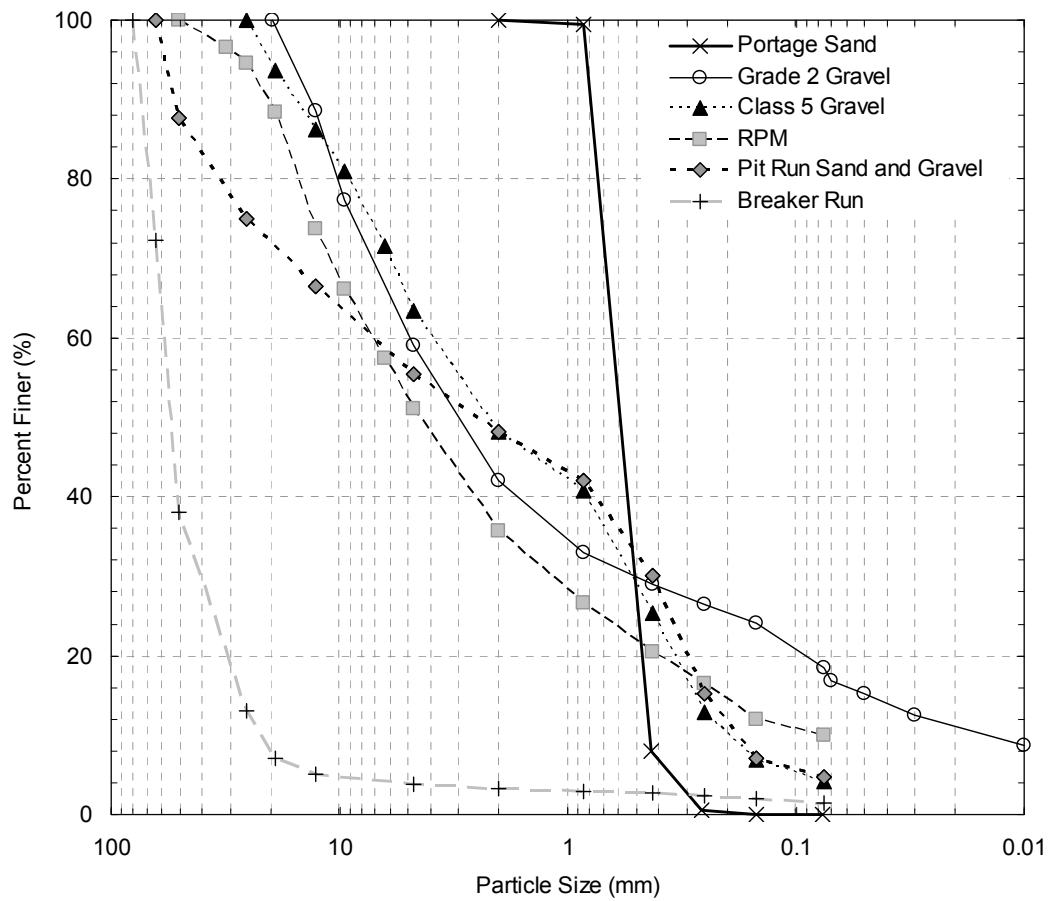


Figure 3.6. Grain size distribution for materials tested in laboratory experiments.

Table 3.2. Physical properties of materials tested in laboratory experiments.

Soil Name	C_u	C_c	Percent Fines	USCS symbol	G_s	$\gamma_{d \max}$ kN/m ³	e_{test}	$\gamma_{d \text{ test}}$ kN/m ³	RC %	D_r %
Portage Sand	1.0	1.0	0	SP	2.65	17.7	0.58	16.5	93.2	52.0
Grade 2	217	1.4	18	SM	2.65	21.5	0.40	18.5	86.0	30.0
Class 5	33.3	0.7	4.1	SP	2.72	20.9	0.42	18.8	90.0	35.5
RPM	89.5	2.5	10.6	GW/GM	2.64	21.2	0.33	19.5	92.0	45.4
Pit Run	39	0.14	4.7	SP/GP	2.65	20.0	0.33	19.5	97.5	79.5
Breaker Run	2.9	1.2	1.4	GW	2.65	20.6	0.70	15.3	74.3	0.0

Notes: C_u = coefficient of uniformity, C_c = coefficient of gradation, G_s = specific gravity, $\gamma_{d \max}$ = standard Proctor maximum dry unit weight (used in the resilient modulus test), e_{test} = void ratio in the test container, RC = relative compaction; and D_r = relative density in the test container

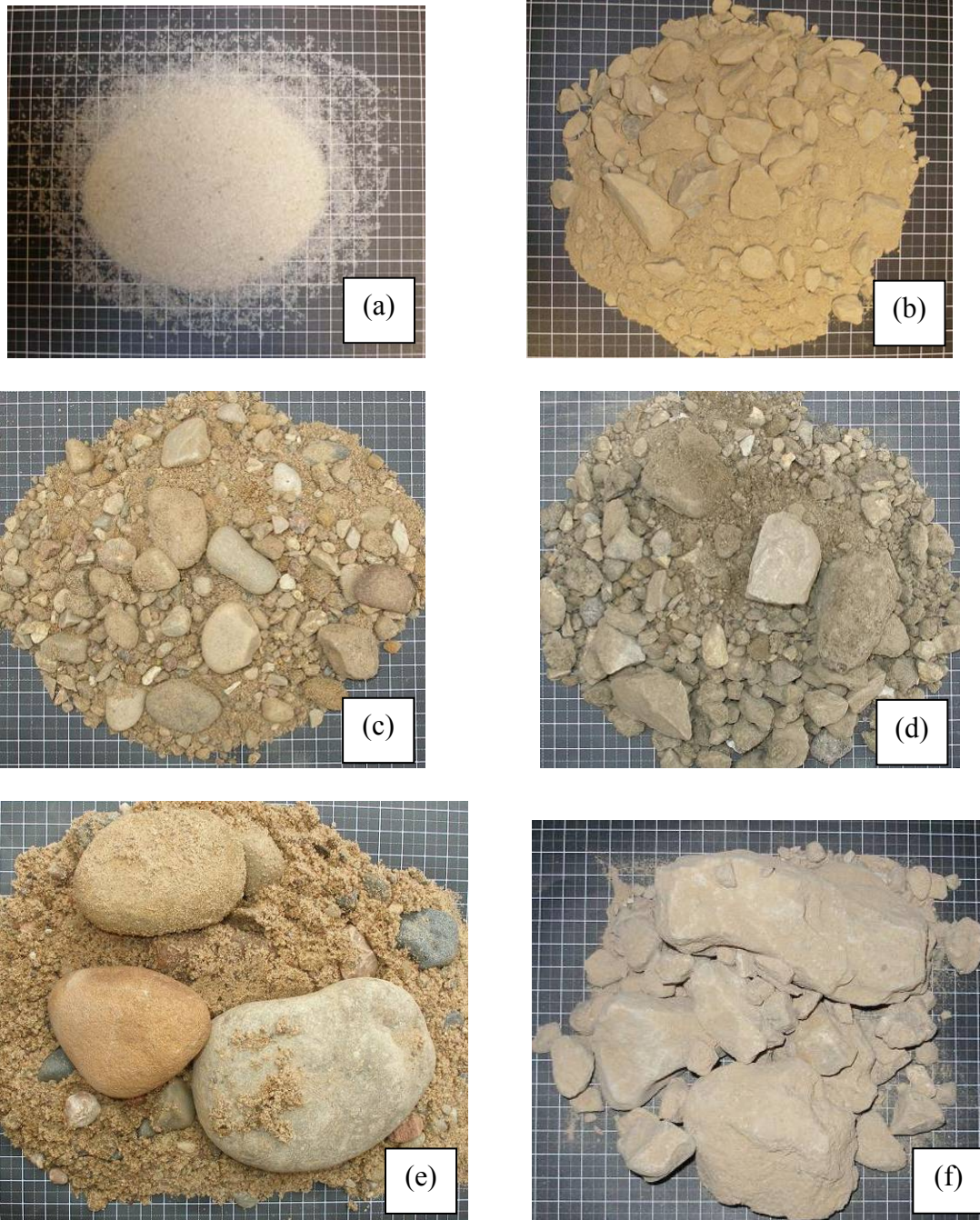


Figure 3.7. Photographs of materials used in research project. Bold divisions on graph paper are 10 mm increments and fine lines are 5 mm increments: a. Portage sand, b. Grade 2 gravel, c. Class 5 gravel, d. RPM, e. Pit run sand and gravel, and f. Breaker run.

Selected properties of two geogrids used in this study are presented in Table 3.3. The first geogrid was a lower-modulus, woven biaxial geogrid with relatively small apertures. Since the first geogrid was rather weak and did not have high initial stiffness, a second geogrid with a modulus of approximately 2.5 times that of the non-stiff geogrid was used in the majority of tests to determine the “zone of influence” of reinforcement. A smaller deformation is required at the point of maximum elastic modulus for the stiffer geogrid, an indication the geogrid may be engaged with surrounding soil at lower applied loads rather than extending concurrently with soil deformation.

Table 3.3. Physical properties of geogrids used in testing

Geogrid	Type	Aperture Size	Peak Tensile Strength (ASTM D 6637)	Maximum Elastic Modulus
	--	mm	kN/m	kN/m
Non-stiff	Woven	19	19.2	213 (@ 7.5% strain)
Stiff	Extruded	38	33.4	534 (@ 3.5 % strain)

3.5 TESTING CELLS

Initial tests were conducted in a 0.36 m diameter PVC pipe with an inside diameter of 0.33 m. The pipe (Figure 3.8) was cut to a depth of 0.61 m. This cylindrical testing cell was constructed quickly to perform initial tests, but the depth-to-width ratio was too large to be used effectively because the side walls of the PVC

cell may refract waves and affect the stress distribution. The circular cell also limited the practicality of testing geogrid reinforcement.

Once initial tests showed that velocity changes with depth and increased static loading, a new test cell was constructed. The new test cell was constructed from wood and is 0.61 m wide and 0.91 m in length (Figure 3.9). Dimensions of the box were determined based on two driving factors. First, the length of the box was extended to 0.91 m to allow for an increased horizontal separation of accelerometers and to minimize “edge effects” on elastic wave propagation and stress distribution. Accelerometers were secured both horizontally and vertically in the test cell depending on desired information. The width of the box was constraint to 0.61 m so that the box would fit in an existing load frame assembly at the University of Wisconsin – Madison. The design depth of the box was 0.61 m and was constrained by equipment already in place and because depth of base course material is not expected to exceed 300 – 600 mm in the field. Stresses applied by a 150 mm diameter plate decrease rapidly at depths exceeding 0.25 to 0.3 m since the load is spread over an increasingly larger area. In addition, a deeper box would require a greater amount of material and more sample preparation time as well as a more involved testing procedure. The box requires 0.34 m³ of material as constructed.



Figure 3.8. Preliminary test cell. The outside diameter of the PVC shell is 35.6 cm, while the inside diameter is 330 mm. The height of the cylindrical cell is 600 mm.



Figure 3.9. Wooden box test cell. The box is 0.91 m long, 0.61 m wide, and 0.61 m deep and is filled with Portage sand in this figure. The bellofram air cylinder is attached to a load frame.

3.6 MODULUS COMPARISON TEST METHODS

3.6.1 *Preliminary Tests*

Preliminary tests were run in the cylindrical test cell. The PVC test cell was constructed quickly so that preliminary analysis of the effects of loading and increased stiffness on velocity could be analyzed. However, the test cell was too small to effectively analyze the relation between stiffness and geogrid.

3.6.2 *Seismic Modulus Tests*

3.6.2.1 Large Box Seismic Tests

Two different methods of acquiring seismic parameters were used in this research project. The first method is more complex, but the robust testing method was performed to ensure that seismic moduli could be effectively calculated in granular materials. Furthermore, these tests were used to determine the effectiveness of collecting seismic parameters near geogrid reinforcement. Accelerometers were positioned 50 mm apart and directly beneath the load plate in the large box (Figure 3.10). The distance between accelerometers was secured with a tensioned string. The string was attached at the bottom of the wood container and at the frame at the top of the container. This string held the accelerometers in place during specimen preparations and it was severed after specimen preparation. Accelerometer wires were secured loosely to the side of the test cell in an attempt to prevent any strengthening effects of the wires from becoming a factor during load application and data acquisition (Figure 3.11).

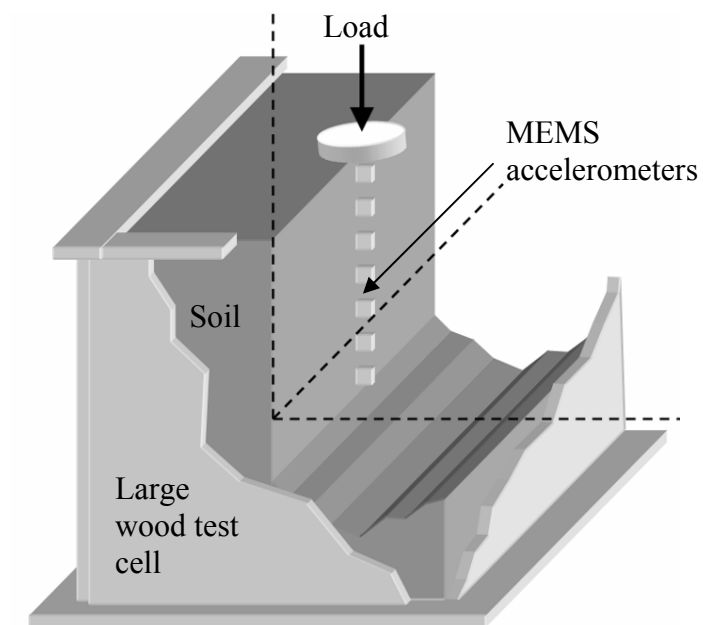


Figure 3.10. Three-dimensional cut-away schematic of the large wood test cell and placement of MEMS accelerometers in both the vertical and horizontal directions.

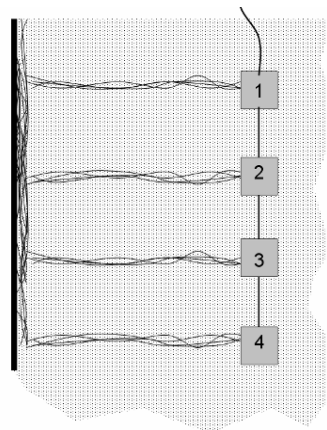


Figure 3.11. Cross section through testing cell with soil and accelerometers in place. The accelerometers are suspended vertically with a string and electrical signals are transmitted via wires from each accelerometer to the side of the testing cell.

The unit weight of uniformity in the large wood test cell was difficult to obtain, but an accurate approximation was made by measuring the weight of 50 pound buckets of soil placed in 3 or 4 lifts in the box. Portage sand was compacted using a concrete vibrator. Other granular materials used in this research were compacted using a tamping compaction method in 76 – 100 mm lifts. When material was to be compared with resilient modulus test data, an attempt was made to compact the soil to the corresponding density and water content of that test (typically 95 % of optimum conditions). Under most circumstances, since the test box is much larger than the resilient modulus testing cell, soil could not be compacted to 95 % of optimum. In this case, soil was compacted to the maximum density achievable.

In the majority of tests performed in the wood box, the source of excitation of elastic waves was a small hammer with a mass of 132.7 grams. The surface of the 150 mm diameter load plate (Figure 3.12) was tapped with the hammer to excite a P-wave to the vertically spaced accelerometers. Static loads were applied to the 150 mm diameter load plate during seismic modulus tests and pressure applied at the surface ranged from 0 to 550 kPa to get a wide range of moduli at differing bulk stress levels. Pressure due to wheel load applied on the surface of a flexible pavement is reduced by the asphalt layer and only about 20% of it is applied on the base course. For a 4-axle trucks (70 kN per axle and 35 kN per wheel set) with a tire pressure of 700 kPa and a circular contact area with radius of 125 mm), this translates to a maximum pressure of 144 kPa at the base course level for a typical pavement (Ebrahimi et al. 2008). The range of static pressures employed in the tests would cover this level of stress as well as stresses applied during construction traffic

when there is no pavement. When such pressure is applied by the plate, the stresses in different parts of the specimen in the large test box would experience the range of bulk and octahedral shear stresses typical of pavement conditions. Not all materials could withstand such loads as compacted in the large box and in this case, the maximum allowable load was applied:

- Portage sand failed at 70 kPa to 80 kPa
- Class 5 gravel failed at 380 kPa
- Pit run gravel failed at 490 kPa

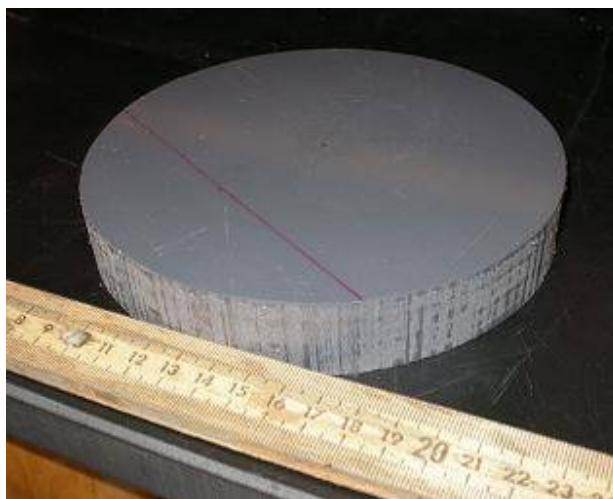


Figure 3.12. The 6 inch (150 mm) diameter load application plate.

3.6.2.2 Small Scale Simple Seismic Tests

The second test method used to acquire seismic moduli is based on the propagation of surface waves and offers a much simpler method of data acquisition to the testing scheme described above in the large test cell. Material was compacted

in a 5-gallon bucket with a volume of $19 \cdot 10^{-3} \text{ m}^3$ for the simplified test to minimize the required amount of material (Figure 3.13). Approximately 0.31 kN of material is required. Since the test only examines the surface of the soil, the amount of material is not too important, although the depth of the sample should be sufficient to avoid density and stiffness effects caused by the base of the soil layer. Material was compacted with a tamper in an attempt to ensure uniform density and the 150 mm diameter load plate was centered in the bucket.

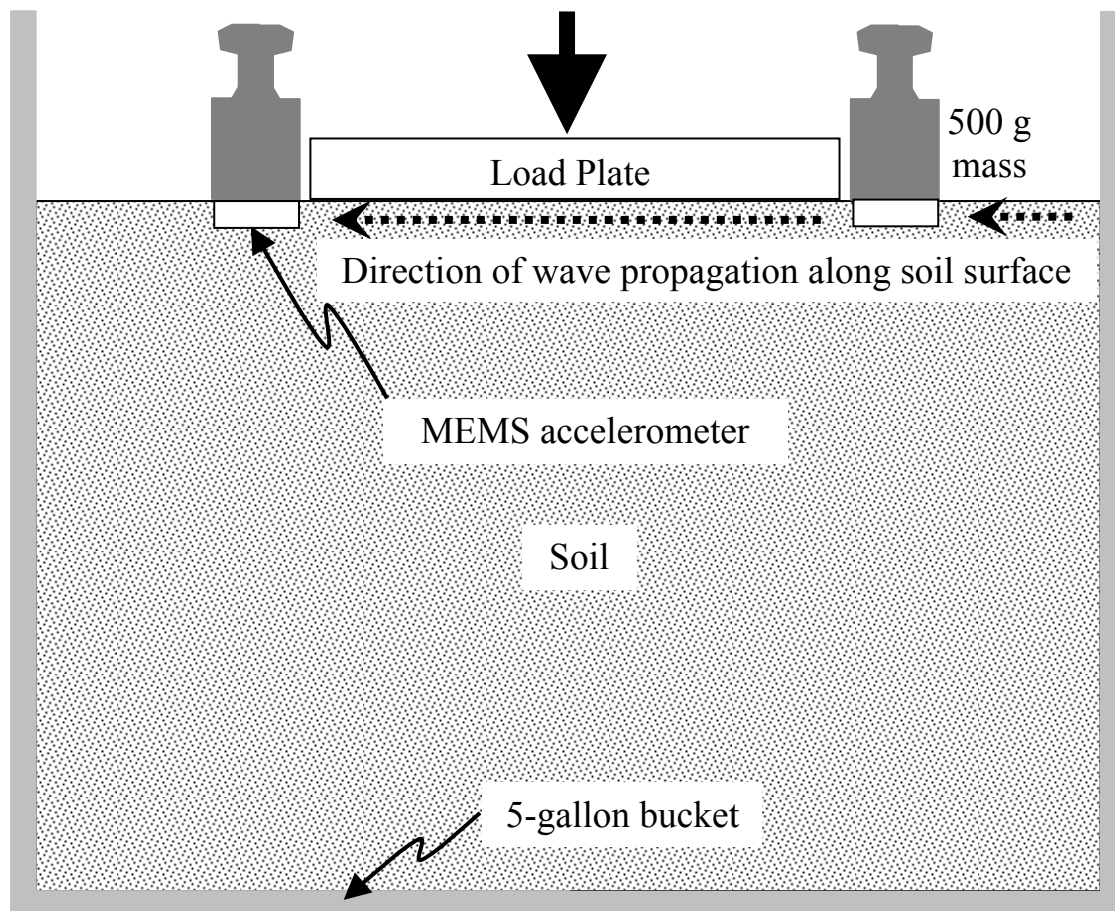


Figure 3.13. Simplified test setup to determine low strain constraint modulus with applied stress near the surface.

A small amount of material was removed on opposite sides of the loading plate and two accelerometers were placed adjacent to the plate (buried approximately 10 mm below the soil surface) so that one of the axes was aligned parallel to the ground surface. The final distance between accelerometers was 184 mm. Accelerometers were held in place by 500 gram masses placed on top of each accelerometer. The masses also acted to couple the accelerometers more closely with the soil so that first arrivals of elastic waves were more distinguishable. Static loads were applied to the soil while acquiring elastic wave velocities. A method of applying stresses greater than 50 kPa is recommended to obtain a better comparison between modulus and stress.

The side of the 5-gallon bucket was tapped with a rubber hammer and the travel time of the wave between accelerometers was recorded under the plate. Through experiments performed in the bucket, it was apparent that the velocity measured by the first arrival in the bucket was not the P-wave arrival, but the arrival of the surface wave. The surface wave has a strong first arrival and travels at slower velocity than the P-wave, inducing an ellipsoidal motion in particles along the surface. Therefore, velocities were multiplied by a conversion factor based on the Poisson's ratio (Santamarina et al. 2001, Kramer 1996):

$$V_p = V_r \frac{(1 + \nu) \sqrt{\frac{2(1 - \nu)}{1 - 2\nu}}}{0.874 + 1.117\nu} \quad (3.2)$$

where V_r is the velocity of the surface wave.

Also, since elastic wave velocity is most influenced by the stress acting parallel to the direction of wave propagation, especially near the surface, the

average radial stress beneath the plate was used to compare moduli to large box seismic tests.

3.6.3 Large-scale Elastic Modulus Test Method

Static loads were simple to apply for seismic modulus tests, but when examining the elastic deformation of the soil surface, cyclic loads are required. Therefore, tests performed in the large-scale wood test cell to measure the modulus of soil based on the deflection of the soil surface (E_{LS}) use a haversine load cycle (Equation (3.3) and Figure 3.14). Typically, the haversine load cycle is used to simulate traffic loading involves applying one complete period of the haversine function over a time of 0.1 seconds with a rest period of 0.9 seconds. However, to apply load to the soil this quickly, a hydraulic fluid other than air is required and air was deemed the most effective method of load application in this study. The bellofram air cylinder was limited in the amount of force that was able to be applied in 0.1 seconds. Therefore, the loading scheme used in this research involved applying the high deviator load for 1 second and the low deviator load for 9 seconds to maintain similar time spacing with resilient modulus tests.

$$\text{Haversine} = \left(\sin\left(\frac{\theta}{2}\right) \right)^2 \quad (3.3)$$

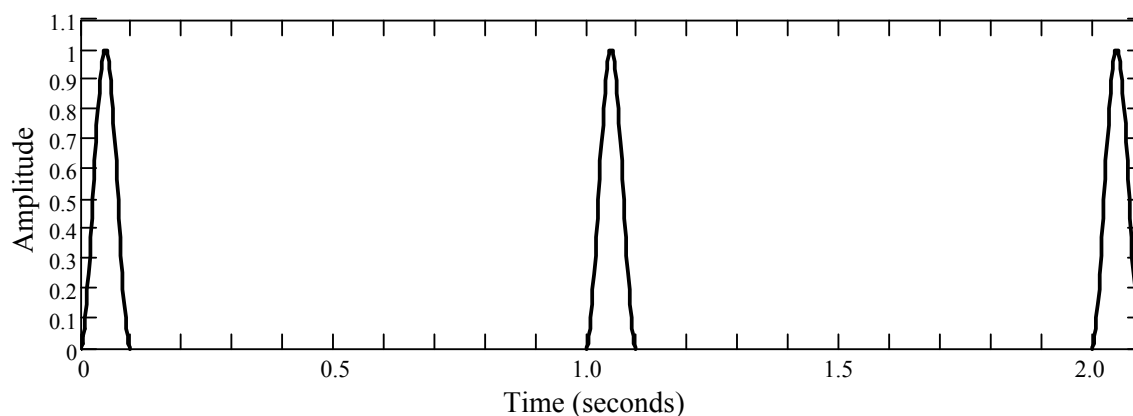


Figure 3.14. The haversine function is used to simulate traffic loading. The period of the cycle is 0.1 seconds. The rest time between haversine functions is 0.9 seconds. Since air was used as the hydraulic fluid in this study, the pulse was applied for 1 second and released for 9 seconds.

A CKC air pressure loader controlled with LabVIEW was used to apply the haversine load cycle. The force applied to the loading plate was monitored with a load cell and a LVDT monitored deformation of the load plate.

All base course and larger granular materials were tested in the large wood box under cyclic loading conditions to determine the elastic response of materials to applied loads. The materials were prepared in the box in the same way as described in Section 3.6.2.1. Portage sand suffered bearing capacity failure at low stresses of approximately 70 – 80 kPa and therefore cyclic loading was not applied to the Portage sand specimens.

Cyclic loading varied between a low deviator stress of 71.5 kPa and a high deviator stress of 275 kPa. After 10 cycles, the cyclic load was removed and the seating load was kept while angles of rotation and wave velocities were measured.

Once all information was gathered, the cyclic load was applied again. The entire testing routine is shown in Table 3.4. A total of 400 loading cycles were used, after which little plastic deformation occurred.

Since seismic parameters and elastic deformation of the surface were commonly measured concurrently, a static load sequence was applied to measure seismic information after cyclic loads were released.

Table 3.4. Test scheme followed for tests performed in the large, wood test cell.

Load Step	Number of Cycles Completed at Time of Measurement*	Cumulative Cycles Completed
1	0	0
	10	10
	100	100
	200	200
Unload		
2	0	200
	10	210
	100	300
	200	400
Unload		
Application of Static Loads		
	Static Load (kPa)	
3	0	-
4	55	-
5	165	-
6	275	-
7	550	-
8	0	-

*Low deviator load of 71.5 kPa and high deviator load of 275 kPa.

3.7 GEOGRID INTERACTION TEST METHODS

3.7.1 *Seismic Tests*

Two test methods were performed to determine the interaction between base course material and geogrid reinforcement. The first test method involves applying the cyclic and static load testing scheme proposed in Table 3.4 to monitor surface deflections and velocities. Accelerometers were positioned 50 mm apart near the geogrid to determine if velocity was affected near a geogrid layer. Geogrid was positioned at 75, 100, and 150 mm depth and tension was applied using a torque system along the longer direction of the geogrid to initiate the reinforcement effects prior to load application and acquisition of velocity measurements.

3.7.2 *Rotation Tests*

A second method of examining the interaction between geogrid and granular materials was considered based on rotation. Rotation was measured in several large box tests with grade 2 gravel and geogrid positioned at depths of 75, 100, and 150 mm. Portage sand was used as a control material to determine how grain size and gradation affect the interaction between each material and the geogrid. Portage sand tests were performed to check whether the rotation of the finer grain sand was affected by the presence of a geogrid with apertures 70 times larger than the D_{50} particle size.

Two test setups were used to monitor the rotation of the material beneath the load plate. The first test setup used a two-dimensional array of MEMS

accelerometers and is shown in Figure 3.15. Soil rotations were monitored in $\frac{1}{2}$ of the box to allow for a higher density of vertical and horizontal measurements. A second test method involves securing a higher vertical density of accelerometers along the edge of the load plate (Figure 3.16) where highest rotations are expected. Measured rotations were plotted to determine how rotation varies with geogrid position, applied load, number of cycles, depth, and distance from the plate.

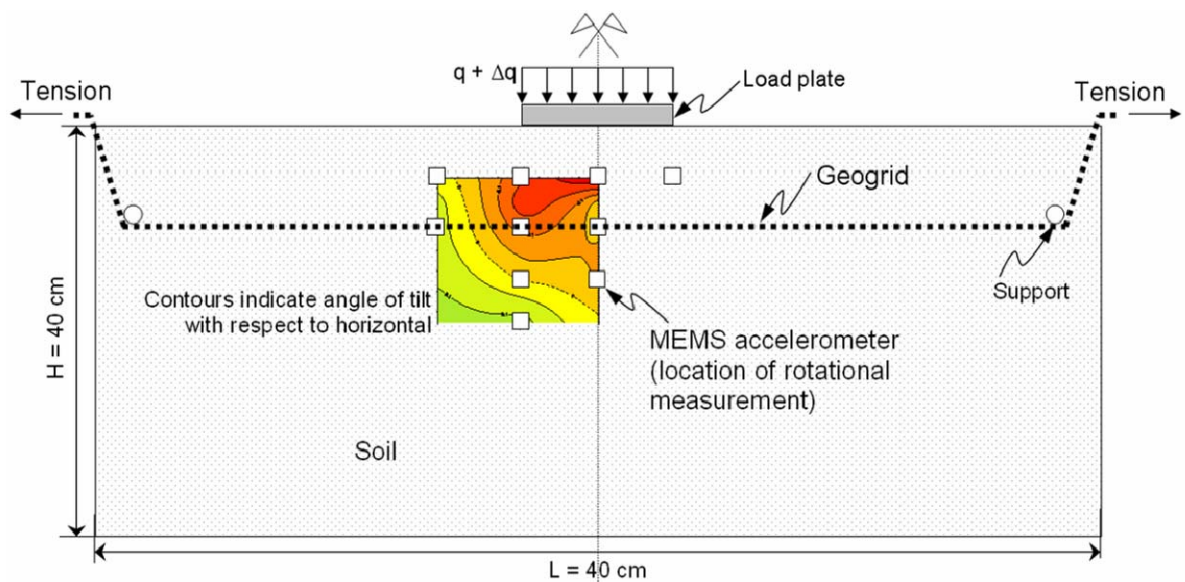


Figure 3.15. Schematic of test setup to measure in situ soil rotation with MEMS accelerometers.

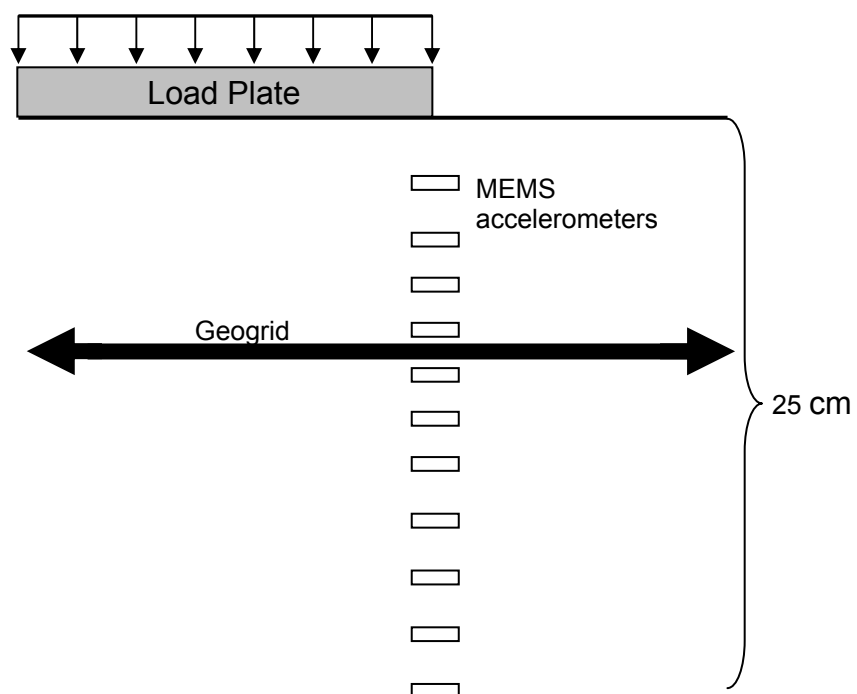


Figure 3.16. Test schematic for rotation measurements of grade 2 gravel. MEMS accelerometers were spaced 20 mm apart (center to center) near the geogrid and 25 mm apart further from the geogrid.

4 RESULTS AND ANALYSIS OF COMPARISON BETWEEN RESILIENT MODULUS AND MODULUS BASED ON SEISMIC MEASUREMENTS

The following discussion focuses on the development of a mechanistic analysis of the relationship between the constraint moduli (P-wave modulus) and the engineering resilient moduli (M_r). The modulus acquired during seismic tests is analyzed in a mechanistic approach to correct for stress level, void ratio and strain level and to convert the P-wave modulus to the Young's modulus. Table 4.1 shows the mechanistic approach used to evaluate the resilient modulus with P-waves velocities.

Table 4.1. Proposed methods for the evaluation of resilient modulus using P-wave velocity information.

Level of Correction	Description of evaluation of resilient modulus based on P-wave velocities
0	Correlation of modulus from unconfined specimen testing* (Figure 2.19 - Nazarian 2003; Williams and Nazarian 2007)
I	Stress correction and correlation
II	Stress and void ratio correction and correlation
III	Strain correction and mechanistic evaluation
IV	Strain correction, mechanistic evaluation and conversion of constraint modulus to Young's modulus
V	Overall mechanistic evaluation for granular soils

*not performed in this research project

4.1 EFFECTIVENESS OF MEMS ACCELEROMETERS TO DETERMINE THE CHANGE IN VELOCITY IN SAND

Prior to calculating P-wave modulus, initial tests were conducted to evaluate the effectiveness of acquiring P-wave velocities in granular material with and without applied loads. These experimental tests seem to indicate that the collected P-wave velocities are sensitive to effective stress changes used in the experimental methodologies. Results from a static load test are shown in Figure 4.1 in terms of P-wave velocity as a function of depth where the depth of each velocity measurement plotted is the average depth between consecutive accelerometers. A schematic of the test setup shows the external loading plate and the accelerometers buried in the soil column.

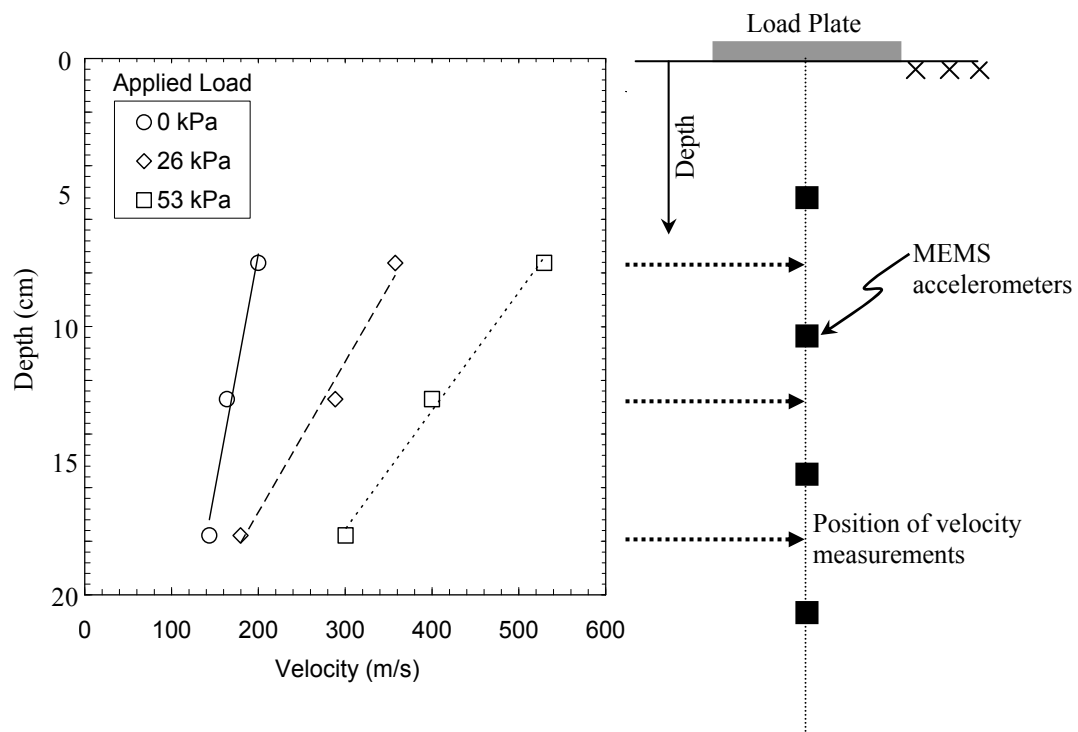


Figure 4.1. Static load test with Portage sand in the cylindrical test cell. The graph shows the depth-velocity relationship and a schematic of the test setup is shown on the right where the plate has a 150 mm diameter and the test cell has a 330 mm diameter.

The P-wave velocity becomes most well-defined when external plate loads increase. Without an applied load, the density of material varies substantially and velocity results are less reliable. With an applied load, the material becomes denser and particles rearrange to provide a more uniform distribution of stresses and velocities. Velocity increases substantially near the surface and less as depth of accelerometers increases. Figure 4.2 presents the velocity as a function of applied pressure. Figure 4.1 and Figure 4.2 show that velocity increases most rapidly directly beneath the load plate and at higher applied loads. The velocity between accelerometers 1 and 2 increases from 200 to 500 m/s when the external load increases from 0 to 53 kPa. In contrast, the velocity between accelerometers 3 and 4 only increases from about 140 m/s to 300 m/s.

Figure 4.2 shows the nonlinear relationship between effective stress and velocity. The velocity increases with applied pressure at all depths, but increases more rapidly directly beneath the load plate than at larger depths. The velocity increases 1.7 times faster at a depth of 127 mm than a depth of 178 mm and 3 times faster at a depth of 76 mm than the depth of 178 mm.

After tests performed in the cylindrical test cell showed that accelerometers were able to differentiate changes in velocity with an applied surface load, the testing scheme was moved to the large wood test cell. The large wood test cell was able to accommodate more accelerometers in the vertical direction beneath the loading plate and accelerometers were also able to be placed in the horizontal direction. A three-dimensional schematic of the initial test setup in the large wood test cell were shown in Figure 3.10. Typically, if velocity measurements were of

concern, accelerometers were positioned directly beneath the load plate rather than near the plate edge. Effective stresses are more uniform beneath the center of the load plate and rotation of accelerometers is minimized.

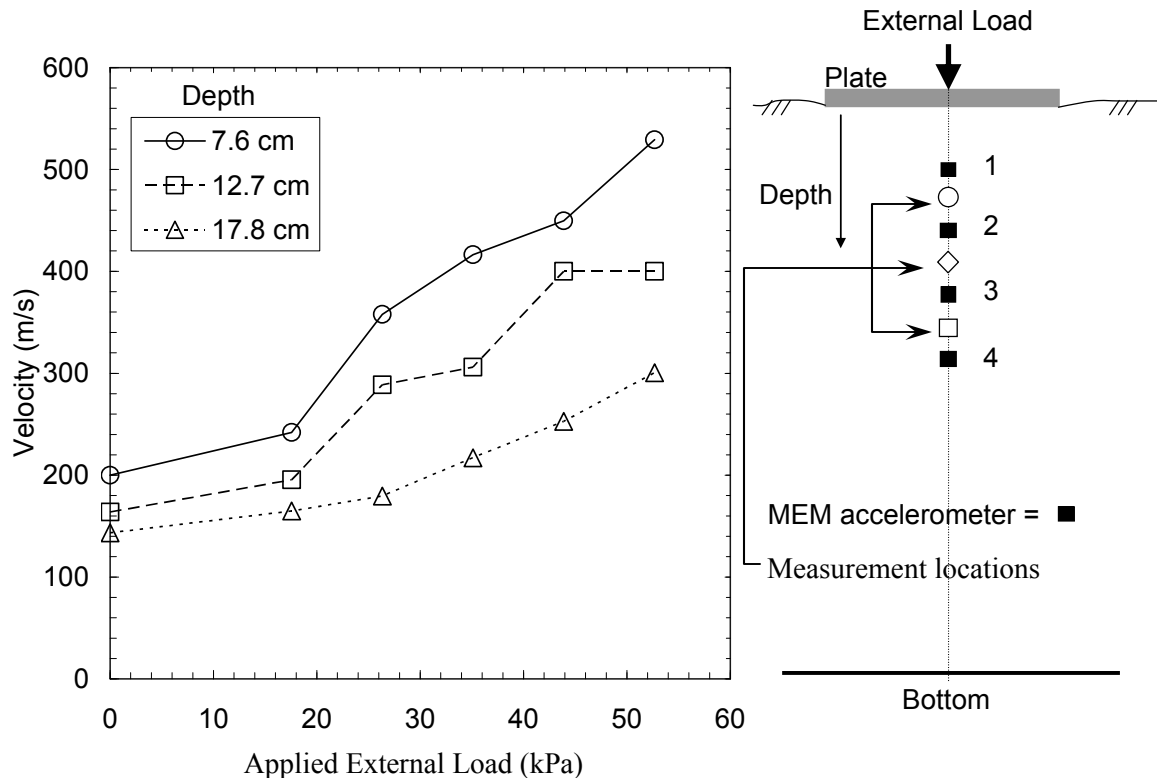


Figure 4.2. A static load test in the cylindrical test cell where velocity is plotted as a function of external applied load at several depths. Velocity increases nonlinearly with depth and applied load.

The results from a test performed with Portage sand in the large wood test cell are presented in Figure 4.3. The figure shows P-wave velocity as a function of applied deviator stress at the loading plate for three depths. As expected, the P-wave velocity increases with applied load at all locations within the test cell. The increase in velocity is most rapid near the surface at a depth of 90 mm and less pronounced at a depth of 290 mm. The velocities calculated from tests performed in

the cylindrical test cell (Figure 4.2) and the large wood box compare reasonably well. Despite slightly different depths (and associated bulk stresses) associated with accelerometers, the velocity at 50 kPa applied deviator stress and shallow depth (80 – 90 mm) remains between 400 and 500 m/s for each test cell. P-wave velocities are even more closely related at greater depths where the state of stress changes less rapidly. At 50 kPa applied deviator stress and depths of 180 – 190 mm, the velocity is approximately 300 m/s in both cases.

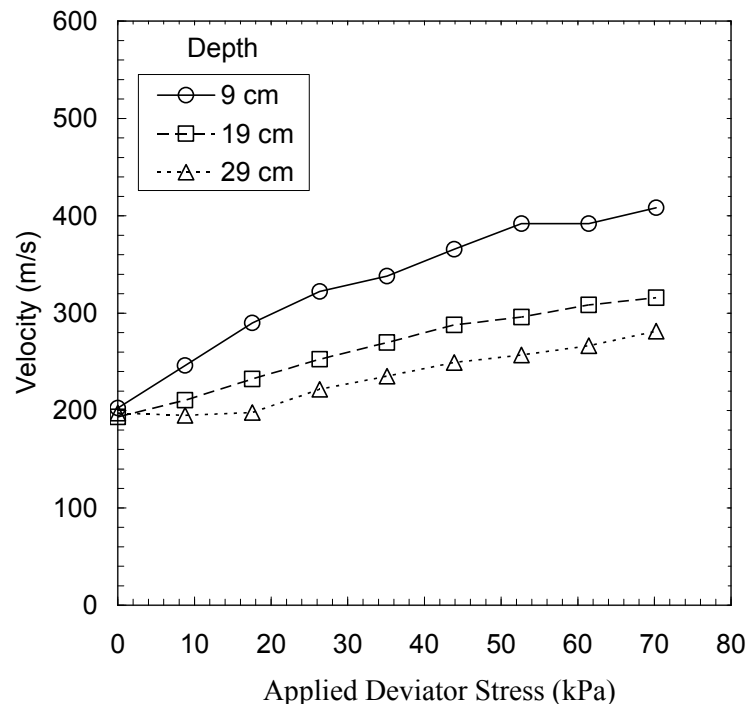


Figure 4.3. Static load test results from a test performed on Portage sand in the large wood test cell.

Static load tests produced much useful information about the distribution of velocities in the subsurface prior to performing more rigorous velocity analysis and cyclic load tests. First, static load tests showed that the accelerometers were

sensitive enough to capture propagating waves generated with a hammer blow to the loading plate from the surface to depths between 300 and 400 mm. Static load tests showed that velocity increased most rapidly in the near subsurface when a deviatoric stress was applied at the surface and much less at greater depths. Although the trend described is expected, the results are a confirmation of the induced stresses (due to body forces and surface forces) and the ability of MEMS accelerometers to react to the effective stress field changes.

4.2 RESILIENT MODULUS TESTS

Based on P-wave velocity measurements, research focused on comparing the P-wave modulus results with those from traditional resilient modulus tests. Resilient moduli were measured on four materials: Portage sand, grade 2 gravel, class 5 gravel, and RPM (Camargo 2008). LVDTs were attached to the specimens to measure the deformation of the center 1/3 of the specimen as recommended by NCHRP 1-28 A and all materials were tested under loading conditions described for base course materials specified in NCHRP 1-28A.

Resilient modulus test results are shown in Figure 4.4 and the specimen properties are given in Table 4.2. Results indicate that for lower bulk stresses (less than 100 – 200 kPa) that are more typical of field pavement conditions, the grade 2 gravel has the lowest resilient modulus, Portage sand and class 5 gravel behave similarly, and RPM has the highest resilient modulus. Final summary moduli (i.e., the moduli reported at a bulk stress of 208 kPa) are given in Table 4.2 along with fitting

parameters to the power model relationship between bulk stress and resilient modulus. It should be noted that the grade 2 gravel specimen was compacted dry and to a density that was 78 % that of the maximum dry density achieved during standard compaction effort. The grade 2 gravel specimen was compacted dry to be compared more easily with seismic test results, which were performed dry and to 82 % maximum dry density. Also, an attempt was made to compact the grade 2 gravel further, but the maximum density achievable in the resilient modulus mold containing a flexible membrane was 78 % that of the maximum. The calculated parameters k_1 and k_2 were used to analyze the relationship between the resilient modulus tests and modulus based on P-wave velocities. All granular, non-bituminous materials tested (Portage sand, grade 2 gravel, and class 5 gravel) have a k_2 that ranges between 0.53 and 0.54, which is near the expected k_2 of 0.5 for granular, unbound materials (see Equation (2.12)). RPM has a k_2 of 0.34, which is much lower than all other specimens tested and may be a result of the higher density of the material or the increased asphalt or fines content (Moossazadeh and Witczak 1981).

The following analysis of the resilient modulus testing procedure and results is presented to establish the need for an additional testing routine for modulus. Problems associated with the resilient modulus test found while performing this research include:

- Scalability effects inherent when testing a relatively small sample compared to larger scale field conditions. Typical resilient modulus tests are performed on materials having grains less than 1 inch (25 mm) in diameter and the largest specimens are a maximum of 150 mm wide (diameter) and 305 mm

tall. Materials containing large particles (>25 mm) either cannot be tested or large particles have to be removed. This places a severe limitation on determining resilient modulus of materials like pit run sand and gravel and breaker run commonly used in pavement structures (e.g., as working platforms)

- Free-standing coarse-grained specimens are difficult and time consuming to construct especially when they are dry because they do not have enough cohesion to stand alone without confining stresses applied.
- Reproducibility and reliability of test results depend somewhat on the experimenter and details of performing the test. The large amount of scatter in resilient modulus tests (Figure 4.4) hinders the ability to obtain reliable fitted parameters.
- Stresses applied during the resilient modulus test can be as much as 500 to 600 kPa higher than actual field conditions (typical bulk stresses in the field range between 100 and 200 kPa). Almost the entire base course resilient modulus testing routine is performed above the actual field stress level conditions and extrapolation of the power model is required to obtain moduli at lower stresses. An extrapolated estimate of modulus provides another source of concern for the validity of final test results and the accuracy of the “summary modulus.”

Further discussion of the resilient modulus test procedure can be found in Pezo et al. (1991) and Claros et al (1990).

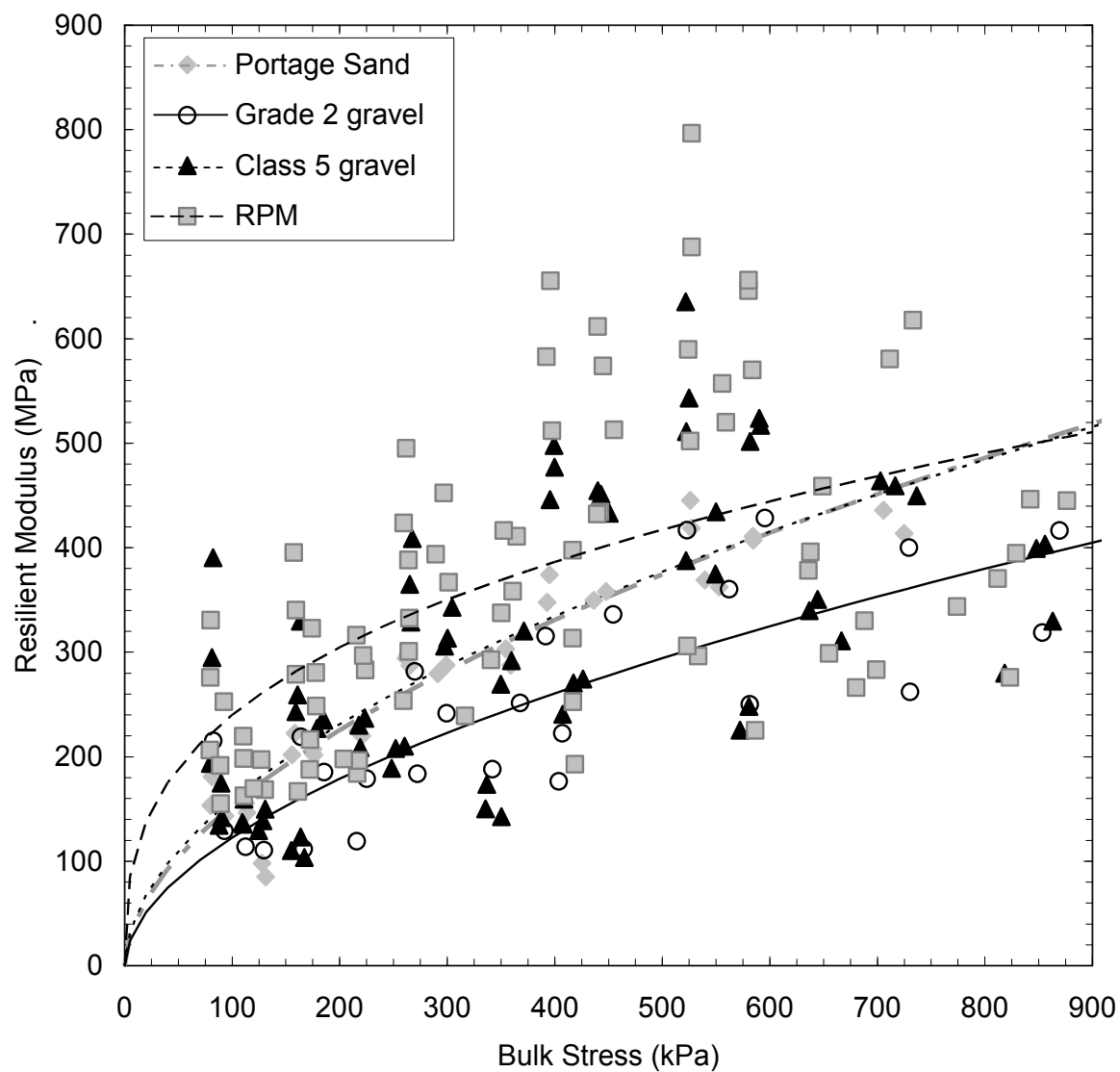


Figure 4.4. Resilient modulus of Portage sand, grade 2 gravel, class 5 gravel, and RPM as a function of bulk stress.

Table 4.2. Physical properties and results of resilient modulus tests on granular materials tested.

Material	Water Content	Relative Compaction	Power Model Fitting Parameters		Summary Resilient Modulus (at $\theta = 208$ kPa)
	w	RC	k_1	k_2	M_r
	%	%	MPa	-	MPa
Portage sand	0	96	11.9	0.55	230
Grade 2 gravel	0	78*	10.0	0.54	183
Class 5 gravel	5	95	13.6	0.53	236
RPM	7	95	49.2	0.34	309

*Maximum relative compaction achievable when compacting dry specimen of grade 2 gravel in resilient modulus test mold.

In despite of these limitations, the test has been found to be a viable tool to predict the resilient modulus of base course and subgrade soils with particles less than 25 mm in diameter subjected to traffic loading conditions.

Calculating a resilient modulus based on seismic tests provides a new method to estimate the resilient modulus of materials. A method comparing the resilient modulus of material to the resilient modulus calculated with P-wave velocities would be a very helpful tool and is an important step toward the advancement of using seismic methods to estimate modulus of base course material more readily in both the field and laboratory.

4.3 LARGE-SCALE CYCLIC LOAD MODULUS TESTS

Large-scale cyclic load moduli (E_{LS}) based on deflection of the cyclically loaded plate are back-calculated from the cyclic load tests performed in the large test cell by monitoring the cyclic load applied and the corresponding deformation caused at the soil surface by that cyclic load. KENLAYER and MICHPAVE analyses allow a means to estimate modulus based on large-scale tests using the power model. Both KENLAYER and MICHPAVE were used in this research project to determine the difference in how each program calculates the bulk stress – modulus relationship.

When recoverable (elastic) strains from large box tests match those of KENLAYER and MICHPAVE analyses, the power model relationship can be used to back-calculate modulus as a function of bulk stress. Trial and error is used to estimate the parameter k_1 of the granular material that is required to reach recoverable strain levels seen on the surface plate of the laboratory box tests (k_2 is assumed 0.5 for granular materials). The recoverable strain for each of the materials tested in large box tests are given in Table 4.3. Table 4.3 shows good agreement between KENLAYER and MICHPAVE results and establishes that either program is suitable for analyzing the flexible pavement system. Because of the similarity in results, KENLAYER results are used to calculate all summary moduli based on large-scale box test results presented from this point forward.

To compare box tests performed in this research to previous large-scale tests, the k_1 calculated from grade 2 gravel was compared to large-scale studies completed by Tanyu (2003). Tanyu (2003) used KENLAYER to calculate a k_1 of 14

MPa for a depth of base course material of 460 mm, agreeing closely with the k_1 calculated for this study. Note that both KENLAYER and MICHPAVE output the elastic modulus, but other types of modulus can be calculated assuming a Poisson's ratio of 0.35 for large strain conditions (Bardet 1997).

Table 4.3. Non-linear constant k_1 and recoverable deformation at the surface used for KENLAYER and MICHPAVE analyses.

Material	KENLAYER	MICHPAVE	Vertical Recoverable Surface Deformation*
	k_1	k_1	δ_v
	MPa	MPa	mm
Grade 2 gravel	14	13.9	0.19
Class 5 gravel	10.1	10.1	0.25
RPM	11.5	11.7	0.25
Pit Run gravel	11	11.2	0.25
Breaker Run	8.4	8.5	0.33

*high plate load 275 kPa, low plate load 71 kPa

E_{LS} is presented in Figure 4.5 as a function of bulk stress. The large-scale cyclic tests indicate that grade 2 gravel is stiffest, followed by RPM and pit run gravel. Breaker run and class 5 gravel have the highest deflections for the loads applied. Despite breaker run having a low modulus in large-scale cyclic load tests,

the calculated modulus may be low because of the inability to effectively compact the large-grained material in the laboratory. Field compaction equipment is much heavier and more able to move the particles against one another than the tamping hand compactor used in the laboratory.

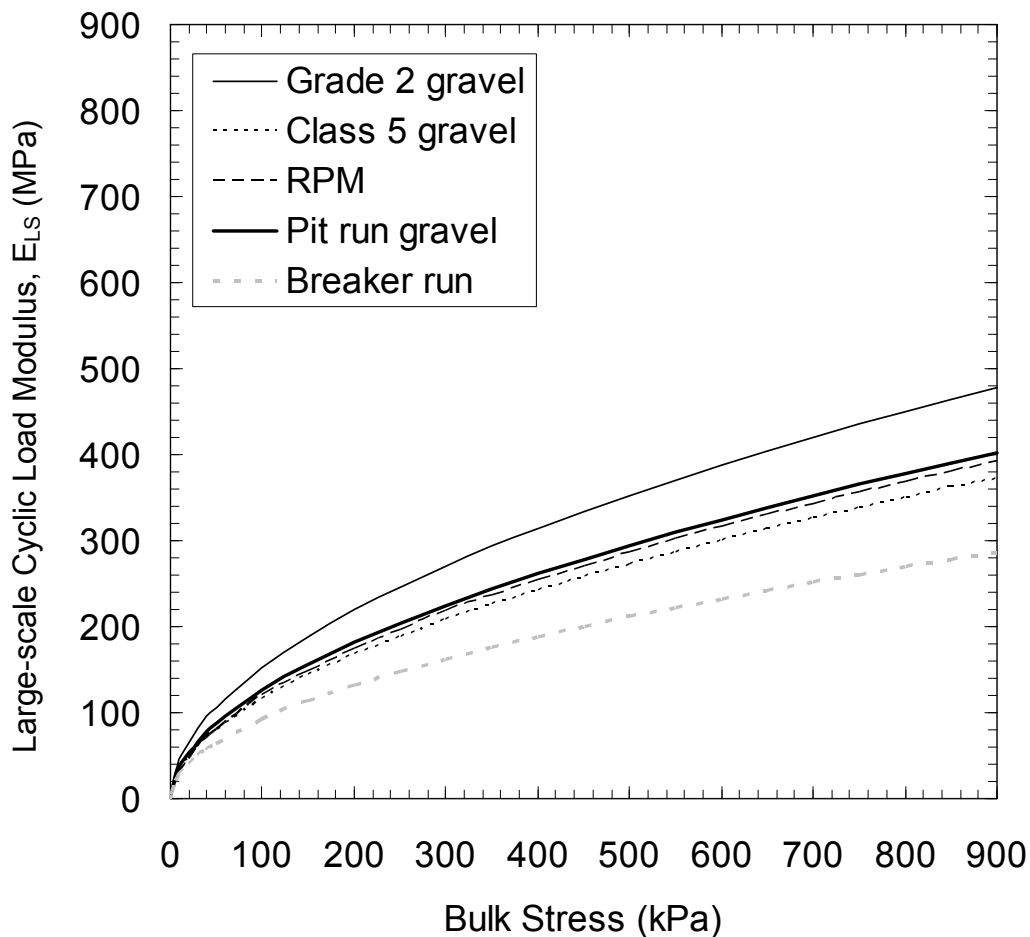


Figure 4.5. Large-scale cyclic load modulus (E_{LS}) as a function of bulk stress.

4.4 SEISMIC MODULUS TESTS

Seismic tests produce constraint moduli (D) when calculated directly from the velocity and density to which material was compacted (Equation (2.29)). The original

constraint modulus is analyzed in a step by step approach to determine the most useful method of comparing resilient modulus based on P-wave velocities to traditional resilient modulus. Constraint moduli computed directly from P-wave velocities as a function of bulk stress are shown in Figure 4.6. The bulk stresses applied in box tests are lower than those of resilient modulus testing, so results between tests need to be interpolated based on functions fitted to the bulk stress – modulus relationship. Initial conditions of each box test and resulting fitting parameters for the seismic modulus based on a power model relationship are given in Table 4.4. The seismic test results have some scatter since several tests were performed on different laboratory specimens in the box; however, the power relationships seem better defined than those of the resilient modulus test.

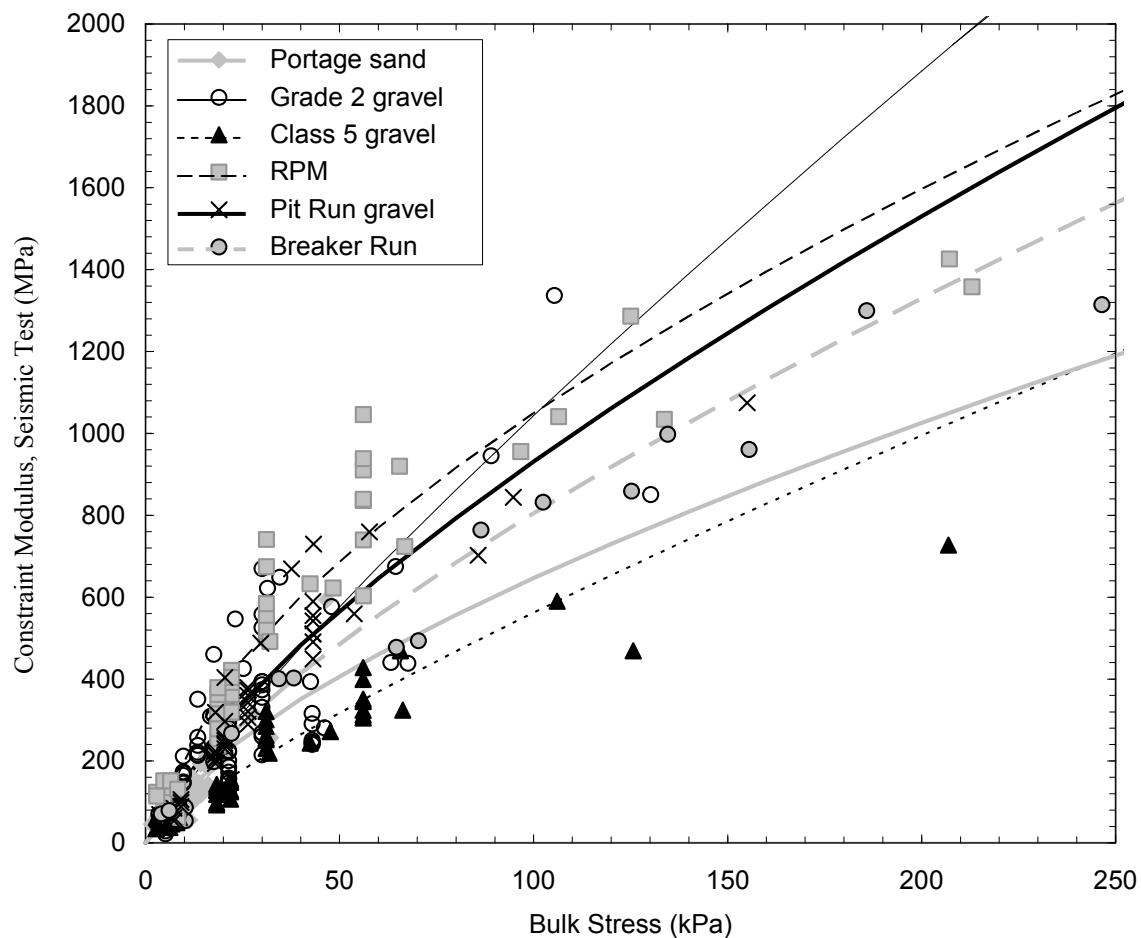


Figure 4.6. Constraint modulus based on P-wave velocities as a function of bulk stress in large wood box tests.

Table 4.4. Physical properties and results of seismic modulus tests on granular materials tested in the large wood box.

Material	Water Content	Relative Compaction	Power Model Fitting Parameters		Summary Modulus (at $\theta = 208$ kPa)
	w	RC	$k_{1\text{seismic}}$	$k_{2\text{seismic}}$	D_{seismic}
	%	%	MPa	-	MPa
Portage sand	~0	93	30.0	0.67	1072
Grade 2 gravel	~0	82	20.5	0.85	1913
Class 5 gravel	4	90	12.7	0.82	1010
RPM	6.4	93	64.3	0.61	1582
Pit run gravel	~0	N/A (19.7 kN/m ³)	34.3	0.72	1570
Breaker run	~0	N/A	28.6	0.72	1364

4.5 MECHANISTIC METHOD FOR DETERMINING THE RESILIENT MODULUS OF BASE COURSE BASED ON ELASTIC WAVE MEASUREMENTS

4.5.1 Stress Level Corrections

The following analysis uses the outline presented in Table 4.1 to evaluate the resilient modulus of materials based on P-wave velocities. Moduli calculated for each material using P-wave velocities are significantly larger than the resilient moduli obtained in traditional resilient modulus tests. Figure 4.7 shows the results of Step I, which is a direct comparison between the two moduli after correcting for

stress level. The trends in Figure 4.7 show that resilient modulus is between 8.3 and 26.1 % that of the low strain constraint modulus based on P-wave velocities.

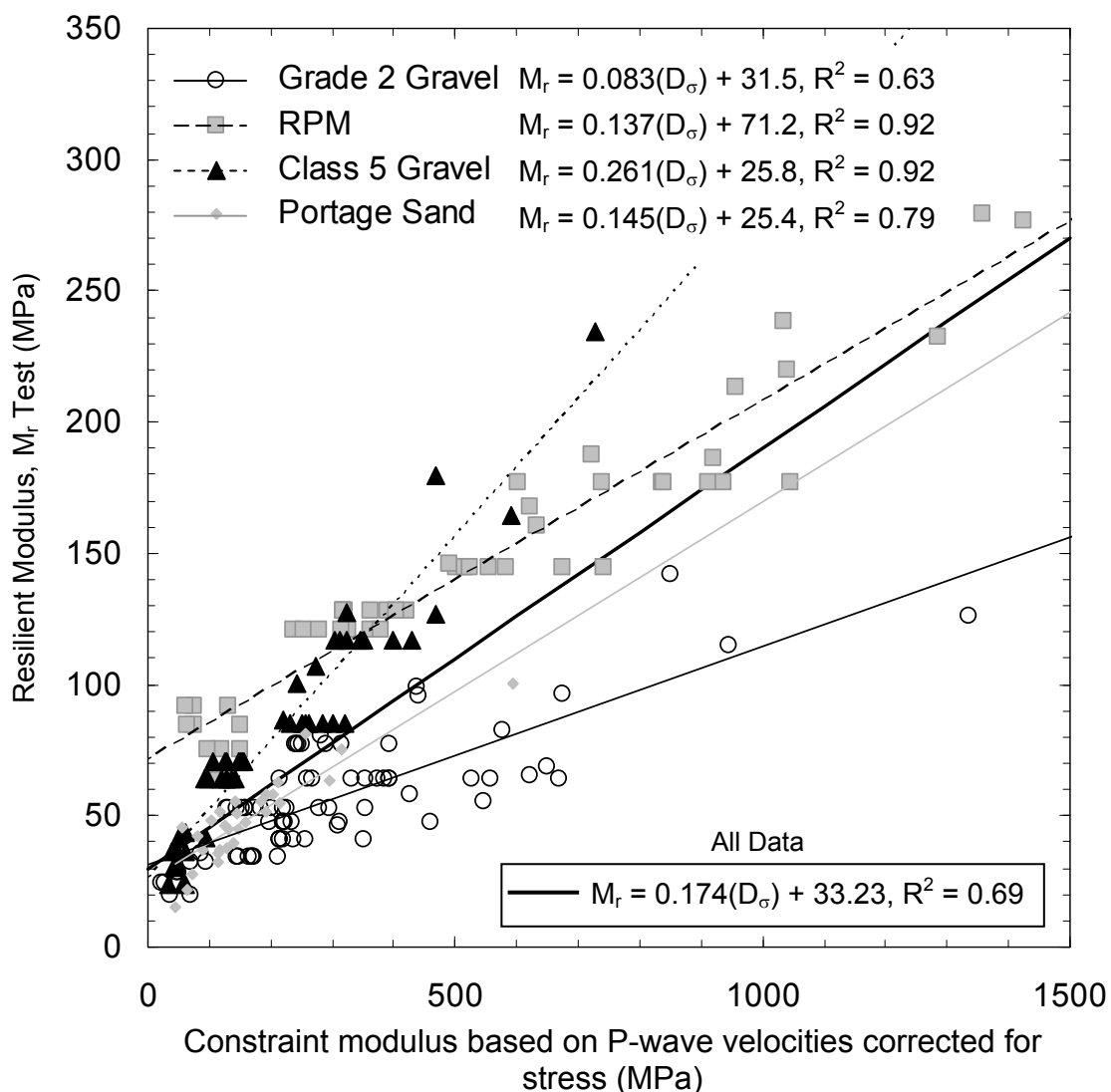


Figure 4.7. Direct comparison of resilient modulus (M_r) as a function of modulus based on P-wave velocities for grade 2 gravel, class 5 gravel, RPM, and Portage sand after correcting for stress.

4.5.2 Void Ratio Corrections

After correcting for stress level, the constraint modulus obtained from P-wave velocity results is corrected based on the void ratio of each specimen (Step II in Table 4.1). To correct for void ratio, the resilient modulus based on P-wave velocity results is multiplied by either:

- an empirical relationship proposed by Hardin and Richart (1963), or
- a normalized multiplication factor based on measured void ratios.

Void ratios for materials in this study varied between 0.32 and 0.58.

Figure 4.8a shows the effects of multiplying each modulus by a constant determined based on the empirical relation between modulus and void ratio given by Hardin and Richart (1963) for sands:

$$\frac{(2.97 - e)^2}{1 + e} \quad (4.1)$$

In the second evaluation, the resilient modulus based on P-wave modulus is multiplied by a normalization constant based on the minimum void ratio of smaller-grained granular materials (i.e., that of RPM, $e_{\min \text{ soil}} = 0.33$, Figure 4.8b):

$$\frac{e_{\min \text{ soil}}}{e_{\text{soil}}} \quad (4.2)$$

Thus all materials are compared at the same void ratio. Results presented in Figure 4.8 show that when corrected for void ratio, the correlation among all materials improves. Correlation R^2 values over all materials increase from 0.69 to 0.76 and 0.79 depending on which method of correction for void ratio is considered;

however, the seismic moduli still remain substantially larger than resilient moduli. Results indicate that the empirical void ratio correction proposed by Hardin and Richart is comparable to normalizing materials with respect to one another using Equation (4.2). Therefore, for simplicity, analysis from this point forward will consider the corrected moduli based on normalization rather than the empirical relationship proposed by Hardin and Richart (1963).

4.5.3 Strain Level Corrections

The resilient modulus test and seismic test induce very different strain levels in subsurface soils. Resilient modulus tests produce high-strain deformations (10^{-4} - 10^{-3} mm/mm strain), which are calculated by measuring the vertical displacement of samples. Seismic modulus is based on small deformations (assumed less than 10^{-6} mm/mm strain, Santamarina et al. 2001). Step III in the mechanistic approach toward analyzing the resilient modulus using P-wave velocity results involves correcting for strain level. To correct for strain level, resilient moduli are plotted on the backbone curve as a function of the strain induced during testing. The equation of the backbone curve is estimated using the hyperbolic model proposed by Hardin and Drnevich where the model is fitted to the modulus/strain relationship using constants a and b . The curve is fitted based on resilient modulus tests.

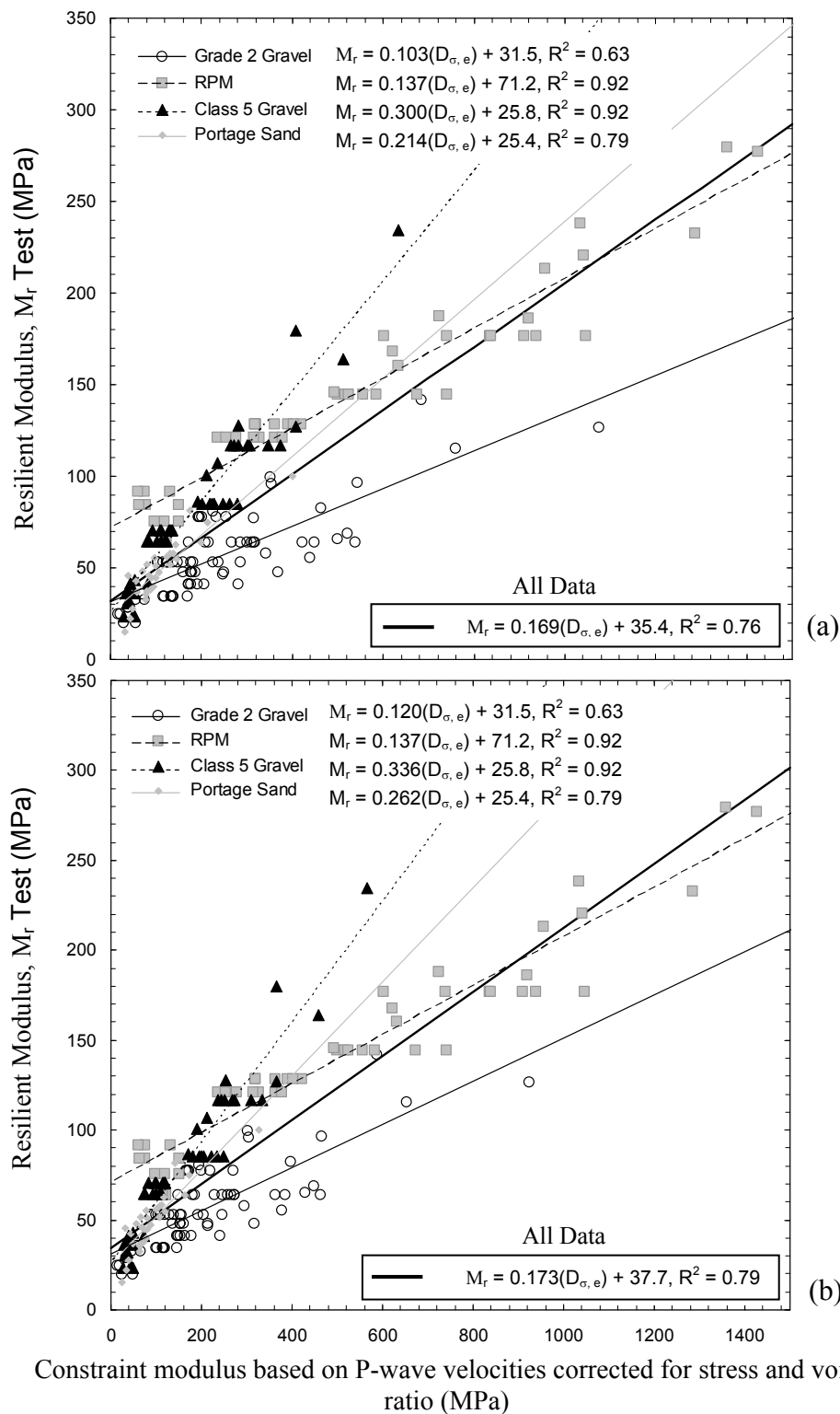


Figure 4.8. Resilient modulus as a function of modulus based on P-wave velocities corrected for stress and void ratio using (a) the expression proposed by Hardin and Richart (1963) and (b) a normalized void ratio correction factor.

The final “average” backbone relationship calculated for all the granular materials tested in the laboratory is presented in Figure 4.9. An average backbone curve was fitted to resilient modulus test moduli by minimizing the difference between expected modulus and calculated modulus for all granular materials tested in resilient modulus testing equipment: Portage sand, grade 2 gravel, class 5 gravel, and RPM. Figure 4.9 shows that M_r appears to be between 0.18 and 0.40 times the modulus based on P-wave velocities depending on material type. Table 4.5 shows the variation in the ratio of resilient moduli to the constraint modulus based on P-wave velocity results corrected for stress and void ratio. The average multipliers listed in Table 4.5 are used to convert the constraint moduli based on P-wave velocity results to a strain-level corrected constraint modulus.

Table 4.5. Ratio of resilient modulus to maximum modulus (based on seismic results) and shear strain induced by resilient modulus tests.

Soil	Range of $M_r/D_{\sigma, e}$	Average $M_r/ D_{\sigma, e}$	Average Resilient Modulus Shear Strain, γ
	MPa/MPa	MPa/MPa	mm/mm
Portage sand	0.26 – 0.27	0.27	2.5×10^{-4}
Grade 2 gravel	0.17 – 0.25	0.19	2.9×10^{-4}
Class 5 gravel	0.30 – 0.40	0.37	2.4×10^{-4}
RPM	0.25 – 0.39	0.33	3.2×10^{-4}
ALL	0.17 – 0.40	0.29	2.7×10^{-4}

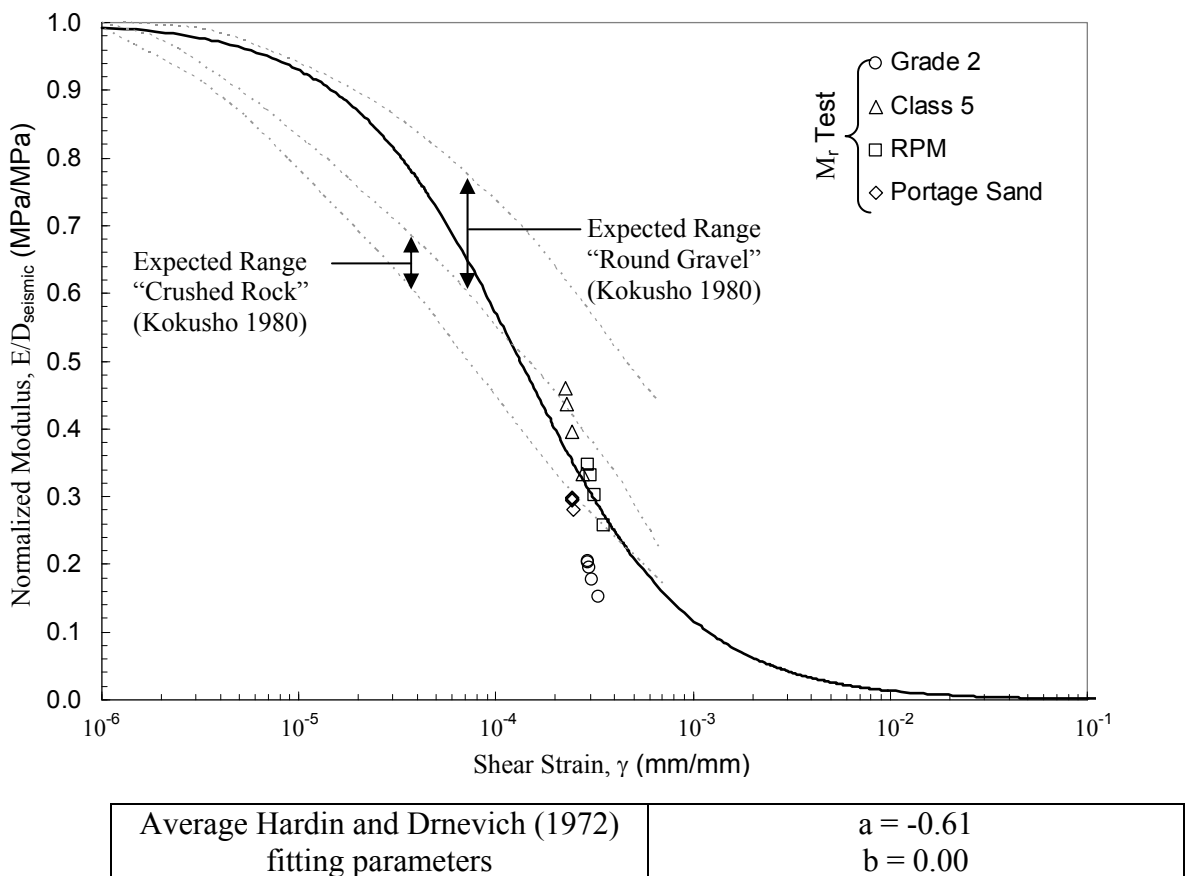


Figure 4.9. Final average backbone curve showing resilient modulus results.

Traditional resilient moduli and constraint moduli from P-wave velocity results corrected for stress, void ratio, and strain level are compared in Figure 4.10. The comparison technique appears to work well for materials when moduli are below about 175 MPa. Above a modulus of 175 MPa, the RPM deviates from the expected 1:1 comparison and has a higher corrected constraint modulus based on P-wave velocity than resilient modulus.

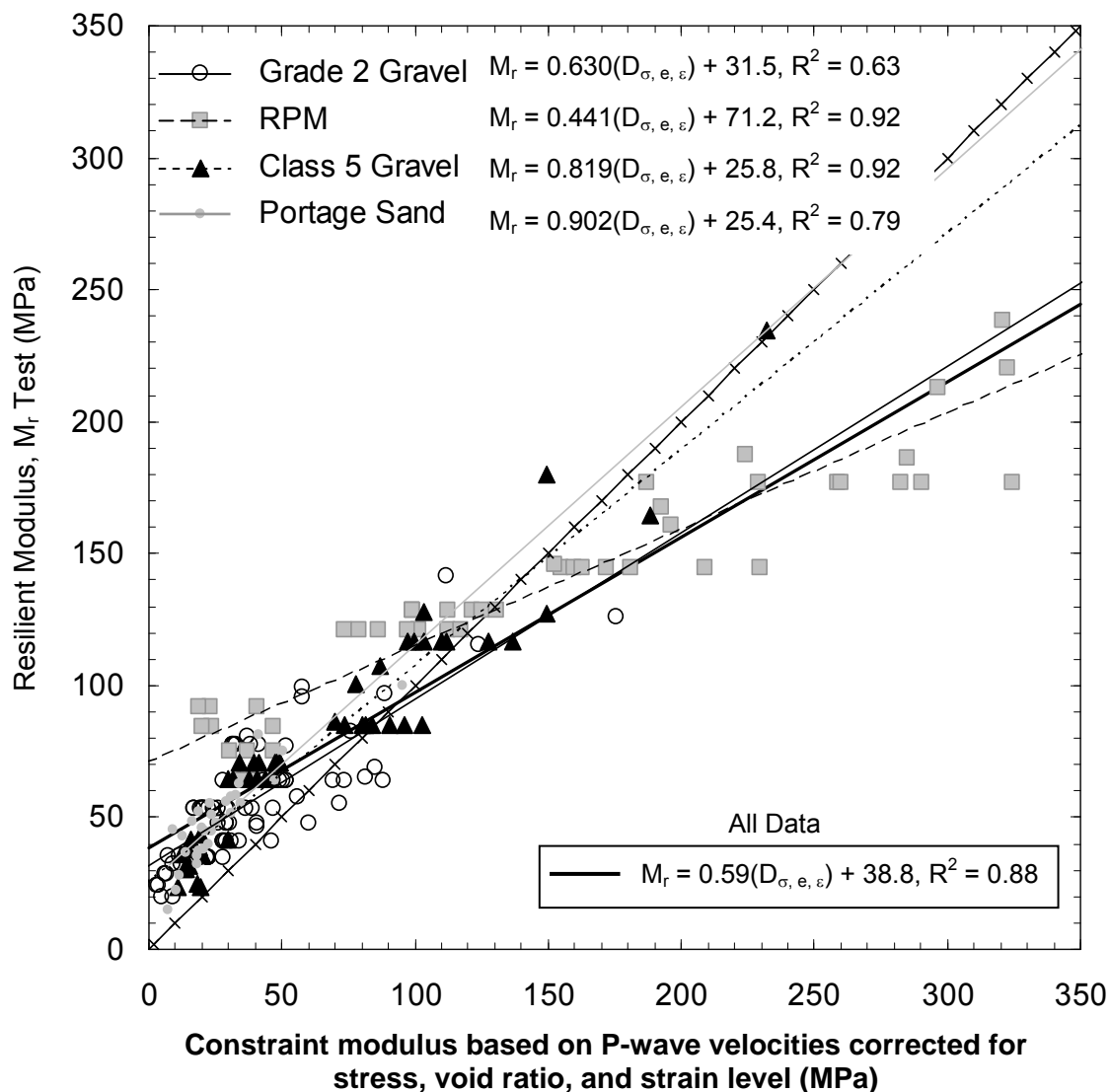


Figure 4.10. Resilient modulus as a function of modulus based on P-wave velocities corrected for stress level, void ratio, and strain level.

4.5.4 Conversion of Constraint Modulus to Young's Modulus

The first three steps of the analysis procedure above have corrected the modulus obtained from P-wave results for stress level, void ratio and strain level. However, the mechanistic approach has yet to consider that resilient modulus is a

form of Young's modulus rather than constraint modulus. Therefore, Step IV in the mechanistic approach to estimate resilient modulus based on P-wave velocities is to find the Poisson's ratio of each material so that the constraint modulus (D) can be corrected to a Young's modulus (E).

The Poisson's ratio of each material is found by measuring both P and S-wave velocities and using Equation (2.11). However, since S-waves were difficult to measure in materials with large grains, only the Poisson's ratio of Portage sand was directly calculated using velocities. The Poisson's ratio for other materials was obtained by measuring the angle of repose (β , Figure 4.11) of each material. Angle of repose corresponds to internal angle of friction in a loosely deposited material and the coefficient of earth pressure at rest (K_0) depends on the angle of internal friction (Jáky 1948; Bardet 1997):

$$K_0 = \frac{v_{at-rest}}{1 - v_{at-rest}} = 1 - \sin \beta \quad (4.3)$$

The low strain Poisson's ratio for other granular materials is estimated based on the velocity results and angle of repose results relative to Portage sand:

$$v_{velocity} = \frac{v_{velocity \text{ Portage sand}}}{v_{\beta \text{ Portage sand}}} v_{\beta} \quad (4.4)$$

where $v_{velocity}$ is the Poisson's ratio of a material, and v_{β} is the Poisson's ratio of the material based on its angle of repose, $v_{velocity}$ is the Poisson's ratio of Portage sand based on velocity analysis, and $v_{\beta \text{ Portage sand}}$ is the Poisson's ratio of Portage sand based on the angle of repose.



Figure 4.11. Determination of angle of repose (β).

The angle of repose is found by measuring the natural angle a soil makes when poured slowly on a level surface. The final Poisson's ratios used to correct the constraint modulus D based on P-wave velocities to resilient moduli are given in Table 4.6. The following is used to convert the constraint modulus to a Young's modulus:

$$E = \frac{D(1 + \nu)(1 - 2\nu)}{1 - \nu} \quad (4.5)$$

Table 4.6. Poisson's ratios based on velocity of elastic waves.

Material	Poisson's ratio based on P and S-wave velocities
	ν_{velocity}
Portage sand	0.35
Grade 2 gravel	0.33
Class 5 gravel	0.35
RPM	0.35
Pit Run gravel	0.35
Breaker run	0.35

The final comparison of the converted Young's modulus is shown in Figure 4.12 for each individual soil and in Figure 4.13 as an average over all soils tested. The mechanistic analysis seems to be an effective way to convert the constraint modulus from velocity results to a Young's modulus. Figure 4.13 shows that the modulus from velocity results is almost a 1:1 relationship when the mechanistic analysis is completed and that performing the traditional resilient modulus test may not be necessary to obtain a reasonable resilient modulus.

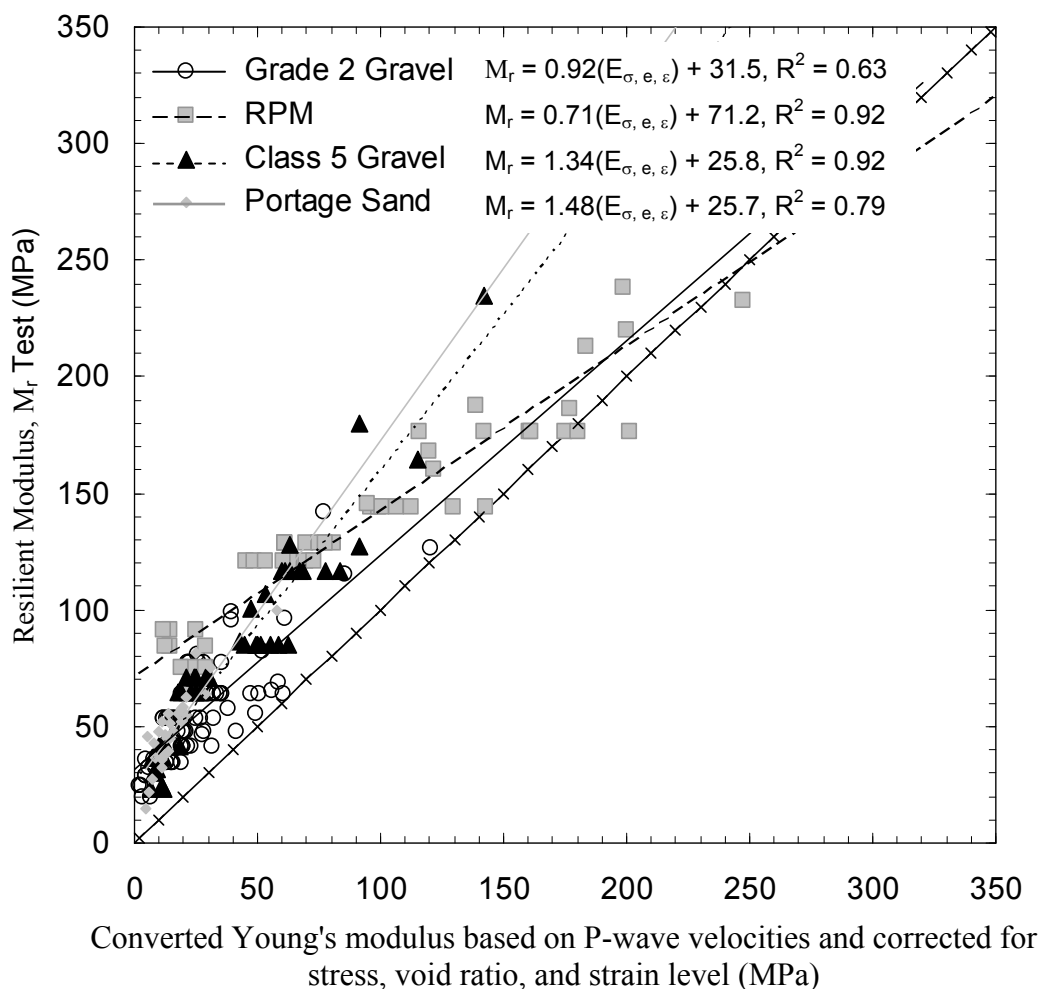


Figure 4.12. Resilient modulus and Young's modulus comparison based on P-wave velocities and corrected for stress, void ratio, and strain level.

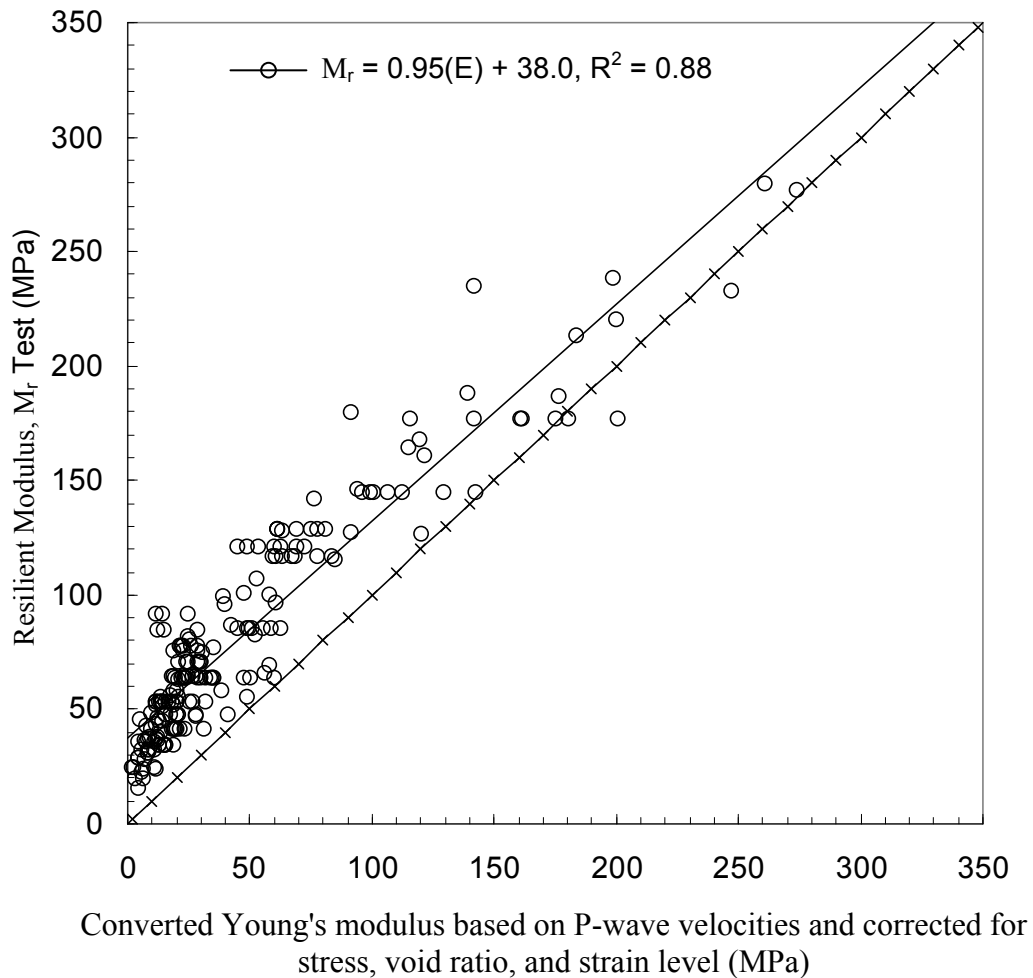


Figure 4.13. General comparison between resilient modulus and Young's modulus based on P-wave velocities and corrected for stress, void ratio, and strain level for all soils.

4.5.5 Evaluation of Corrected Seismic Modulus on Base Course Materials and Large-Grain Materials

To evaluate the procedure for comparing seismic moduli and resilient moduli, two coarse-grained materials (pit run gravel and breaker run) with grains too large to be tested in traditional resilient modulus equipment were tested using the mechanistic approach outlined above. The materials were corrected for stress level

and void ratio in a similar manner to smaller-grained soils. An average multiplier of 0.29 was used to correct the constraint modulus for strain level (see Table 4.5) since resilient modulus tests cannot be compared for the large-grained materials.

Figure 4.14 shows the final comparison of summary moduli calculated using all the proposed methods, each converted to an equivalent resilient modulus. Summary moduli for all conditions are based on the bulk stress level of 208 kPa.

The equivalent resilient modulus based on individual conversion factors show that moduli do not vary from resilient moduli by more than 22 % (Portage sand) and results are generally within approximately 50 MPa of the resilient modulus. When global factors are used (Figure 4.13), the resilient modulus varies by as much as 42 % from the corrected modulus for Portage sand, but is below 17 % (<31 MPa) for all other soils.

In general, breaker run, pit run gravel, and RPM have the highest moduli based on P-wave velocity results; all three are above 240 MPa. Class 5 and grade 2 gravels behave similarly and having moduli near 200 MPa. Portage sand has the lowest modulus (< 170 MPa) even though Portage sand appears stiffer than grade 2 gravel and comparable to class 5 gravel in resilient modulus tests. Portage sand may be stiffer because of the increased confinement of soils in the resilient modulus test setup.

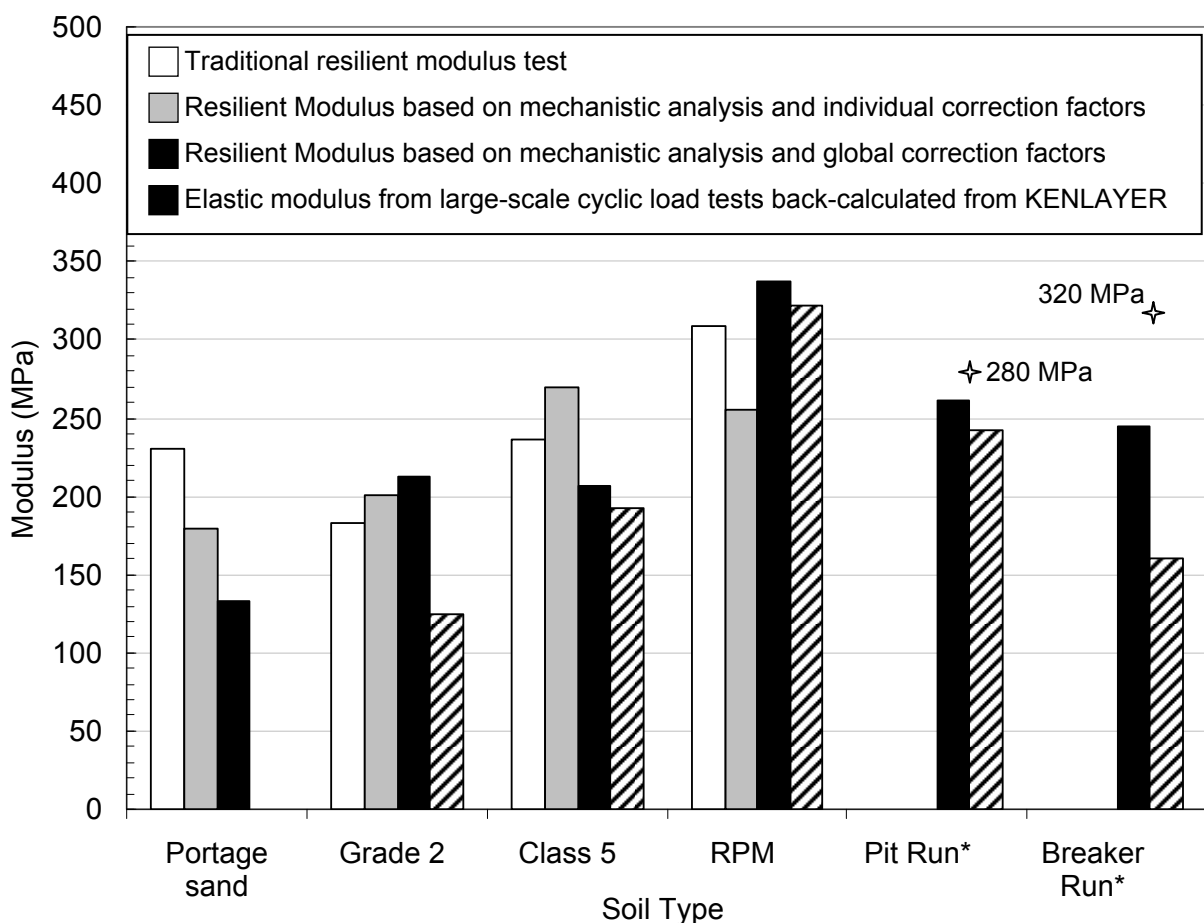


Figure 4.14. Summary moduli (computed at bulk stress = 208 kPa) based on resilient modulus tests, Young's modulus based on velocity results, and KENLAYER (box) tests for Portage sand, grade 2 gravel, class 5 gravel, RPM, Pit run gravel, and Breaker run.

* Pit run and Breaker run contain particles too large for traditional resilient modulus tests.

✦ indicates the modulus of Pit run gravel and Breaker run corrected for density at field conditions where the field densities of Pit run gravel and Breaker Run are estimated at 21 kN/m³ and 20 kN/m³, respectively.

4.5.6 Summary of Mechanistic Evaluation of Resilient Modulus Using P-wave

Velocities

Table 4.7 summarizes the results of comparing moduli based on the mechanistic analysis presented in the above discussion. The simplest comparison techniques avoid some steps of the mechanistic analysis and may be more

applicable in the field (correction levels I, II, and III). More complex mechanistic analyses (correction levels IV and V) are applicable for design purposes and when resilient modulus is desired for materials where the traditional resilient modulus test is not possible.

Table 4.7. An analysis of the mechanistic approach of converting a resilient modulus based on P-wave velocities to a traditional resilient modulus.

Level of Correction	R ² of comparison	Description of
0		<ul style="list-style-type: none"> -Simplest method of comparison -Good correlation requires an M_r test on each soil -Not a mechanistic approach based on measured soil parameters (i.e., void ratio, strain level, stress level)
I	0.69	<ul style="list-style-type: none"> -Resilient modulus test required for power model comparison -Correction for stress level allows calculation of modulus at different stress conditions
II	0.79	<ul style="list-style-type: none"> -Resilient modulus test required -Density of material should be monitored to calculate a void ratio
III	0.88	<ul style="list-style-type: none"> -Resilient modulus test required to obtain the modulus as a function of strain level -The mechanistic analysis of the backbone curve puts the resilient modulus from seismic tests on a similar scale as that of the traditional resilient modulus tests -The R² improves greatly over all soils producing a comparison technique more applicable over many soils
IV	--	<ul style="list-style-type: none"> -Resilient modulus test required

		<ul style="list-style-type: none"> -P and S-wave analysis required to obtain an approximate value for Poisson's ratio - Mechanistic approach of correcting the constraint modulus to a Young's modulus produces a stronger 1:1 correlation between moduli
V	0.88	<ul style="list-style-type: none"> -Does not require resilient modulus tests under the assumption that granular soils are behaving similarly -Can be applied to a granular soils when P-wave velocity results are available -Resilient modulus can be estimated knowing the Young's modulus from a velocity analysis

4.5.7 Large-Scale Cyclic Load Test Moduli

The backbone curve contains other information besides the relationship between resilient and seismic moduli and the following discusses the relation of resilient modulus to large-scale cyclic load tests. Large-scale cyclic load tests are shown on the backbone curve in Figure 4.15 along with resilient modulus tests. Figure 4.15 shows the relationship between large-scale cyclic load tests and resilient modulus tests using KENLAYER analyses of the bulk stress – modulus relationship. The strain levels induced in large-scale cyclic load tests are slightly higher than those of the resilient modulus test and are also corrected for strain level based on the backbone curve. For this analysis, resilient modulus appears to be approximately 0.56 to 1.7 times the large-scale cyclic load modulus and individual multiplication factors were obtained for each material to convert the large-scale cyclic load

modulus test results from KENLAYER analyses to an equivalent resilient modulus (E_{LS}). Final summary moduli are presented in Figure 4.14.

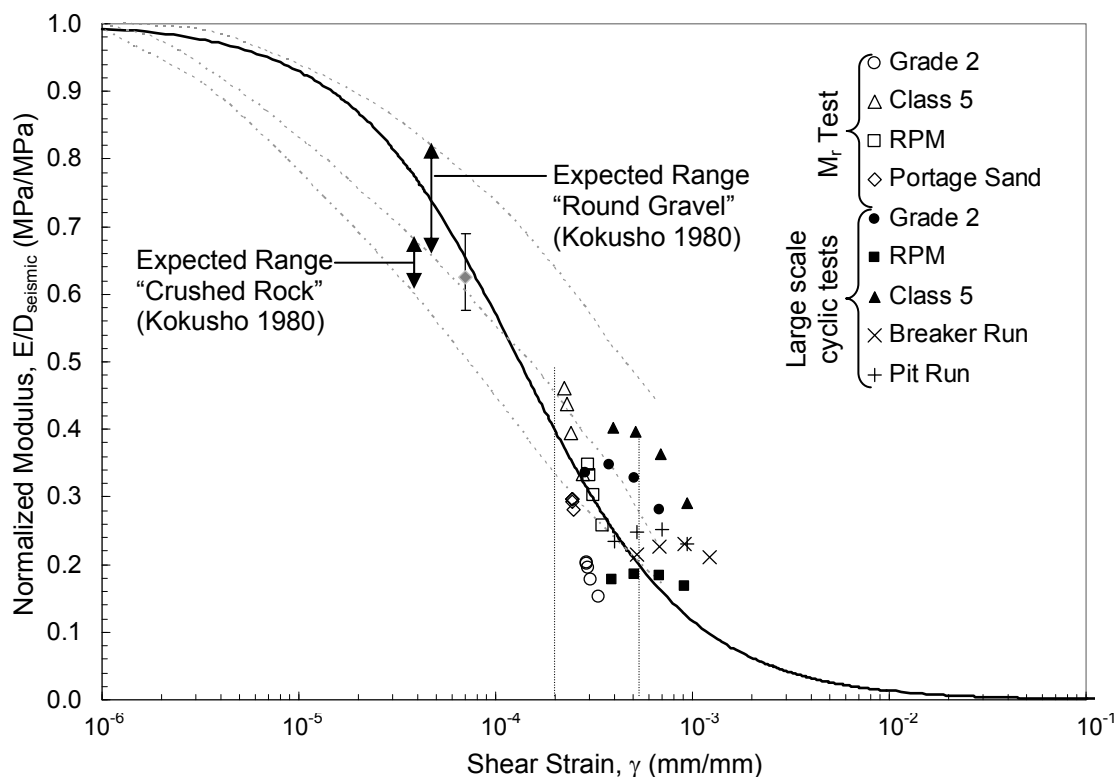


Figure 4.15. Final average backbone curve showing resilient modulus results, large scale cyclic load tests, SSG results (grey diamond), and previous results from Kokusho (1980). The error bars for the SSG results show the range over which the SSG estimated modulus of the grade 2 gravel.

4.5.8 Additional Backbone Curve Results

Also plotted on Figure 4.15 are SSG results and previous experimental results for comparison. Modulus based on soil stiffness gauge (SSG) readings taken on grade 2 gravel samples prepared in the large wood box show that the SSG results are on average 4 % lower than the expected results based on the backbone

curve. The SSG is manufactured by Humboldt Manufacturing Company and applies a dynamic acceleration to soil to obtain a modulus at another strain level (Sawangsurriya 2001).

Normalized moduli results for crushed rock and round gravel from Kokusho (1980) show the expected range of results. Kokusho's studies are presented for comparison with results from this research. The RPM, class 5 gravel, breaker run, and pit run gravel fall within the ranges seen by Kokusho; however, grade 2 gravel and Portage sand fall below the expected range of crushed rock or at the lower boundary of the expected normalized modulus of crushed rock. The normalized moduli may be lower due to differences in density and grain properties of materials considered by Kokusho and the fact that Kokusho's tests were performed in a small-scale triaxial cell with a specimen height of 100 mm and a diameter of 50 mm.

4.6 SMALL SCALE SIMPLE SEISMIC TEST RESULTS

Thus far, seismic modulus results have considered only velocities of wave propagation calculated from large-scale box tests. Since these tests require a substantial amount of soil, moduli calculated with small-scale tests are considered for comparison on two soils: grade 2 and pit run gravels.

Through experiments performed in the small-scale testing cell, the highest amplitude acceleration at accelerometers signals the arrival of the surface wave instead of the P-wave (see Equation (3.2)). Therefore, velocities were multiplied by a factor based on the Poisson's ratio of each soil (Table 4.6).

Since wave velocity is most influenced by the stress acting parallel to the direction of wave propagation, especially near the surface, the average radial stress beneath the plate was used to compare moduli to previous velocity tests. The stress near the surface depends greatly on the depth of the propagating wave, so results are sensitive to the depth of the propagating surface wave, so accelerometers were carefully placed 10 mm below the surface and were secured with a 500 g mass. Simplified test results are presented in Figure 4.16. Results show a good agreement between large-scale box tests, simplified tests, and resilient modulus tests, although simplified test results have moduli approximately 14 % lower than moduli calculated in large-scale box tests. The modulus will depend greatly on the distribution of particles and the effect these particles have on elastic wave velocity between accelerometers. This test methodology could be implemented to evaluate the resilient modulus in coarse-grained materials that cannot be tested in traditional cells.

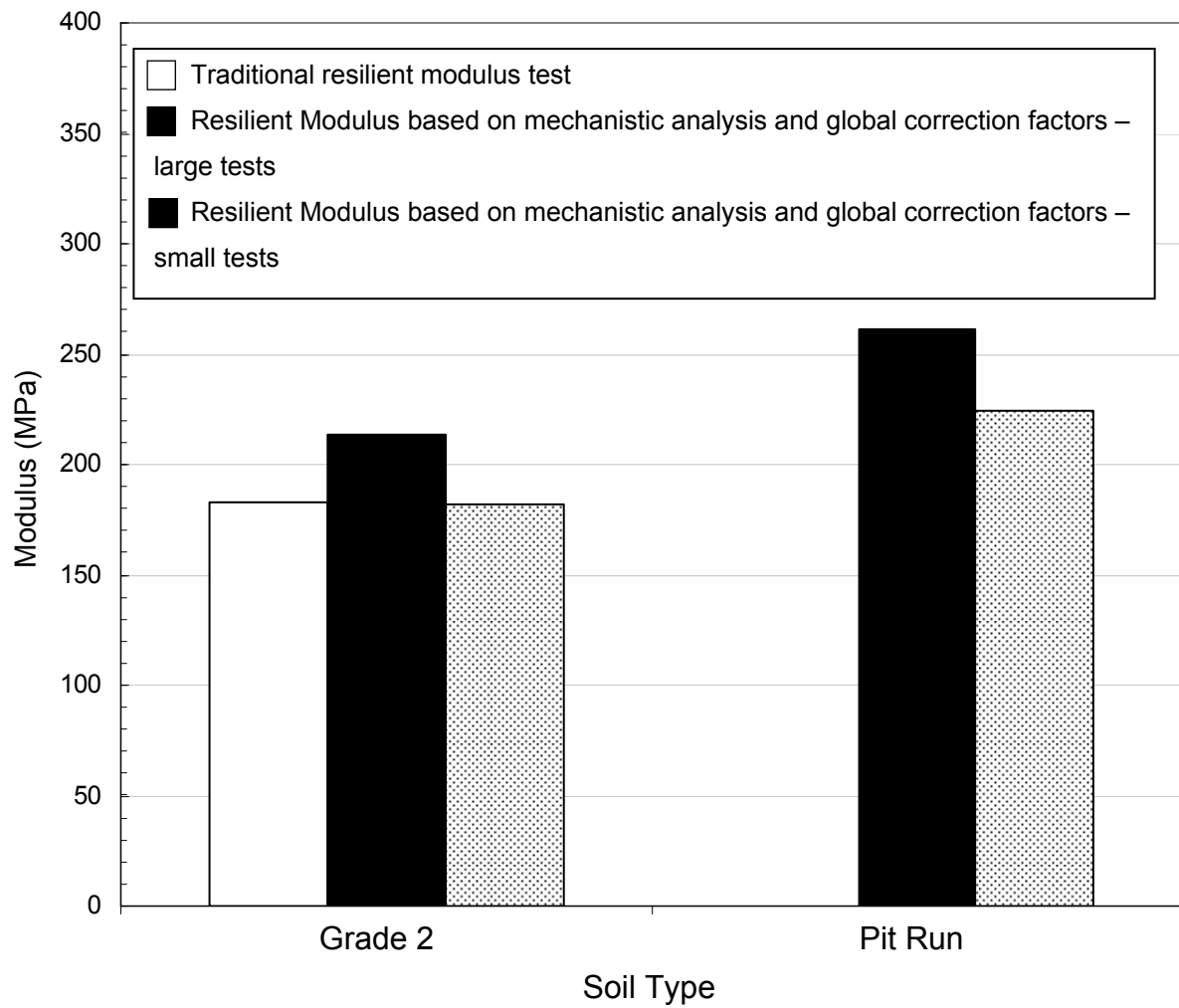


Figure 4.16. Comparison of corrected moduli based on large box test and simple test. Moduli compared at bulk stress of 208 kPa.

5 RESULTS AND ANALYSIS OF THE INFLUENCE OF GEOGRID ON ELASTIC WAVE PROPAGATION AND ROTATION

To evaluate the depth range of interaction between geogrid and base course material, three laboratory test methods were analyzed. First, plastic and elastic surface deflections were monitored to determine the influence of the geogrid with cyclic loads. Second, P-wave velocities in vicinity of the geogrid were evaluated. Third, the rotations of the materials induced by loading with and without geogrid were measured.

5.1 SURFACE DISPLACEMENTS

Surface displacements were monitored with an LVDT attached to the 150 mm diameter load plate for both cyclic and static loading conditions. Plastic and elastic surface displacements were monitored during cyclic loading tests to determine the geogrid position that best minimizes deformation of the surface.

Figure 5.1 shows that a geogrid positioned at 75 mm appears to best minimize plastic deformation of the surface for several loads. Geogrid at 150 mm depth does not greatly impact plastic deflection at 550 kPa applied load, which is approximately 40 % the expected construction traffic load, but 200 % the expected post-construction load from a dump truck after pavement is applied over the base course. The load was chosen as a compromise to obtain the behavior of the geogrid reinforced soil. Since the post-construction load is greater than what is expected, the depth of influence of the load at the surface will be smaller and the optimal position

of the geogrid will change. Surface deflections are decreased by 35 % and 16 % when geogrids are secured at 75 and 100 mm depth, respectively.

Elastic deflections were also examined to determine the effect cyclic loads have on surface deflections with and without geogrid. The modulus of reaction, k , is typically used to describe the amount of elastic deformation (Δ) that occurs with applied vertical surface load (P). Equation (2.8) defines the modulus of reaction (Yoder and Witczak 1975).

Figure 5.2 shows the modulus of reaction as a function of geogrid position. A higher modulus of reaction indicates that a greater load is required to induce the same elastic deformation of the surface. Therefore, a higher modulus of reaction corresponds to a stiffer structure and better position of geogrid reinforcement. The modulus of reaction increases by 19 and 5 % when geogrid is secured at 7.5 and 100 mm, respectively. A geogrid at 150 mm depth has no apparent effect on elastic deformation.

Despite surface deflections indicating that a shallower geogrid is best at minimizing surface deflections, the surface deflections indicate little about the distribution of shear stresses and confinement of particles in subsurface materials. Therefore, elastic wave velocities and rotations induced by plate loads are examined to better understand the deformation of the reinforced pavement system.

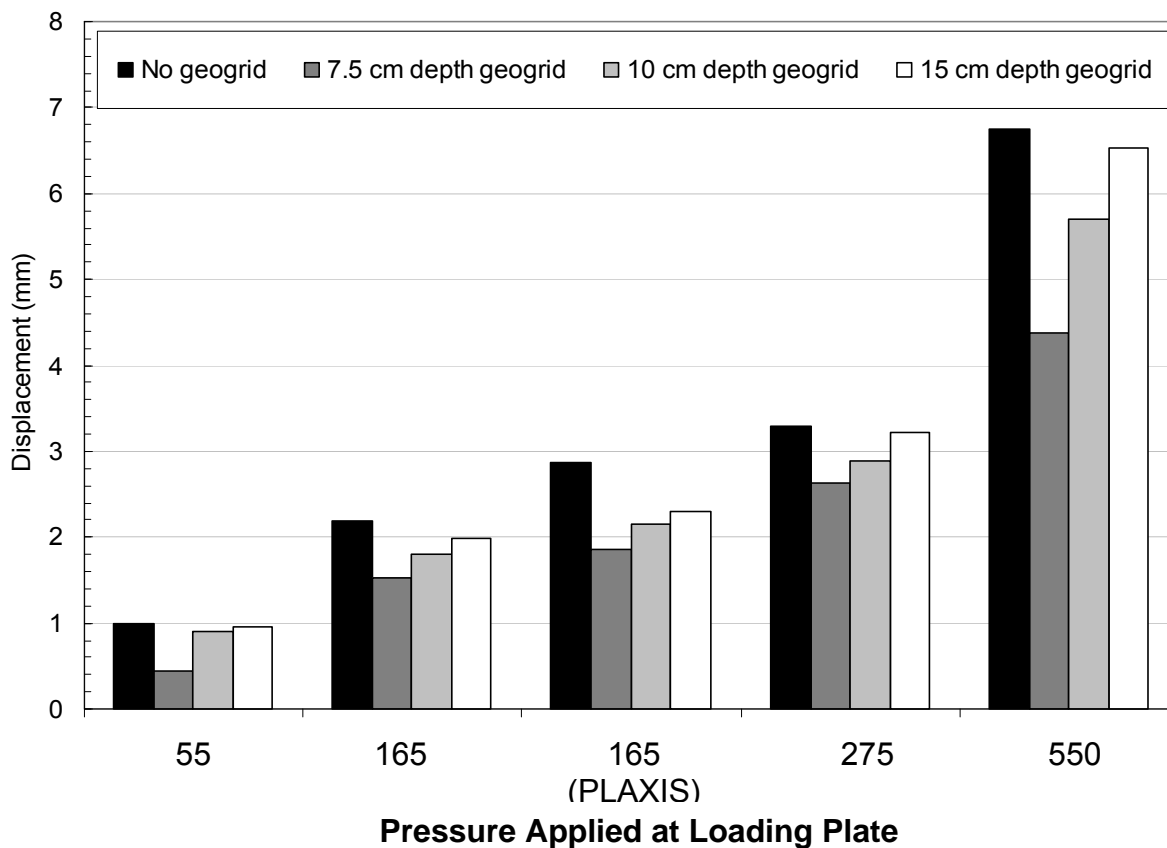


Figure 5.1. Surface displacement at several static loads and geogrid positions in grade 2 gravel after the application of 400 cycles of loading. PLAXIS deformations at 165 kPa applied load are shown for comparison.

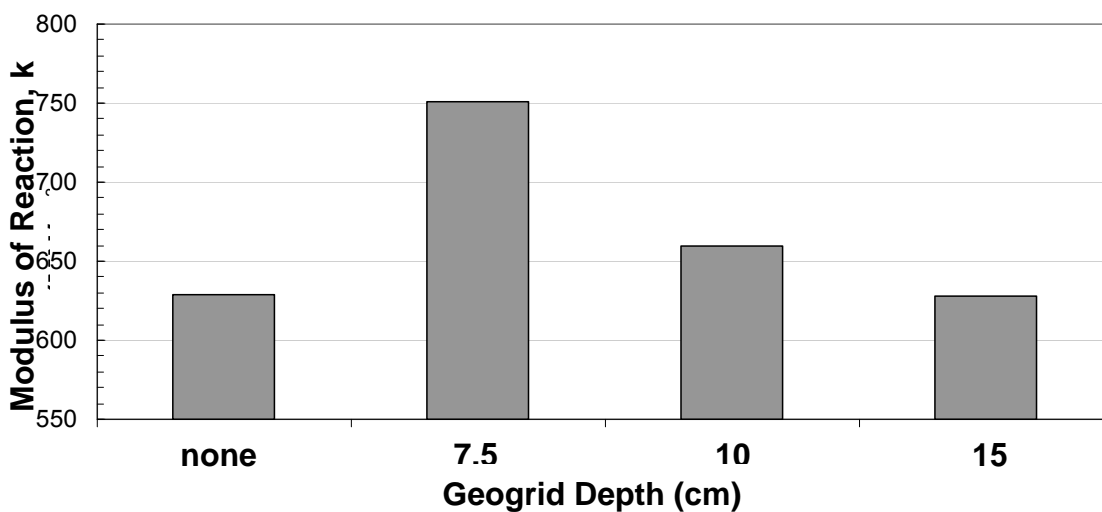


Figure 5.2. Modulus of reaction as a function of geogrid position for cyclic loading conditions.

5.2 FINITE ELEMENT ANALYSIS OF GEOGRID-REINFORCED BASE COURSE MATERIAL IN LARGE LABORATORY TESTING CELL

Although surface deflections are a good indicator of optimal geogrid location, the interaction of geogrid and granular material cannot be studied from the surface. Therefore, laboratory and PLAXIS analyses were performed to monitor subsurface materials in more detail.

Prior to understanding the interaction between soil and geogrid in the laboratory, PLAXIS finite elements (FE) analyses were performed to obtain clues to the system response to the effect of a circularly loaded plate and the interaction of aggregate materials with a horizontally positioned geogrid. PLAXIS can be used to analyze the stress-strain characteristics of geomaterials subjected to external and self-induced loads. This finite element code was helpful to determine stress and strain characteristics of loaded material in box tests and was also used as a confirmation that the box was large enough that the walls had little influence on the stress distribution.

5.2.1 Material Models and Properties

The first step in PLAXIS involves creating material models for the soil, plate, and geogrid used in the model. One of the largest downfalls of PLAXIS is the inability to approximate the stress/modulus behavior of soil using a simple power model. However, PLAXIS does contain an advanced soil model defined as the “hardening soil model” that allows for the analysis of elastoplastic behavior (hyperbolic relation between stress and strain) where modulus can be calculated

based on the stress induced in the soil (Brinkgreve 2002). The “hardening soil model” was used for all analyses presented in this research in an attempt to model deformation of the granular material more accurately at higher strain levels. The load plate was assumed to have a stiffness of 7.6×10^4 MN/m to ensure that deformation of the plate was insignificant relative to the soil. The 25.4 mm thick plate is assumed to have very little deformation in laboratory tests and therefore is modeled with a rigid, elastic object in the model. The tensile stiffness of the geogrid was assumed to be 500 kN/m to compare results with the stiffer geogrid used in laboratory tests. The interface distance or “virtual thickness” was also required to be entered into PLAXIS models. The “virtual thickness” is defined as the soil adjacent to and affected by the geogrid reinforcement and is a zone where more elastic deflections occur (Brinkgreve 2002). This layer thickness changes depending on the position of the geogrid, but laboratory tests provided a method of estimating the layer thickness on each side of the reinforcement. The “virtual thickness” will be explained in more detail when laboratory test results are presented. A summary of the soil and other model parameters entered into PLAXIS is given in Table 5.1.

Table 5.1. Material properties of grade 2 gravel used in PLAXIS analyses.

Material Property	Units	Input Value
Unit Weight, γ_d	kN/m ³	18.5
Primary Loading Modulus, E_{50}	MPa	124 [†]
Primary Compression Modulus, E_{oed}	MPa	124 [†]
Unloading/Reloading Modulus, E_{ur}	MPa	498.5 ^{††}
Power, m	--	0.5
Cohesion, c_{ref}	kPa	1*
Angle of Friction, ϕ	Degrees	35
Poisson's Ratio, ν	--	0.35
Reference Stress, p_{ref}	kPa	100
Lateral Earth Pressure Coefficient, K_0	--	0.426
Suction, ψ	kPa	0
Strength Reduction Factor, R_{inter}	--	1

[†]Approximated from stress/strain behavior for initial loading conditions in large-scale laboratory box tests.

^{††}Approximated from stress/strain behavior for initial loading conditions in large-scale laboratory box tests and recommendations that E_{ur} is approximately three to four times E_{50} in PLAXIS manual. This analysis was conducted with $E_{ur} = 4E_{50}$

*Although grade 2 gravel does not have strength at 0 applied stress when dry, PLAXIS recommends a small value of c_{ref} to help the model converge on a solution.

5.2.2 Model Setup

Two-dimensional FE models were run using axis-symmetric modeling behavior in PLAXIS. The axis-symmetric approach allows for the modeling of a

symmetric slice to be taken out of the problem and only half of the problem to be analyzed. The smaller area considered for modeling decreases the time required for modeling and also most accurately approximates a circularly loaded plate, which is symmetric in orthogonal horizontal directions. A model of the setup is shown in

Figure 5.3. The mesh used to analyze the problem is shown in Figure 5.4 where initial conditions could be specified. Initial geostatic stresses are calculated automatically in PLAXIS assuming a mass density of soil and coefficient of lateral earth pressure. Contributions from groundwater are neglected since granular materials used in laboratory tests have hygroscopic moisture contents.

Running a model in PLAXIS requires much time and computing power, therefore a simplified loading condition that only considers static load application was used. PLAXIS results were used to determine the shear stresses and strains induced in subsurface soil with an applied surface load and deformation. The simulation involves two stages:

1. The first stage involves the application of a 71.5 kPa seating load (the load applied in large box laboratory tests).
2. Stage 2 involves applying 550 kPa to the surface to monitor the maximum loading condition applied to grade 2 gravel samples.

The models were run until the deformation of the surface plate in the model approximately matched that of the corresponding large box test in the laboratory by varying the applied load. The deformation of the surface was of greater concern than

the load applied in PLAXIS since material rotation will be a result of deformations at the surface instead of the magnitude of load.

5.2.3 *PLAXIS Model Results*

Results of PLAXIS analyses are shown in Figure 5.5 in terms of shear strain amplitude and Figure 5.7 in terms of horizontal displacement. All PLAXIS results were run to vertical displacements of the plate between 6.2 and 6.8 mm so that results could be more easily compared against one another. The expected behavior of material without the presence of a geogrid is shown in Figure 5.5a. Without geogrid present, the shear strains are maximized near the plate edge and propagate down the plate edge to a depth of influence of approximately 200 mm. Shear failure surfaces develop along all sides of the plate and shear failure planes induced below the plate can be followed vertically down from the plate edge. The results of PLAXIS analyses without geogrid follow the expected results for bearing capacity failure of a circularly loaded area (such as those presented in Figure 2.7).

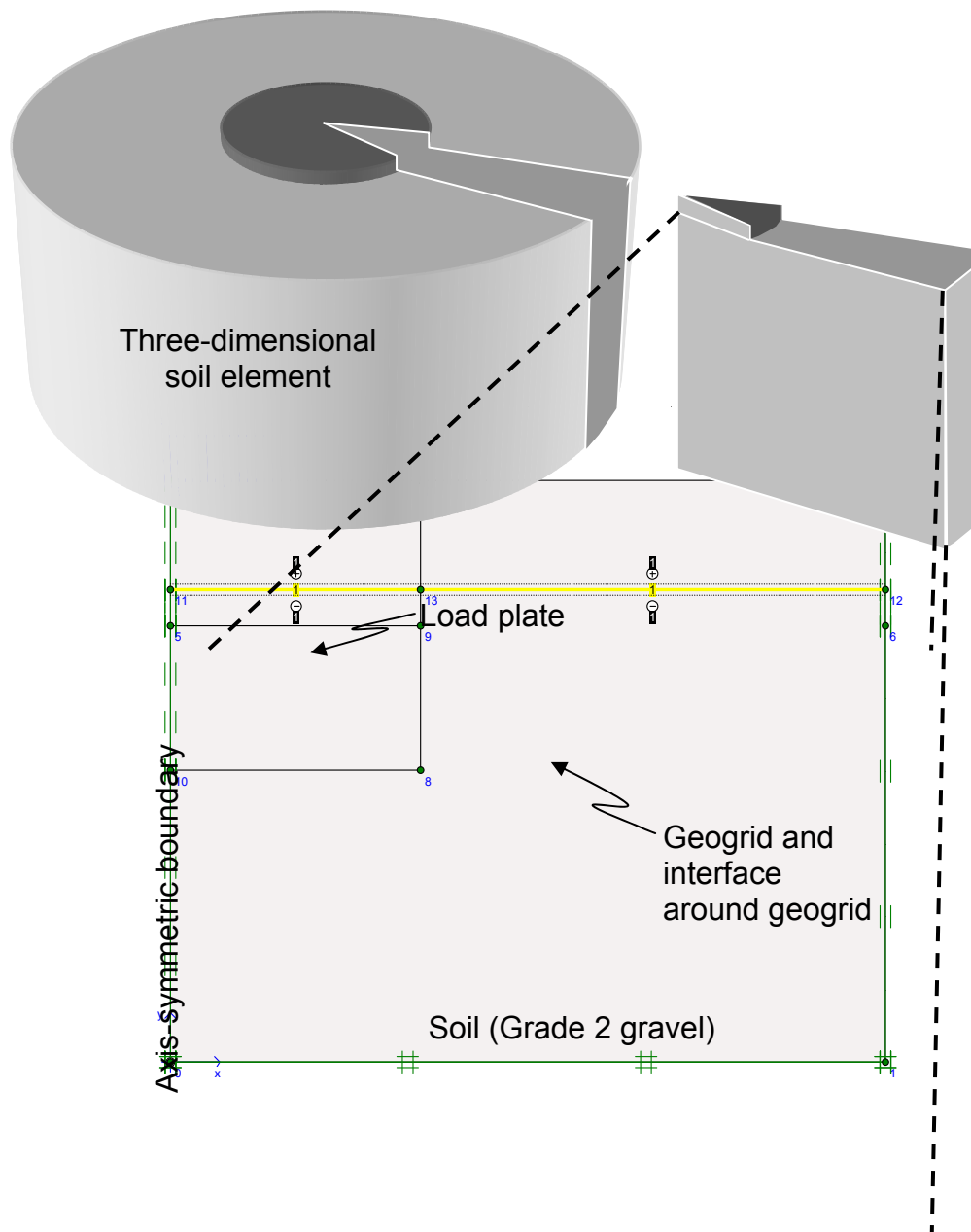


Figure 5.3. Axis-symmetric FE model simulation using PLAXIS. The axis-symmetric method allows a symmetric slice to be removed from a three-dimensional space for analysis.

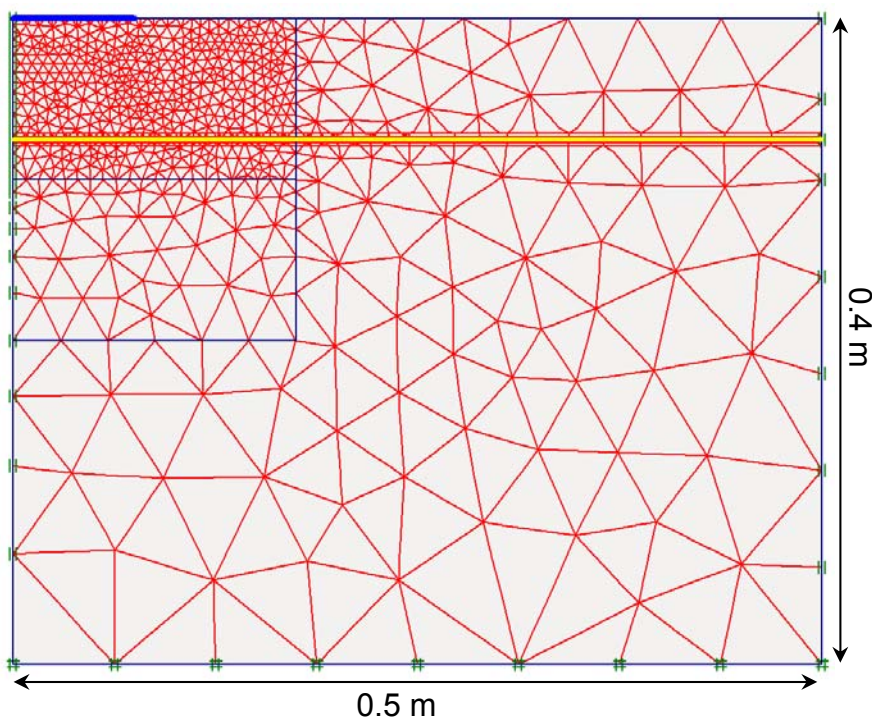
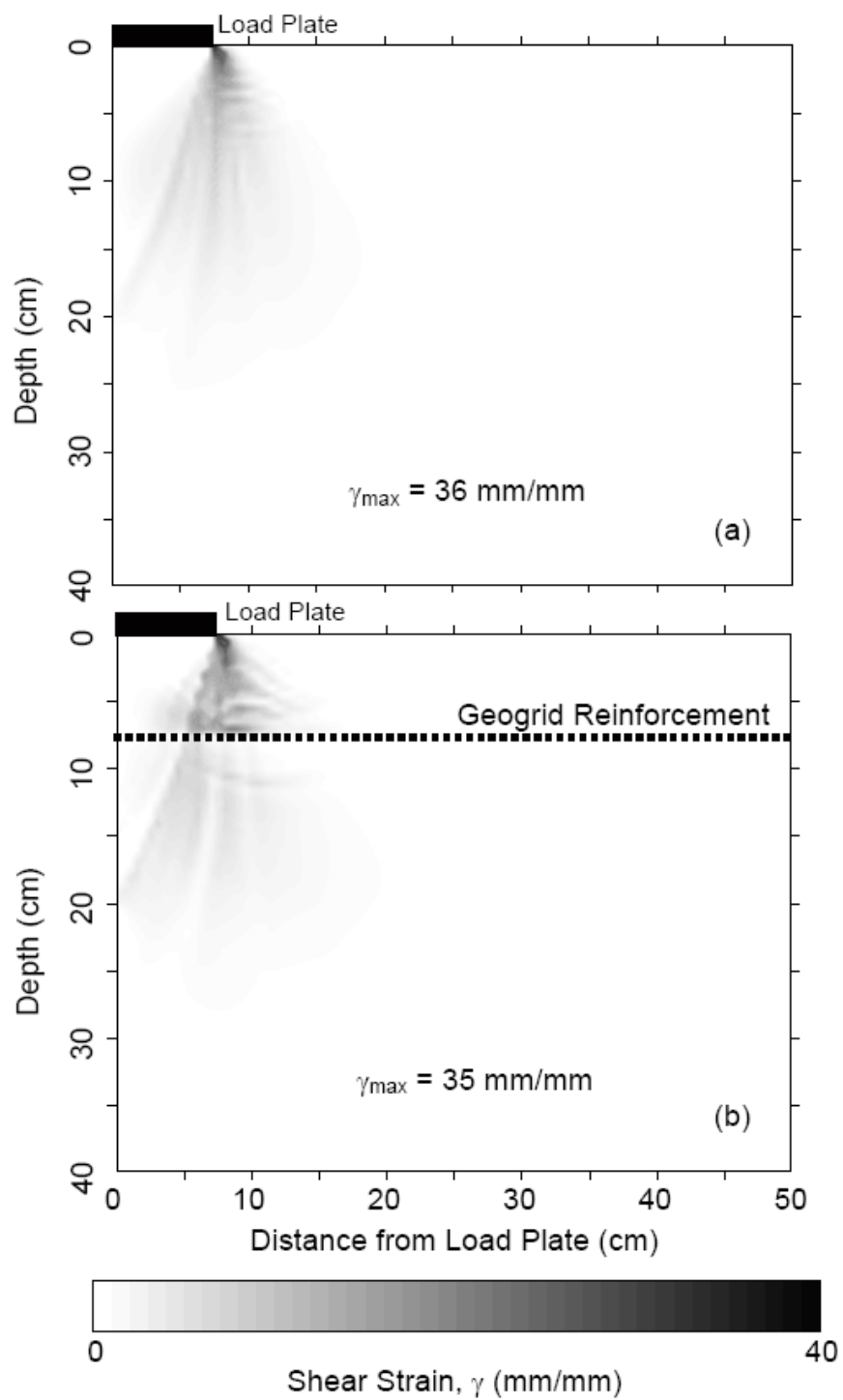


Figure 5.4. Final FE mesh used in PLAXIS analysis for the case with geogrid at 75 mm depth.

Figure 5.5b shows shear strain amplitude when a geogrid is placed at a depth of 75 mm. The shear strains are highest at the plate edge and propagate at relatively high amplitude to the depth of the geogrid, not dissimilar to the shear strains calculated without a geogrid present. However, shear strains are higher 20 – 30 mm above the geogrid than when no geogrid is present, an indication that more shearing is concentrated above the geogrid. As angular particles tend to try and shear against one another, the stiffness of the soil system in this small zone above the geogrid is expected to increase as well. Also, the shear strains dissipate quickly in the 30 mm space directly below the geogrid. The decrease in relative shear strain amplitude seems to indicate that the geogrid is acting to dissipate some of the shear stresses, distributing them in the geogrid as opposed to the underlying soil. Shear failure

planes proposed in Figure 2.2b seem to be modeled similarly with PLAXIS analyses. However, after a depth of approximately 100 – 120 mm, the shear strain amplitude increases. The increase in shear strain is an indication that shear stresses are propagating below the geogrid.

Figure 5.5c and d show the shear strain amplitude when geogrid is placed at depths of 100 and 150 mm. Shear strains are maximized directly beneath the plate edge and dissipate before increasing above the geogrid reinforcement layer, again showing the tendency of the shear failure plane to be concentrated in an area directly above the geogrid instead of propagating below the geogrid. The increase in shear strain amplitude indicates material is expected to be disturbed and is most likely the zone where soil is interlocking with the geogrid. In contrast to when the geogrid is placed at 75 mm depth, relative shear strains beneath the geogrid are low in the 100 mm case and nearly zero when geogrid is at 150 mm depth.



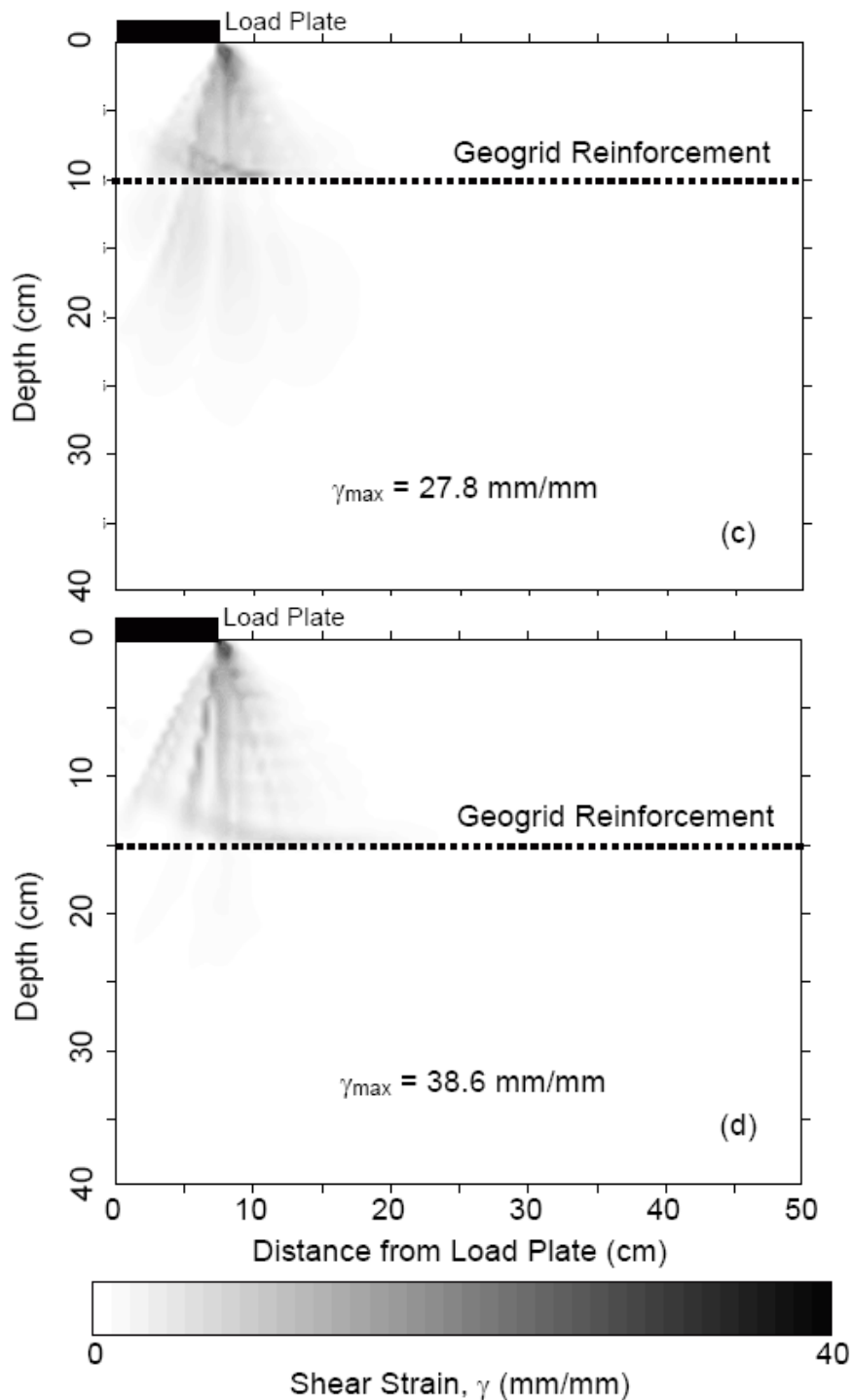


Figure 5.5. Shear strain from PLAXIS analysis below a circularly loaded plate when (a) no geogrid is present, (b) geogrid is buried at 75 mm depth, (c) geogrid is buried at 100 mm depth, and (d) geogrid is buried at 150 mm depth.

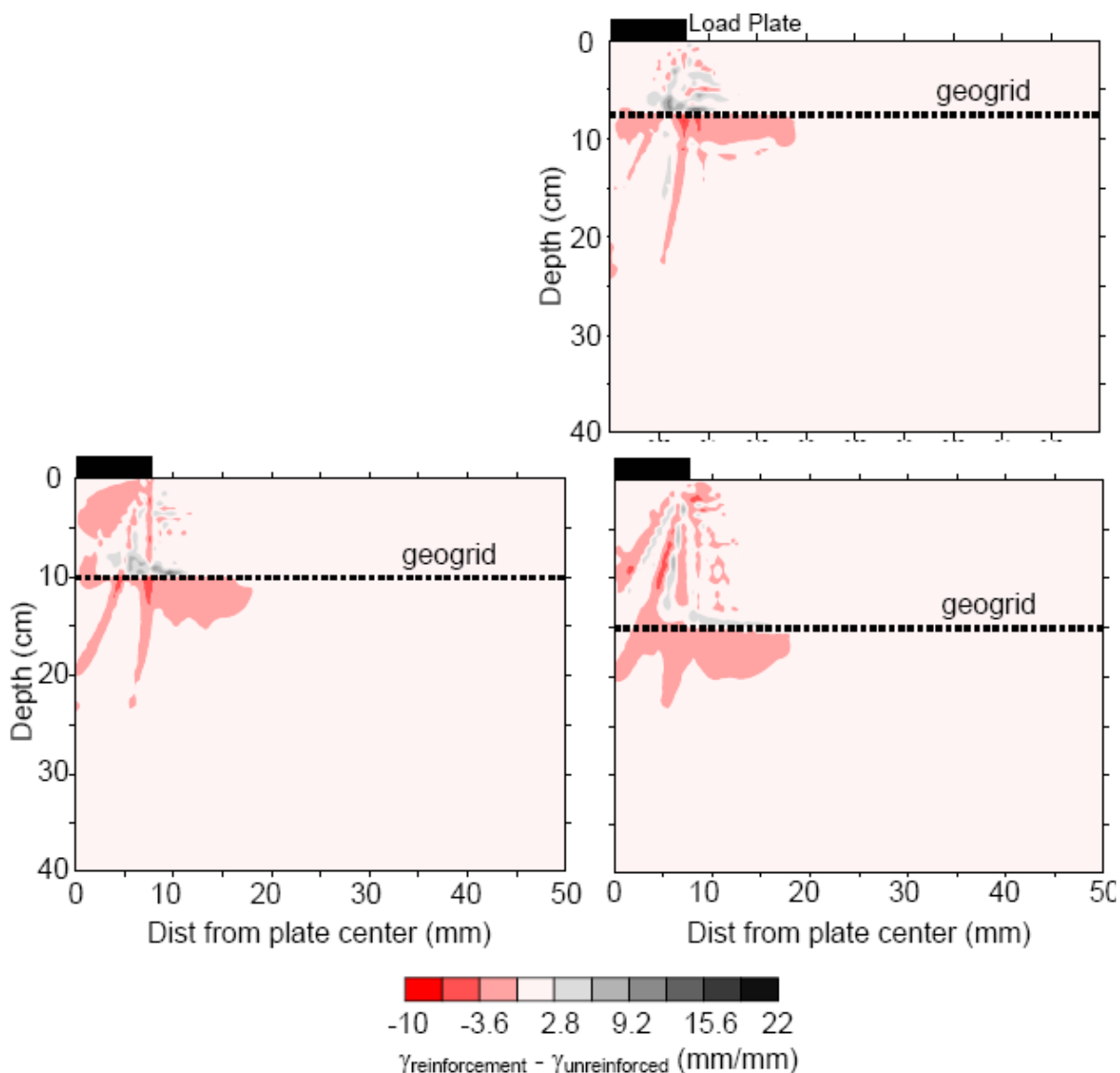
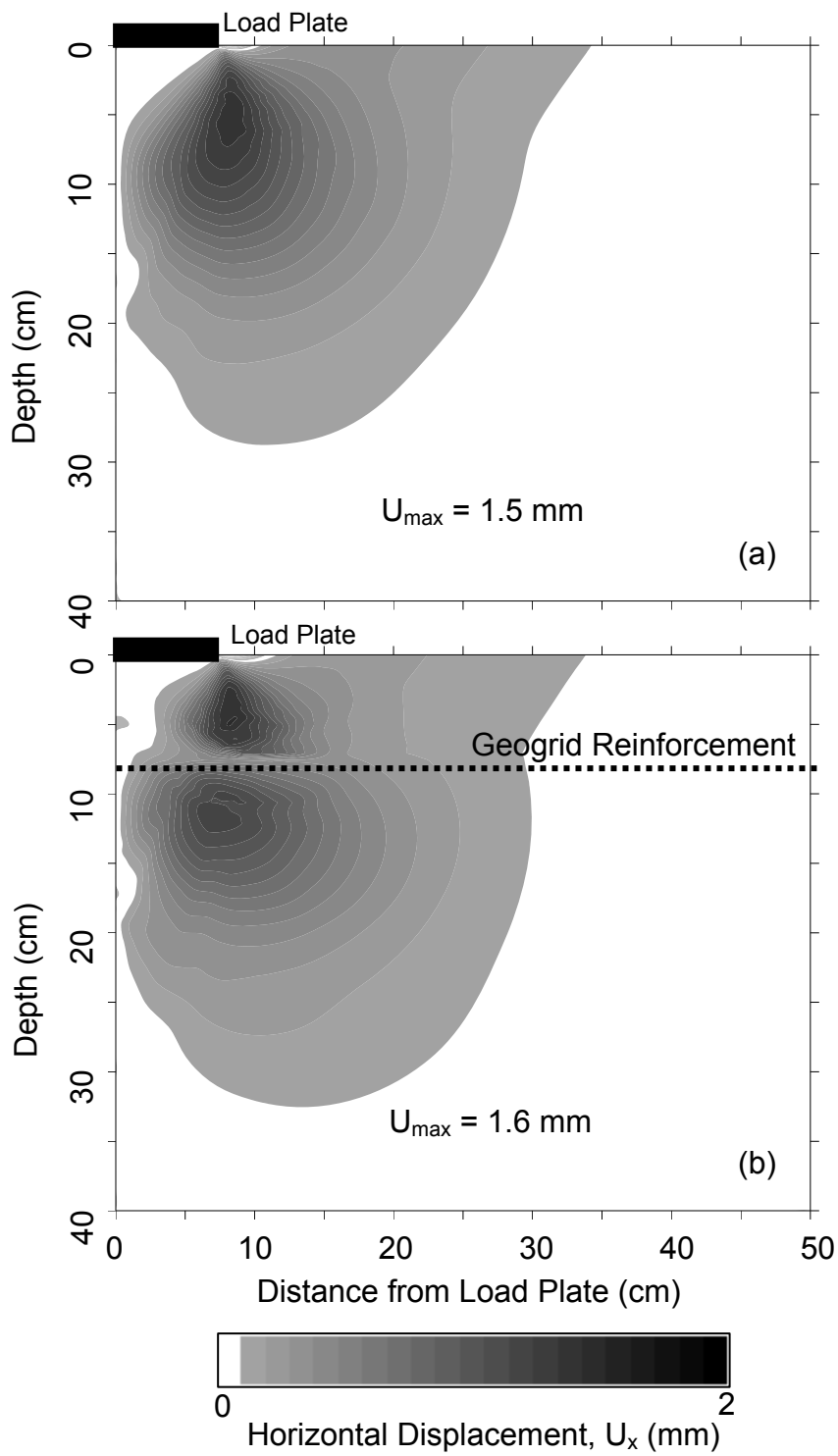


Figure 5.6. Difference in shear strain between reinforced and unreinforced sections for geogrid at 75, 100, and 150 mm depth.

Figure 5.7 shows the horizontal displacement (u_x) of soil in the PLAXIS models. The horizontal displacement may be the best method of examining the confinement of soil since horizontal movement of soil is an indication that particles are compressing and unable to move freely. Without the presence of geogrid (Figure

5.7a), the maximum u_x is approximately 1.5 mm and displacements propagate to a depth of about 200 mm, beyond which horizontal displacements are nearly zero.

Figure 5.7b and c show horizontal displacements when geogrid is placed at depths of 75 and 100 mm. The maximum horizontal displacements when the geogrid is placed at 75 and 100 mm are 1.6 and 1.8 mm, respectively. Therefore, when geogrid is placed at a depth of 100 mm, the soil appears to displace more laterally in the uppermost 50 – 70 mm of material. The greater displacements may be an indication that rotation is confined to shallow depths when geogrid is secured in the shallow subsurface. Figure 5.7b and c also show the decrease in horizontal displacement in close proximity to the geogrid. Although the influence area of the geogrid appears relatively small (~10 mm) on either side of the geogrid, the geogrid is reducing the horizontal movement of particles near the reinforcement, forcing displacement of particles above and below the geogrid.



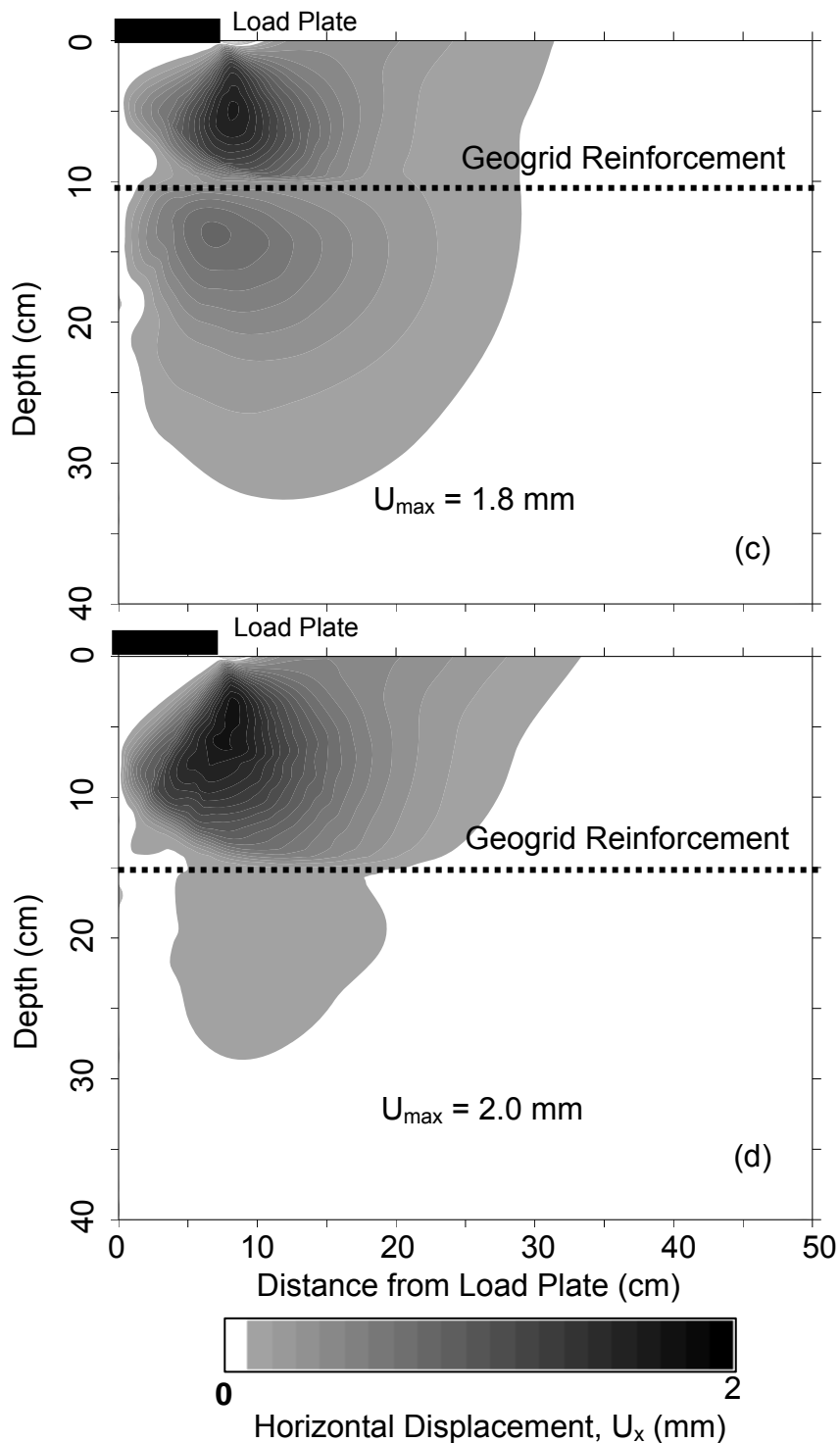


Figure 5.7. Horizontal displacement from PLAXIS analysis below a circularly loaded plate when (a) no geogrid is present, (b) geogrid is buried at 75 mm depth, (c) geogrid is buried at 100 mm depth, and (d) geogrid is buried at 150 mm depth.

Figure 5.7d shows the horizontal displacement of soil when geogrid is secured at a depth of 150 mm. The maximum horizontal displacement is 2.0 mm, greater than when the geogrid is at depths of either 75 or 100 mm. The most beneficial aspect of placing the geogrid at 150 mm depth appears to be that very little displacement of particles occurs below the depth of the geogrid. However, horizontal displacements remain large and particles above the geogrid are expected to experience a greater amount of strain. A geogrid at 150 mm depth appears to be too deep to effectively provide stiffening effects to the soil based on PLAXIS analysis. However, there may be other considerations in deciding the location of the geogrid in the base course such as practicality during construction.

5.2.4 Summary of PLAXIS Results

Shear strains indicate that, for a circular load plate with a 150 mm diameter loading plate, geogrid should be placed below a depth of 100 or 150 mm to constrain shear stresses more effectively and prevent shearing of material below the reinforcement layer, which is especially important if subgrade material is compacted directly beneath the base course and reinforcement layer.

Horizontal displacement information gathered from PLAXIS indicates that geogrid reinforcement does constrain soil particles around the geogrid, but the displacements are transferred to a smaller volume of soil above and below the geogrid. Greater horizontal displacements are calculated when geogrid is secured in the subsurface than when geogrid is omitted for the same surface deflections.

Geogrid reinforcement appears most effective when secured at 100 mm depth based on the combined shear strain and horizontal displacement information. At a depth of 75 mm, the geogrid may be too shallow and shear stresses too high, allowing more shear stresses to propagate beneath reinforcement. When placed at 100 mm, the shear stresses have decreased and less strain is imparted in the geogrid layer. As a result, the geogrid remains stiffer and is better able to prevent horizontal movement of soil and further propagation of shear stress. Geogrid placed at 150 mm appears to be too deep for effective confinement of soil in the near surface. Although shear stresses and horizontal displacements are confined to the area above the geogrid, the shear strains and horizontal displacements above the geogrid are greater in magnitude than when the geogrid is placed at either 75 or 100 mm.

5.3 MEASURING GEOGRID INTERACTION WITH ELASTIC WAVE VELOCITY

5.3.1 Portage Sand Tests

Results from preliminary tests on Portage sand reinforced with a non-stiff geogrid at several depths are shown in Figure 5.8. Without the presence of a geogrid and with no applied load, the P-wave velocity appears to increase with depth. An increase in the wave velocity accompanies an increase in applied deviator load, especially nearer to the surface (depths less than 250 mm). Wave velocity increases more rapidly near the surface as is expected based on the calculated induced stress distribution beneath a circular plate. Wave velocities range between

400 m/s directly below the loaded plate (depth of about 60 mm) to approximately 220 m/s at a depth of 360 mm.

Results from a test with a tensioned geogrid placed 110 mm below the soil surface show highest P-wave velocities near the surface and lowest P-wave velocities at depth when an external load is applied, similar to the behavior seen in the test without geogrid. There is no apparent evidence that the velocity changes substantially near the geogrid, but P-wave velocity does drop from 400 m/s to 360 m/s in the 50 mm below the geogrid. The following discussion presents three hypotheses of the geogrid-soil interaction:

1. Soil stiffening is occurring, evidenced by the change in velocity from above the geogrid to below the geogrid.
2. Density of near surface sandy sediments is changing and may be affecting the velocity of sediments near the geogrid.
3. Velocity results may be masked from the measurements because of the large velocity contrasts near the surface caused by high applied loads and the inability of a geogrid with apertures much larger than the D_{50} grain sizes to constrain the soil.

A final test was performed with the geogrid placed at a depth of 220 mm below the soil surface. Similar to when geogrid was placed at 110 mm depth, velocity appears to drop more quickly immediately below the geogrid, especially under higher deviatoric loads. The test is an indication that the geogrid is helping to stiffen soil directly above and in close proximity to reinforcement, while soil beneath the grid has a reduced stiffness. In effect, the geogrid is acting similar to a beam,

supporting soil above the geogrid and inducing a state of reduced stress below the geogrid.

After the test with geogrid placed at a depth of 220 mm, the tension in the geogrid was released at a peak applied load of 70 kPa. The velocity is shown with depth at 70 kPa before releasing the tension in the geogrid and at 70 kPa after releasing tension in the geogrid in Figure 5.9. An increase in velocity immediately above the geogrid and a decrease in velocity beneath the geogrid are observed after the tension was released. The changes in velocity are thought to be caused by the rearrangement of internal stresses that are causing a change in the modulus of materials near the geogrid. The “beam” model described above no longer applies; instead the material appears to be more confined near the geogrid. A hypothesis is that soil grains constrained by the tensile forces in the geogrid have been released to rearrange themselves in a more densely packed structure. Further beneath the geogrid, velocities are lower after tension was released and may be a sign that grains have moved into the area directly around the geogrid, partially releasing load held by grains at greater depths.

In summary, when geogrid was placed at a depth of 110 mm, stiffening effects from the geogrid were more difficult to distinguish and may have been masked by changes in velocity directly beneath the loading plate in the clean sand. When placed at a depth of 220 mm, the geogrid seems to be acting as a beam or bridge; the stiffness appears to increase in close proximity to the geogrid, but decrease beneath the geogrid layer, especially at higher deviatoric loading. The stiffening of material at the geogrid interface is a good indication that the applied

load is being distributed over a larger area. However, the greater depth of reinforcements indicates that limited reinforcement may be occurring.

The thickness of influence of a horizontally tensioned geogrid at a depth of 220 mm below the soil surface in sand is ambiguous from these test results. At most, the soil may be affected in a zone up to 50 mm in thickness on either side of the geogrid. The use of a more coarsely grained materials may be able to more effectively delineate a “zone of influence” since particles with size more appropriate for the geogrid apertures will produce more “interlocking.”

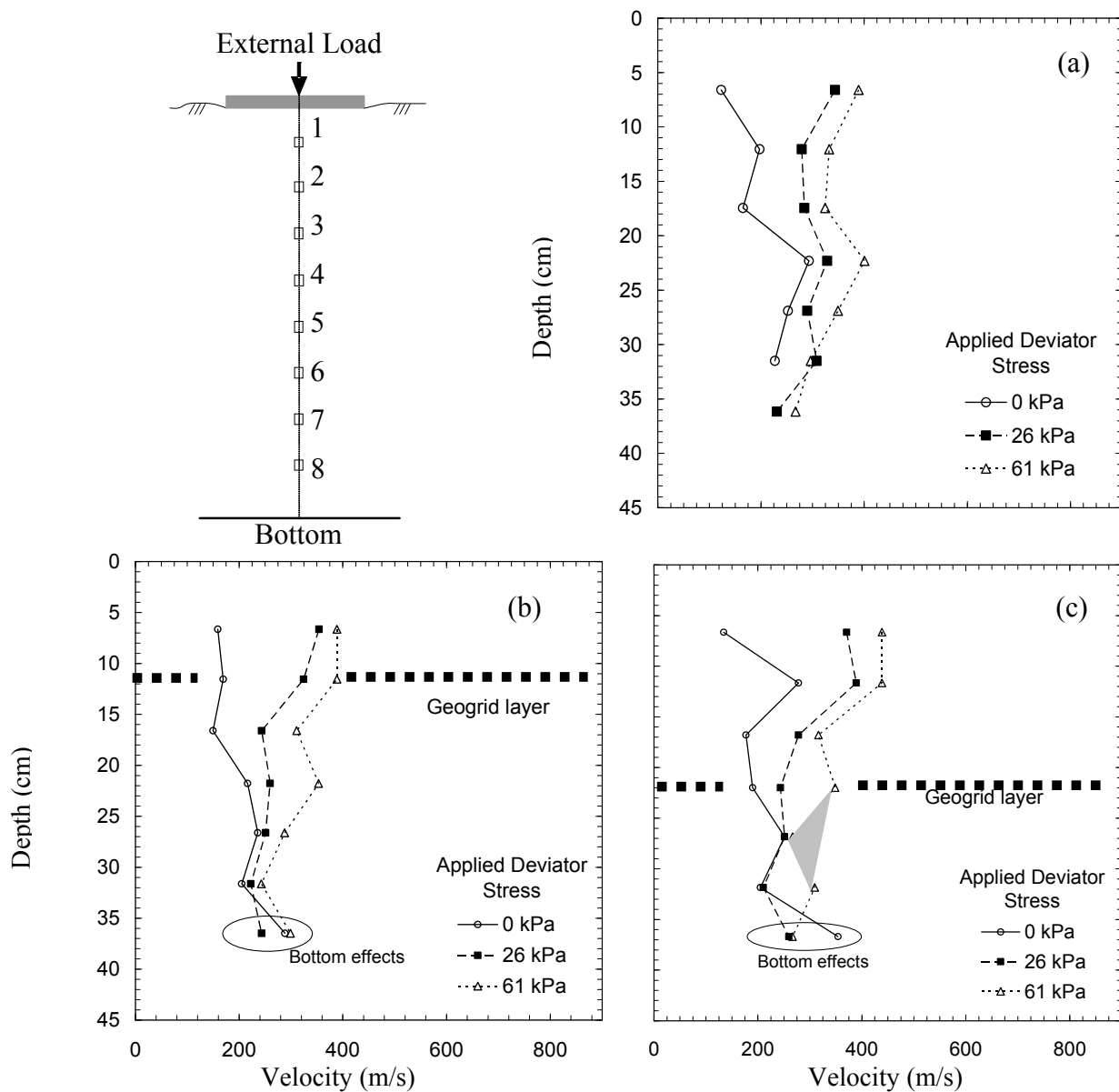


Figure 5.8. Depth vs. velocity profile at three external loads with (a) no geogrid layer (b) geogrid layer at 110 mm depth, and (c) geogrid layer at 220 mm depth. The shaded area shows the decrease in velocity beneath the geogrid, especially at high applied deviator stress.

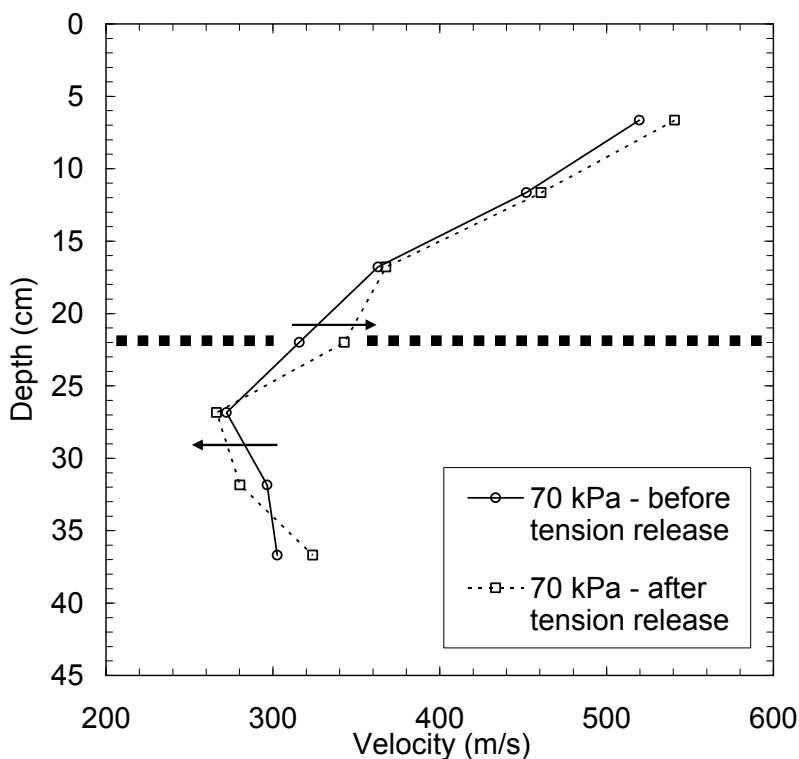


Figure 5.9. A velocity-depth comparison at the peak applied load of 70 kPa before and after tension was released in the geogrid. The arrows on the graph indicate the direction of velocity change adjacent to the geogrid.

5.3.2 Grade 2 Gravel Tests

5.3.2.1 Stiff Geogrid

Because of the difficulty in determining the influence zone of the geogrid based on velocity analysis, a stiffer geogrid was chosen to perform further analysis of the reinforcing effects of the geogrid. A tensile force of approximately 0.26 kN/m was applied to the stiffer geogrid to ensure that the geogrid was “engaged” with the surrounding particles when load was applied at the surface.

Wave velocity results appear more consistent with respect to velocity results performed with the non-stiff geogrid. Velocities increase with applied load, but also increase near and above the geogrid (Figure 5.10). The increased wave velocity above the geogrid is expected from both PLAXIS models and tests performed with Portage sand since particles interlock and tend to push against each other in zones of constrained horizontal movement (see section 5.2.3). When the geogrid is secured at 75, 100, and 150 mm depth and 550 kPa pressure is applied at the surface, velocity decreases by 326, 417, and 242 m/s, respectively from a point approximately 25 mm above the geogrid to a point 25 mm below the geogrid. Without reinforcement, the decreases in velocity over these same depths are 281, 255, and 203 m/s. Therefore, the change in velocity across the geogrid under the reinforced condition ($\Delta V_{\text{reinforced}}$) is consistently more than the change in velocity under the unreinforced condition ($\Delta V_{\text{unreinforced}}$). To analyze the observed change in stiffness, a factor f is defined:

$$f = \frac{\Delta V_{\text{reinforced}}}{\Delta V_{\text{unreinforced}}} \quad (5.1)$$

where f is equal to 1.16, 1.63, and 1.19 for geogrid positioned at 75, 100, and 150 mm. Therefore, the velocity difference increases when geogrid is secured at all depths, but is more pronounced when geogrid is secured at 100 mm where the change in velocity with reinforcement is substantially higher than would be expected from the stress distribution.

P-wave velocity results with geogrid at 75, 100, and 150 mm depth show that the stiffness reinforcement factor around the geogrid appears to be 1.35, 2.66, and 1.42 (i.e., square of factor f) greater than soil without geogrid. These values are representative of the modulus reinforcement factors calculated over the entire base course soil thickness calculated by Kim (2003). Kim (2003) calculated a modulus reinforcement factor of 2.0 for Grade 2 gravel, agreeing well with results of this research; however the zone over which to apply this factor may depend on the thickness of engagement of the geogrid and thickness of the base course layer. More work is necessary to constrain a well-defined “zone of influence” desired from this research project. As a result, shear stresses and strains were analyzed by monitoring subsurface material rotation.

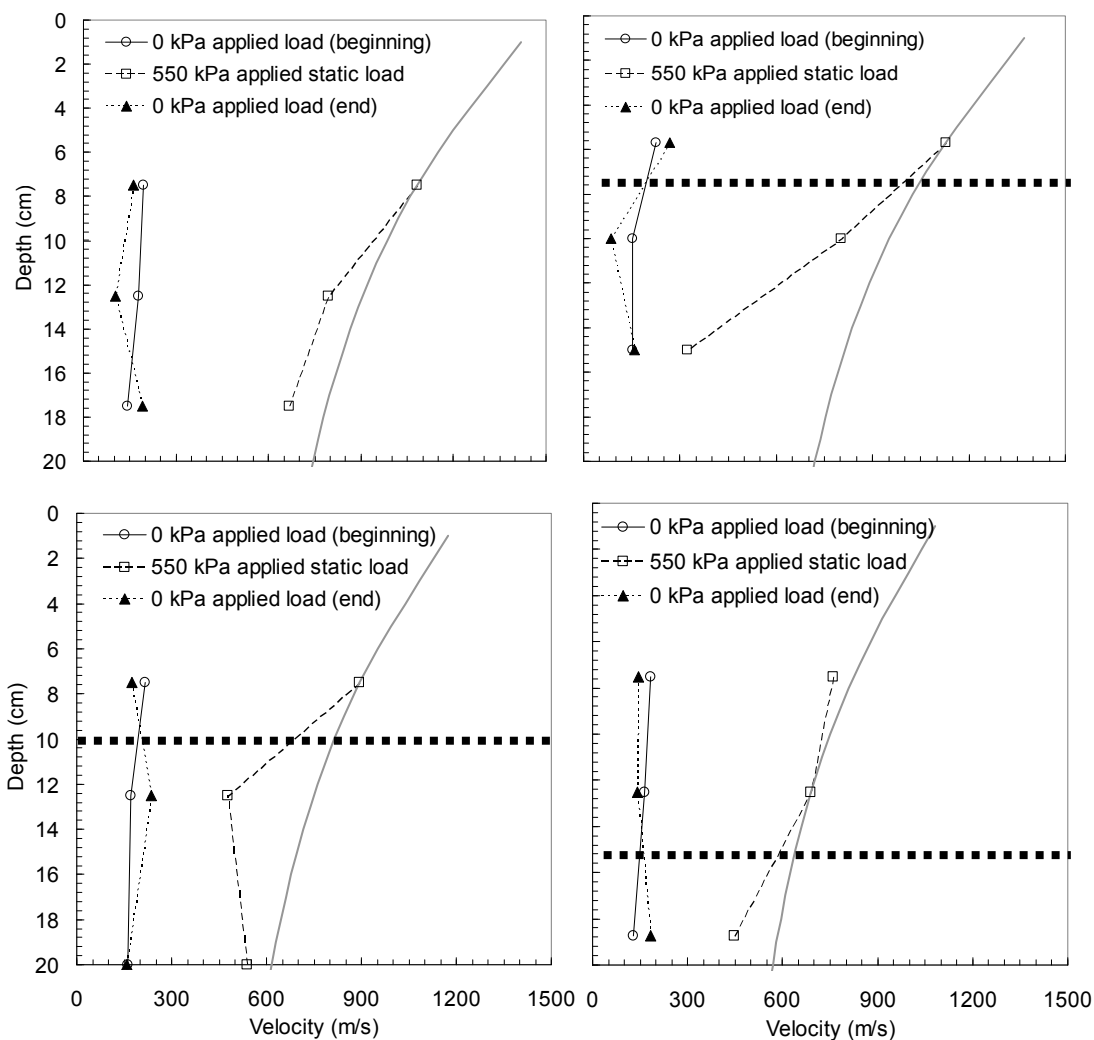


Figure 5.10. Velocity as a function of depth for three tests performed on grade 2 gravel with stiff geogrid. The grey line represents the theoretical change in velocity with changing stress without geogrid.

5.4 MEASURING STIFF GEOGRID INTERACTION WITH ROTATION ANGLE OF GRADE 2 GRAVEL

5.4.1 Test Method One – Measuring a Two-Dimensional Array of Rotations

Both cyclic and static loads were used for testing the rotation of a two-dimensional array of accelerometers and results are presented at several different

cycles and applied static loads. Geogrid was omitted from the first test, but was incorporated at 75, 100, and 150 mm depth in three subsequent tests.

Without geogrid present (Figure 5.11 and Figure 5.12), tilt angles are highest near the plate edge and extend vertically down into subsurface materials before diminishing substantially at approximately 170 mm depth. Maximum rotation angles are about 4° measured beneath the edge of the load plate at highest applied stress and the largest vertical displacement. Directly beneath the center of the load plate where principal stress axes are orthogonal to loading, rotation angle is lower or close to zero.

Figure 5.13 and Figure 5.14 show the rotation angle of grade 2 gravel when geogrid is secured at 75 mm depth. The two-dimensional plots show that rotation angle is highest beneath the plate edge, but reduces to approximately zero directly under the center of the plate. Below the geogrid, rotations diminish and reinforcement appears to dissipate shear stresses. The “zone of influence” of the geogrid layer appears to extend only 20 – 30 mm above the geogrid and up to 50 mm below the geogrid in these tests. However, at higher applied loads (550 kPa), accelerometer tilt increases substantially below the geogrid as reinforcement seems to deform with the material instead of dissipating shear stress within the fabric.

Geogrid was secured and tensioned as described before at a depth of 100 mm in rotation plots presented in Figure 5.15 and Figure 5.16. When at 100 mm depth, a well defined “zone of influence” appears around the geogrid reinforcement layer. Although rotation angle measured at 50 mm depth is higher for the 100 mm deep geogrid than the 75 mm deep geogrid, the rotation angle diminishes more

quickly when geogrid is secured at 100 mm depth. The rotation angle appears to be arrested in a zone 20 – 30 mm on both sides of the geogrid reinforcement layer, but further tests are required with more closely spaced accelerometers to confirm this “zone of influence.” At depths beyond 150 mm the rotation angle remains low beneath the geogrid reinforcement layer.

Figure 5.17 and Figure 5.18 show the measured rotation angle of gravel when geogrid is placed at 150 mm depth. Results of the 150 mm depth test show that rotation angle is again highest along the plate edge and a higher zone of rotation appears to extend under the plate near the geogrid. Beneath the geogrid, rotation angle diminishes. The “zone of influence” of the geogrid is 20 – 30 mm above the geogrid. Below the geogrid, a “zone of influence” is difficult to distinguish and further tests with more closely spaced MEMS accelerometers will constrain a zone on either side of the geogrid.

Figure 5.11. Measured rotation of soil at different stages of cyclic loading. Cyclic loading was applied for 200 cycles, removed, and applied for another 200 cycles. No geogrid was incorporated into the soil. δ is vertical deflection of the surface plate in mm.

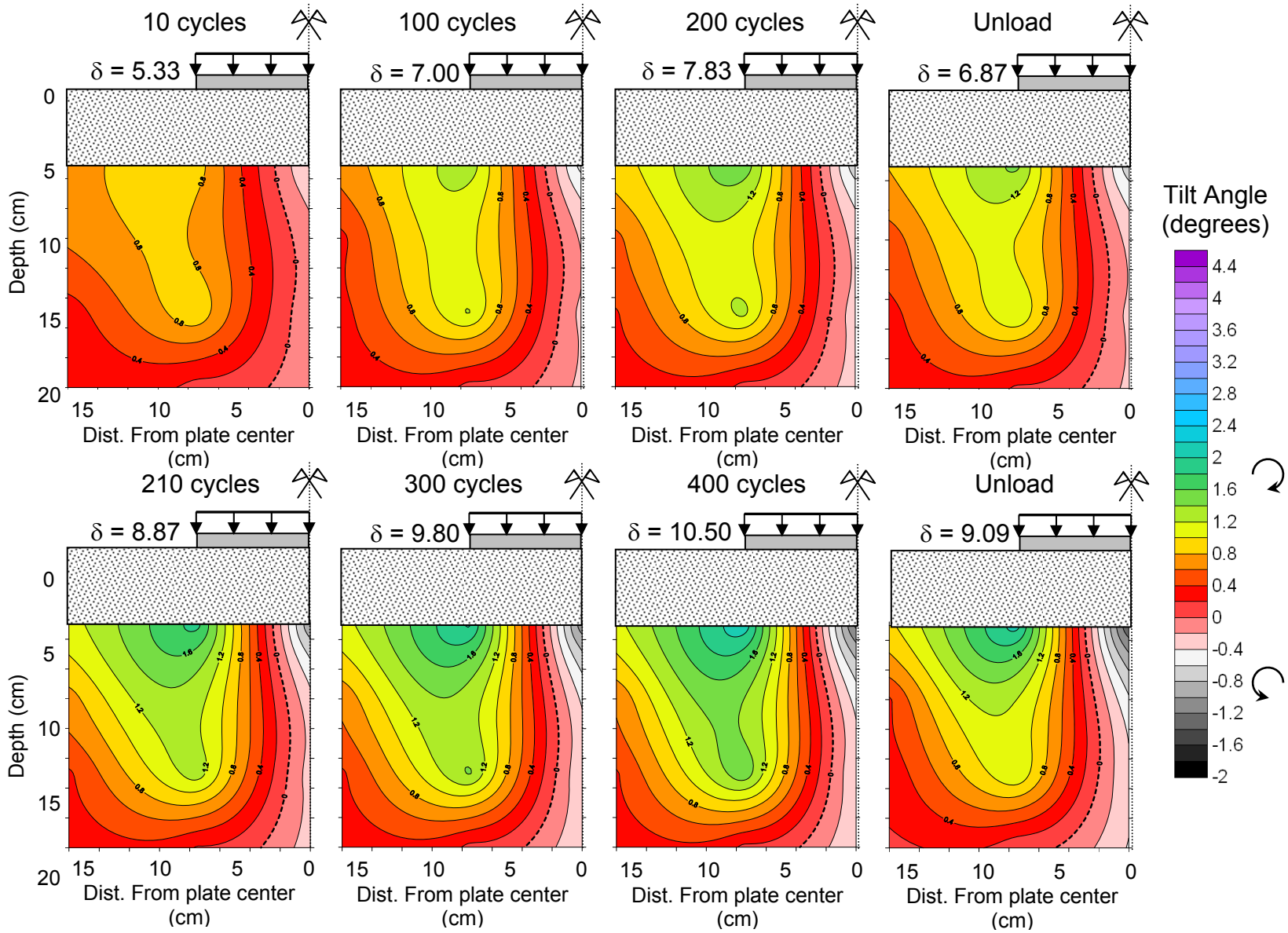


Figure 5.12. Measured rotation of soil at different stages of static loading. Static loading was applied after 400 cycles of cyclic loading. No geogrid was incorporated into the soil. δ is vertical deflection of the surface plate in mm.

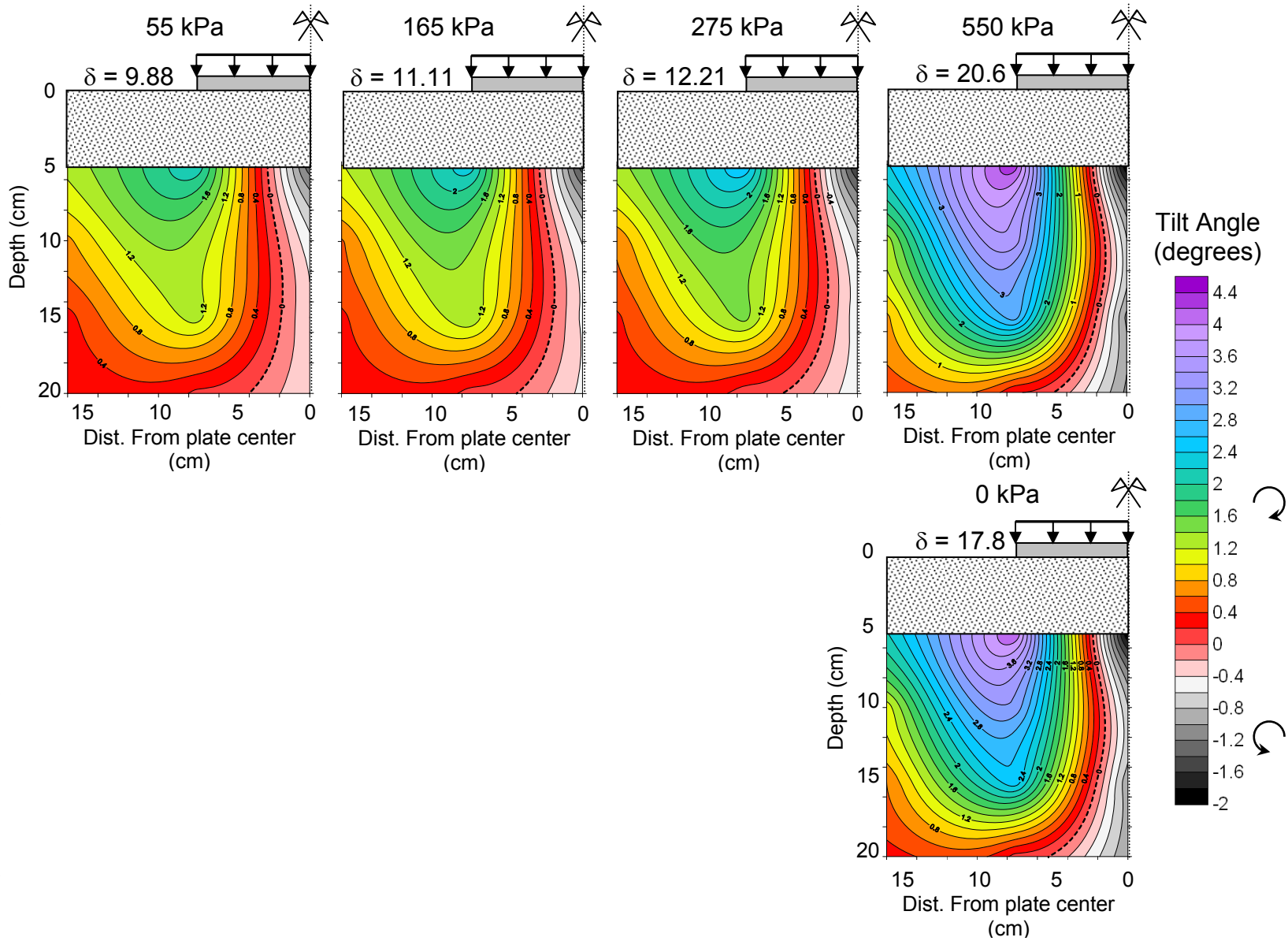


Figure 5.13. Measured rotation of soil at different stages of cyclic loading. Cyclic loading was applied for 200 cycles, removed, and applied for another 200 cycles. Tensioned geogrid was placed at 7.5 cm depth. δ is vertical deflection of the surface plate in mm.

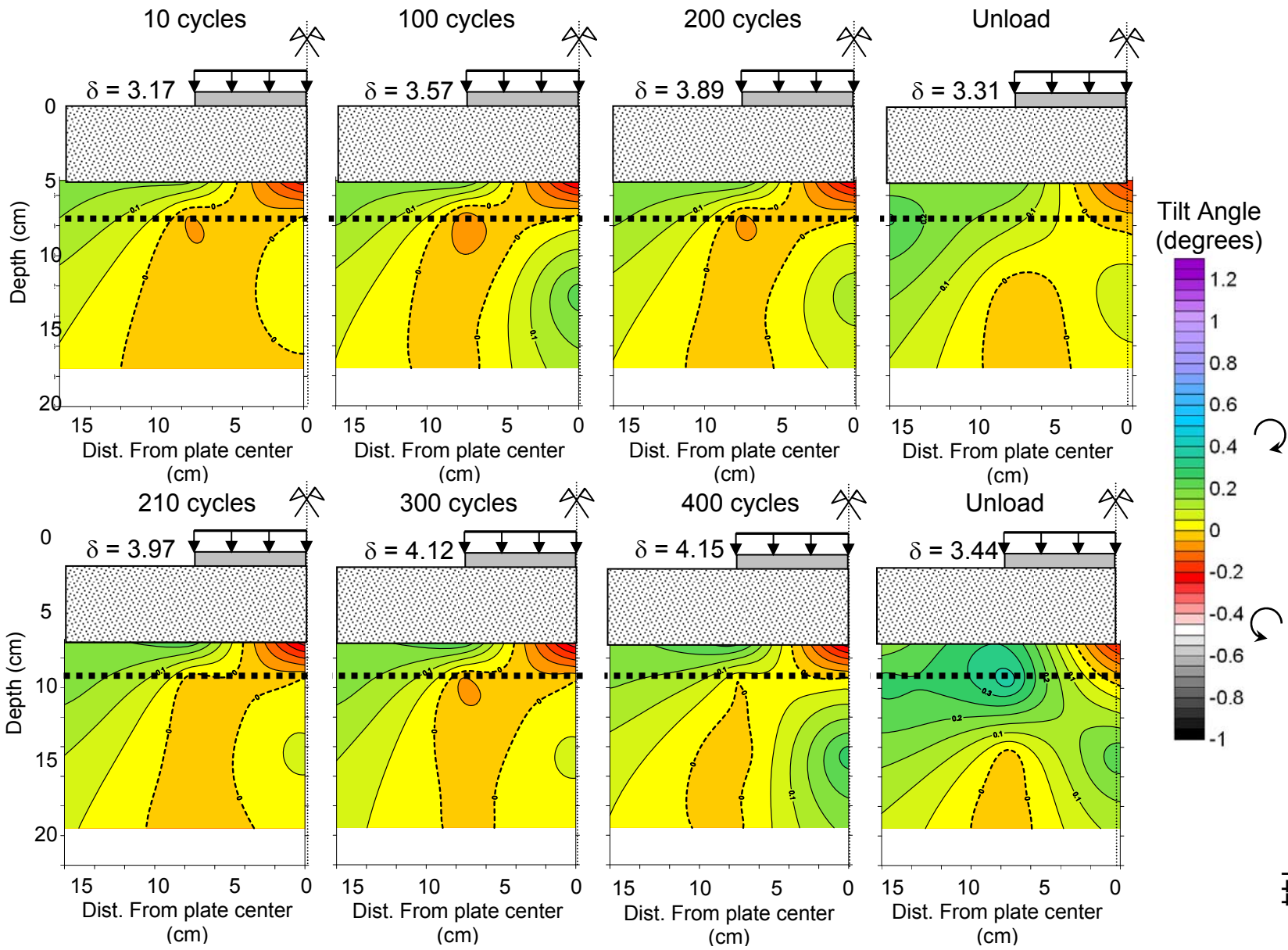


Figure 5.14. Measured rotation of soil at different stages of static loading. Static loading was applied after 400 cycles of cyclic loading. Tensioned geogrid was placed at 7.5 cm depth. δ is vertical deflection of the surface plate in mm.

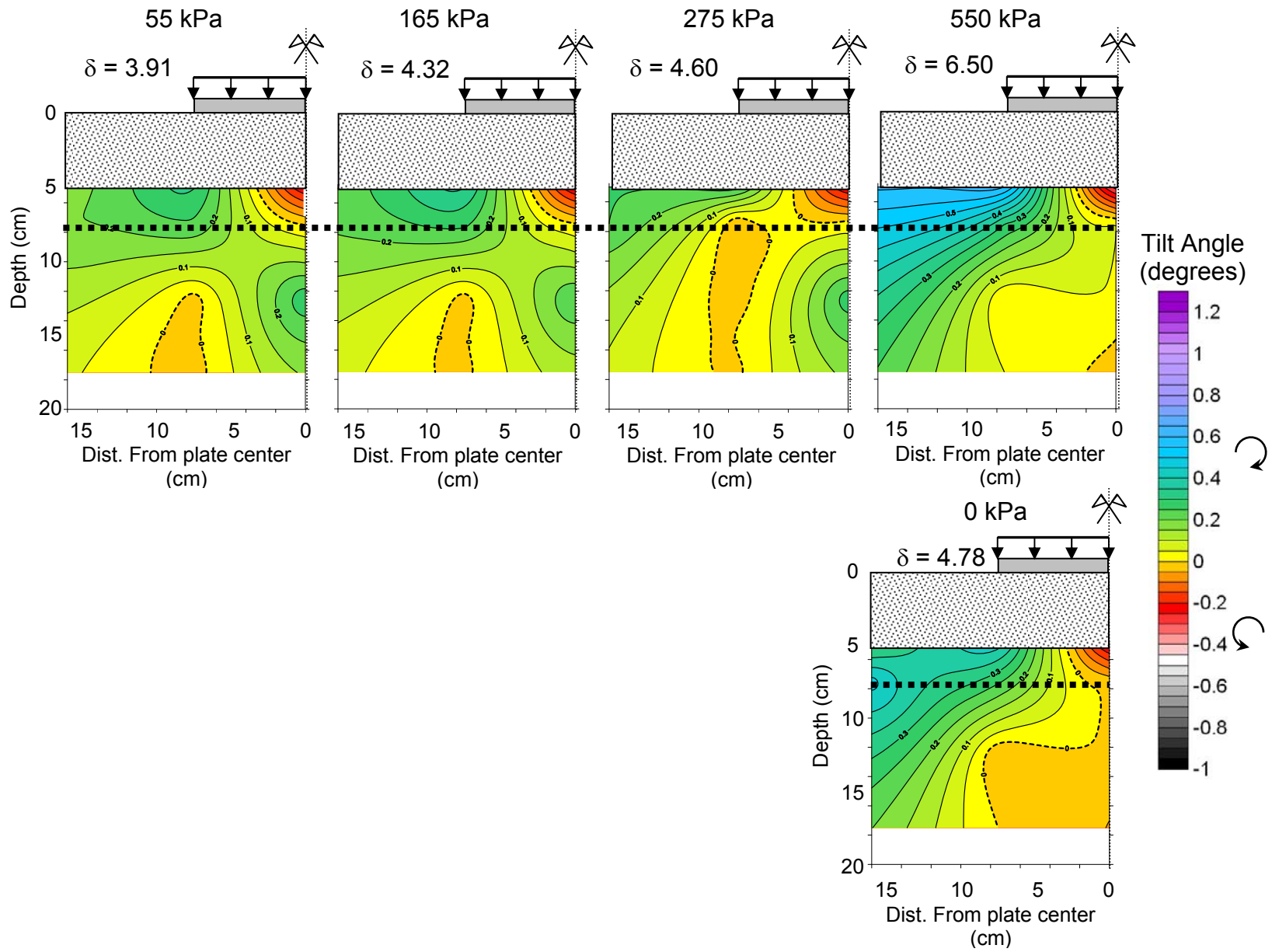


Figure 5.15. Measured rotation of soil at different stages of cyclic loading. Cyclic loading was applied for 200 cycles, removed, and applied for another 200 cycles. Tensioned geogrid was placed at 10 cm depth. δ is vertical deflection of the surface plate in mm.

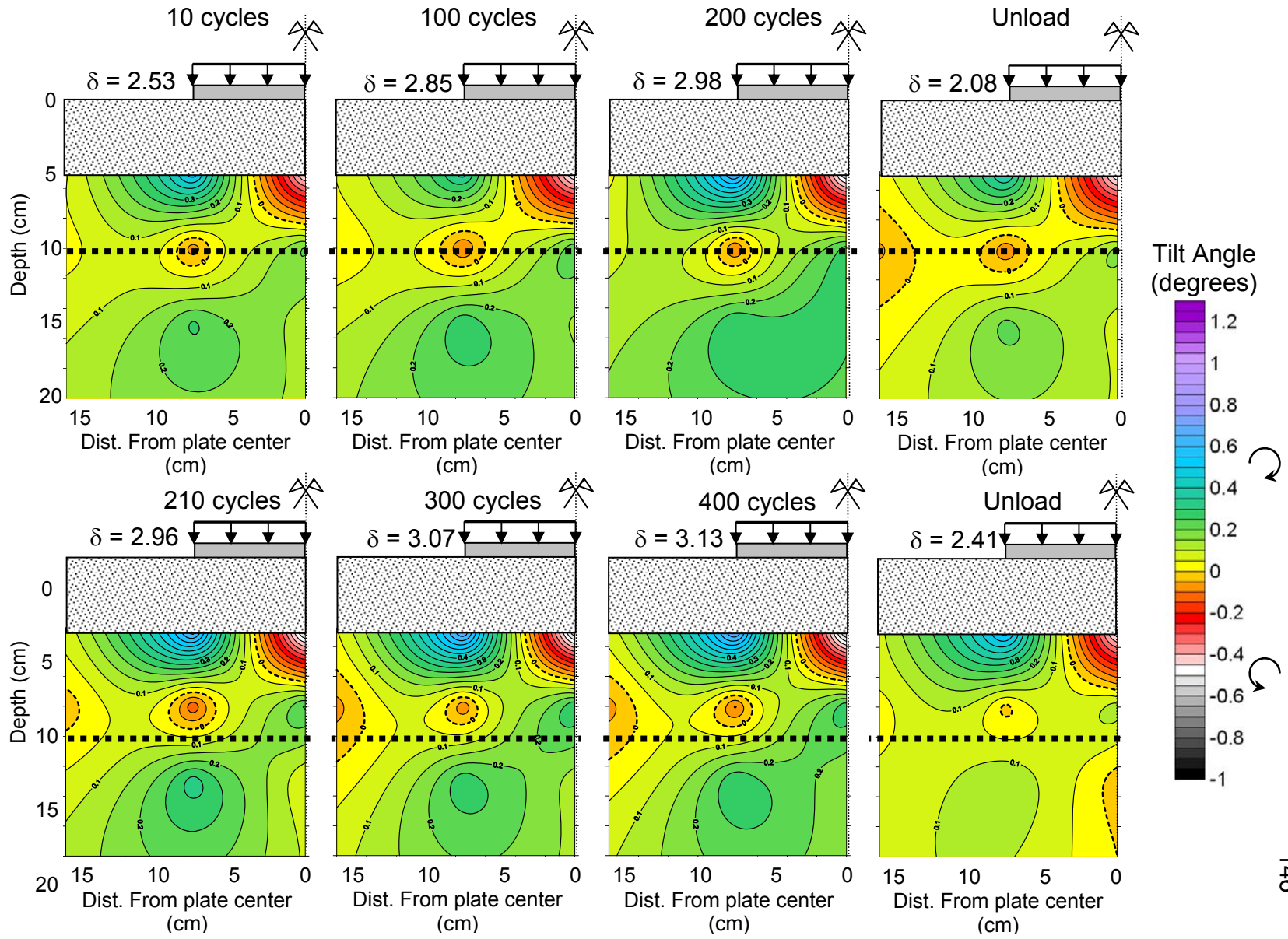


Figure 5.16. Measured rotation of soil at different stages of static loading. Static loading was applied after 400 cycles of cyclic loading. Tensioned geogrid was placed at 10 cm depth. δ is vertical deflection of the surface plate in mm.

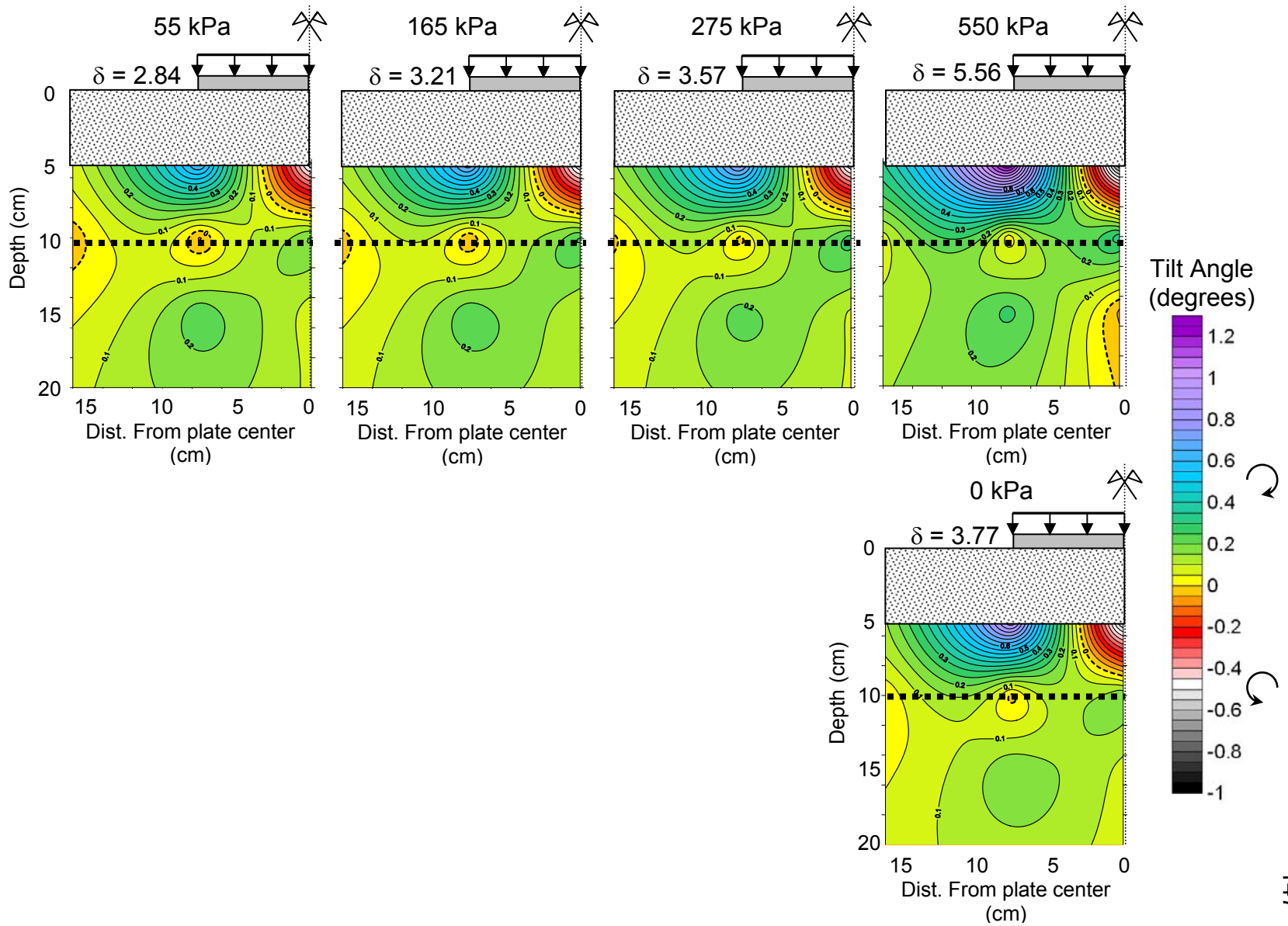


Figure 5.17. Measured rotation of soil at different stages of cyclic loading. Cyclic loading was applied for 200 cycles, removed, and applied for another 200 cycles. Tensioned geogrid was placed at 15 cm depth. δ is vertical deflection of the surface.

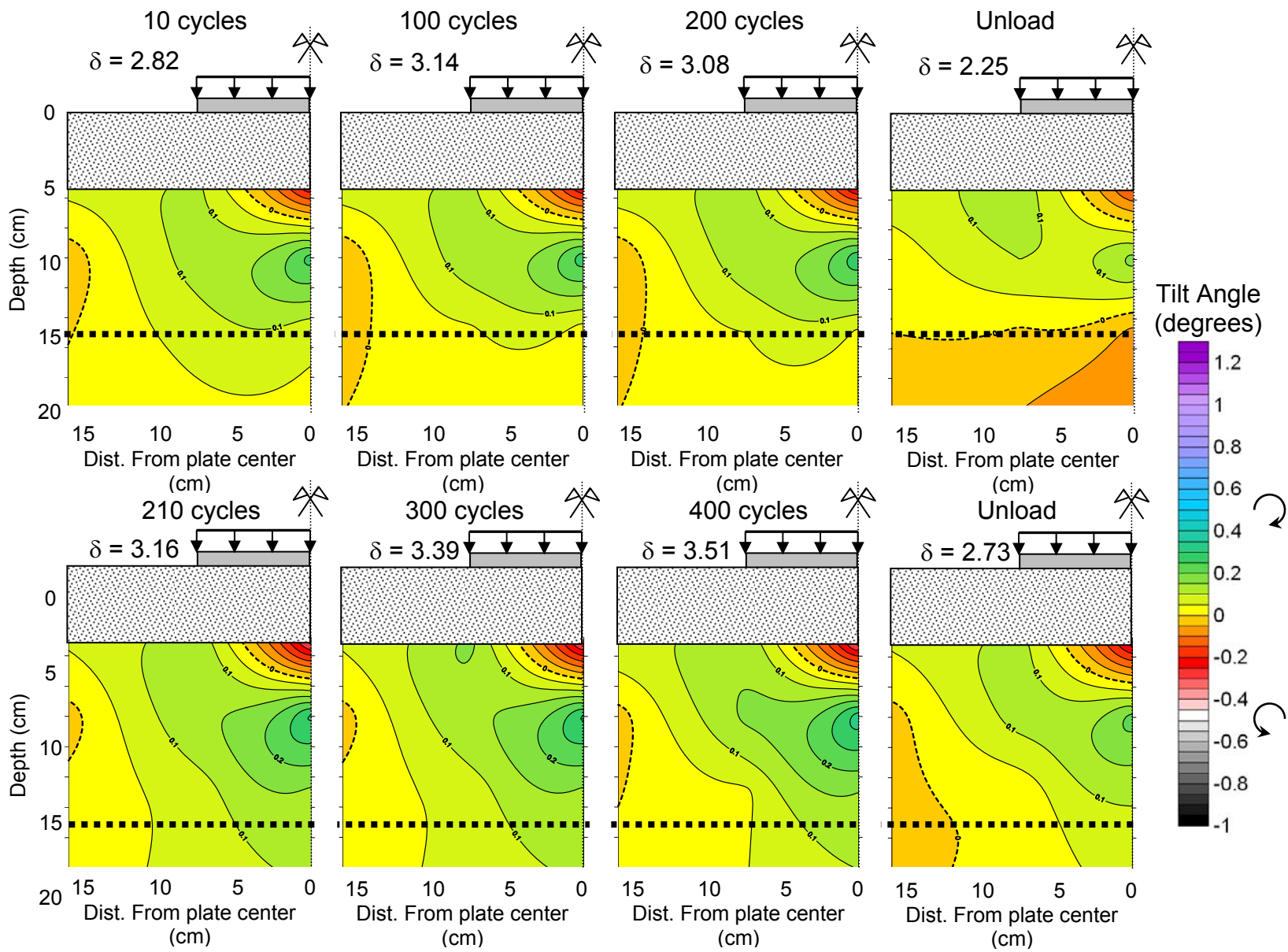
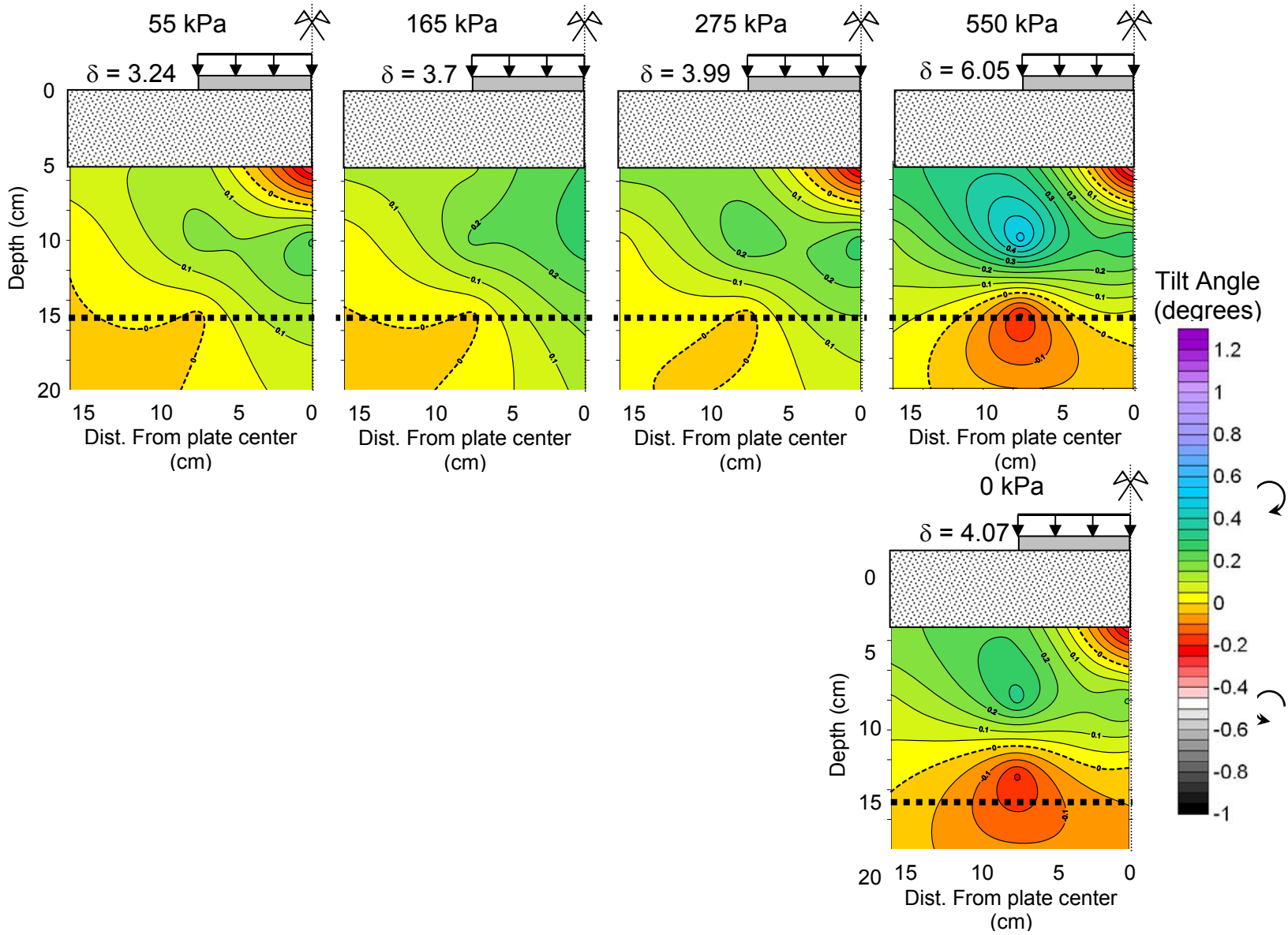


Figure 5.18. Measured rotation of soil at different stages of static loading. Static loading was applied after 400 cycles of cyclic loading. Tensioned geogrid was placed at 15 cm depth. δ is vertical deflection of the surface plate in mm.



5.4.2 Test Method Two – Measuring a Dense Array of Rotation Angles Along the Plate Edge

Results of two-dimensional tests with coarsely spaced accelerometers constrain a rough “zone of influence” of geogrid reinforcement, but a more closely spaced array of accelerometers surrounding the geogrid is necessary to delineate a well-defined “zone of influence.” The more well-defined zone can then be analyzed in more detail and compared to PLAXIS analyses and velocity results. The following discussion focuses on describing test results where accelerometers were buried between 20 and 25 mm apart directly beneath the plate edge with geogrid at 75, 100, and 150 mm depth. Rotation angle results are plotted at several surface deformations.

Each condition was modeled with PLAXIS and model parameters (physical soil parameters, geogrid stiffness, interface zone, etc.) were based on laboratory test conditions. The “interface zone” or “virtual thickness” specified in PLAXIS changes for each geogrid reinforcement position based on accelerometer information. The “interface zone” is the area in PLAXIS models where a greater amount of shear deformation occurs. The “interface zone” is the area simulated by PLAXIS where interlock between particles occurs producing more elastic deformation. The strength reduction factor (R_{int} – the ratio of interface strength to soil strength - Brinkgreve 2002) is set equal to 1 for geogrid since strengthening of the pavement system is expected and shear stresses are transferred perfectly to the geogrid reinforcement layer.

Without geogrid present, the rotation angle as a function of depth and surface deflection is shown in Figure 5.19. The rotation angle is highest at the surface and increases with applied load as is expected. Measured rotation angles are typically lower than PLAXIS analyses at shallow depth, but show similar trends as those shown in the numerical simulation. Maximum rotation angle is measured to be approximately 2° at 50 mm depth and 550 kPa applied load. Laboratory tests and PLAXIS models show a depth of influence of shearing to 180 – 200 mm (tilt angles are consistently less than $\sim 0.2^\circ$).

Some scatter in rotation angle data is due to the fact that grade 2 gravel is a well-graded material with particles ranging from fines (0.075 mm) to 19 mm diameter (approximately of the same size as the accelerometers) crushed rock. Although an effort was made to prevent contact between the large gravel particles and accelerometers, any contact between accelerometers and gravel may distort the stress field around accelerometers and alter the rotation. Despite these alterations, the rotation angles seem reasonable to the expected trends calculated from PLAXIS.

Rotation results from a geogrid placed at 75 mm depth are shown in Figure 5.20. At shallow depth, the maximum rotation angle is 4.5° at 50 mm depth, higher than in the case without geogrid present. The rotation angle is higher due to the fact that shearing is being confined to a smaller volume of soil above the geogrid. Rotation angles are lower in a 30 mm zone above and below the geogrid; however, rotation angle increases once again at 125 mm in both laboratory and PLAXIS tests. Rotation angle results indicate a deeper zone where shear strains are above $0 - 0.2^\circ$, as laboratory test and PLAXIS results extend to depths beyond 200 mm.

Rotation results with a geogrid reinforcement layer at 100 mm depth are presented in Figure 5.21. The virtual thickness extends approximately 30 mm on each side of the geogrid. The “zone of influence” below the geogrid is less than that when geogrid is positioned at 75 mm, indicating the “zone of influence” shifts depending on the shear stresses coming into contact with the reinforcement layer. At 50 mm depth, the rotation angle is 4.1° , similar, but less than the rotation angle for geogrid reinforcement at 75 mm depth. Rotation angle decreases rapidly between 50 and 70 mm and remains low before increasing at 150 mm depth. PLAXIS also predicts an increased rotation angle at 150 – 160 mm depth. Beyond 160 mm depth, the PLAXIS results agree well with laboratory tests as rotation angle decreases from 1° to 0.4° .

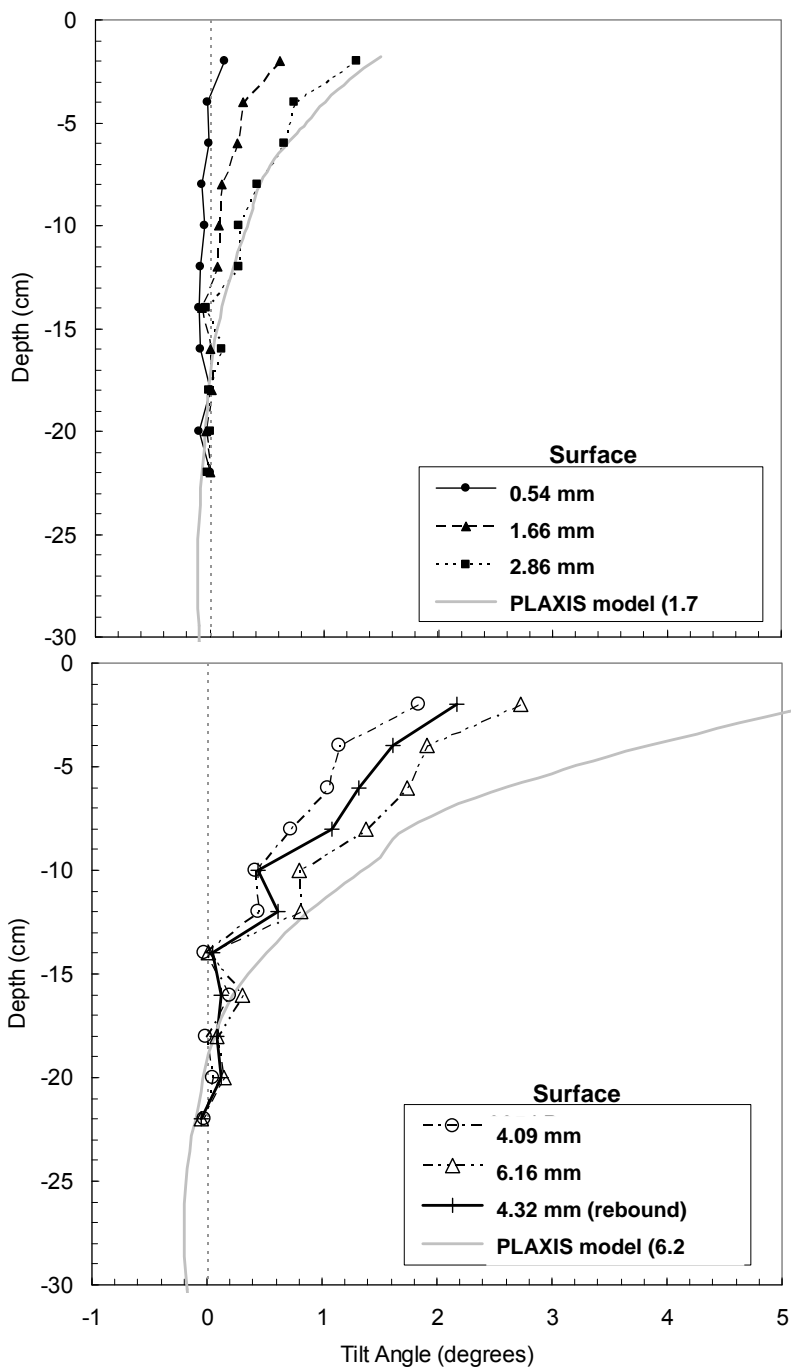


Figure 5.19. Rotation angle at the plate edge as a function of depth and applied surface load without geogrid reinforcement. PLAXIS analyses are shown at two deformation levels for comparison.

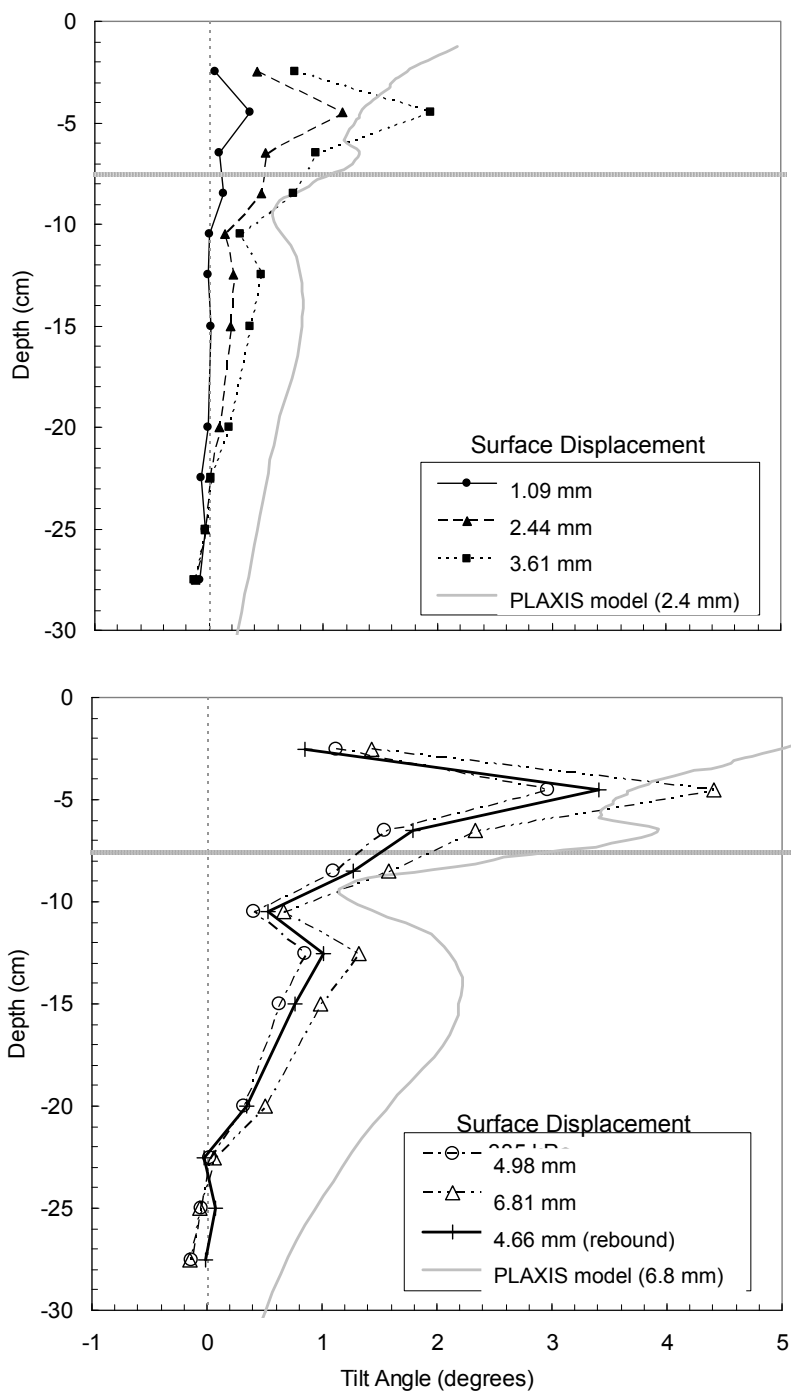


Figure 5.20. Rotation angle at the plate edge as a function of depth and applied surface load with geogrid reinforcement at 75 mm depth. PLAXIS analyses are shown at two deformation levels for comparison.

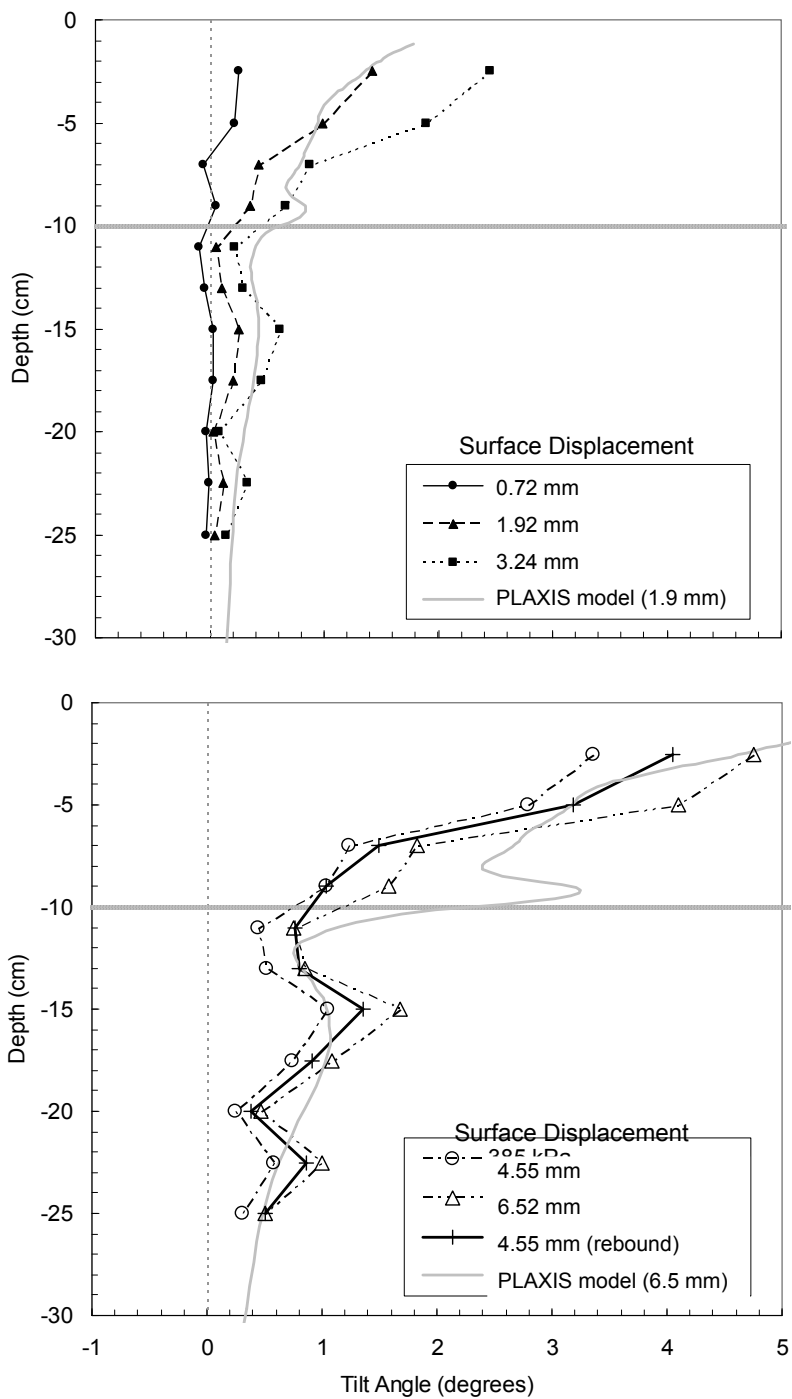


Figure 5.21. Rotation angle at the plate edge as a function of depth and applied surface load with geogrid reinforcement at 100 mm depth. PLAXIS analyses are shown at two deformation levels for comparison.

Figure 5.22 shows rotation results from tests performed with geogrid reinforcement at 150 mm depth. The virtual thicknesses used for PLAXIS analyses are 50 mm above the geogrid and 10 mm below the geogrid (10 mm is the minimum allowed in PLAXIS) based on measured laboratory results. The maximum rotation is 2.86° , similar to the deflection without geogrid present. However, in contrast to the rotation angles measured without reinforcement, a geogrid incorporated at a depth of 150 mm confines rotation nearer the surface and little deformation occurs in a 50 mm zone above geogrid. PLAXIS predicts a leveling of rotation angles between 100 and 140 mm depth, but does not model the rotations to be zero above the geogrid. Beyond the depth of the geogrid, both PLAXIS and laboratory tests show rotation angle decreasing from a maximum of 1 to 0° at about 220 mm depth.

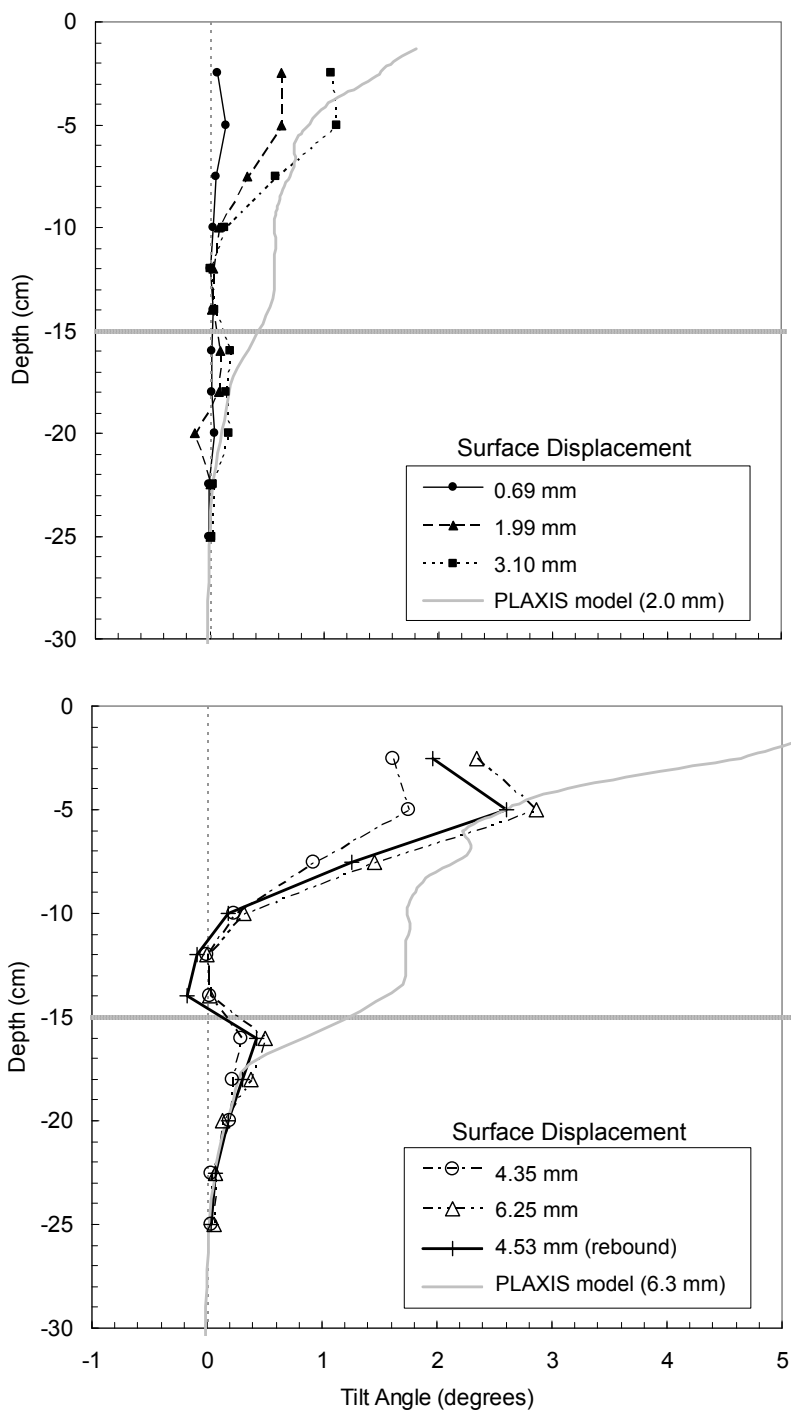


Figure 5.22. Rotation angle at the plate edge as a function of depth and applied surface load with geogrid reinforcement at 150 mm depth. PLAXIS analyses are shown at two deformation levels for comparison.

5.4.3 *Discussion of Possible Mechanisms of Geogrid Reinforcement*

5.4.3.1 Effect of Tension on Reinforcement

To determine the influence of tension on geogrid reinforcement, a test was performed on grade 2 gravel with non-tensioned geogrid at 75 mm depth. Accelerometers were secured along the plate edge and static loads were applied to determine the influence of the non-tensioned geogrid on soil shearing. Figure 5.23 shows tilt angle results with and without geogrid. From the results of this test, non-tensioned geogrid results are most comparable to results when no geogrid is incorporated in the pavement system. Therefore, it appears that without some engagement of the geogrid with the material, little change in shearing occurs.

5.4.3.2 Measurement of Rotation Angle on Portage sand

The purpose of measuring rotation of Portage sand with the same stiff geogrid during testing of grade 2 gravel is to determine whether the reinforcing effects on grade 2 gravel are due to an “interlocking” mechanism. Portage sand is not expected to be greatly influenced by the presence of a geogrid reinforcement layer since the apertures of the geogrid are about 70 times the D_{50} particle size. Instead, rotation is not expected to be influenced by reinforcement.

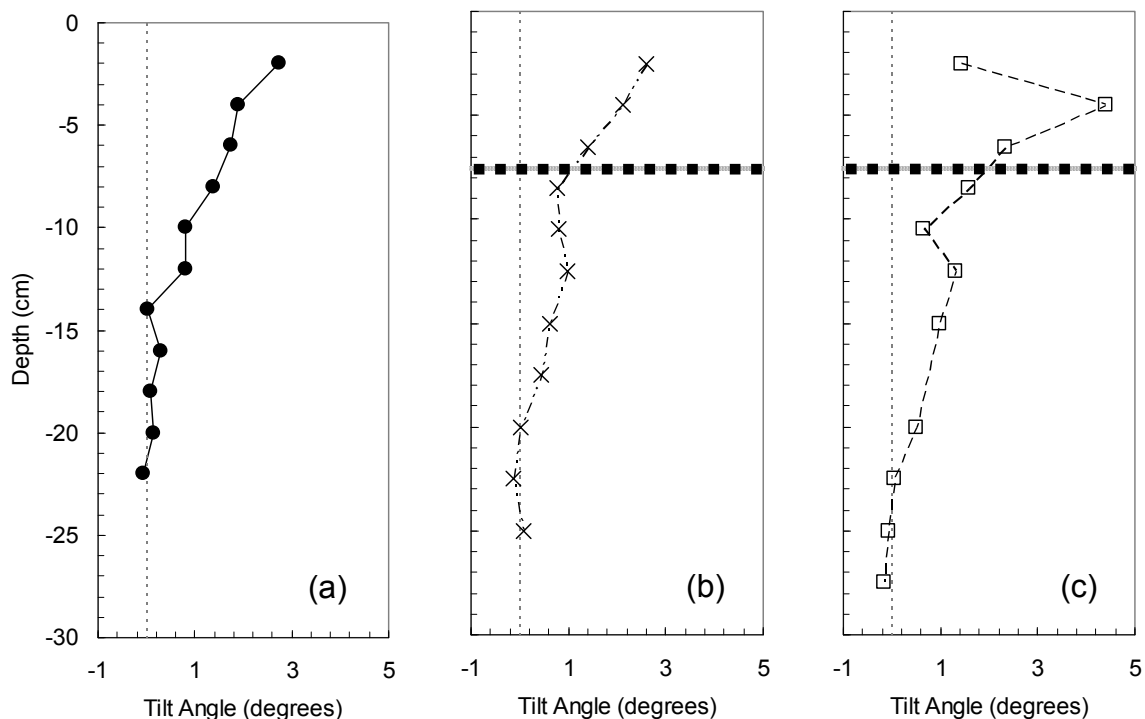


Figure 5.23. Measured tilt angles in grade 2 gravel and at 550 kPa applied load and geogrid positions: (a) no geogrid, (b) non-tensioned geogrid at 75 mm depth, (c) tensioned geogrid at 75 mm depth.

Four tests were completed with Portage sand with reinforcement positioned at the same depths as the grade 2 gravel tests (75, 100, and 150 mm). Summary rotation angle test results on Portage sand are shown for each geogrid depth at maximum surface displacements between 6.3 and 7.3 mm (Figure 5.24).

All rotation angle tests with reinforcement on Portage sand show similar behavior. Rotation angle increases rapidly near the surface and a maximum rotation angle at 50 mm depth is typically between 2 and 3°. Rotation angles diminish quickly between 20 and 100 mm depth and the depth of influence of the applied load on shearing of the material extends to 140 mm, shallower than the depth of influence for grade 2 gravel and closer to PLAXIS results. The decrease in rotation angle with

increasing depth agrees well with results from PLAXIS analysis on Portage sand and confirmed that the geogrid does not influence the soil response because the sand grains do not “engage” the geogrid.

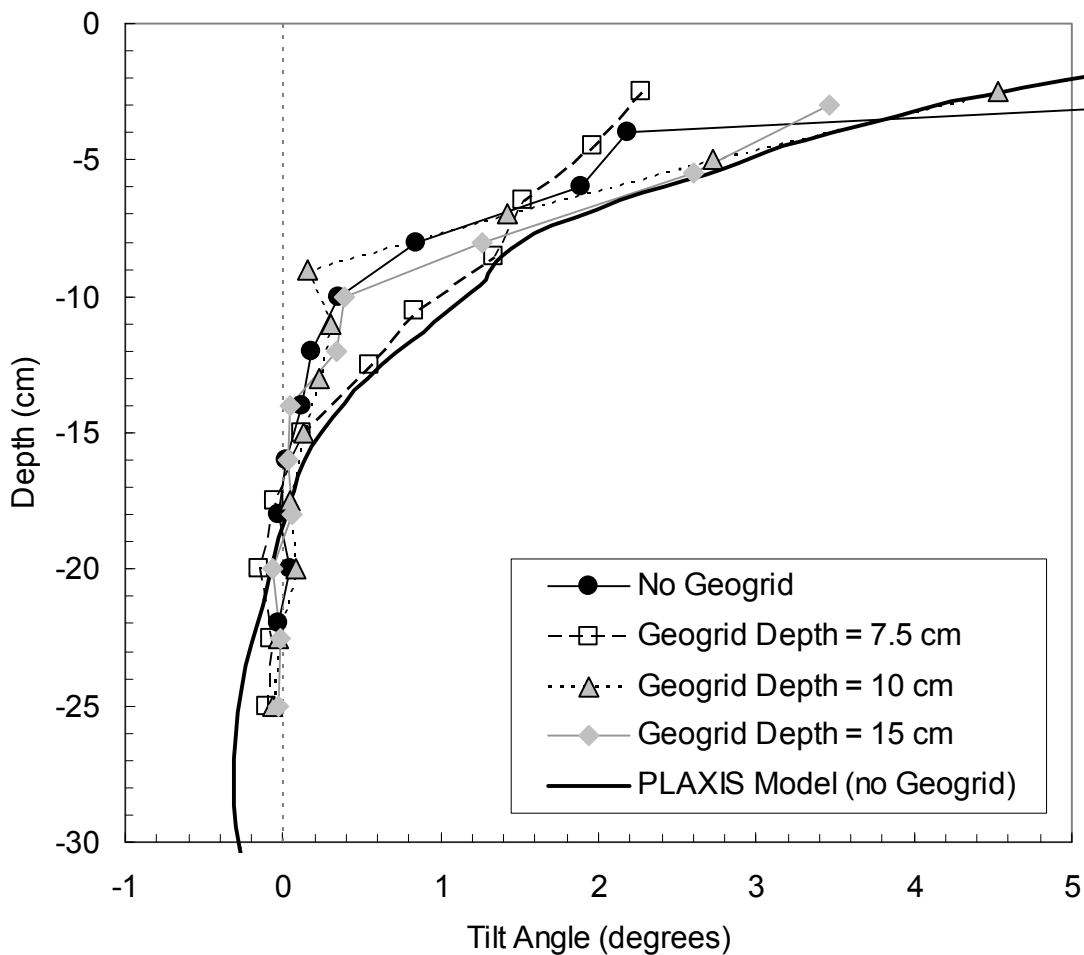


Figure 5.24. Rotation angles at the plate edge and for maximum surface displacement (6.3 - 7.3 mm) in Portage sand.

5.5 SUMMARY AND RECOMMENDATIONS OF GRADE 2 GRAVEL TESTS WITH STIFF GEOGRID

Surface deflections, P-wave velocity, and rotation test results are summarized below for a circularly loaded plate with a diameter of 150 mm:

- Cyclic load tests show that a shallower geogrid will minimize both plastic and elastic surface deflections.
- P-wave velocity results indicated an increase in stiffness above the geogrid and decreased stiffness below the geogrid. The change in stiffness due to the presence of a geogrid varies between 1.35 and 2.66 times the change in stiffness that can be attributed to the change in effective stress.
- Rotation is greatest at the plate edge and is highest at shallow depths when geogrid is secured at 75 mm and 100 mm.
- Laboratory-measured results show an effective normalized depth of influence (depth of influence divided by plate diameter) of loading of 1.2 without reinforcement and 1.3 – 1.7 with reinforcement, agreeing closely with PLAXIS models. The normalized depth of influence remains low (<1.0) when loading plate deflections are less than 3 – 4 mm and do not change substantially regardless of surface displacements when they exceed 4 mm.
- Stiff geogrid arrests material rotation both above and below the geogrid, with much of the confinement occurring beneath the geogrid when secured at shallower depth (75 and 100 mm). Greater confinement occurs above the more deeply secured geogrid (150 mm, Figure 5.25 and Table 5.2). Figure 5.25 shows the difference between rotation angles measured with and without reinforcement

at each depth and the effective “zone of influence” in each geogrid-reinforced condition:

$$\Delta\theta = \theta_{re\ inf\ orced} - \theta_{unre\ inf\ orced} \quad (5.2)$$

- Measured rotations agree well with PLAXIS modeling results in both magnitude and expected rotation behavior; however, PLAXIS typically limits rotation to a smaller area around the geogrid than laboratory test results. This disagreement may be related to the influence of the accelerometers used for measuring rotations and indicate a discrete element model may be more appropriate for this type of analysis (see McDowell et al. 2006).

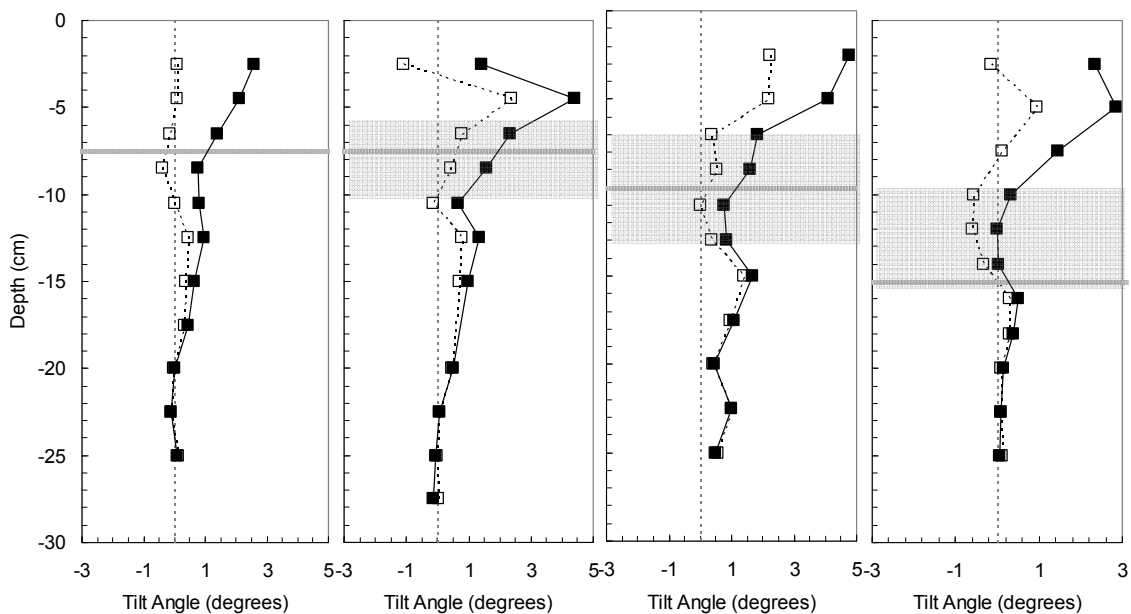


Figure 5.25. “Zone of influence” from rotation angle test results: (a) non-tensioned geogrid at 75 mm depth, (b) geogrid at 75 mm depth, (c) geogrid at 100 mm depth, and (d) geogrid at 150 mm depth. The solid symbols represent the raw rotation angles for each reinforcement test and the open symbols represent the difference between the rotation angles with and without reinforcement. The shaded area is the “zone of influence” of each reinforcement case.

Table 5.2. Virtual thicknesses or "zone of influence" based on laboratory tests with stiff geogrid and grade 2 gravel.

Geogrid Depth	Upper interface virtual thickness	Lower interface virtual thickness	Total "zone of influence"
mm	mm	mm	mm
75	15	30	45
100	30	30	60
150	50	10	60

6 SUPPLEMENTAL ANALYSES THE EFFECT OF GEOGRID ON MODULUS AND ZONE OF INFLUENCE

6.1 SUMMARY OF TESTS COMPLETED TO DETERMINE INTERACTION BETWEEN GEOGRID AND AGGREGATE MATERIAL

Table 6.1 shows the tests completed to evaluate the interaction between base course and geogrid and the most important conclusions drawn from each of the tests. Five soils, three geogrids, and three depths of geogrid reinforcement were used in the majority of tests. Tests typically involved measuring either (1) P-wave velocities for modulus calculations, or (2) particle rotations for the determination of the zone of influence. A 150 mm diameter plate was used to apply loads to the specimens simulating wheel pressures. The knitted geogrid and one of the extruded geogrids (Extruded - L) had a flexural stiffness of 250,000 mg-cm, while the other extruded geogrid (Extruded - H) had a flexural stiffness of 750,000 mg-cm.

Table 6.1. Geogrid/aggregate interaction tests performed.

SOIL	GEOGRID	GEOGRID DEPTH (mm)	PARAMETERS MONITORED	REMARKS	
Portage sand ($D_{50}/\text{aperture} = 0.014$)	None	-	-P-wave velocity -Rotation	-Obtain control values for rotation and velocity with applied stresses	
	Knitted	110	-P-wave velocity	-P-wave velocity decreased below geogrid reinforcement	
		220			
	Extruded – L	None	-	-Rotation (plate edge)	-All rotation results on different depth geogrids show similar behavior as the $D_{50}/\text{aperture}$ ratio is too small to induce interlocking
			75		
			100		
Grade 2 gravel ($D_{50}/\text{aperture} = 0.08$)	None	-	-Rotation (2D array)	-Rotation minimized in the zone surrounding the geogrid, but the zone is not well-defined and appears to extend up to 50 mm on either side of geogrid	
	Knitted	75			
		100			
	Knitted	None	-	-P-wave velocity	-P-wave velocity results inconclusive as velocities vary widely between tests -P-wave velocities do not show a consistent trend of decreasing velocity below the geogrid as Portage sand tests showed
			75		
			100		
		150			

*If not specified, geogrids are pre-tensioned to a force per unit length of 0.26 kN/m.

Table 6.1. Geogrid/aggregate interaction tests performed (continued).

SOIL	GEOGRID	GEOGRID DEPTH (mm)	PARAMETERS MONITORED	REMARKS
Grade 2 gravel ($D_{50}/\text{aperture} = 0.08$)	None	-	-Rotation (plate edge)	-Well-defined "zone of influence" calculated for each depth of reinforcement (typically 30 mm on each side of geogrid, but up to 50 mm in thickness) -"Zone of influence" changes depending on depth of reinforcement
	Extruded – H	75		
		100		
		150		
	None	-	-P-wave velocity	-P-wave velocity decreases across geogrid indicating change in modulus across reinforcement (1.4x for 75 and 150 mm depth geogrid, 2.6x for 100 mm depth geogrid)
	Extruded – H	75		
		100		
	None	-	-Elastic surface deformation -Plastic surface deformation	-Elastic and plastic deflections lower (19% and 35%, respectively) with shallow (75 mm) depth geogrid as compared to 150 mm depth geogrid -Elastic and plastic deformations with 150 mm deep geogrid close to deformations without geogrid present (providing little benefit)
	Extruded – H	75		
		100		
	Extruded - H (non-tensioned*)	75	-Rotation (plate edge)	-Without tension to induce interlocking between particles and geogrid, rotation results agree most closely with grade 2 gravel test without reinforcement

*If not specified, geogrids are pre-tensioned to a force per unit length of 0.26 kN/m.

Table 6.1. Geogrid/aggregate interaction tests performed (continued).

SOIL	GEOGRID	GEOGRID DEPTH (mm)	PARAMETERS MONITORED	REMARKS	
Pit run gravel ($D_{50}/\text{aperature} = 0.066$)	None	-	-P-wave velocity	-Little useful information because of distribution of large particles (no consistent decrease in velocity across geogrid)	
	Extruded – H	75			
		100			
		150			
	None	-	-Rotation (plate edge)	-Similar rotations as grade 2 gravel -Decrease in rotation near geogrid; “zone of influence” is approximately 30 – 40 mm (comparable to grade 2 gravel results)	
		Extruded – H			75
					100
150					
Breaker run ($D_{50}/\text{aperature} = 1.45$)	Extruded – H	100	-P-wave velocity -Rotation (plate edge)	-P-wave velocities vary widely regardless of depth and applied surface load (no helpful information near geogrid) -Rotations opposite from grade 2 gravel and pit run gravel test results; rotation increases near geogrid -Grain contacts accelerometer at few locations producing unreliable results	
Modified Grade 2 gravel [†] ($D_{50}/\text{aperature} = 0.12$)	Extruded - L (BX1100)	100	-P-wave velocity -Rotation (plate edge)	-P-wave velocities decreased around geogrid; no substantial decrease in velocity around geogrid (opposite stiff geogrid results) -Rotation results show “zone of influence” 30 mm above geogrid, but no visible effects below	

*If not specified, geogrids are pre-tensioned to a force per unit length of 0.26 kN/m.

[†]Based on grain size distribution of base course material given by Kwon et al. (2008).

6.2 FIELD-SCALE COMPARISON I (KWON ET AL. 2008)

Reinforced sections were compared with field test results performed by Kwon et al. (2008). The summary resilient modulus of the base course material used by Kwon et al. was 124 MPa. A base course aggregate was manufactured at the University of Wisconsin – Madison by modifying grade 2 gravel to better match the grain size distribution given by Kwon et al. (Figure 6.1) and a series of new tests were performed for the purpose of field comparison. P-wave velocities were measured in a 100 mm zone below the load plate to obtain a relationship between bulk stress and modulus of the manufactured material (Figure 6.2). P-wave velocities indicate that the equivalent resilient modulus after corrections for stress, void ratio, and strain level is 159 MPa (28 % greater than resilient modulus measured by Kwon et al.). Although the modulus is greater for the soil tested at the University of Wisconsin – Madison, the values are comparable to one another considering that the resilient modulus variability is substantial.

Laboratory geogrid reinforced sections from this research are compared to geogrid-reinforced sections from Kwon et al. (2008). Laboratory and field tests used both the lower-modulus and one higher-modulus geogrid in a state of tension. The geogrids were anchored in the field tests with bolt and washer sets, while the geogrids were tensioned in the laboratory tests by pulling them around metal supports secured in the large box.

Field-scale results (Kwon et al. 2008) indicate that the modulus increases by approximately 30 – 40 % in the area directly surrounding geogrid reinforcement. This

increase in modulus is caused by the residual stresses assigned to a zone that is either (1) between 25 – 76 mm above reinforcement or (2) a 100 mm zone on both sides of the geogrid as proposed by McDowell (2006) based on DEM experiments.

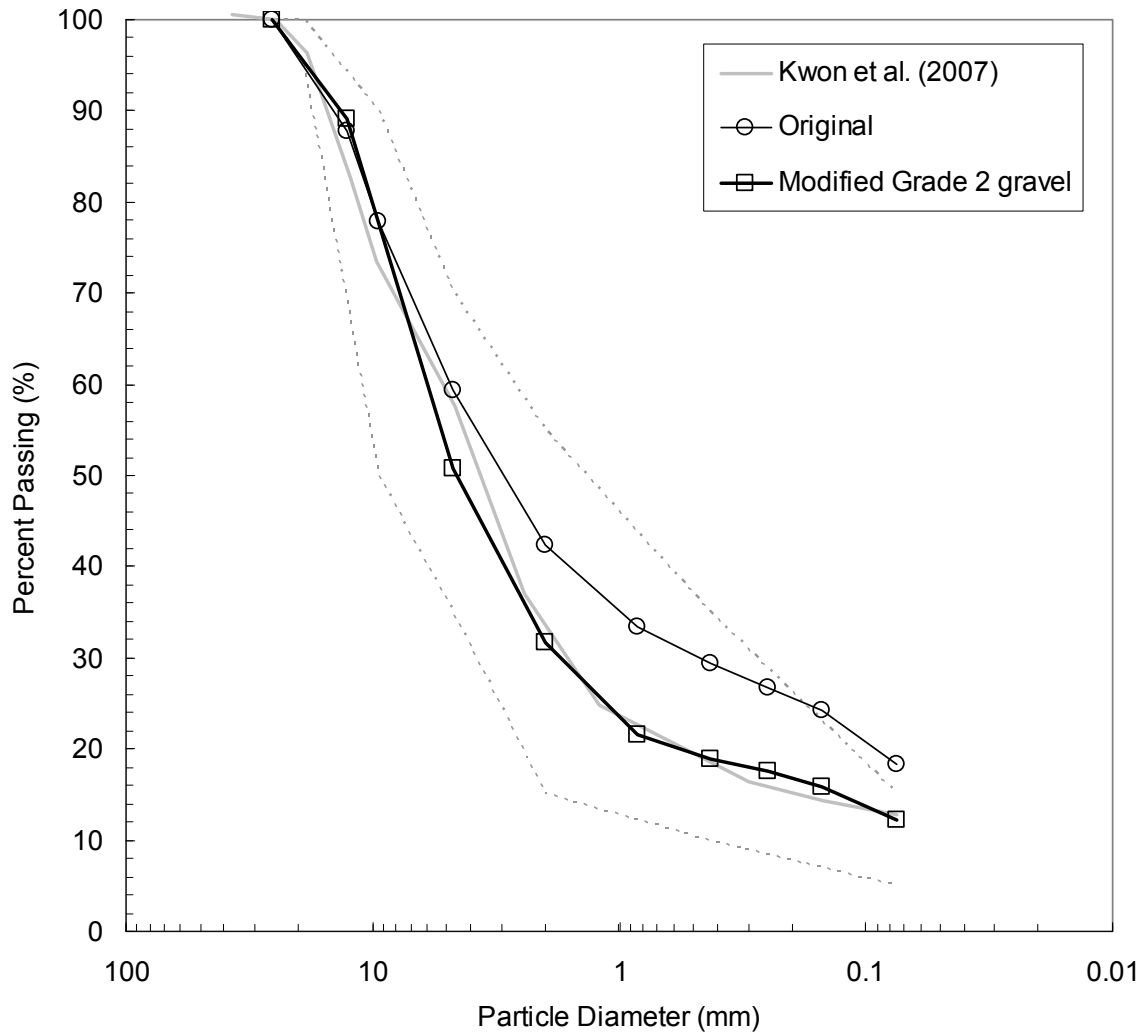


Figure 6.1. Grain size distribution of aggregate used by Kwon et al. (2008) and the aggregate manufactured at the University of Wisconsin – Madison (modified from grade 2 gravel).

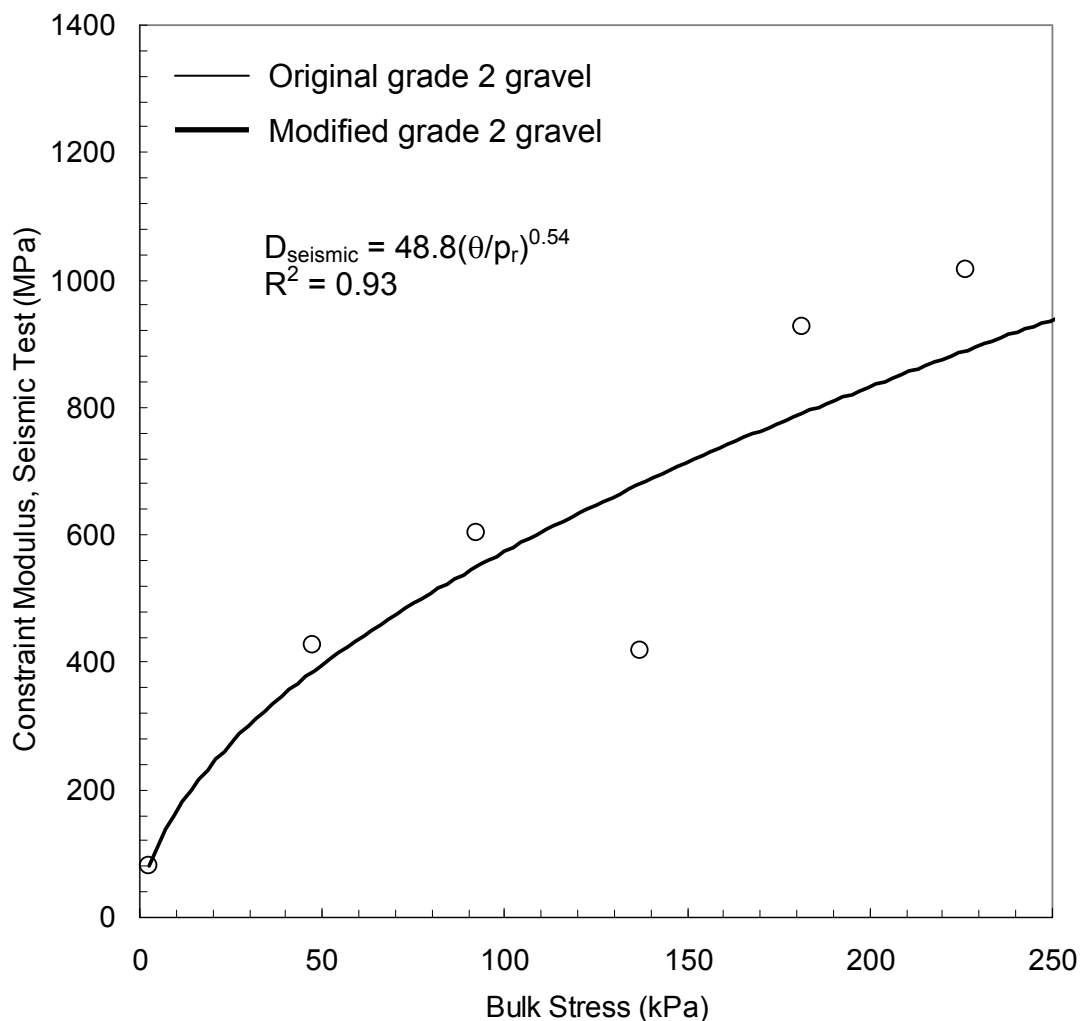


Figure 6.2. Constraint modulus of seismic test on modified grade 2 gravel (based on grain size distribution from Kwon et al. 2008).

In laboratory experiments, the modulus increase factor ranges between 1.4 and 2.6 for the zone above the geogrid. The increase in modulus is slightly higher in the case of laboratory tests, but a smaller area of aggregate material seems to be affected by reinforcement (<30 – 50 mm). Therefore, the laboratory/field test results indicate that a smaller modulus improvement factor may be applied to a larger area

(100 mm) or a higher modulus improvement factor may be able to be applied to a smaller area (< 50 mm) resulting in essentially the same outcome. A modulus reinforcement factor of between 1.4 and 2.0 for the 30 – 40 mm zone above the geogrid reinforcement layer seems like the most reasonable compromise between field and laboratory analyses.

Table 6.2 presents further analysis and comparison of the reinforcement of the base course material directly above reinforcement. Kwon et al. (2008) noticed a decrease in the vertical pressure at the top of the subgrade when the zone above the reinforcement was assigned a higher modulus. The decrease in pressure was 8%. A KENLAYER model was produced and calibrated given parameters from tests performed on an unreinforced section from Kwon's studies. A modulus improvement factor of 2.5 was assigned to the 30 mm zone above the geogrid based on laboratory tests performed in this research to examine the effects of reinforcement on the KENLAYER model to be compared with results from Kwon et al. (2008). The decrease in pressure using the KENLAYER model is 5% when the modulus in a 30 mm zone above the geogrid was improved by a factor of 2.5. Despite this large increase in modulus, the vertical pressure remains slightly less than that expected by Kwon at the top of the subgrade in the field. A more conservative approach seems to improve the modulus in a 30 mm zone above the geogrid by a factor of 1.4 % as described above. This improvement factor is more comparable between laboratory tests and field-scale tests.

Table 6.2. Comparison between KENLAYER and field results from Kwon et al. (2008).

Field Test	Vert. Pressure @ top of subgrade kPa (Kwon 2007)	Vert. Pressure @ top of subgrade kPa (KENLAYER)	k_1 (MPa)
Control	45.0	45.4	6.7
Reinforced Section (30 mm influence zone, 2.5 times modulus)	41.4	43.2	6.7 (16.8 in 30 mm zone above reinforcement)

Also, to calibrate the model with Kwon's study, the k_1 of the base course had to be increased by 176% to provide similar vertical stress distributions. The increase of k_1 may be due to the fact that Kwon et al. (2008) used a combination of vertical and horizontal resilient moduli to represent the stiffness of the system. For example, at bulk stress of 208 kPa, the vertical modulus is 133 MPa and the horizontal modulus is 18 MPa based on k_1 (kPa), k_2 , and k_3 for vertical modulus calculations and k_4 (kPa), k_5 , and k_6 for horizontal modulus calculations:

$$M_{r \text{ vertical}} = k_1 \theta^{k_2} \sigma_d^{k_3}$$

$$M_{r \text{ horizontal}} = k_4 \theta^{k_5} \sigma_d^{k_6}$$

where θ is bulk stress and σ_d is deviator stress. The isotropic modulus at 208 is 55 MPa with the measured k_1 . When k_1 is increasing 176% to 6.7, the resulting isotropic modulus becomes 97 MPa and gives comparable vertical stress on the subgrade.

6.3 FIELD SCALE COMPARISON II (KIM 2003)

P-wave velocity results in laboratory tests performed in this research with geogrid at 75, 100, and 150 mm depth show that the stiffness reinforcement factor around the geogrid appears to be 1.35, 2.66, and 1.42 greater than soil without geogrid. These values are representative of the modulus reinforcement factors over the entire base course soil thickness calculated by Kim (2003). Kim (2003) calculated an overall modulus reinforcement factor of 2.0 for grade 2 gravel in a field application at STH 60, agreeing well with results of this research; however the zone over which to apply this factor may depend on the thickness of engagement of the geogrid and thickness of the base course layer. Kim (2003) assumed an application of his reinforcement factor over the entire base course, but this research seems to indicate the factor may be better applied over a smaller “zone of influence” directly above the geogrid in a 30 to 50 mm zone.

6.4 MODIFIED GRADE 2 GRAVEL TEST WITH LOWER-MODULUS EXTRUDED GEOGRID

A test was performed using a lower-modulus geogrid with a flexural stiffness of 250,000 mg-cm that was used in the tests by Kwon et al. (2008). The lower-modulus geogrid has one-third the flexural stiffness of the higher-modulus geogrid used in the majority of grade 2 gravel laboratory tests (flexural stiffness of 750,000 mg-cm).

Figure 6.3 shows the aggregate rotations and P-wave velocity distribution results for the lower-modulus geogrid incorporated at a depth of 100 mm. Rotation

results show a “zone of influence” that extends in a similar distance (i.e., 30 mm - Figure 5.21) as the zone that was above the stiff reinforcement. However, when the lower-modulus geogrid is used, the “zone of influence” below the geogrid is indistinguishable. Instead, the rotation angles tend to decrease at a constant rate.

P-wave velocities are highest near the surface with a large applied surface load and decrease rapidly near the geogrid. The P-wave velocity remains constant near the geogrid and no decrease in velocity is seen across the geogrid as was seen when the higher-modulus geogrid was incorporated in the system (see Figure 5.10). Therefore, no modulus improvement is evident from P-wave velocity analyses around the geogrid.

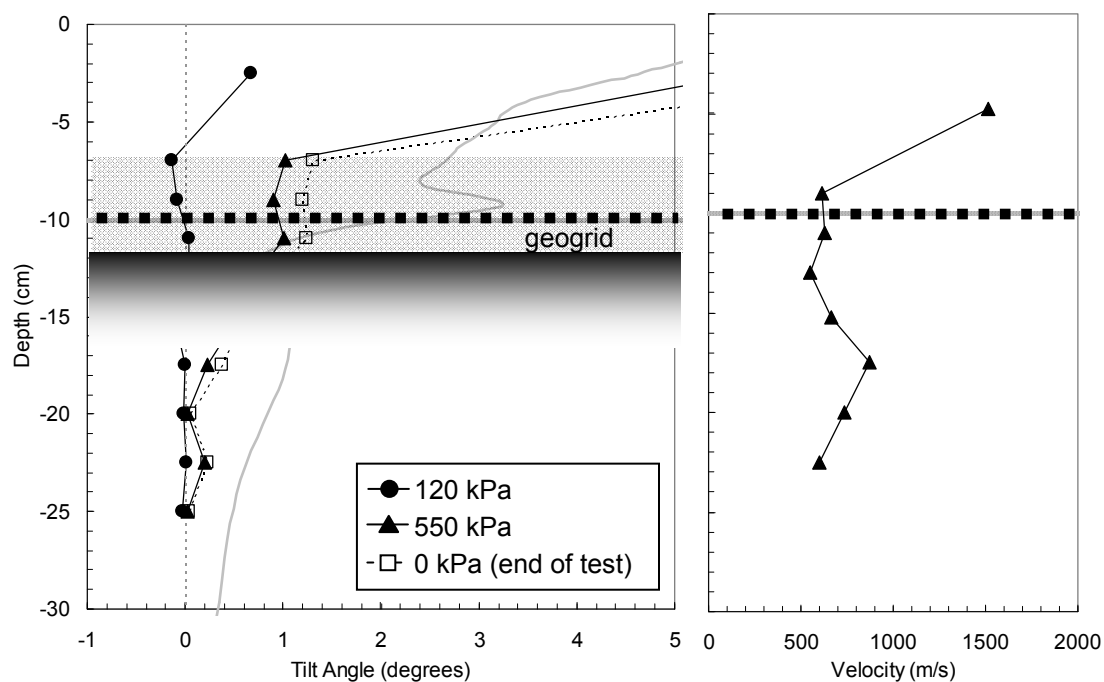


Figure 6.3. “Zone of influence” (grey area) of lower-modulus geogrid at 100 mm depth and two plate loads on modified grade 2 gravel. PLAXIS results show the expected rotation at the larger load. Also shown is the velocity distribution for the corresponding rotation measurements.

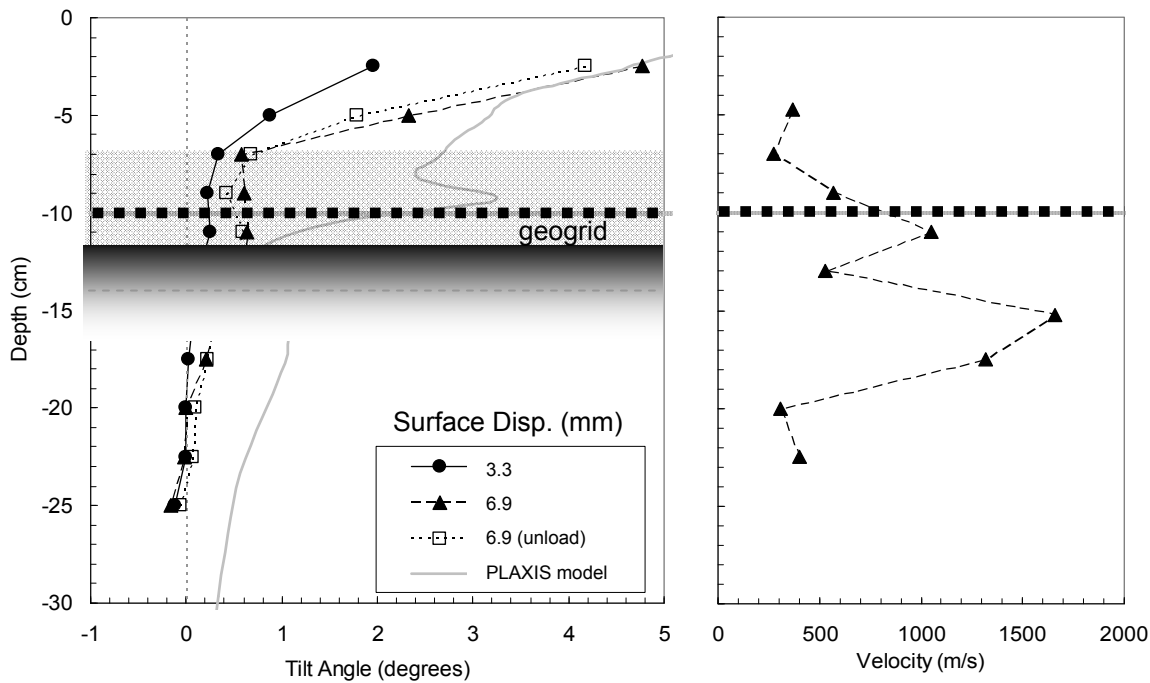
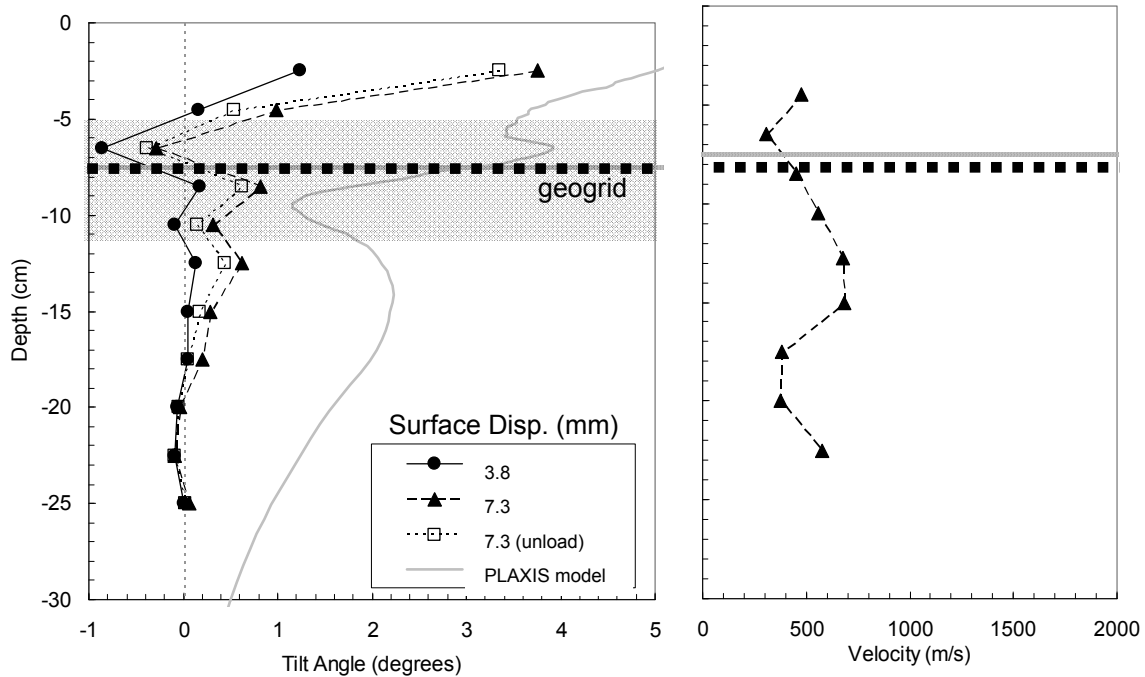
6.5 PIT RUN SAND AND GRAVEL GEOGRID TESTS

Rotation and velocity results from tests on pit run gravel reinforced with the higher-modulus geogrid (Tenax MS 724) at 75, 100, and 150 mm are shown in Figure 6.4 for surface loads corresponding to 120 – 140 kPa (for 3.5 mm surface displacement) and 240 kPa (for 6.5 mm surface displacement). A 120 kPa load corresponds to the stress expected on the base course when an asphalt surface layer has been applied and the 240 kPa was the maximum applied load that could be applied without a bearing capacity failure. The “zone of influence” of the geogrid on the surrounding particles is outlined in grey. The PLAXIS simulation results are also shown for comparison. In general, these results show that rotations are less for the pit run gravel than for the grade 2 gravel (see Figure 5.20, Figure 5.21, and Figure 5.22). However, the “zone of influence” remains between 30 and 50 mm on both sides of the geogrid similar to grade 2 gravel despite the large particles in the pit run gravel. The mean particle size ($D_{50} = 2.5$ mm) of the pit run gravel appears to be small enough to engage the geogrid (aperture of 38 mm) and cause an interlock between the reinforcement and aggregate. This interlocking decreases the particle rotation near the reinforcement.

In the case of the 75 mm and 100 mm depth geogrids, the “zone of influence” extends approximately 30 – 40 mm on either side of the geogrid. Less material seems to be confined in the zone above the 150 mm deep geogrid and the “zone of

influence” below the geogrid is difficult to distinguish in the case of the 100 and 150 mm deep geogrid locations.

P-wave velocity results seem to provide little information as to the confinement and increased stiffness of the system. P-wave velocity decreases directly above the reinforcement and increases on the deeper side of reinforcement. P-wave velocity measurements show increased velocity in a 20 mm zone around the geogrid and a decreased velocity in a 40 mm zone below a 100 mm deep geogrid. The P-wave velocities below the 150 mm deep geogrid reach a maximum at a shallow depth, decreasing at a constant rate to a depth 20 mm below the geogrid, indicating about reinforcing effect. The presence of large particles in the pit run gravel specimens impacts the propagation of elastic waves through the medium. P-wave velocity results fluctuate more rapidly than grade 2 gravel velocity results, an indication that elastic waves are impacted by the presence of large particles. Large particles could also be occupying a higher portion of the space between accelerometers, producing unreasonably high velocities (> 1000 m/s) for subsurface soils subjected to external plate loads of less than 300 kPa.



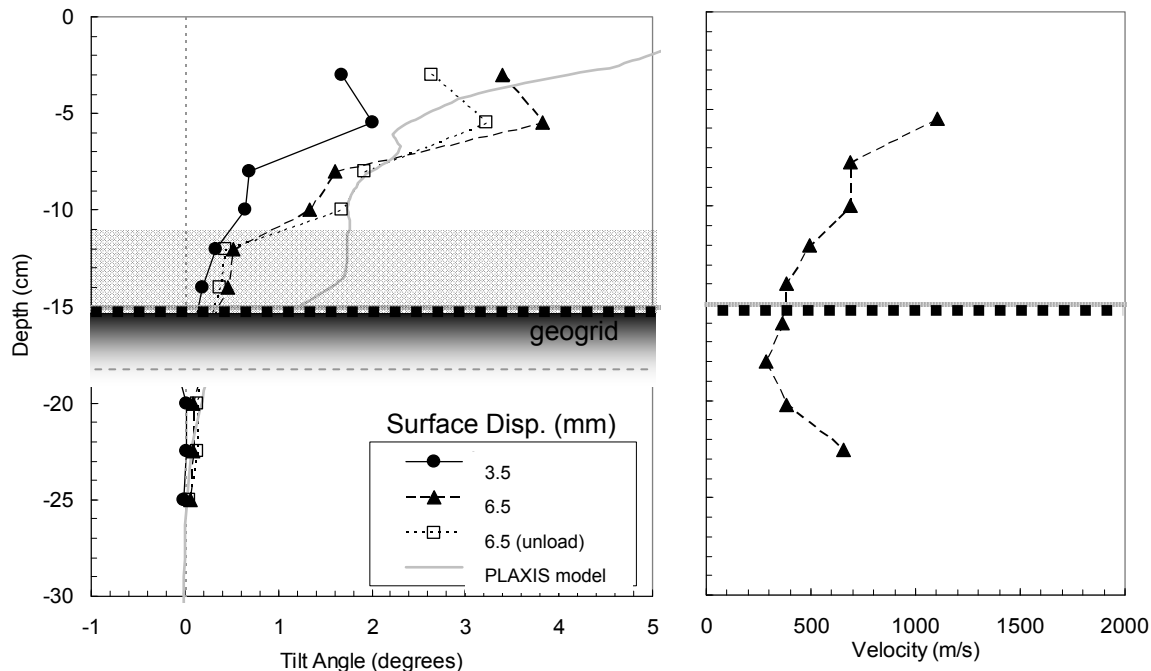


Figure 6.4. “Zone of influence” (grey area) of the higher-modulus geogrid at three depths and two surface displacements on pit run sand and gravel. PLAXIS results show the expected rotation at the larger surface displacement (~7 mm). Also shown is the velocity distribution for the corresponding rotation measurements.

6.6 BREAKER RUN TESTS

As a means of comparison, P-wave velocity and rotation tests were performed on breaker run samples with the higher-modulus geogrid (Tenax MS 724) secured at a depth of 100 mm under a 150 mm diameter loading plate. Loads between 0 and 550 kPa were applied to measure particle rotation and velocity of P-waves. With a mean particle size of about 55 mm, the geogrid and aggregate are not expected to interlock effectively with one another. Koerner (1998) suggested that the geogrid apertures be about 3.5 times greater than the mean particle size, but with breaker run, the geogrid aperture (38 mm) is only about 0.7 times that of the mean particle size.

Figure 6.5 shows rotation and velocity results from tests on breaker run. The rotation results behave oppositely from the rotation results on both grade 2 gravel and pit run sand and gravel (Figure 5.20, Figure 5.21, Figure 5.22, and Figure 6.4 respectively). The rotation angle is minimized near the surface and comes to a maximum near the geogrid. The increased rotation near the geogrid is an unexpected result of geogrid reinforcement and is most likely a result of large particles trying to re-arrange with the applied load. The rotations observed in the breaker run tests are unreliable since grains and accelerometers could not be efficiently compacted together. The particle-accelerometer contacts have a large influence on rotations and may change drastically depending on how many large particles from the breaker run are in contact with each accelerometer as depicted in Figure 6.6.

P-wave velocity results are also ambiguous for the geogrid improvement measurements for breaker run although it provides a clear assessment of the unreinforced breaker run. The P-wave velocity fluctuates between 250 and 650 m/s regardless of depth and applied load, indicating that grain contacts from the beginning of the experiment are most important to the velocities instead of applied load and geogrid reinforcement. The expected drop in velocity across the geogrid does not occur and little information is attained by the velocity-depth profile given for breaker run.

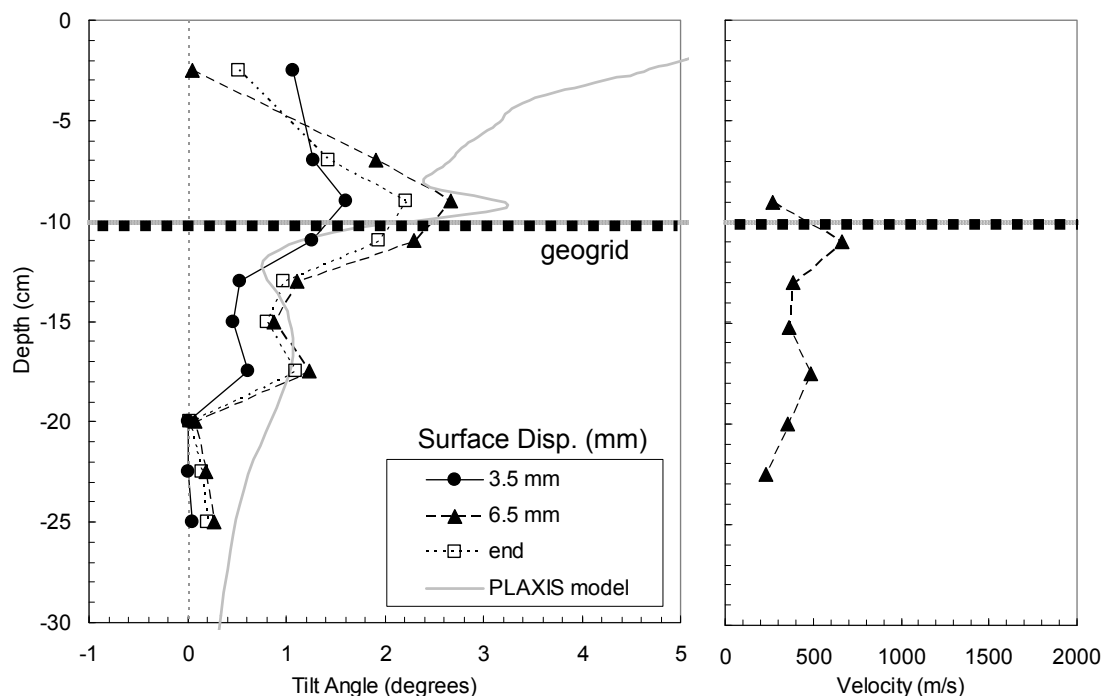


Figure 6.5. Rotation and P-wave velocity results from Breaker run tests. PLAXIS results show the expected rotation at the larger surface displacement (~7 mm). Also shown is the P-wave velocity distribution for the corresponding rotation measurements.

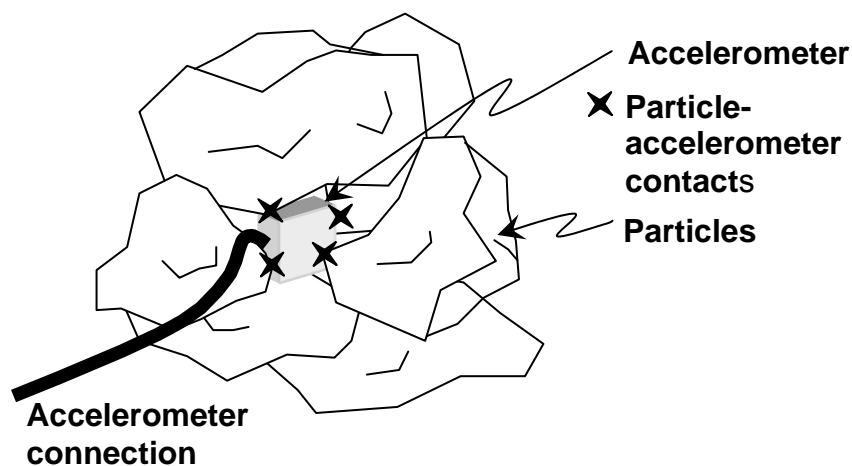


Figure 6.6. Particle-accelerometer interaction in breaker run tests. The accelerometer may only contact a few particles, providing questionable results of rotation and P-wave velocity.

6.7 SUMMARY OF FIELD AND LABORATORY TESTS AND EFFECT OF FLEXURAL STIFFNESS

Two field-scale studies were compared to geogrid reinforcement laboratory tests performed in this research project. Tests performed by Kwon et al. (2008) show a modulus improvement factor of 1.3 to 1.4 in a distance less than 100 mm on both sides of the geogrid reinforcement. Tests performed by Kim (2003) show a modulus reinforcement factor of 2.0 for the entire base course layer. Based on a large-scale model experiment, Edil et al. (2007) back-calculated a modulus improvement factor of 1.7 to 2.6 for a geogrid reinforced sublayer with an assumed zone of influence of 100 mm. Results from the laboratory tests with the higher-modulus geogrid (similar to Kwon's and Kim's) reported herein follow the field and large-scale laboratory model experiments closely; the modulus reinforcement factor is between 1.4 and 2.6 in distance within 30 – 40 mm of the reinforcement, with the largest reinforcement factor corresponding to a geogrid secured at 100 mm for a 150 mm diameter plate.

Geogrid stiffness and aggregate size were also investigated to determine the reinforcing effects from these materials. When the geogrid flexural stiffness was reduced by 30 %, it did not provide modulus improvement according to both rotation and P-wave velocity results although the flexural stiffness of this geogrid would classify it as a stiff geogrid. Discussions with national renowned geosynthetics designers and experts (Messrs. B. Christopher, M. Simac, R. Holtz – personal communication) indicated that flexural stiffness is an irrelevant property for base course applications where modulus is important although it may have some relevance for unpaved roads over soft subgrades where bearing capacity/rutting and

strength are important. In-plane modulus, web and node strengths are more important design considerations.

Breaker run does not effectively interlock with the geogrid because of the large mean particle size. Both P-wave velocity and particle rotation results do not effectively display either a modulus improvement or a “zone of influence”. Also Portage sand with much smaller grains did not display measurable interaction with the geogrid. Pit run sand and gravel has a mean particle size (2.5 mm) small enough to induce interlocking and engagement of the geogrid, with a “zone of influence” of 30 – 40 mm on either side of the geogrid. However, P-wave velocity results do not effectively provide a modulus improvement factor because of large particles in the material.

7 CONCLUSIONS AND RECOMMENDATIONS

The main objectives of this study were twofold: first, research was performed to determine the resilient modulus based on seismic techniques. Second, research used both seismic techniques and an analysis of shear stresses to assess the interaction of a geogrid reinforcement layer with granular base coarse material when the pavement system was loaded with a 150 mm diameter load plate up to 550 kPa.

Laboratory tests were performed to determine a relationship between resilient modulus and moduli calculated using seismic, large-scale model, and SSG tests. Each test imparts a different magnitude of strain on the sample and a correspondingly different modulus. Resilient moduli were found to be approximately 29 % of those moduli calculated using seismic methods and were typically greater than moduli calculated in large-scale cyclic load tests. A mechanistic analysis was performed to compare moduli based on increasing levels of complexity between seismic results and traditional resilient modulus results. The mechanistic analysis involves a direct relationship to modulus based on P-wave velocity with corrections for stress level, void ratio, and strain level. Ultimately, the constraint moduli acquired from P-wave velocity are converted to Young's moduli to relate mechanistically to equivalent resilient moduli.

The mechanistic analysis is an effective method to estimate resilient moduli from moduli based on P-wave velocities, with the error between results of less than 22 %. Furthermore, moduli of materials containing large grains (>25 mm) can be easily approximated with the P-wave velocity results. Modulus of materials having

particles too large to be tested in typical resilient modulus cells were analyzed using seismic methods and large-scale cyclic load tests. The moduli of aggregates with large grains were generally 40 to 50 MPa higher than those of smaller-sized aggregates, which is to be expected. However, the inability to efficiently compact materials with large grains with sufficiently high energies in the laboratory may have an effect on the corrected modulus. Field tests on the large grained materials are recommended for a more accurate modulus.

A simplified test method that can be performed on the surface of granular materials was performed and results were compared to large-scale laboratory tests. Results show that corrected summary seismic moduli calculated with the simple test performed on the surface of the soil are 14 % lower than those calculated with large-scale laboratory tests and are comparable to resilient modulus tests.

Once moduli based on P-wave velocities are calculated, an attempt was made to use the seismic modulus along with surface deflections and soil rotation to determine the “zone of influence” of a geogrid reinforced base course and a reinforcement factor of that zone. Cyclic load tests show that a shallower geogrid will most effectively limit both plastic and elastic surface deflections; however, a deeper geogrid may be more able to distribute shear stresses in subsurface materials.

Seismic methods show that material stiffness increases above the geogrid and decreases below the geogrid. The change in stiffness caused by the geogrid ranges between 1.35 and 2.66 times the change in stiffness expected from the effective stress.

Rotation measurements clearly show a “zone of influence” surrounding geogrid reinforcement when a stiff geogrid layer is incorporated into granular base course material. The “zone of influence” shifts vertically depending on the depth of the reinforcing layer. Shallower reinforcement has a greater “zone of influence” below the geogrid layer, while deeper reinforcement more effectively confines aggregates above the geogrid. Tests with granular base course and a stiff geogrid provided reinforcing effects in an area that is 30 mm in thickness on either side of a 100 mm deep geogrid. A geogrid positioned at 100 mm seems to offer the best compromise based on rotation results, surface deflections, and stiffening of the pavement system.

Measured rotations agree well with PLAXIS modeling results in both magnitude and expected rotation behavior; however, PLAXIS typically limits rotation to a smaller area around the geogrid than laboratory test results. This disagreement may be related to the influence of the accelerometers used for measuring rotations and indicate that a discrete element model may be more appropriate for analysis.

Tests using different size plates and other geogrid depths would be necessary to generalize the results presented in this research using dimensionless factors. Each geogrid/soil combination should be tested to more effectively evaluate the “zone of influence” of the geogrid on a particular material, as both the soil and geogrid have properties that potentially influence the interlocking strength of the system.

8 PRACTICAL IMPLICATIONS

The following is a brief summary of the practical implications of this research project. First, a mechanistic analysis is presented to compare the modulus calculated from P-wave velocity results to the traditional resilient modulus. Second, a simple, small-scale test is described that can be performed quickly in a 5-gallon bucket to obtain velocities and corresponding moduli. Finally, the test methods presented are shown to be useful for calculating moduli of granular soils containing large particles (>25 mm diameter) that cannot be tested in the traditional resilient modulus test. Further research demonstrated the “zone of influence” of a geogrid.

Based on the research reported above, certain observations relevant to practical applications can be advanced.

1. Pit run gravel and breaker run have P-wave calculated resilient moduli of 280 MPa and 320 MPa, respectively, at specified field compaction densities. As a means of comparison, these moduli are 25 % and 34 % greater than the moduli of grade 2 gravel at field density conditions.
2. Mean grain size relative to geogrid aperture size is an important factor to generate geogrid interaction and should be carefully considered. Materials with too large or too small mean grain size may not effectively engage the geogrid depending on the aperture size.
3. In-plane modulus, web and node strengths as well as aperture size of the geogrid should be specified for unbound material modulus improvement purposes taking into consideration of the grain size of the granular material.

4. A conservative resilient modulus improvement of 1.5 can be used with a reinforced zone thickness of 50 mm on both sizes of the geogrid.
5. There seems to be an optimum location for placing the geogrid (e.g., 100 mm below the loading plate); however, this conclusion cannot be simply extrapolated to the field without further investigation. Practical considerations also determine the location of the geogrid.

The following table summarizes the recommendations for different materials reinforced with appropriate geogrid.

Table 8.1. Recommended Moduli for Select Working Platform Materials

Working Platform Material	Recommended Modulus for Design (MPa)	Recommended Modulus for Design (psi)	Layer Coefficient	Thickness (in)	Structural Number
Breaker run stone	300	42918	0.18	16	2.8
Granular backfill Grade 2	125	17883	0.08	20	1.6
Granular backfill Grade 2 with Geogrid	188	26896	0.13	13	1.6
Pit run sand and gravel	280	40057	0.17	18	3.0
Pit run sand and gravel with geogrid	400	57225	0.21	12	2.5

8.1 SMALL SCALE SEISMIC TEST

A simplified test method to acquire seismic moduli is based on the propagation of elastic waves and offers a methodology for data acquisition and analysis to the testing scheme described in the large test cell. The granular material is compacted in a 5-gallon bucket with a volume of $19 \cdot 10^{-3} \text{ m}^3$ to minimize the required amount of material (i.e., approximately 0.31 kN of material is required - Figure A.1). Material is compacted with a tamper to ensure uniform density and the 150 mm diameter load plate is centered in the bucket.

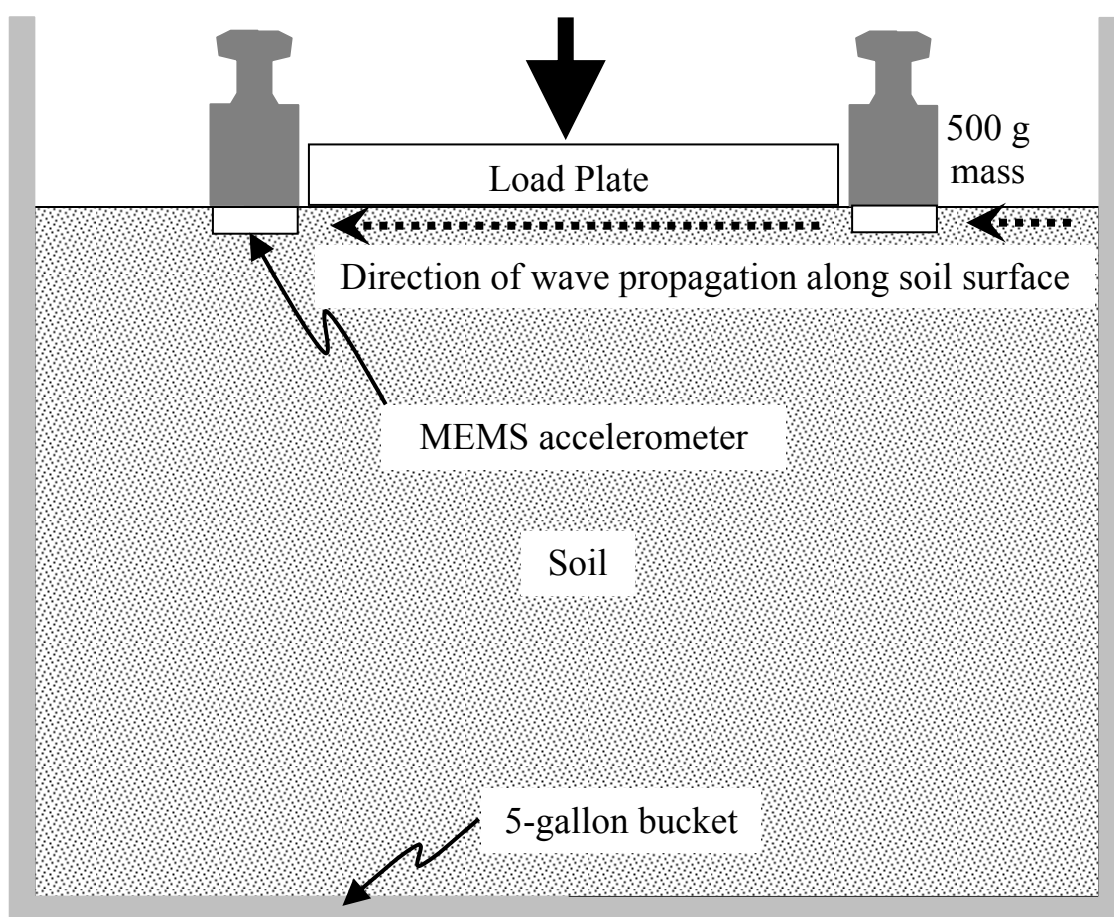


Figure 8.1. Simplified test setup to evaluate elastic wave velocities under applied stress near the surface.

Two accelerometers are placed adjacent to the plate so that sensing axes are aligned parallel to the ground surface and in the direction of wave propagation. Measure the distance between accelerometers. Static loads are applied to increase the bulk stress θ in the soil to acquire elastic wave velocities (i.e., $\theta = \sigma_t \cdot (1 + 2 \cdot K) / 3$ where σ_t is the applied vertical stress and $K \sim 0.5$ is the lateral stress coefficient). A method of applying stresses greater than 50 kPa is recommended to obtain a better comparison between modulus and stress.

The side of the 5-gallon bucket is tapped with a small hammer and the travel time of the wave between accelerometers is recorded under the plate. The measured wave velocity approaches more that of the surface waves than the P-waves. Therefore, calculated wave velocities are multiplied by a conversion factor based on the Poisson's ratio (Santamarina et al. 2001, Kramer 1996):

$$V_p = V_r \frac{(1 + \nu) \sqrt{\frac{2(1 - \nu)}{1 - 2\nu}}}{0.874 + 1.117\nu} \quad (8.1)$$

where V_r is the velocity of the surface wave. Then, the wave velocity data is reduced using the methodology presented in the section 8.2 to calculate the resilient modulus for the soil. Stress, strain, and Poisson's ration corrections are needed as in the case of the test in the large box.

Required Equipment and Instrumentation:

- Granular material (approx. 0.4 kN of material)
- 5 gallon bucket

- Tamper of Proctor hammer
- Two accelerometers
- Load plate
- Frame or weights to add surface loads.
- Hammer to trigger signals
- Oscilloscope (or data acquisition card) to collect propagation wave data and compute travel times

8.2 USE OF PROPOSED SIMPLIFIED METHODOLOGY FOR FIELD STUDIES

The methodology presented in this report justifies the use of the P-wave velocity to evaluate the resilient modulus in granular material, especially in materials with particles larger than 25 mm. The methodology can be applied to other materials to obtain an estimate of the resilient modulus in the field. The procedure is simple:

- Compact the granular material in the field and measure its density.
- Drive a truck over the spot the material needs to be tested. Determine approximately the tire pressure σ_t and calculate the bulk stress as $\theta = \sigma_t \cdot (1+2 \cdot K)/3$ (where K is the lateral stress coefficient and it can be assumed to be 0.5).
- Place next to the both sides of the truck wheel two accelerometers or standard geophones.
- Use a hammer to excite the propagation of surface waves along the axis of the accelerometers

- Measure the wave velocity as $V_p=L/\Delta t$, where L is the separation between accelerometers and Δt is the measured travel time.
- Knowing the density ρ of the compacted material, the constraint modulus can be calculated as: $D=V_p^2 \cdot \rho$.
- Calculate the resilient modulus at bulk stress θ as:

$$M_R(\theta) = 0.3 \cdot \frac{1+\nu}{1-\nu} (1-2\nu) \cdot D \quad (8.2)$$

where the factor 0.3 corresponds to the average modulus strain-degradation multiplier. Equation 8.2 may be further simplified if Poisson's ratio is assumed to be known, for example:

$$M_R(\theta) = 0.25 \cdot D \quad \text{for} \quad \nu = 0.25 \quad (8.3)$$

$$M_R(\theta) = 0.20 \cdot D \quad \text{for} \quad \nu = 0.33 \quad (8.4)$$

- Finally, the reference resilient modulus (i.e., at the reference bulk stress $\theta_{ref} = 208$ kPa) is calculated as:

$$M_R(\theta_{ref}) = M_R(\theta) \cdot \left(\frac{\theta_{ref}}{\theta} \right)^{k_2} \quad (8.5)$$

where k_2 can be assumed to be 0.5.

This methodology could rapidly estimate the field resilient modulus of granular base and subbase layers and allow the evaluation of the performance of the pavement systems using the empirical-mechanistic design procedure (NCHRP project 1-37A – NCHRP 2004).

REFERENCES

- Acar, C. and Shkel, A.M. (2003). Experimental Evaluation of Comparative Analysis of Commercial Variable-Capacitance MEMS Accelerometers. *Journal of Micromechanics and Microengineering*, Vol. 13, pp. 634 – 645.
- Achenbach, J.D. (1975). *Wave Propagation in Elastic Solids*. Elsevier Science Publishers B.V., Amsterdam, Netherlands.
- Al-Qadi, I.L., Tutumluer, E., Kwon, J., and Dessouky, S.H. (2007). Accelerated Full-Scale Testing of Geogrid-Reinforced Flexible Pavements. *86th Annual Meeting Transportation Research Board*.
- Analog Devices (2007). Analog Devices, Inc. Web Site. <http://www.analog.com>
- Bardet, J.-P. (1997). *Experimental Soil Mechanics*. Prentice Hall. Upper Saddle River, NJ.
- Bareither, C. A., Edil, T. B., Benson, C. H. and Mickelson, D. M. (2008) Geological and Physical Factors Affecting the Friction Angle of Compacted Sands, *Journal of Geotechnical and Geoenvironmental Engineering*, American Society of Civil Engineers, Vol. 134, No. 10, pp. 1476-1489.
- Barksdale, R.D., Brown, S.F., and Chan, F. (1989). Potential Benefits of Geosynthetics in Flexible Pavement Systems. *National Cooperative Highway Research Program Report 315, Transportation Research Board*, National Research Council, Washington D.C., 56 pp.
- Bender, D.A. and Barenberg, E.J. (1978). Design and Behavior of Soil-Fabric-Aggregate Systems. *Transportation Research Record 671*, pp. 64-75.
- Brinkgreve, R.B.J., ed. (2002). *PLAXIS Version 8 Manual*. A.A. Balkema Publishers, Lisse, NL.
- Camargo, F.F. (2008). Strength and Stiffness of Recycled Pavement Materials Blended with Flyash. *Master's Thesis, University of Wisconsin – Madison*.
- Christopher, B.R., Hayden, S.A., and Zhao, A. (2000). Roadway Base and Subgrade Geocomposite Drainage Layers. *Testing Performance of Geosynthetics in Subsurface Drainage, ASTM STP 1390*, West Conshohocken, PA.

- Claros, G., Hudson, W.R., and Stokoe II, K.H. (1990). Modifications to Resilient Modulus Testing Procedure and Use of Synthetic Samples for Equipment Calibration, *Transportation Research Record* 1278, pp. 51-62.
- Damasceno, V.M. (2007). Use of Electrical Resistivity Tomography to Evaluate Processes in Soils. *PhD. Thesis, University of Wisconsin – Madison*.
- DeMerchant, M.R., Valsangkar, A.J., and Shriver, A.B. (2002). Plate Load Tests on Geogrid-Reinforced Expanded Shale Lightweight Aggregate. *Geotextiles and Geomembranes*. Vol. 20, pp. 173-190.
- Ebrahimi, A., Kootstra, B., Edil, T.B. and Benson, C.H. (2008). Use of Fly Ash for Reconstruction of Bituminous Roads: Large Scale Model Experiments, Report on Tasks 2 and 3 to LRRB, Geo Engineering Report No. 08-32, Department of Civil and Environmental Engineering, University of Wisconsin-Madison.,
- Edil, T.B., Krizek, R.J., and Zelasko, J.S. (1975). Effect of Grain Characteristics on Packing of Sands, Istanbul Conference on SM and FE, Vol. 1, pp. 46-54.
- Edil, T. B. and Luh, G. F. (1978) Dynamic Modulus and Damping Relationships for Sands, *Proceedings of the Geotechnical Engineering Specialty Conference on Earthquake Engineering and Soil Dynamics*, American Society of Civil Engineers, Pasadena, California, Vol. I, pp. 394-409.
- Edil, T.B., Benson, C.H., Bin-Shafique, M.S., Tanyu, B.F., Kim, W., and Senol, A. (2002). Field Evaluation of Construction Alternatives for Roadway Over Soft Subgrade. *Transportation and Research Board: 81st Annual Meeting*. Washington D.C.
- Edil, T. B., Kim, W.-H., Benson, C. H., and Tanyu, B. F. (2003). Contribution of Geosynthetic Reinforcement to Granular Layer Stiffness, *Geo-Denver 2007* 232, 1.
- Federal Highway Administration (2003). Vehicle Registrations. Office of Highway Policy Information, United States Department of Transportation. Website: www.fhwa.dot.gov/ohim/onh00/line2.htm.
- Fratta, D., Tanner, W.M., and Damasceno, V.M. (2004). Using Elastic Waves for the Tomographic Imaging of Stresses in Soils, *Fast Times - Environmental and Engineering Geophysical Society*, pp. 37 – 45.
- Geosynthetic Materials Association (1999). GMA White Paper 1: Geosynthetics in Pavement Systems Applications-Section One: Geogrids; and Section Two: Geotextiles, Prepared for AASHTO by the GMA.

- Giroud, J.P. and Han, J. (2004). Design Method for Geogrid-Reinforced Unpaved Roads. I. Development of Design Method. *Journal of Geotechnical and Geoenvironmental Engineering*. Vol. 130, No. 8, p. 775-786.
- Gnanendran, C.T. and Selvadurai, A.P.S. (2001). Strain Measurement and Interpretation of Stabilizing Force in Geogrid Reinforcement. *Geotextiles and Geomembranes*. Vol. 19, p. 177-194.
- Graff, K.F. (1975). Wave Motion in Elastic Solids. Oxford University Press, London, England.
- Haas, R., Walls, J., and Carroll, R.G. (1989). Geogrid Reinforcement of Granular Bases in Flexible Pavements. *Transportation Research Record*, No. 1188, pp. 19-27.
- Hardin, B.O. and Richart, F.E., Jr. (1963). Elastic Wave Velocities in Granular Soils, *Journal of the Soil Mechanics and Foundations Division, Proceedings of the ASCE*, Vol. 89, No. SM 1, pp. 33 – 65.
- Hardin, B.O. and Black, W.L. (1968). Vibration Modulus of Normally Consolidated Clay. *Journal of the Soil Mechanics and Foundation Division, Proceedings of the ASCE*, Vol. 94, No. SM2, pp. 353 – 369.
- Hardin, B.O. and Drnevich, V.P. (1972). Shear Modulus and Damping in Soils: Design Equations and Curves. *Journal of the Soil Mechanics and Foundation Division, Proceedings of the ASCE*, Vol. 98, No. SM7, pp. 667 – 692.
- Hicks, R.G. and Monismith, C.L. (1971). Factors Influencing the Resilient Response of Granular Materials. *Highway Research Record*, No. 345, pp. 15 – 31.
- Holtz, R.D. and Kovacs, W.D. (1981). An Introduction to Geotechnical Engineering. Prentice Hall, Englewood Cliffs, NJ.
- Hsieh, C. and Mao, H.-L. (2005). A Bench-Scale Performance Test for Evaluation the Geosynthetic Reinforcement Effects on Granular Base Courses. *Proceedings of the Sessions of the Geo-Frontiers 2005 Congress*.
- Huang, Y.H. (1993). Pavement Analysis and Design. Prentice Hall, Englewood Cliffs, NJ.
- Huntington, G. and Ksaibati, K. (2000). Evaluation of Geogrid-Reinforced Granular Base. *Geotechnical Fabrics Report*. January/February, pp. 22-26, 28.

- Ishihara, K. (1996). *Soil Behaviour in Earthquake Engineering*. Clarendon Press. Oxford, England.
- Jáky, J. (1948). Earth Pressure in Silos, *Proceedings of the Second International Conference on Soil Mechanics and Foundation Engineering*, Rotterdam, Vol. I, pp. 103-107.
- Johnson, K.L., Kendall, K., and Roberts, A.D. (1971). Surface Energy and the Contact of Elastic Solids, *Proceedings of the Royal Society of London Series A*, Vol. 324, pp. 301-313.
- Kim, W.H., Edil, T.B., Benson, C.H., and Tanyu, B.F. (2005). Structural Contribution of Geosynthetic-Reinforced Working Platforms in Flexible Pavement. *Transportation Research Board. 84th Annual Meeting*.
- Kim, W.H. (2003). Behavior of Geosynthetic-Reinforced Aggregate Platforms Over Soft Subgrades. *PhD. Thesis, University of Wisconsin – Madison*.
- Koerner, R.M. (1998). *Designing with Geosynthetics*, 4th Edition, Prentice Hall, Upper Saddle River, NJ.
- Kokusho, T. (1980). Cyclic Triaxial Test of Dynamic Soil Properties for Wide Strain Range. *Soils and Foundations*, Vol. 20, No. 2, pp. 45-60.
- Kramer, S.L. (1996). *Geotechnical Earthquake Engineering*. Prentice Hall. Upper Saddle River, NJ.
- Kwon, J., Kim, M., and Tutumluer, E. (2005). Interface Modeling for Mechanistic Analysis of Geogrid Reinforced Flexible Pavements. *Proceedings of the Sessions of the Geo-Frontiers 2005 Conference, Austin, TX, USA*.
- Kwon, J., Tutumluer, E. and Konietzky, H. (2008) 'Aggregate base residual stresses affecting geogrid reinforced flexible pavement response', *International Journal of Pavement Engineering*, Vol. 9, No. 4, pp. 275-285.
- Lambe, T.W. and Whitman, R.V. (1969). *Soil Mechanics*, SI Version. John Wiley and Sons. New York, NY.
- Lee, J.-S. and Santamarina, J. C. (2005). Bender Elements: Performance and Signal Interpretation, *Journal of Geotechnical and Geoenvironmental Engineering*, ASCE, Vol. 131, No. 9, pp. 1063-1070.
- Leonard, M. (2000). Comparison of Manual and Automatic Onset Time Picking. *Bulletin of the Seismological Society of America*. Vol. 90, No. 6, pp. 1384-1390.

- Li, D. and Selig, E.T. (1994). Resilient Modulus for Fine-Grained Subgrade Soils. *Journal of Geotechnical Engineering*, Vol. 120, No. 6, pp. 939 – 957.
- Love, J.P., Burd, H.J., Milligan, G.W.E., and Houlsby, G.T. (1987). Analytical and Model Studies of Reinforcement of a Layer of Granular Fill on a Soft Clay Subgrade. *Canadian Geotechnical Journal*. Vol. 24, pp. 611-622.
- McDowell, G. R. Harireche, O., Konietzky, H., Brown, S.F. and Thom, N.H. (2006). Discrete Element Modeling of Geogrid-Reinforced Aggregates, *Geotechnical Engineering*, Vol. 159, No. GE1, pp. 35–48.
- Mindlin, R.D. (1949). Compliance of Elastic Bodies in Contact, *Journal of Applied Mechanics*, September, pp. 259 – 268.
- Minnesota Department of Transportation (Mn/DOT). Mn/ROAD Aggregate Profile.
- Moghaddas-Nejad F. and Small J. (2003). Resilient and Permanent Characteristics of Reinforced Granular Materials by Repeated Load Triaxial Tests. *ASTM Geotechnical Testing Journal*. Vol. 26, No. 2, pp. 152-166
- Moossazadeh, J., and Witczak, M.W. (1981). Prediction of Subgrade Moduli for Soil that Exhibits Nonlinear Behavior. *Transportation Research Record*, No. 810, pp. 9 – 17.
- National Cooperative Highway Research Program (NCHRP) 1-28 A - Laboratory Determination of Resilient Modulus for Flexible Pavement Design (2004). *Transportation Research Board of the National Academies*.
- National Road Maintenance Condition Survey: 2006 (2007). Department of Transport, United Kingdom.
- Nazarian, S., Yuan, D., and Williams, R.R. (2003). A Simple Method for Determining Modulus of Base and Subgrade Materials. *Resilient Modulus Testing for Pavement Components, ASTM STP 1437*, pp. 152 – 164.
- Perkins, S.W. and Ismeik, M. (1997). A Synthesis and Evaluation of Geosynthetic-Reinforced Base Layers in Flexible Pavements: Part I. *Geosynthetics International*. Vol. 4, No. 6, pp. 549-604.
- Perkins, S.W., Bowders, J.J., Christopher, B.R., and Berg, R.R. (2005a). Geosynthetic Reinforcement for Pavement Systems: US Perspectives, *Proceedings of the Sessions of the Geo-Frontiers 2005 Conference, Austin, TX, USA*.

- Perkins, S.W., Christopher, B.R., Eiksund, G.R., Schwartz, C.S., and Svano, G. (2005b). Modeling Effects of Reinforcement on Lateral Confinement of Roadway Aggregate. *Proceedings of the Sessions of the Geo-Frontiers 2005 Conference, Austin, TX, USA*.
- Pezo, R.F., Kim, D-S., Stokoe II, K.H., and Hudson, W.R. (1991). A Reliable Resilient Modulus Testing System. *Transportation Research Record* 1307, pp. 90-98.
- Richart, F.E., Jr., Hall, J.R., and Woods, R.D. (1970). *Vibrations of Soils and Foundations*, Prentice Hall, Inc., Eaglewood Cliffs, NJ.
- Sanchez-Salinerio, I., Roesset, J. M., and Stokoe, K. H. I. (1986). Analytical Studies of Body Wave Propagation and Attenuation, *Geotechnical Engineering*, GR86-15, University of Texas at Austin.
- Santamarina, J.C. and Fratta, D. (2005). *Discrete Signals and Inverse Problems: An Introduction for Engineers and Scientists*, John Wiley & Sons, Chichester, UK, 350 pp.
- Santamarina, J.C., Klein, K.A., and Fam, M.A. (2001). *Soils and Waves*. John Wiley & Sons Ltd., West Sussex, England, 488 pp.
- Sarsby, R.W. (1985). The Influence of Aperture Size/Particle Size on the Efficiency of Grid Reinforcement, *Proceedings of the 2nd Canadian Symposium on Geotextiles and Geomembranes*, Edmonton, Canada, The Geotechnical Society of Edmonton, pp. 212-217.
- Sawangsurriya, A. (2001). Evaluation of the Soil Stiffness Gauge. *Master's Thesis, University of Wisconsin – Madison*.
- Sprague, C.J. and Cashatt, C. (2005) Relating Geogrid Confinement Testing to Mechanistic-Empirical Base Reinforcement Design, *Geo-Frontiers 2005 Conference Proceedings, ASCE*.
- Steward, J.E., Williamson, R., and Mohny, J. (1977). Guidelines for Use of Fabrics in Construction and Maintenance of Low-Volume Roads. *USDA, Forest Service report PB-276972*, Portland, Oregon, 172 p.
- Takanami, T. and Kitagawa, G. (1991). Estimation of the Arrival Times of Seismic Waves by Multivariate Time Series Model. *Annals of the Institute of Statistical Mathematics*. Vol. 43, No. 3, pp. 407-433.
- Tanyu, B.F. (2003). Working Platforms for Flexible Pavements Using Industrial By-Products. *PhD. Thesis, University of Wisconsin – Madison*.

- Terzaghi, K. and Peck, R. B. (1967). *Soil Mechanics in Engineering Practice*, 2nd ed., John Wiley & Sons, Inc., NY.
- Tutumluer, E. and Kwon, J. (2006). Evaluation of Geosynthetics Use for Pavement Subgrade Restraint and Working Platform Construction. *Proceedings of the 13th Annual Great Lakes Geotechnical/Geoenvironmental Conference on Geotechnical Applications for Transportation Infrastructure, University of Wisconsin-Milwaukee, May, 2005.*
- Williams, R.R. and Nazarian, S. (2007). Correlation of Resilient Modulus Test Results. *Journal of Materials in Civil Engineering*. Vol. 19, No. 12, pp. 1026 – 1032.
- Wisconsin (1996). *Standard Specification for Highway and Structure Construction*, Wisconsin Department of Transportation, Madison, WI.
- Yoder, E.J. and Witczak, M.W. (1975). *Principles of Pavement Design*, 2nd ed. John Wiley & Sons Inc., NY.

Appendix A. TYPES OF ELASTIC MODULUS

The elastic modulus of soil is typically used when considering immediate settlement of a soil system. However, soil does not behave linearly except at the smallest of applied loads and the modulus changes with the amount of deformation of the soil. Several different methods of determining the elastic modulus of soil are defined on a plot of stress as a function of strain in Figure A.1. The secant modulus (E_s) is defined as the modulus at some predefined stress level (e.g., 50% σ_{max}) with respect to the origin. E_t is the tangent modulus at a single state of stress and is the slope of the tangent line drawn on the stress-strain plot. The initial tangent modulus (E_i) provides the largest predicted modulus of the soil system, but can under-predict deformation if the soil is disturbed. Nevertheless, E_i is typically used for the elastic modulus of soil since this initial straight-line portion of the stress strain curve is the only portion where the soil remains elastic (Holtz and Kovacs 1981).

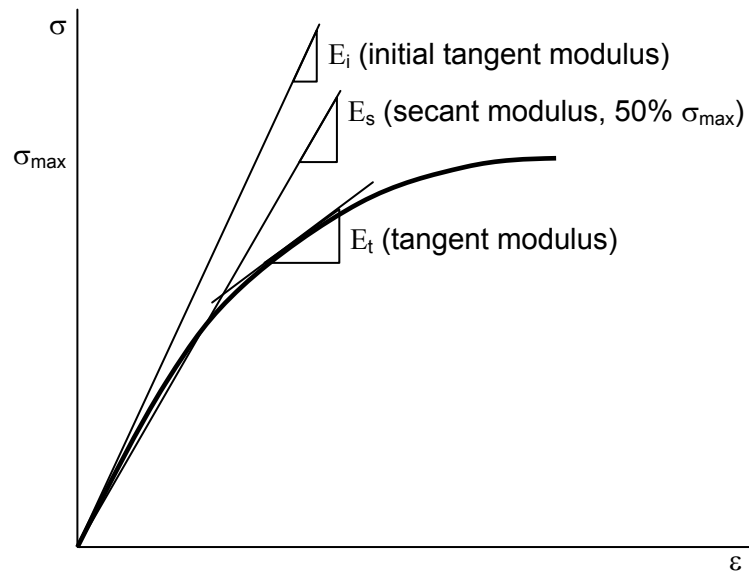


Figure A.1. Methods of determining the elastic modulus of soil.

Appendix B. SHEAR (S) WAVES

Shear waves propagate in the x direction, but particle movement is in the y direction. Figure 2.22b shows that particles move in the positive y and negative y directions as the wave propagates along the x direction. The wave equation for a shear wave is similar to that for the P-wave and is expressed below in terms of the shear modulus (Santamarina et al. 2001):

$$\frac{\partial^2 u_y}{\partial t^2} = \frac{G}{\rho} \frac{\partial^2 u_y}{\partial x^2} \quad (\text{BE.1})$$

The S-wave velocity is defined below in terms of the shear modulus and density in a similar expression to that of the P-wave (Santamarina et al. 2001):

$$V_s = \frac{\omega}{\kappa} = \sqrt{\frac{G}{\rho}} \quad (\text{BE.2})$$

The S-wave velocity can also be written in terms of the effective stress in the soil and is also related to stress by a power relationship. S-wave velocity depends not only on the effective stress parallel to wave propagation, but the effective stress perpendicular to wave propagation and parallel to particle motion (σ'_{\perp}):

$$V_s = \alpha \left(\frac{\sigma'_{\parallel} + \sigma'_{\perp}}{2p_r} \right)^{\beta} \quad (\text{BE.3})$$

Appendix C. WAVE ATTENUATION

Wave attenuation and repeatability of seismic tests can have an influence on the results obtained from seismic analyses and resulting seismic moduli. Attenuation is the loss of energy of a wave traveling through particulate media and has two primary components: geometric attenuation or spreading of the wave-front, and damping or attenuation due to frictional losses in the material (Santamarina et al. 2001; Sanchez-Salinerio et al. 1986). Wave attenuation is an important aspect of this study since the velocity calculated between accelerometers is very sensitive to attenuation, especially at the wavefront.

Geometric spreading refers to the decrease in amplitude of the wave due to an increased area over which the energy of the wave extends. The energy transmitted by a wave propagating through space becomes spread over a larger area. The amplitude of the wave (A) at a distance r from the source is proportional to the inverse of the distance r squared:

$$A \propto \frac{1}{r^2} \quad (\text{CE.1})$$

Material loss or damping is due to the frictional losses that occur when particles try to slide past one another under external forces. Wave amplitude decays exponentially with distance from the source under material losses where α is the attenuation coefficient for a specific material and r_2 and r_1 refer to two distances from the source:

$$A \propto e^{-\alpha(r_2-r_1)} \quad (\text{CE.2})$$

Equations CE.1 and CE.2 can be combined to define total attenuation, which can be written (Santamarina et al. 2001):

$$A = \left(\frac{r_2}{r_1} \right)^\zeta e^{-\alpha(r_2-r_1)} \quad (\text{CE.3})$$

where ζ represents the geometry of the propagating wave front ($\zeta = 0$ for plane waves in infinite media, $\zeta = 0.5$ for cylindrical fronts, $\zeta = 1$ for spherical fronts).

Wave attenuation has a great effect on both the amplitude of the wave and the ability to pick a first arrival. The decreased amplitude of wave propagation decreases the ability to choose a well-defined first arrival; however, at the small distances in this study less than approximately 0.5 to 1 meter, the amplitude of the wave does not greatly affect the chosen position of the first arrival.

In contrast, attenuation due to frictional losses deforms the wavefront and makes picking a first arrival difficult. Expansion of the wavefront increases as the distance from the source increases. Picking the first arrival becomes far more difficult at accelerometers far from the excitation source because of amplitude reduction and wave distortion due to both material and geometric losses.

Appendix D. PICKING THE FIRST ARRIVAL

The difficulty in picking the first arrival is present in many forms of geophysical research including seismic studies and electromagnetic studies such as ground penetrating radar (GPR). Arguably the most important part of determining the elastic velocity of soils in laboratory scale experiments is picking the travel time of the wave between accelerometers. A small variation in the arrival time of the wave to an accelerometer in a laboratory scale study can produce significant errors in the calculated velocity.

Several different methods were attempted to try and establish the time of first arrival without having to manually pick the first arrivals of each wave. Three methods of picking the first arrival are discussed below.

Akaike Information Criteria (AIC)

Travel time between arrivals was calculated based on three methods in this research project, with examples of each automatic method shown in Figure D.1. When a strong first arrival dominated (experiments with accelerometers buried at shallow depths), the Akaike Information Criteria (AIC) could be used. The AIC function (Figure D.1a) breaks the signal response into segments, calculating the variance of wave amplitude before and after each chosen time (represented by a data point). If the variance of the signal from time zero to the first arrival is below a defined level, the variance of the wave amplitude before the time is plotted. When the variance is not below the defined threshold, then the variance of the second part

of the wave amplitude is plotted. The variance of the signal prior to the first arrival should be much less than the variance of the signal once the wave arrives; therefore, the minimum value of the AIC function is the point at which the signal is most different between past and future responses (Leonard 2000; Takanami 1991). The AIC function relies on this contrast between past and future responses from each wave to determine the first arrival of the wave. Once the AIC function is applied to each wave function, the velocity is calculated by dividing the distance between accelerometers by the shifted travel time between the AIC-picked arrivals.

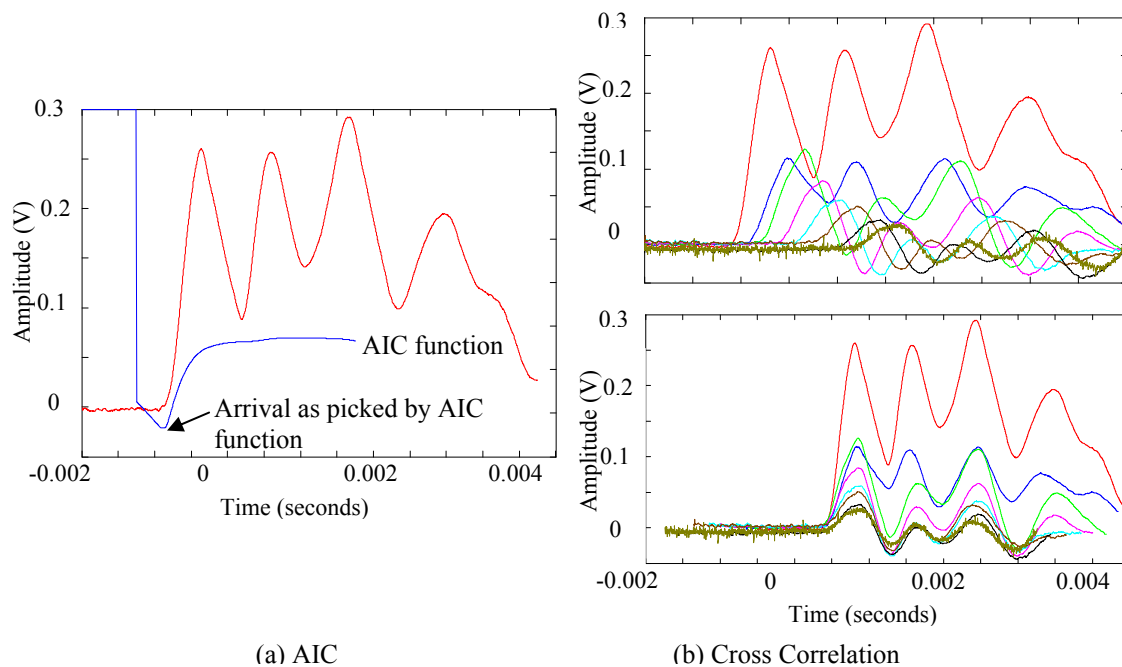


Figure D.1. (a) Single wavelet and first arrival chosen with the AIC picker function. (b) Eight P-wave signals acquired during testing and the same wavelets shifted based on the cross correlation technique. The time between arrivals corresponds to the distance shifted.

Although the AIC function effectively picks the first arrival, attenuation of the propagating wave front makes the AIC picker less efficient for waves traveling longer distances and for signals with less well defined wavefronts (Lee and Santamarina 2005). The AIC function will pick false early arrivals of the waves at greater distance from the source due to the spreading and attenuation of the wave (Santamarina et al. 2001). Figure D.2 depicts attenuation and longer wavelengths associated with wave propagation in particulate material. As the wave progresses, the wave also becomes more attenuated and the difference between past and future responses becomes muted. As a result, the AIC method may choose a false arrival due to a decreased signal to noise ratio and decreased amplitude. Figure D.3a shows the arrival of S-waves at the accelerometers and the difficulty in picking the first arrival of an S-wave. An alternative technique would be to pick arrivals by comparing the energy of waves at different depths.

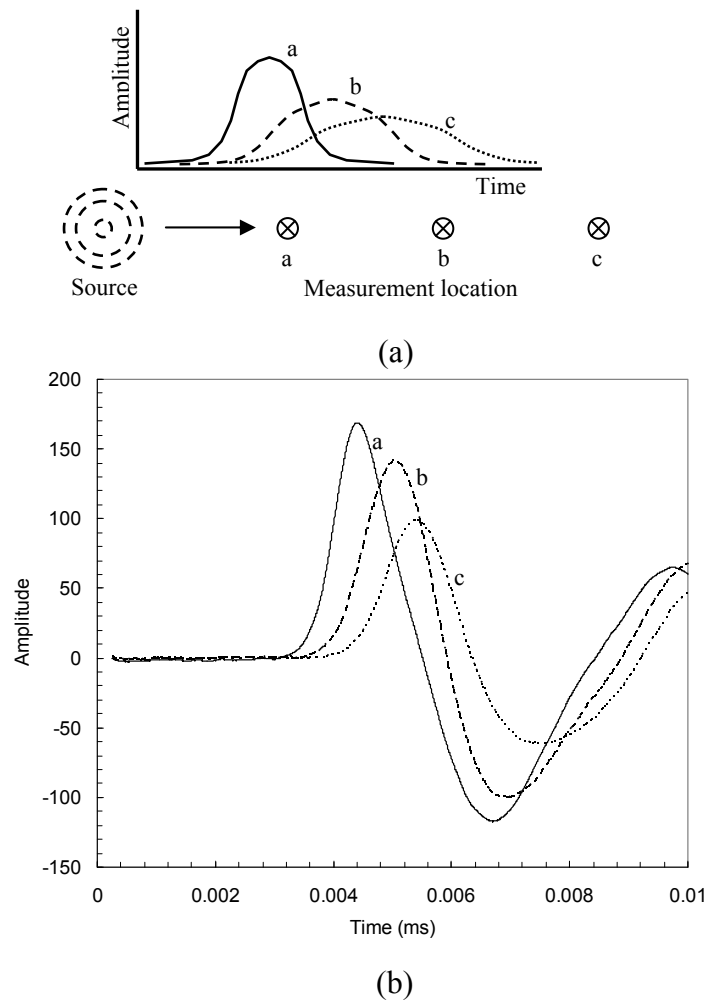


Figure D.2. Spreading of wave due to attenuation while traveling through particulate media. Theoretical behavior of waves (a) and experimental behavior seen in laboratory tests (b).

Cross Correlation

Travel time between waves can be calculated based on the energy of responses using cross correlation. Given two signals, x and z , the cross correlation function (cc) can be defined as the sum of the multiplications of functions x and z for a certain time shift, k and across all points i :

$$cc_k^{(x,z)} = \sum_i x_i z_{i+k} \quad (\text{DE.1})$$

The multiplication procedure is then repeated for different k time shifts until a maximum value of the function cc is acquired. A maximized cc function at a certain time shift k is the point at which the functions are most similar to one another. Time between arrivals is calculated based on the time shift applied to each function (Figure D.3 - Santamarina and Fratta 2005). Cross correlation is most effective when accelerometers are buried at depth and the first arrival is difficult to distinguish due to attenuation and dispersion at the front edge of an elastic wave. In particular, lower signal to noise responses such as those acquired from S-waves are more easily interpreted using the cross correlation technique. Cross correlation relies on matching wavelets together based on similarities over the amplitude-time relationship (Figure D.1b and Figure D.3). Cross correlation seems to be an effective means of aligning the energy of wave responses, but fails at defining a precise first arrival due to attenuation and change in frequency with propagation.

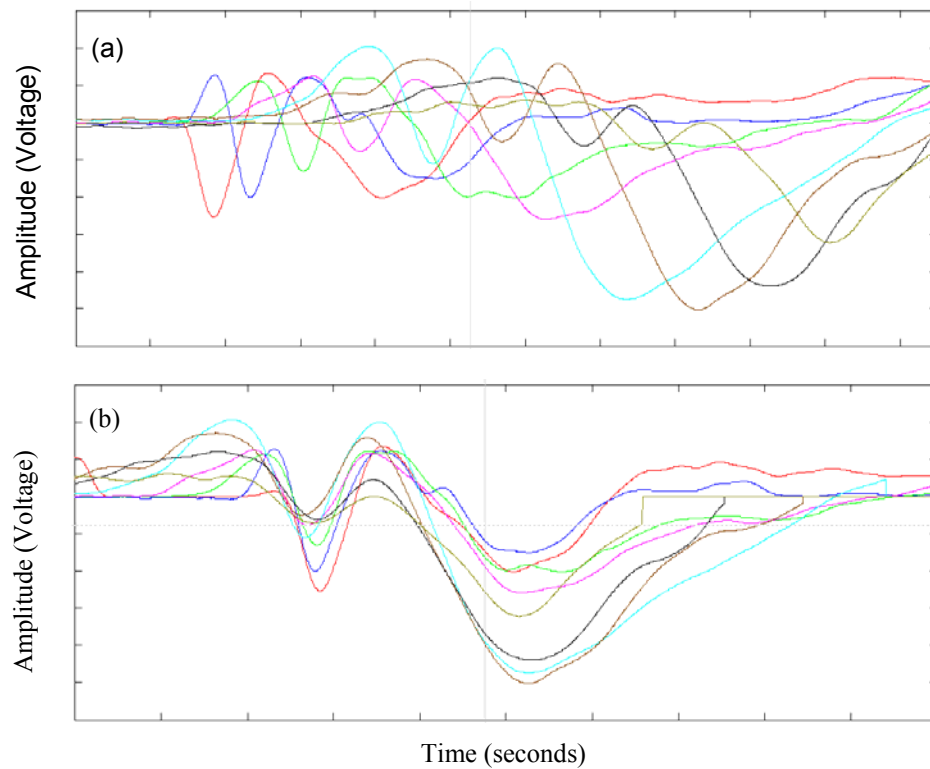


Figure D.3. (a) S-wave signals acquired during testing and (b) cross correlation of the S-wave arrivals.

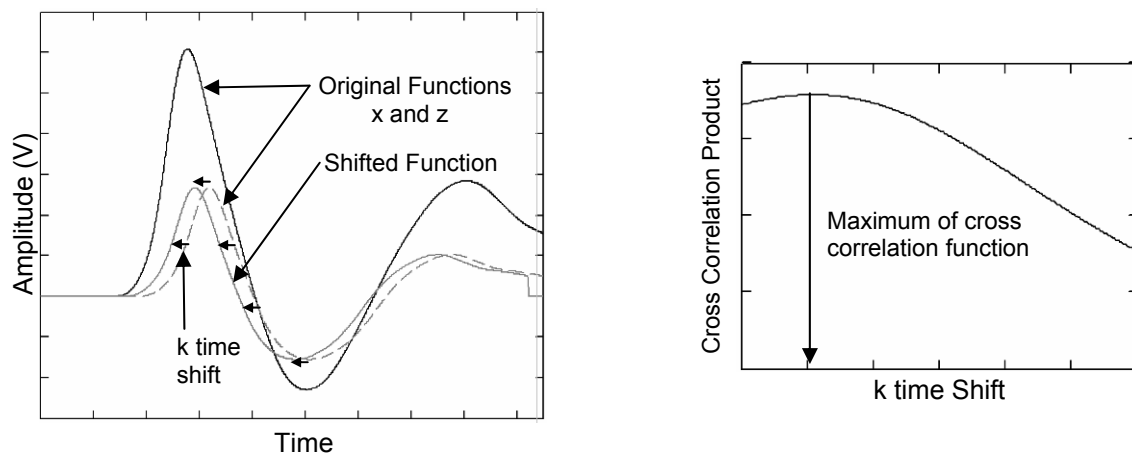


Figure D.4. (a) Cross correlation shifts the later function until it is in a position most similar to the first function. (b) The cross correlation function where the maximum value specifies the amount of time to shift the function so that it is correctly aligned.

An Analysis of the AIC Picker and Cross Correlation

The AIC picker and cross correlation seem to be good methods of picking the first arrival for several reasons:

- They are both rapid methods of determining the first arrival, especially when the first arrival is required for several functions
- The methods can be standardized and a computer can be programmed to perform the calculations identically on all datasets
- Both methods largely ignore operator bias
- Cross correlation more effectively takes the energy of the wave into consideration as well as the first arrival to avoid effects from attenuation and dispersion, especially at the wavefront

Although the AIC picker and cross correlation are fast and easy methods to calculate the first arrival of a wave, they may produce inaccurate results based on several factors noticed in this research. Waves were propagating through particulate media such as sand and gravel where the distribution of certain particles will contribute to dispersion and refraction of waves.

- Amplitude of response and differences in amplitude based on the depth of embedment of each accelerometer
- Frequency of excitation
 - The frequency of excitation caused by the source (hammer) produces a high frequency response nearer to the source that diminishes with depth as the wave attenuates (Lee and Santamarina 2005). Attenuation of the wave is proportional to

the frequency of the wave, so high frequency sources attenuate more rapidly than low frequency sources.

- Time over which performing cross correlation
 - One of the largest downfalls of using cross correlation is trying to determine the segment of the wave over which to perform the cross correlation. Should the cross correlation be performed over the entire wave, or should only the first period of the wave be considered because of attenuation and dispersion? Unfortunately, in this small laboratory study, the time over which to perform the cross correlation greatly affects the amount each wave function is shifted and the eventual calculated velocity. This problem severely limited the reliability of picking the first arrival by cross correlation.

Manual Picking

To check the validity of the AIC and cross correlation picking schemes, the travel time between waves was determined by manually picking first arrivals of each wave. Manually picking the first arrival can be tedious, but is also quite efficient when dealing with small datasets or when more accurate arrivals are required. Experiments performed in this study require an accurate and repeatable picking scheme because of the proximity of MEMS accelerometers to one another and potentially large errors in calculated velocity associated with picking the first arrival. Well defined wavefronts and wavelets with a high signal to noise ratio allow a

manual picking scheme to be effective. The waves acquired in most P-wave tests performed in this research have very high signal to noise ratios and a clearly defined wavefront is not difficult to distinguish from background noise.

When the travel time between two waves is of particular concern, picking the first arrival based on tangent lines drawn to the wavelet is most efficient. Tangent lines are drawn at two points of the arriving wavelet: the silent part of the signal prior to the wave reaching the accelerometer, and the slope immediately following the first break (Figure D.5). The intersection of the two tangent lines provides an arrival time for each wave. The velocity is calculated based on the arrival times picked by hand.

Another method to decrease errors associated with calculated velocities is to calculate velocity over a greater distance. Errors are reduced because of the increased distance and time over which the wave propagates. In most tests performed in this research, vertically spaced accelerometers were positioned approximately 5 cm apart (from center to center); however, the amount of soil between adjacent PCBs attached to each accelerometer was reduced to about 3.5 cm. The velocity can be calculated between adjacent accelerometers or accelerometers 10 cm apart to increase the resolution of velocity calculations.

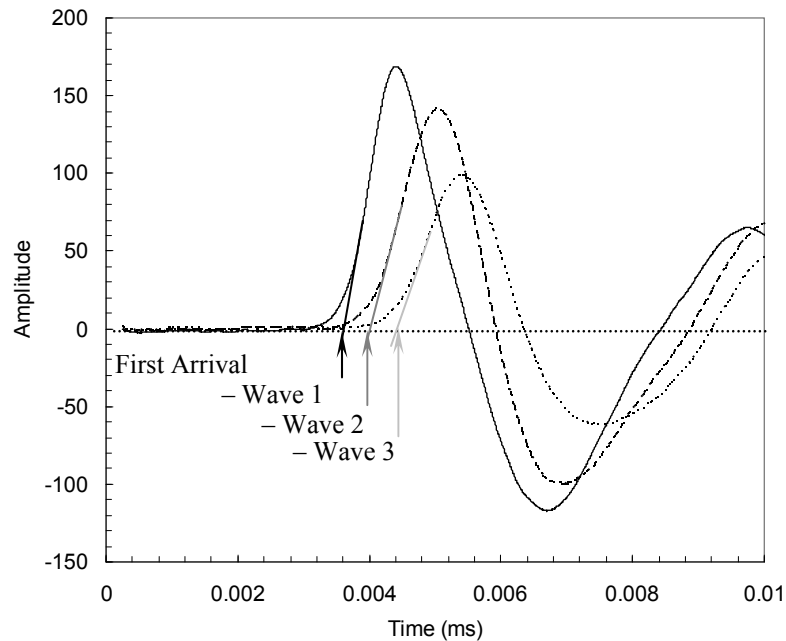


Figure D.5. Picking the first arrival manually based on tangent lines to wavelets.

The method of manually picking arrivals is both an efficient means to get the travel time between the arrival of the wave at two different accelerometer locations and a good check on the automatic picking schemes such as the AIC picker and cross correlation.

A comparison between the picker schemes is shown in Figure D.6 along with the theoretical velocities calculated based on the density of the soil and the state of stress. Evidence from the picking schemes analyzed suggests that the most effective method of picking the first arrival is the manual technique.

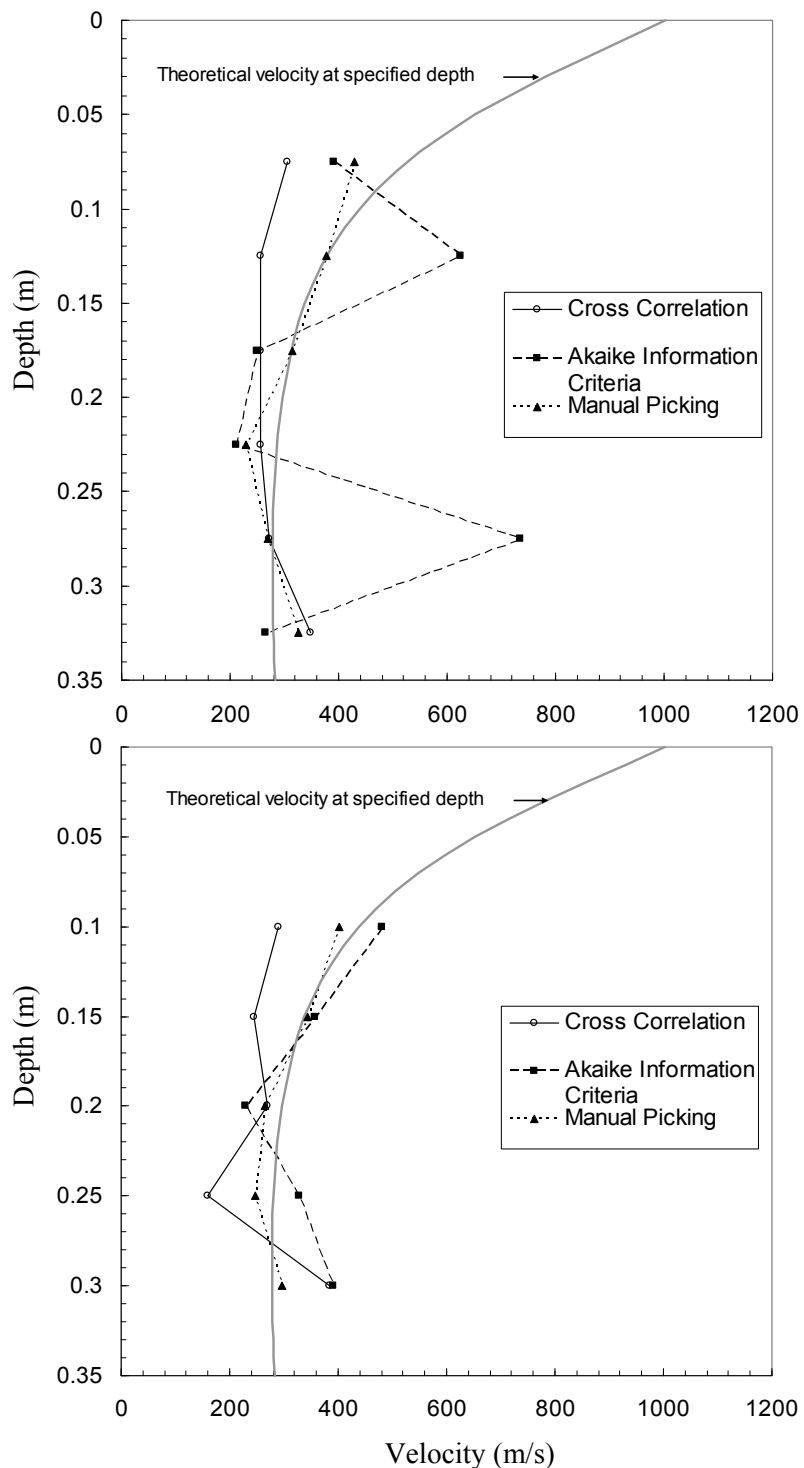


Figure D.6. a) Velocity calculated as a function of depth based on the first arrival of the wave by cross correlation, Akaike Information Criteria (AIC), and manual picking of the arrival. b) The same velocities calculated between every other MEMS accelerometer. In both cases, the grey line shows the theoretical velocity based on the compacted density and state of stress.

Appendix E. DETAILED ROUTINE OF CALCULATING ROTATION ANGLE FROM PLAXIS RESULTS

Section 2.7.1 talked about calculating soil rotation using the rotation tensor described by Achenbach (1975). Since the FE space in PLAXIS does not contain rectangular elements, an alternate method is required to use the information output by PLAXIS to calculate rotation based on the rotation tensor equation. The following discussion focuses on a routine to calculate the rotation of an average node between 4 random points in the FE space.

Consider Figure E.1 with four independent coordinates, defined with numbers 1, 2, 3, and 4. Each coordinate has an x and y position in the PLAXIS 2D FE space (i.e., point 1 will be defined with x_1 and y_1). Each of the random four coordinates also has a corresponding displacement in both the x-direction (u_x) and y-direction (u_y). The average node where the rotation will be calculated has coordinates x_{ave} and y_{ave} where:

$$x_{ave} = \frac{x_1 + x_2 + x_3 + x_4}{4} \quad (EE.1)$$

and

$$y_{ave} = \frac{y_1 + y_2 + y_3 + y_4}{4} \quad (EE.2)$$

The first part of the rotation tensor is calculated with the following expression using output PLAXIS information of x, y, and u_x :

$$\frac{\partial u_x}{\partial y} = \frac{\left(\frac{u_{x1} + u_{x2}}{2} - \frac{u_{x3} + u_{x4}}{2} \right)}{\left(\frac{y_1 + y_2}{2} - \frac{y_3 + y_4}{2} \right)} \quad (\text{EE.3})$$

That is, the derivative of u_x with respect to y is based on the average u_x of the top two nodes minus the average u_x of the bottom two nodes. The derivative of u_y with respect to x can be written in a similar manner:

$$\frac{\partial u_y}{\partial x} = \frac{\left(\frac{u_{y1} + u_{y3}}{2} - \frac{u_{y2} + u_{y4}}{2} \right)}{\left(\frac{x_1 + x_3}{2} - \frac{x_2 + x_4}{2} \right)} \quad (\text{EE.4})$$

Once equations EE.10 and EE.11 have been calculated as a function of depth, Equation (2.32) can be solved for the rotation tensor ω_{xy} . The rotation tensor can then be plotted as a function of x_{ave} and y_{ave} for several locations within the soil and compared to laboratory results.

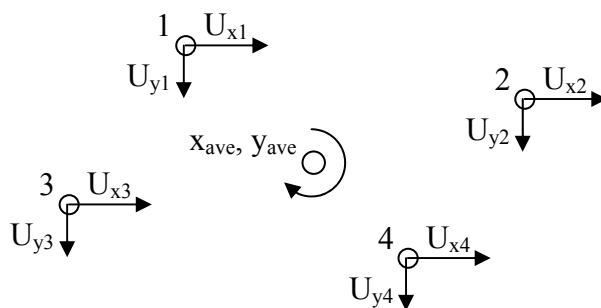


Figure E.1. Coordinate system and displacement vectors used to calculate the average rotation between particles 1, 2, 3, and 4.

Appendix F. TAMPING COMPACTION EFFORT

The tamping compactor used to compact soil in the large test cell has a weight of 10.1 kg and a compaction surface area of 413 cm². Compactive effort is defined as the force applied divided by the volume of soil compacted. A sample calculation of the compactive effort is given below in terms of energy per unit volume of soil:

$$\text{Compactive Effort} = \frac{M_H g h n b}{V} \quad (\text{FE.1})$$

where:

- M_H = hammer mass
- g = gravitational acceleration
- h = height of hammer drop
- n = number of layers
- b = number of blows per layer
- V = volume of soil compacted

$$\text{Compactive Effort} = \frac{(10 \text{ kg})(9.81 \text{ m/s}^2)(0.2 \text{ m})(3 \text{ layers})(60 \text{ blow / layer})}{0.156 \text{ m}^3} \quad (\text{FE.2})$$

$$\text{Compactive Effort} = 22.6 \text{ kJ/m}^3$$

Appendix G. SOIL STIFFNESS GAUGE (SSG) DATA

Grade 2 Gravel - No Geogrid Reinforcement
 - No Applied Load

Test number	SSG Reading (Stiffness, kN/m)
A1	2.00
A2	2.45
A3	2.20
A4	2.22
A5	2.27
A6	2.38
A7	2.23
B1	2.42
B2	2.63
B3	2.51
B4	2.63
B5	2.50
B6	2.58
Average	2.39
G, MPa ($\nu = 0.35$, $\theta = 5.5$ kPa)	20.22
G/Gmax	0.63